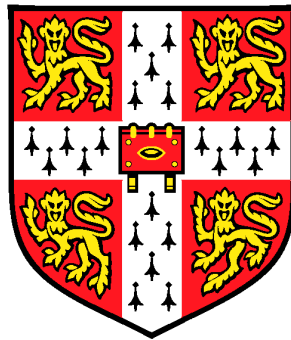


# The quasi-static and dynamic responses of metallic sandwich structures

Luc St-Pierre  
St. Catharine's College



Submitted to the University of Cambridge  
for the degree of Doctor of Philosophy

April 2012



# Preface

This thesis is submitted for the degree of Doctor of Philosophy, at the University of Cambridge. The work presented in this thesis was carried out at the Cambridge University Engineering Department from October 2007 to October 2011, under the supervision of Professor Norman A. Fleck. The research work was sponsored by the Material Innovation Institute (M2i) under the project no. MC2.06261 and by the Fonds Québécois de la Recherche sur la Nature et les Technologies (FQRNT).

This dissertation is the result of my own work and includes nothing which is the outcome of work done in collaboration except where specifically indicated in the text. This document, in whole or in parts, has not been submitted for any other degree, diploma or qualification.

This thesis contains approximately 44,000 words, 85 figures and 10 tables, which does not exceed the requirements of the Degree Committee.

Luc St-Pierre  
Cambridge, UK  
April 2012



# Summary

Lattice materials are used as the core of sandwich panels to construct light and strong structures. This thesis focuses on metallic sandwich structures and has two main objectives: (i) explore how a surface treatment can improve the strength of a lattice material and (ii) investigate the collapse response of two competing prismatic sandwich cores employed in ship hulls.

First, the finite element method is used to examine the effect of carburisation and strain hardening upon the compressive response of a pyramidal lattice made from hollow tubes or solid struts. The carburisation surface treatment increases the yield strength of the material, but its effects on pyramidal lattices are not known. Here, it is demonstrated that carburisation increases the plastic buckling strength of the lattice and reduces the slenderness ratio at which the transition from plastic to elastic buckling occurs. The predictions also showed that strain hardening increases the compressive strength of stocky lattices with a slenderness ratio inferior to ten, but without affecting the collapse mode of the lattice.

Second, the quasi-static three-point bending responses of simply supported and clamped sandwich beams with a corrugated core or a Y-frame core are compared via experiments and finite element simulations. The role of the face-sheets is assessed by considering beams with (i) front-and-back faces present and (ii) front face present, but back face absent. These two beam designs are used to represent single hull and double hull ship structures, and they are compared on an equal mass basis by doubling the thickness of the front face when the back face is absent. Beams with a corrugated core are found to be slightly stronger than those with a Y-frame core, and two collapse mechanisms are identified depending upon beam span. Short beams collapse by indentation and for this collapse mechanism, beams without a back face outperform those with front-and back faces present. In contrast, long beams fail by Brazier plastic buckling and for this collapse mechanism, the presence

of a back face strengthens the beam.

Third, drop weight tests with an impact velocity of 5 m/s are performed on simply supported and clamped sandwich beams with a corrugated core or a Y-frame core. These tests are conducted to mimic the response of a sandwich hull in a ship collision. The responses measured at 5 m/s are found to be slightly stronger than those measured quasi-statically. The measurements are in reasonable agreement with finite element predictions. In addition, the finite element method is used to investigate whether the collapse mechanism at 5 m/s is different from the one obtained quasi-statically. The predictions indicate that sandwich beams that collapse quasi-statically by indentation also fail by indentation at 5 m/s. In contrast, the simulations for beams that fail quasi-statically by Brazier plastic buckling show that they collapse by indentation at 5 m/s.

Finally, the dynamic indentation response of sandwich panels with a corrugated core or a Y-frame core is simulated using the finite element method. The panels are indented at a constant velocity ranging from quasi-static loading to 100 m/s, and two indenters are considered: a flat-bottomed indenter and a cylindrical roller. For indentation velocities representative of a ship collision, *i.e.* below 10 m/s, the predictions indicate that the force applied to the front face of the panel is approximately equal to the force transmitted to the back face. Even at such low indentation velocities, inertia stabilisation effects increase the dynamic initial peak load above its quasi-static value. This strengthening effect is more important for the corrugated core than for the Y-frame core. For velocities greater than 10 m/s, the force applied to the front face exceeds the force transmitted to the back face due to wave propagation effects. The results are also found to be very sensitive to the size of the flat-bottomed indenter; increasing its width enhances both inertia stabilisation and wave propagation effects. In contrast, increasing the roller diameter has a smaller effect on the dynamic indentation response. Lastly, it is demonstrated that material strain-rate sensitivity has a small effect on the dynamic indentation response of both corrugated and Y-frame sandwich panels.

# Acknowledgements

First, I want to thank my supervisor, Prof. Norman Fleck, and my advisor, Prof. Vikram Deshpande. I am indebted for all their contributions of time, ideas and funding that made my PhD possible. Their enthusiasm, dedication, intelligence and the quality of their work will continue to inspire me during my future career.

I would like to thank Joep Broekhuijsen of Damen Schelde Naval Shipbuilding for many insightful discussions on the Y-frame ship structure and for sharing his industrial expertise. I am also grateful to other Dutch collaborators including Bert van Haastrecht of M2i and Prof. Marc Geers and Dr. Ron Peerlings of TU Eindhoven for their feedback on the project.

I am very grateful to all the technicians that made my experimental work possible, especially Alan Heaver, Simon Marshall and Gareth Ryder. Thanks also to all my colleagues at the Centre for Micromechanics for providing an enjoyable and stimulating working environment, long-lasting friendship and numerous technical and non-technical advices.

I would like to acknowledge many people outside the department, which have contributed to balance, relaxation and fun during my studies. Thanks to my friends from St. Catharine's College — Amy, Catherine, Ivana, Julia, Nick and Rich — for making me laugh and for making the college feels like home. I am also grateful to my ice hockey teammates, especially Bill, Carl, Pete, Kevin and Owen. Playing hockey with them has been a memorable experience to say the very least.

This thesis is dedicated to my parents, Aline and Claude, who have provided constant support in all my pursuits. Thanks to Oli and all the guys from home as their friendship has not been weakened by the distance. Lastly, I would like to thank Rose for her understanding, encouragement and love that made this experience such an *incroyable* journey.



# Table of Contents

<b>Preface</b>	<b>i</b>
<b>Summary</b>	<b>iii</b>
<b>Acknowledgements</b>	<b>v</b>
<b>Table of Contents</b>	<b>vii</b>
<b>List of Figures</b>	<b>xi</b>
<b>List of Tables</b>	<b>xxi</b>
<b>1 Introduction</b>	<b>1</b>
1.1 Lattice materials . . . . .	1
1.2 Sandwich structures . . . . .	2
1.3 Scope of this thesis . . . . .	5
<b>2 Literature review</b>	<b>7</b>
2.1 Lattice materials used as core topologies . . . . .	7
2.1.1 Metal foams . . . . .	8
2.1.2 Truss cores . . . . .	9
2.1.3 Prismatic cores . . . . .	12
2.1.4 Hierarchical topologies . . . . .	14
2.1.5 Multifunctionality . . . . .	15
2.2 Sandwich structures under quasi-static three-point bending . . . . .	16
2.2.1 Collapse mechanisms . . . . .	16
2.2.2 Sandwich beams with a metal foam core . . . . .	21
2.2.3 Sandwich beams with a truss core . . . . .	21
2.2.4 Sandwich beams with a prismatic core . . . . .	22
2.2.5 Optimisation studies . . . . .	22

2.3	Lattice materials and sandwich structures under dynamic loading . . .	23
2.3.1	Dynamic compressive response of lattice materials . . . . .	24
2.3.2	Sandwich structures subjected to a low-velocity impact . . . . .	26
2.3.3	Sandwich structures subjected to blast loading . . . . .	27
2.4	Ship hull design . . . . .	29
2.4.1	Regulations . . . . .	30
2.4.2	Evaluating the resistance of ship hulls . . . . .	30
2.4.3	Design against collision and grounding . . . . .	31
2.4.4	Development of the Y-frame sandwich hull design . . . . .	32
2.5	Concluding remarks . . . . .	34
<b>3</b>	<b>Compressive response of a carburised pyramidal lattice</b>	<b>37</b>
3.1	Introduction . . . . .	38
3.2	Geometry and analytical collapse load of the pyramidal lattice . . . . .	41
3.2.1	Relative density . . . . .	41
3.2.2	Analytical collapse load . . . . .	42
3.3	Influence of strain hardening . . . . .	43
3.3.1	Description of the finite element models . . . . .	43
3.3.2	Results for an inclined tube . . . . .	45
3.3.3	Results for an inclined solid strut . . . . .	48
3.3.4	Comparison between tube and solid strut . . . . .	49
3.4	Influence of carburisation . . . . .	53
3.4.1	Description of the finite element models . . . . .	54
3.4.2	Results for an inclined tube . . . . .	55
3.4.3	Results for an inclined solid strut . . . . .	58
3.4.4	Comparison between tube and solid strut . . . . .	61
3.4.5	Position of carburised lattices on the strength-density chart . . . . .	62
3.5	Concluding remarks . . . . .	63
3.A	Influence of geometric imperfections . . . . .	64
3.A.1	Influence of the number of superimposed modes . . . . .	65
3.A.2	Influence of amplitude . . . . .	66
3.A.3	Influence of imperfection on the deformed meshes . . . . .	67
<b>4</b>	<b>The influence of the back face on the bending response of prismatic sandwich beams</b>	<b>69</b>
4.1	Introduction . . . . .	70
4.1.1	Choice of test material . . . . .	72

4.1.2	Scope of study . . . . .	73
4.2	Methodology . . . . .	74
4.2.1	Specimen manufacture . . . . .	74
4.2.2	Geometry of the three-point bending tests . . . . .	76
4.2.3	Finite element models . . . . .	78
4.3	Experimental results . . . . .	79
4.3.1	Simply supported beams . . . . .	79
4.3.2	Clamped beams . . . . .	82
4.3.3	Collapse mechanisms . . . . .	82
4.4	Finite element predictions . . . . .	88
4.4.1	Comparison between measurements and simulations . . . . .	88
4.4.2	Sensitivity of the sandwich panel response to span and proportion of mass in the core . . . . .	89
4.5	Concluding remarks . . . . .	100
4.A	Influence of parent material . . . . .	101
<b>5</b>	<b>Drop weight tests on prismatic sandwich beams</b>	<b>103</b>
5.1	Introduction . . . . .	104
5.2	Methodology . . . . .	105
5.2.1	Geometry of the tested sandwich beams . . . . .	105
5.2.2	Drop weight apparatus . . . . .	106
5.2.3	Finite element models . . . . .	106
5.3	Experimental results . . . . .	110
5.3.1	Simply supported beams . . . . .	110
5.3.2	Clamped beams . . . . .	112
5.3.3	Collapse mechanisms . . . . .	114
5.4	Finite element predictions . . . . .	114
5.4.1	Comparison between simulations and measurements . . . . .	116
5.4.2	Sensitivity of the peak load and collapse mechanism to the loading velocity . . . . .	117
5.5	Concluding remarks . . . . .	120
5.A	Finite element predictions with the projectile and roller modelled as deformable parts . . . . .	120
5.A.1	Simulations without the rubber pad . . . . .	121
5.A.2	Simulations with the rubber pad . . . . .	123
5.B	Analytical prediction of the contact force . . . . .	125

<b>6</b>	<b>Dynamic indentation of prismatic sandwich panels</b>	<b>127</b>
6.1	Introduction . . . . .	128
6.1.1	Review of the dynamic uniform compressive response . . . . .	129
6.1.2	Scope of study . . . . .	133
6.2	Finite element models . . . . .	133
6.2.1	Geometric imperfections . . . . .	134
6.2.2	Material properties . . . . .	135
6.3	Results . . . . .	135
6.3.1	Indentation responses . . . . .	135
6.3.2	Deformed meshes . . . . .	136
6.3.3	Influence of velocity . . . . .	141
6.3.4	Influence of indenter size . . . . .	143
6.3.5	Force distribution on the back face . . . . .	146
6.3.6	Influence of material strain-rate sensitivity . . . . .	147
6.4	Concluding remarks . . . . .	149
6.A	Finite element model for uniform compression . . . . .	150
<b>7</b>	<b>Conclusions and future work</b>	<b>151</b>
7.1	Compressive response of a carburised pyramidal lattice . . . . .	151
7.2	The influence of the back face on the bending response of prismatic sandwich beams . . . . .	152
7.3	Drop weight tests on prismatic sandwich beams . . . . .	152
7.4	Dynamic indentation of prismatic sandwich panels . . . . .	153
7.5	Future work . . . . .	154
7.5.1	Dynamic compressive response of a hollow pyramidal lattice . . . . .	154
7.5.2	Measured compressive response of a carburised pyramidal lattice . . . . .	154
7.5.3	Fracture of corrugated and Y-frame sandwich panels . . . . .	155
	<b>Bibliography</b>	<b>157</b>

# List of Figures

1.1	Material property chart of strength versus density for lattice and fully-dense engineering materials. Text boxes are used to distinguish lattice materials from fully-dense materials. Adapted from Russell (2009).	2
1.2	Examples of sandwich structures in nature: bird skulls of (a) a magpie and (b) a long-eared owl. Adapted from Gibson et al. (2010).	3
1.3	Examples of sandwich structures in industrial applications: (a) the car body of a high speed train in Japan (Shinkansen 700 series) and (b) Y-frame ship hull design developed by Damen Schelde Naval Shipbuilding. Adapted from Matsumoto et al. (1999) and McShane (2007).	4
2.1	Classification of lattice materials proposed by Evans et al. (2001) and Wadley (2002).	8
2.2	Aluminium metal foams with (a) closed-cell and (b) open-cell. Reproduced from Paul and Ramamurty (2000) and Nieha et al. (2000).	9
2.3	Relative strength as a function of relative density $\bar{\rho}$ for different core topologies. The relative strength is defined as the compressive strength of the core $\bar{\sigma}_{pk}$ divided by the yield strength of the material $\sigma_Y$ . Examples of (b) bending- and (c) stretching-dominated lattices. Adapted from Ashby (2005).	10
2.4	Examples of truss cores: (a) tetrahedral, (b) pyramidal and (c) Kagomé lattices. Reproduced from Kooistra and Wadley (2007).	10
2.5	Two manufacturing routes for truss cores: (a) perforating and folding and (b) slitting, flattening and folding. Reproduced from Kooistra and Wadley (2007).	11
2.6	Lattices made from hollow tubes arranged in (a) square and (b) diamond orientations. Reproduced from Queheillalt and Wadley (2005a).	12

2.7	Measured normalised peak strength of stainless steel lattices loaded in (a) compression and (b) shear. The lattice compressive strength $\bar{\sigma}_{pk}$ and shear strength $\bar{\tau}_{pk}$ are normalised by the relative density $\bar{\rho}$ and the yield strength of stainless steel $\sigma_Y$ . Data taken from Côté et al. (2004); Côté et al. (2006); Queheillalt and Wadley (2011); Rubino et al. (2008a); Zok et al. (2004). . . . .	13
2.8	Examples of prismatic cores: (a) corrugated, (b) Y-frame, (c) square honeycomb and (d) diamond cores. Reproduced from Zok et al. (2005) and Côté et al. (2006). . . . .	13
2.9	Photographs showing the collapse mechanisms of (a) second order and (b) first order corrugated cores, both with a relative density $\bar{\rho} = 0.02$ . Reproduced from Kooistra et al. (2007). . . . .	15
2.10	A sandwich beam with a metal foam core loaded in three-point bending that collapsed by (a) face yield, (b) core shear (mode B) and (c) indentation. For each collapse mechanism, simply supported and clamped sandwich beams are shown. Reproduced from Tagarielli and Fleck (2005). . . . .	16
2.11	(a) Simply supported and (b) clamped sandwich panels loaded in three-point bending. . . . .	17
2.12	Face yield collapse mechanism for (a) simply supported and (b) clamped sandwich panels. . . . .	18
2.13	Core shear collapse mechanisms: (a) mode A and (b) mode B. . . . .	18
2.14	Indentation collapse mechanism. . . . .	19
2.15	Collapse mechanism maps for a simply supported sandwich panel: (a) contours of normalised collapse load $\bar{F} = F/(2bL\sigma_Y^f)$ for $a/(2L) = 0.1$ and (b) influence of the normalised indenter size $a/(2L)$ upon the operative collapse mechanism. In both cases, $\sigma_Y^c/\sigma_Y^f = 0.005$ and $\tau_Y^c/\sigma_Y^f = 0.005$ . Adapted from Ashby et al. (2000). . . . .	21
2.16	A simply supported sandwich beam with a Y-frame core loaded in three-point bending and collapsing by indentation: (a) experiment and (b) finite element prediction. A side view showing half the beam (left) and a view of the core deformation obtained by sectioning the beam at mid-span (right) are included. Reproduced from Rubino et al. (2010). . . . .	23
2.17	Direct impact Kolsky bar setup in (a) back face and (b) front face configurations. Adapted from Lee et al. (2006). . . . .	25

2.18	Normalised maximum back face deflection $w/L$ as a function of the normalised blast impulse $I/(M\sqrt{\sigma_Y/\rho_f})$ . Adapted from Rathbun et al. (2006a). . . . .	28
2.19	Photographs and finite element simulations of (a) monolithic, (b) Y-frame and (c) corrugated plates impacted by a metal foam projectile with a momentum of 3 kNs/m <sup>2</sup> . All plates have the same mass. Reproduced from Rubino et al. (2009). . . . .	29
2.20	Four hull designs considered in full-scale collision tests: (a) a conventional single hull, (b) a conventional double hull, (c) a double hull with a Y-frame core and (d) a double hull made from two corrugated panels. Adapted from ISSC (2006a). . . . .	33
2.21	Photographs of full-scale collision tests performed on the Y-frame double hull structure. Adapted from Konter et al. (2004) and Wevers and Vredeveldt (1999). . . . .	33
2.22	Construction of inland waterway tankers with a Y-frame single hull structure. Adapted from Graaf et al. (2004) and Vredeveldt and Roeters (2004). . . . .	34
3.1	(a) Unit cell of the hollow pyramidal lattice. (b) Top view of the lattice.	39
3.2	Collapse mechanism map for a hollow pyramidal lattice made from AISI 304 stainless steel. Examples of the six collapse modes (A-F) are also included. Representative geometries considered in this study are indicated by filled black circles and contours of relative density $\bar{\rho}$ are plotted as grey lines. Adapted from Pingle et al. (2011a). . . . .	40
3.3	Finite element model used to simulate the compressive response of an inclined tube. . . . .	44
3.4	Uniaxial tensile responses of the two material models employed in the finite element simulations analysing the influence of strain hardening.	45
3.5	Influence of the strain hardening modulus $E_t$ on the compressive response of an inclined tube $t/d = 0.1$ . Results are given for (a) $l/d = 1$ , (b) $l/d = 3$ , (c) $l/d = 20$ (d) $l/d = 100$ . . . . .	46
3.6	Influence of the strain hardening modulus $E_t$ on the compressive response of an inclined solid strut $t/d = 0.5$ . Results are given for (a) $l/d = 3$ , (b) $l/d = 20$ and (c) $l/d = 100$ . . . . .	50
3.7	Influence of the strain hardening modulus $E_t$ on the compressive strength of an inclined tube $t/d = 0.1$ and an inclined solid strut $t/d = 0.5$ . . . . .	52

3.8	Cross-sections of a carburised (a) tube and (b) solid strut. . . . .	53
3.9	Uniaxial tensile responses of annealed and carburised stainless steels employed in the finite element simulations analysing the influence of carburisation. . . . .	54
3.10	Influence of the carburisation depth $h/d$ on the compressive response of an inclined tube $t/d = 0.1$ . Results are given for (a) $l/d = 1$ , (b) $l/d = 3$ , (c) $l/d = 20$ (d) $l/d = 100$ . . . . .	56
3.11	Influence of the carburisation depth $h/d$ on the compressive response of an inclined solid strut $t/d = 0.5$ . Results are given for (a) $l/d = 3$ , (b) $l/d = 20$ and (c) $l/d = 100$ . . . . .	59
3.12	Influence of the carburisation depth $h/d$ on the compressive strength of an inclined tube $t/d = 0.1$ and an inclined solid strut $t/d = 0.5$ . . .	61
3.13	Strength versus density material chart. The simulated compressive strength of a pyramidal lattice made from carburised tubes ( $t/d = 0.1$ , $h/d = 0.05$ ) is also included. Al, aluminium; CRFP, carbon fibre reinforced polymers; Ti, titanium; TMC, titanium matrix composites. . . . .	63
3.14	Influence of imperfection shape on the compressive response of an inclined tube $t/d = 0.1$ . In all cases, the imperfection amplitude is $\zeta = 0.05t$ . Results are given for (a) $l/d = 1$ , (b) $l/d = 3$ , (c) $l/d = 20$ (d) $l/d = 100$ . . . . .	65
3.15	Influence of imperfection amplitude on the compressive response of an inclined tube $t/d = 0.1$ . In all cases, the imperfection shape is in the form of the 1 <sup>st</sup> buckling mode. Results are given for (a) $l/d = 1$ , (b) $l/d = 3$ , (c) $l/d = 20$ (d) $l/d = 100$ . . . . .	66
4.1	The Y-frame sandwich core in (a) double hull and (b) single hull designs. . . . .	71
4.2	The design space for mass distribution within a sandwich panel of areal mass $m$ . The proportion of mass in the core, in the front face and in the back face are denoted by $m_c/m$ , $m_f/m$ and $m_b/m$ , respectively. The mass distribution of the test geometries is indicated for two choices of areal mass. . . . .	72
4.3	Measured uniaxial tensile responses of as-brazed AISI 304 stainless steel and Lloyd's Grade A steel, at a strain rate of $10^{-3} \text{ s}^{-1}$ . . . . .	73
4.4	Cross-sectional dimensions of the sandwich beams: (a) corrugated core and (b) Y-frame core. (c) The chosen values of face-sheet thickness used in the experimental study. All dimensions are in mm. . . . .	75

4.5	The test fixtures used for (a) simply supported and (b) clamped beams. A sandwich beam with a Y-frame core and without a back face is shown. All dimensions are in mm. . . . .	77
4.6	Three-point bending responses of simply supported sandwich beams. Sandwich beams with an areal mass $m = 9.1 \text{ kg/m}^2$ are shown with (a) a corrugated core and (b) a Y-frame core. Likewise, sandwich beams with an areal mass $m = 13.8 \text{ kg/m}^2$ are shown with (c) a corrugated core and (d) a Y-frame core. . . . .	80
4.7	Three-point bending responses of clamped sandwich beams. Sandwich beams with an areal mass $m = 9.1 \text{ kg/m}^2$ are shown with (a) a corrugated core and (b) a Y-frame core. Likewise, sandwich beams with an areal mass $m = 13.8 \text{ kg/m}^2$ are shown with (c) a corrugated core and (d) a Y-frame core. . . . .	81
4.8	Photographs of the simply supported sandwich beams with a corrugated core ( $m = 13.8 \text{ kg/m}^2$ ) (a) with front-and-back faces and (b) without a back face. Deformed finite element meshes of the same sandwich beam (c) with front-and-back faces and (d) without a back face. A side view showing half of the beam and a view of the core deformation at mid-span are given. To clarify the predicted deformation modes, the undeformed (dashed line) and deformed (solid line) cross-sections at mid-span are included in (c) and (d). The images are for beams loaded to $\delta = 0.2L$ and then unloaded. . . . .	83
4.9	Photographs of the simply supported sandwich beams with a Y-frame core ( $m = 13.8 \text{ kg/m}^2$ ) (a) with front-and-back faces and (b) without a back face. Deformed finite element meshes of the same sandwich beam (c) with front-and-back faces and (d) without a back face. A side view showing half of the beam and a view of the core deformation at mid-span are given. To clarify the predicted deformation modes, the undeformed (dashed line) and deformed (solid line) cross-sections at mid-span are included in (c) and (d). The images are for beams loaded to $\delta = 0.2L$ and then unloaded. . . . .	84

4.10	Photographs of the clamped sandwich beams with a corrugated core ( $m = 13.8 \text{ kg/m}^2$ ) (a) with front-and-back faces and (b) without a back face. Deformed finite element meshes of the same sandwich beam (c) with front-and-back faces and (d) without a back face. A side view showing half of the beam and a view of the core deformation at mid-span are given. To clarify the predicted deformation modes, the undeformed (dashed line) and deformed (solid line) cross-sections at mid-span are included in (c) and (d). The images are for beams loaded to $\delta = 0.2L$ and then unloaded. . . . .	85
4.11	Photographs of the clamped sandwich beams with a Y-frame core ( $m = 13.8 \text{ kg/m}^2$ ) (a) with front-and-back faces and (b) without a back face. Deformed finite element meshes of the same sandwich beam (c) with front-and-back faces and (d) without a back face. A side view showing half of the beam and a view of the core deformation at mid-span are given. To clarify the predicted deformation modes, the undeformed (dashed line) and deformed (solid line) cross-sections at mid-span are included in (c) and (d). The images are for beams loaded to $\delta = 0.2L$ and then unloaded. . . . .	86
4.12	Cross-sectional dimensions of the sandwich panels considered in the numerical analysis: (a) corrugated core and (b) Y-frame core. (c) The sandwich panels, shown here with a corrugated core, are simply supported and loaded in three-point bending. . . . .	91
4.13	Normalised peak load $\hat{F} = F_{pk}/(\sigma_Y bc)$ as a function of the normalised span $2L/c$ for simply supported sandwich panels and selected values of $m_c/m$ ( $m/(\rho c) = 0.052$ ). Results are shown for sandwich panels with (a) a corrugated core and (b) a Y-frame core. . . . .	94
4.14	The boundary conditions on finite element models to simulate (a) indentation and (b) bending. A sandwich panel without a back face is shown. . . . .	95
4.15	(a) The predicted indentation response of sandwich panels with $m_c/m = 0.5$ resting on a rigid foundation. (b) Normalised indentation strength $\hat{F}_I = F_I/(\sigma_Y bc)$ as a function of $m_c/m$ ( $m/(\rho c) = 0.052$ ). . . . .	95
4.16	(a) The predicted bending response of sandwich panels with $m_c/m = 0.5$ . (b) Normalised Brazier buckling moment $\hat{M} = M_B/(\sigma_Y bc^2)$ as a function of $m_c/m$ ( $m/(\rho c) = 0.052$ ). . . . .	97

4.17	Normalised peak load $\hat{F} = F_{pk}/(\sigma_Y bc)$ as a function of the normalised span $2L/c$ for simply supported sandwich panels and selected values of $m_c/m$ ( $m/(\rho c) = 0.052$ ). The three-point bending results are reproduced from Fig. 4.13. The indentation and Brazier buckling strengths are included as short and long dashed lines, respectively. Sandwich panels with front-and-back faces are shown with (a) a corrugated core and (b) a Y-frame core. Likewise, sandwich panels without a back face are shown with (c) a corrugated core and (d) a Y-frame core. . . . .	98
4.18	Normalised indentation strength per unit mass $\rho c \hat{F}_I/m$ as a function of $m_c/m$ for selected values of $m/(\rho c)$ . Results are shown for sandwich panels with (a) a corrugated core and (b) a Y-frame core. . . . .	100
4.19	Normalised Brazier buckling moment per unit mass $\rho c \hat{M}/m$ as a function of $m_c/m$ for selected values of $m/(\rho c)$ . Results are shown for sandwich panels (a) with front-and-back faces present and (b) without a back face. . . . .	100
4.20	Sensitivity of the three-point bending response of a sandwich beam with a Y-frame core to the choice of material. (a) Front-and-back faces are present and (b) the back face is absent. . . . .	102
5.1	Cross-sectional dimensions of the tested sandwich beams with (a) a corrugated core and (b) a Y-frame core. All dimensions are in mm. . . . .	105
5.2	Experimental setup used to perform drop weight tests at 5 m/s on (a) simply supported and (b) clamped sandwich beams. A sandwich beam with a corrugated core is shown. All dimensions are in mm. . . . .	107
5.3	Finite element models used to simulate the drop weight tests on (a) simply supported and (b) clamped sandwich beams. All dimensions are in mm. . . . .	108
5.4	(a) The quasi-static ( $\dot{\epsilon}_p = 10^{-3} \text{ s}^{-1}$ ) uniaxial tensile response of AISI 304 stainless steel and the estimated high strain-rate responses based on the data of Stout and Follansbee (1986). (b) Dynamic strengthening ratio $R$ as a function of plastic strain rate $\dot{\epsilon}_p$ . . . . .	109
5.5	Quasi-static and 5 m/s responses of simply supported sandwich beams with (a) a corrugated core and (b) a Y-frame core. . . . .	111
5.6	Influence of the mid-span roller mass upon the measured 5 m/s response of a simply supported sandwich beam with a Y-frame core. The measured response with a steel mid-span roller is reproduced from Fig. 5.5(b). . . . .	112

5.7	Quasi-static and 5 m/s responses of clamped sandwich beams with (a) a corrugated core and (b) a Y-frame core. . . . .	113
5.8	High-speed images captured during a drop weight test at 5 m/s on (a) a simply supported and (b) a clamped sandwich beam with a Y-frame core. The deformed beams are shown for two selected values of mid-span roller displacement $\delta/L$ . All images are showing a side view of the beam. . . . .	115
5.9	FE predictions of the quasi-static and 5 m/s responses of simply supported and clamped sandwich beams. Beams with front-and-back faces are shown with (a) a corrugated core and (b) a Y-frame core. Likewise, beams with the back face absent are shown with (a) a corrugated core and (b) a Y-frame core. Beams with front-and-back faces present collapse quasi-statically by indentation whereas those with the back face absent fail quasi-statically by Brazier plastic buckling. . . . .	118
5.10	Finite element model with the projectile and the assembly of the load cell and mid-span roller modelled as two separate deformable parts. The model is shown for a simply supported sandwich beam with a corrugated core. All dimensions in mm. . . . .	121
5.11	Simulated 5 m/s response of a simply supported beam with a corrugated core. The projectile and the mid-span roller are modelled as separate deformable parts in the simulations. The contact forces between (a) the projectile and the mid-span roller and (b) the mid-span roller and the beam are given. The simulations presented in Section 5.4.1 where the projectile and mid-span roller were modelled as one rigid body are included in part (b) for comparison. . . . .	122
5.12	(a) Measured quasi-static ( $\dot{\epsilon} = 10^{-3} \text{ s}^{-1}$ ) compressive response of the rubber pad used in the drop weight experiments. (b) Comparison between the measured and simulated 5 m/s responses of a simply supported beam with a corrugated core. The measured response is reproduced from Fig. 5.5(a) whereas the simulations are using the data shown in part (a) to model the contact between the projectile and the mid-span roller. . . . .	124
5.13	Analytical model to predict the contact force between the projectile and the assembly of the mid-span roller and load cell. . . . .	125

6.1	Finite element models used to simulate (a) uniform compression, (b) indentation by a flat-bottomed indenter and (c) indentation by a cylindrical roller. The models are shown for a sandwich panel with a Y-frame core. All dimensions are in mm. . . . .	130
6.2	Uniform compressive responses of sandwich panels with (a) a corrugated core and (b) a Y-frame core. Results are given for quasi-static loading and for crushing at 10 m/s. These simulations were re-executed based on previous work done by Tilbrook et al. (2007). . . . .	131
6.3	(a) The normalised peak stress and (b) the normalised average stress up to $\delta/c = 0.2$ for corrugated and Y-frame sandwich cores crushed at a constant velocity $V_0$ . Those simulations were re-executed based on previous work done by Tilbrook et al. (2007). . . . .	132
6.4	Cross-sectional dimensions of the sandwich panels: (a) corrugated core and (b) Y-frame core. All dimensions in mm. . . . .	133
6.5	Responses of sandwich panels indented by a flat-bottomed indenter of normalised width $a/L = 0.05$ . Results are shown at selected velocities: quasi-static and 1 m/s for (a) corrugated core and (b) Y-frame core; 10 m/s for (c) corrugated core and (d) Y-frame core and 100 m/s for (e) corrugated core and (f) Y-frame core. . . . .	137
6.6	Responses of sandwich panels indented by a cylindrical roller of normalised diameter $D/c = 0.41$ . Results are shown at selected velocities: quasi-static and 1 m/s for (a) corrugated core and (b) Y-frame core; 10 m/s for (c) corrugated core and (d) Y-frame core and 100 m/s for (e) corrugated core and (f) Y-frame core. . . . .	138
6.7	(a) The normalised initial peak load and (b) the normalised average load up to $\delta/c = 0.2$ for corrugated and Y-frame sandwich panels indented at a constant velocity $V_0$ by a flat-bottomed indenter of normalised width $a/L = 0.05$ . . . . .	142
6.8	(a) The normalised initial peak load and (b) the normalised average load up to $\delta/c = 0.2$ for corrugated and Y-frame sandwich panels indented at a constant velocity $V_0$ by a cylindrical roller of normalised diameter $D/c = 0.41$ . . . . .	142
6.9	Influence of the normalised width $a/L$ of the flat-bottomed indenter on the normalised initial peak load for (a) the corrugated core and (b) the Y-frame core. Likewise, the influence of $a/L$ on the normalised average load up to $\delta/c = 0.2$ is shown for (c) the corrugated core and (d) the Y-frame core. . . . .	144

6.10	Influence of normalised roller diameter $D/c$ on the normalised initial peak load for (a) the corrugated core and (b) the Y-frame core. Likewise, the influence of $D/c$ on the normalised average load up to $\delta/c = 0.2$ is shown for (c) the corrugated core and (d) the Y-frame core. . . . .	145
6.11	Distribution of the normal traction $T$ on the back face at an indentation depth $\delta/c = 0.2$ . Results are shown for a sandwich panel indented by a cylindrical roller of normalised diameter $D/c = 0.41$ : (a) corrugated core and (b) Y-frame core. . . . .	146
6.12	Influence of scale and material strain-rate sensitivity on the normalised initial peak load for (a) the corrugated core and (b) the Y-frame core. Likewise, the influence of scale and material strain-rate sensitivity on the normalised average load up to $\delta/c = 0.2$ is shown for (c) the corrugated core and (d) the Y-frame core. Results are shown for panels indented by a cylindrical roller of normalised diameter $D/c = 0.41$ . The force on the front and back faces are given by solid and dashed lines, respectively. . . . .	148

# List of Tables

3.1	Influence of the strain hardening modulus $E_t$ on the deformed meshes of an inclined tube $t/d = 0.1$ . Results are given for selected values of $l/d$ . . . . .	47
3.2	Influence of the strain hardening modulus $E_t$ on the deformed meshes of an inclined solid strut $t/d = 0.5$ . Results are given for selected values of $l/d$ . . . . .	51
3.3	Influence of the carburisation depth $h/d$ on the deformed meshes of an inclined tube $t/d = 0.1$ . Results are given for selected values of $l/d$ . . . . .	57
3.4	Influence of the carburisation depth $h/d$ on the deformed meshes of an inclined solid strut $t/d = 0.5$ . Results are given for selected values of $l/d$ . . . . .	60
3.5	Influence of a geometric imperfection on the deformed meshes of an inclined tube $t/d = 0.1$ . Results are given for selected values of $l/d$ . . . . .	67
4.1	The measured and predicted values of normalised peak load $\hat{F} = F_{pk}/(\sigma_Y bc)$ . . . . .	87
5.1	Equivalent plastic strain distribution for simply supported sandwich beams with a Y-frame core. Beams with and without a back face are shown. Results are given for quasi-static loading and 5 m/s. All images are showing a side view of the beam focusing on a portion of length $0.35L$ from the beam mid-span. . . . .	119

6.1	Deformed meshes of sandwich panels with a corrugated core shown at selected velocities. The results are given for uniform compression, indentation by a flat-bottomed indenter of normalised width $a/L = 0.05$ and indentation by a cylindrical roller of normalised diameter $D/c = 0.41$ . For indentation, the cross-section underneath the indenter is shown along with a side view of the panel. All images are given for $\delta/c = 0.35$ . . . . .	139
6.2	Deformed meshes of sandwich panels with a Y-frame core shown at selected velocities. The results are given for uniform compression, indentation by a flat-bottomed indenter of normalised width $a/L = 0.05$ and indentation by a cylindrical roller of normalised diameter $D/c = 0.41$ . For indentation, the cross-section underneath the indenter is shown along with a side view of the panel. All images are given for $\delta/c = 0.35$ . . . . .	140
6.3	Positive and negative traction forces on the back face of a sandwich panel indented by a cylindrical roller of normalised diameter $D/c = 0.41$ . The forces are for an indentation depth $\delta/c = 0.2$ , the values are integrated from the curves shown in Fig. 6.11. . . . .	147

# Chapter 1

## Introduction

Minimising the mass without sacrificing the strength of a structure is an engineering challenge that has led to the development of new materials, such as lattice materials, and new structural designs, such as sandwich structures. These two examples constitute fundamental components of this dissertation which aims to (i) improve the strength of lattice materials and (ii) give a better understanding of the quasi-static and dynamic behaviour of sandwich structures. The concepts of lattice materials and sandwich structures are both introduced below, followed by the scope of this thesis.

### 1.1 Lattice materials

A lattice is defined as “a connected array of struts or plates” (Ashby, 2005). Lattices can be made from metals, ceramics or polymers. The term “material” here emphasises that the lattice is considered at a macroscopic length scale, much larger than the length scale of its constituent lattice elements. Hence, the macroscopic properties of lattice materials, such as their density, stiffness and strength, can be directly compared to those of fully-dense solid materials.

The strength of both lattice materials and fully-dense materials is plotted in Fig. 1.1 as a function of density. The figure indicate clearly that lattice materials (which include polymer and metal foams, composite pyramidal and aluminium lattices) occupy a region of the material property space that is left empty by fully-dense materials; this region is the left hand side of the figure where the density is less than

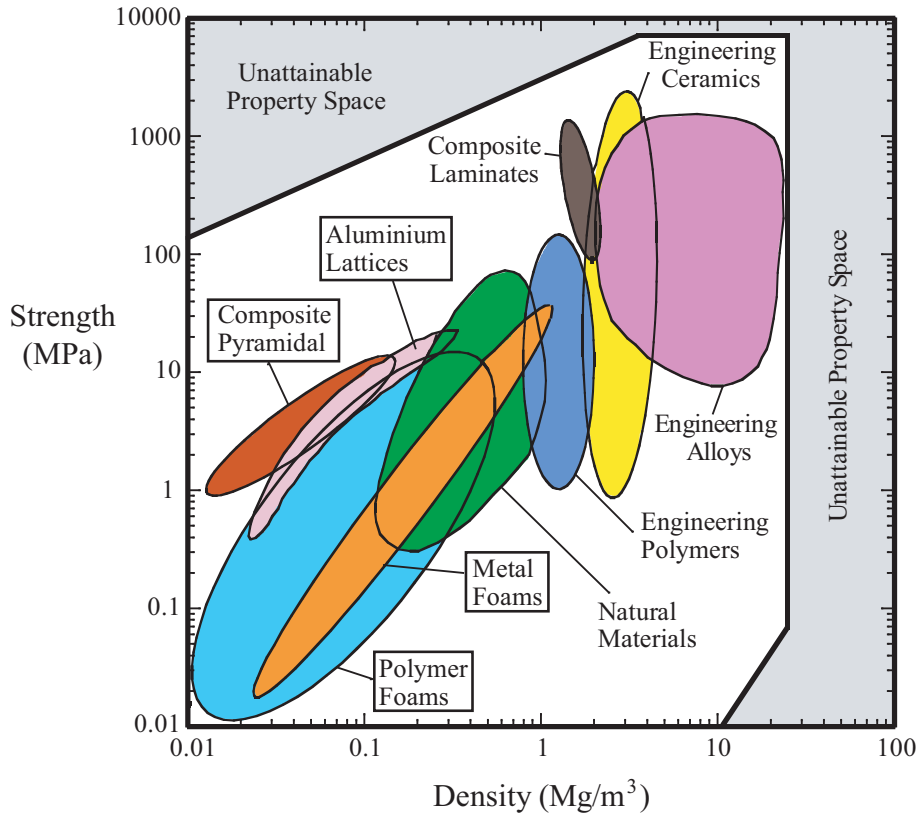


**Figure 1.1:** Material property chart of strength versus density for lattice and fully-dense engineering materials. Text boxes are used to distinguish lattice materials from fully-dense materials. Adapted from Russell (2009).

0.1 Mg/m<sup>3</sup>. The low density of lattice materials makes them ideal candidates for the core of sandwich structures, which are presented in the next section.

## 1.2 Sandwich structures

A sandwich structure usually consists of two thin but stiff face-sheets, made from a fully-dense material, separated by a thick and light core. The result is a structure with a high bending stiffness and strength with a low overall density. In fact, the bending stiffness and strength of a sandwich structure is always superior to that of a monolithic structure made from the same material and having the same mass.

Numerous examples of sandwich structures are found in nature. In this regard, Galileo (1638) writes:

Art, and nature even more, makes use of these in thousands of operations

in which robustness is increased without adding weight, as is seen in the bones of birds and in many stalks that are light and very resistant to bending and breaking.

The skull of birds present a variety of sandwich topologies. For example, the skull of a magpie is a double sandwich construction (see Fig. 1.2(a)) whereas the skull of larger birds, such as owls, is a multiple sandwich construction (see Fig. 1.2(b)). Another example is the stiff toucan beak, which constitutes one third of the bird's length, but only one twentieth of its weight (Seki et al., 2005).

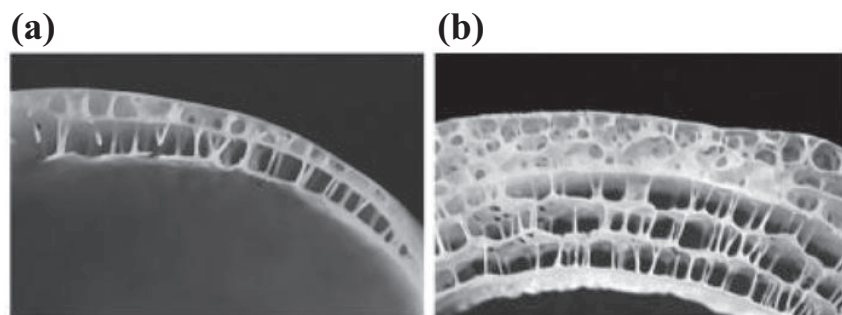
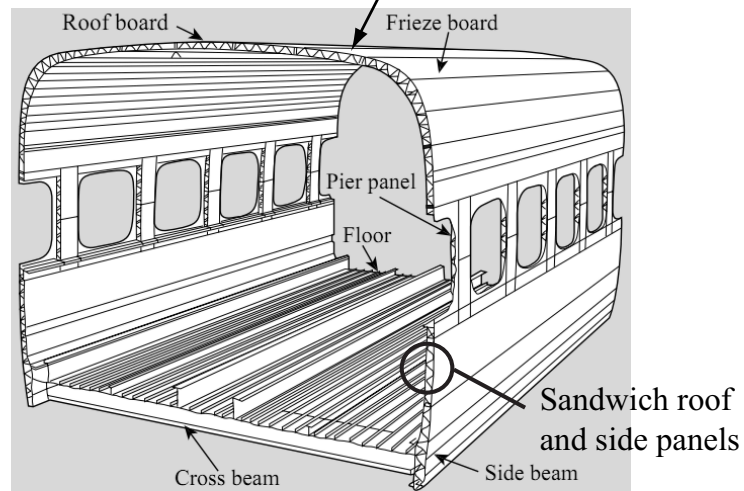
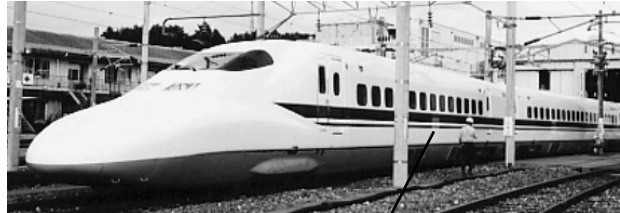


**Figure 1.2:** Examples of sandwich structures in nature: bird skulls of (a) a magpie and (b) a long-eared owl. Adapted from Gibson et al. (2010).

The first industrial application of a sandwich construction is attributed to Fairbairn (1849) who used iron face-sheets riveted to a wooden core in the construction of bridges. However, the potential of sandwich structures was limited by the core materials available; restricted to Balsa and other types of wood. The popularity of sandwich structures increased significantly when novel cores were introduced such as the honeycomb core in the 1940s and polymer foams in the 1950s. The sandwich construction was adopted rapidly by the aerospace and aeronautic industries (Hermann et al., 2005) and more recently, it has been applied in high speed trains and ship hulls (Vinson, 2005), as illustrated in Fig. 1.3.

A sandwich structure can be made from different materials; aluminium, steel or carbon fibre reinforced polymers are some examples. This thesis focuses only on metallic sandwich panels. These have two main advantages over their composite counterparts: (i) the joining process for metals is well known, avoiding debonding problems between the face-sheets and core and (ii) the ductility of metals enable the sandwich structure to be used in energy absorption applications. This thesis will focus on one particular industrial application where energy absorption is important, ship hull design.

(a)



(b)



gas storage tank

Y-frame core

**Figure 1.3:** Examples of sandwich structures in industrial applications: (a) the car body of a high speed train in Japan (Shinkansen 700 series) and (b) Y-frame ship hull design developed by Damen Schelde Naval Shipbuilding. Adapted from Matsumoto et al. (1999) and McShane (2007).

## 1.3 Scope of this thesis

This thesis focuses on metallic sandwich structures and has two main objectives:

1. explore how a surface treatment can improve the strength of a lattice material and
2. investigate the collapse response of two competing prismatic sandwich cores employed in ship hulls.

A considerable amount of work has been published on metallic sandwich structures and a review is presented in **Chapter 2**. First, lattice materials are introduced with an emphasis on their manufacturing route and their compressive and shear strengths. Second, the collapse mechanisms of a sandwich panel loaded quasi-statically under three-point bending are presented. Third, the dynamic responses of sandwich structures subjected to (i) low-velocity impacts and (ii) blast loads are reviewed and finally, the potential of using a sandwich construction to increase the resistance of ship hulls against collision and grounding is also discussed.

As it will be shown in Chapter 2, the pyramidal lattice possesses a high compressive strength. The potential of using a surface treatment, such as carburisation, to increase its strength is investigated in **Chapter 3**. In this chapter, the finite element method is used to predict the compressive response of a carburised pyramidal lattice made from hollow tubes or solid struts. The effect of carburisation upon the compressive strength and the collapse mode of the lattice is examined.

The pyramidal lattice is strong, but more difficult to manufacture than prismatic lattices such as the corrugated core and Y-frame core. Consequently, prismatic cores are more attractive for industrial applications like ship hull design. The quasi-static three-point bending response of sandwich beams with a corrugated core or a Y-frame core is investigated in **Chapter 4**. The role of the face-sheets is addressed by considering beams with (i) front-and-back faces present and (ii) front face present, but back face absent. Those two beam designs are used to represent double hull and single hull ship structures, respectively. Experimental tests are complemented by finite element simulations to gain additional insight into the collapse mechanisms.

Large vessels such as oil and chemical tankers are exposed to ship collisions that occur at relatively low speeds, roughly 5 m/s. The response of a sandwich hull construction to a ship collision is mimicked in **Chapter 5** by performing drop weight

## Chapter 1. Introduction

---

tests, with an impact velocity of 5 m/s, on sandwich beams with a corrugated core or a Y-frame core. The beam response at 5 m/s is compared to its quasi-static response to assess the effect of velocity. This comparison is done via experiments and finite element simulations.

Full-scale ship collision tests on a Y-frame sandwich hull have indicated that the structure deforms by indentation (Wevers and Vredeveldt, 1999). For this reason, the dynamic indentation response of sandwich panels with a corrugated core or a Y-frame core is simulated in **Chapter 6** using the finite element method. The objective is to quantify the importance of (i) material strain-rate sensitivity, (ii) inertia stabilisation effects and (iii) wave propagation effects upon the indentation response.

Finally, **Chapter 7** contains a summary of the conclusions reached in this thesis and suggestions for future work.

# Chapter 2

## Literature review

### Summary

An overview of the literature on metallic sandwich panels is presented in this chapter. First, three families of lattice materials are introduced: metal foams, truss cores and prismatic cores. The manufacturing route and the strength of each family of lattices are reviewed. Second, the quasi-static three-point bending strength of a sandwich panel is discussed with an emphasis on three collapse mechanisms: face yield, core shear and indentation. Third, the dynamic behaviour of lattice materials and sandwich structures is reviewed for both low-velocity impacts and blast loadings. Finally, the potential of employing a sandwich construction to increase the structural performances of ship hulls is addressed as it constitutes an important industrial application of the work done in this thesis.

### 2.1 Lattice materials used as core topologies

The concept of lattice materials was introduced previously in Section 1.1. Lattice materials possess a reasonably high strength at very low densities, which makes them ideal candidates for the core of sandwich structures. The mechanical properties of lattice materials are governed by three factors (Ashby, 2006):

1. the topology of the lattice,
2. the parent material and

- the relative density  $\bar{\rho}$  defined as the volume fraction of solid material.

Several different topologies have been developed with the objective of maximising the strength and minimising the density of the lattice. These topologies can be classified in three families (Evans et al., 2001; Wadley, 2002): foams, truss cores and prismatic cores, see Fig. 2.1. Foams have a random microstructure and accordingly they fall in the stochastic category. In contrast, truss cores and prismatic cores are constructed from a precise unit cell, which is repeated in an array. Consequently, they form the category of periodic lattice materials. The research done for each of these three families is presented below.

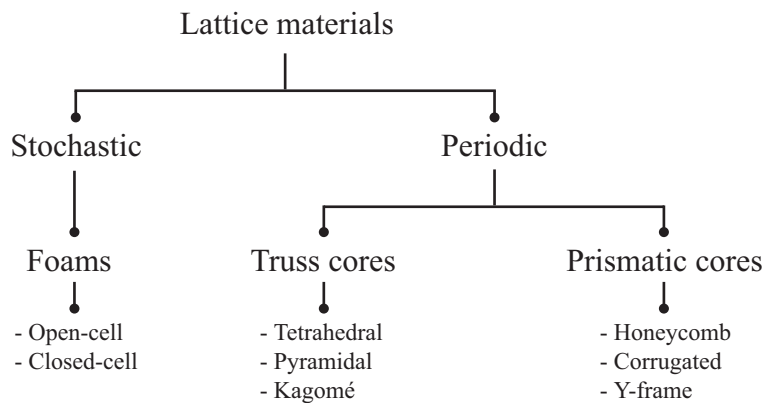


**Figure 2.1:** Classification of lattice materials proposed by Evans et al. (2001) and Wadley (2002).

### 2.1.1 Metal foams

Metal foams are frequently made from aluminium filled with gas pores to form a cellular structure. These pores can be either sealed (closed-cell, see Fig. 2.2(a)) or interconnected (open-cell, see Fig. 2.2(b)). Numerous techniques have been developed to manufacture metal foams; the method employed influences the pore size and their type (closed or open). For example, closed-cell foams can be manufactured by bubbling gas through molten aluminium whereas open-cell foams can be fabricated by casting using a polymer or a wax template. For more information about the manufacturing process, the reader is referred to the textbooks of Gibson and Ashby (1997) and Ashby et al. (2000).

Metal foams have poor structural performances. When a remote compressive stress is applied, the ligaments forming the foam pores deform in bending. Consequently,

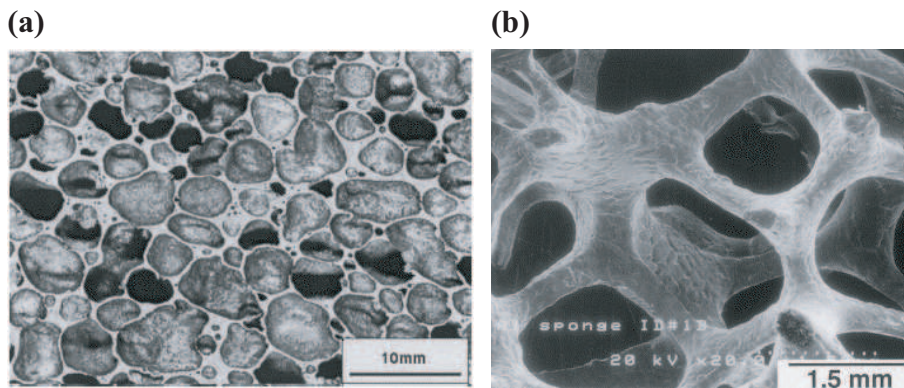


**Figure 2.2:** Aluminium metal foams with (a) closed-cell and (b) open-cell. Reproduced from Paul and Ramamurty (2000) and Nieha et al. (2000).

the stiffness and compressive strength of metal foams scale with  $\bar{\rho}^2$  and  $\bar{\rho}^{3/2}$ , respectively (Ashby, 2006). The yield behaviour of metal foams can be predicted using the constitutive model of Deshpande and Fleck (2000a); this model has been implemented in finite element simulations and the predictions were found to be in good agreement with the measured deformation of metal foams (Bart-Smith et al., 2001; Chen et al., 2001).

### 2.1.2 Truss cores

The bending-dominated behaviour of metal foams explains their poor compressive strength. This led to the development of truss cores, which are designed to be stretching-dominated rather than bending-dominated. Ashby (2006) demonstrated that for stretching-dominated structures, the stiffness and strength of the lattice both scale linearly with the relative density  $\bar{\rho}$ . This implies that the strength of a stretching-dominated structure is three times greater than that of a bending-dominated structure when  $\bar{\rho} = 0.1$ . The behaviour of bending- and stretching-dominated lattices is compared in Fig. 2.3.

Examples of truss cores include the tetrahedral, pyramidal and Kagomé lattices, see Fig. 2.4. The stiffness and strength of tetrahedral lattices was investigated analytically and experimentally by Wallach and Gibson (2001) and Deshpande et al. (2001). In both studies, the authors note the superior performances of the tetrahedral lattice compare to metal foams. Furthermore, experimental (Wang et al., 2003) and numerical (Hyun et al., 2003) work on the Kagomé lattice revealed that it is slightly stronger than the tetrahedral lattice.

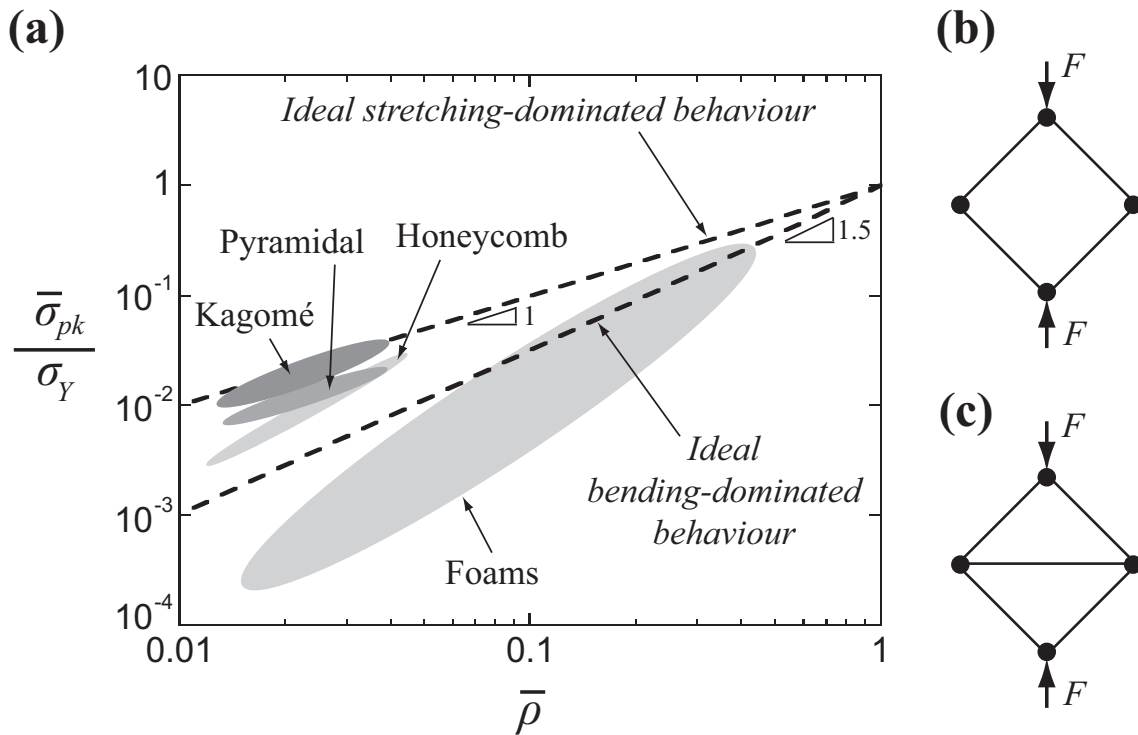


**Figure 2.3:** Relative strength as a function of relative density  $\bar{\rho}$  for different core topologies. The relative strength is defined as the compressive strength of the core  $\bar{\sigma}_{pk}$  divided by the yield strength of the material  $\sigma_Y$ . Examples of (b) bending- and (c) stretching-dominated lattices. Adapted from Ashby (2005).

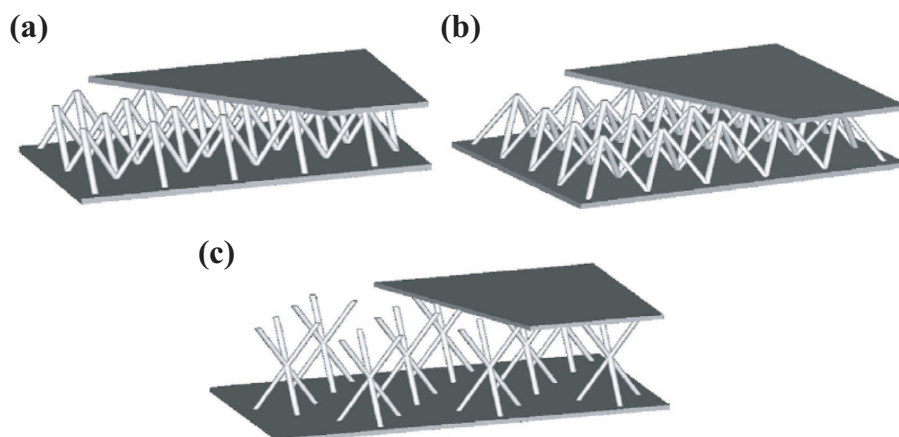


**Figure 2.4:** Examples of truss cores: (a) tetrahedral, (b) pyramidal and (c) Kagomé lattices. Reproduced from Kooistra and Wadley (2007).

## 2.1 Lattice materials used as core topologies

In the experimental studies reported above, the tetrahedral and Kagomé lattices were fabricated by investment casting. This manufacturing route has important limitations; low relative densities are difficult to manufacture because of their susceptibility to casting defects and the process requires an alloy with a high fluidity. So far, aluminium-silicon and copper-beryllium alloys have been used, but their poor ductility impairs the structural performances of the lattice. A novel manufacturing route was proposed by Kooistra et al. (2004) to overcome those limitations. The process involves perforating and folding a metallic sheet, as shown in Fig. 2.5(a). Using this method, tetrahedral lattices with a relative density as low as  $\bar{\rho} = 0.02$  were manufactured with ductile 6061 aluminium (Kooistra et al., 2004) and type 304 stainless steel (Sypeck and Wadley, 2002).

The fabrication method illustrated in Fig. 2.5(a) wastes a lot of material, especially for lattices with a low relative density. This waste can be avoided by using the

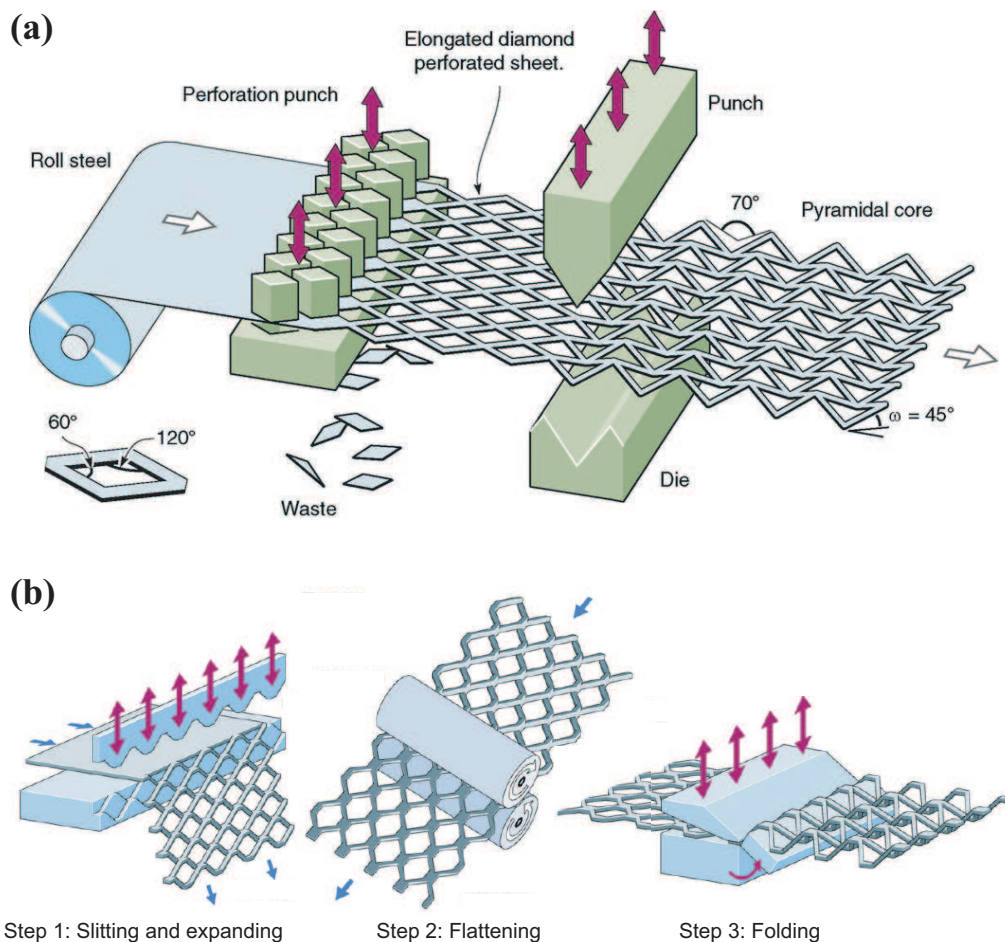


**Figure 2.5:** Two manufacturing routes for truss cores: (a) perforating and folding and (b) slitting, flattening and folding. Reproduced from Kooistra and Wadley (2007).

manufacturing process proposed by Kooistra and Wadley (2007). The fabrication method is illustrated in Fig. 2.5(b) and involves slotting and expanding a metal sheet. Note that only the pyramidal core can be manufactured with this method.

The strength of truss cores can be significantly increased at low relative densities if the solid struts are replaced by hollow tubes. Queheillalt and Wadley (2005a) fabricated a lattice by brazing together an array of stainless steel tubes as shown in Fig. 2.6. At low relative densities, the compressive strength of this lattice was found to be higher than that of a pyramidal core.

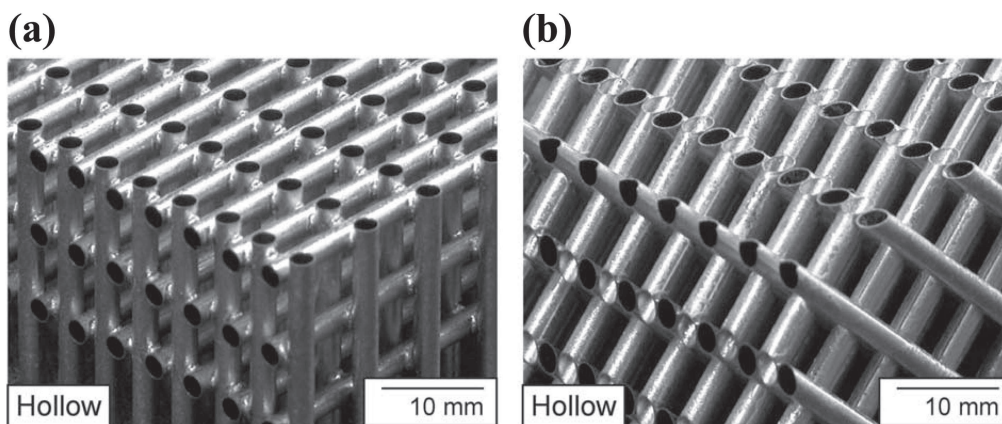


**Figure 2.6:** Lattices made from hollow tubes arranged in (a) square and (b) diamond orientations. Reproduced from Queheillalt and Wadley (2005a).

The potential of a lattice made from hollow tubes was extended further by Queheillalt and Wadley (2005b, 2011) who fabricated a pyramidal core made from hollow tubes. The measured compressive and shear strengths of this hollow pyramidal lattice are compared to other core topologies in Fig. 2.7; the hollow pyramidal lattice is significantly stronger than other lattices at low values of relative density. This experimental work was extended by finite element simulations to develop collapse mechanism maps for the hollow pyramidal lattice loaded in compression (Pingle et al., 2011a) and in shear (Pingle et al., 2011b). In Chapter 3, the finite element method will be used to examine the potential of using a surface treatment to increase the compressive strength of the hollow pyramidal lattice.

### 2.1.3 Prismatic cores

Prismatic cores are composed of an assembly of plates; four examples are given in Fig. 2.8. Prismatic cores are easier to manufacture than truss cores and consequently

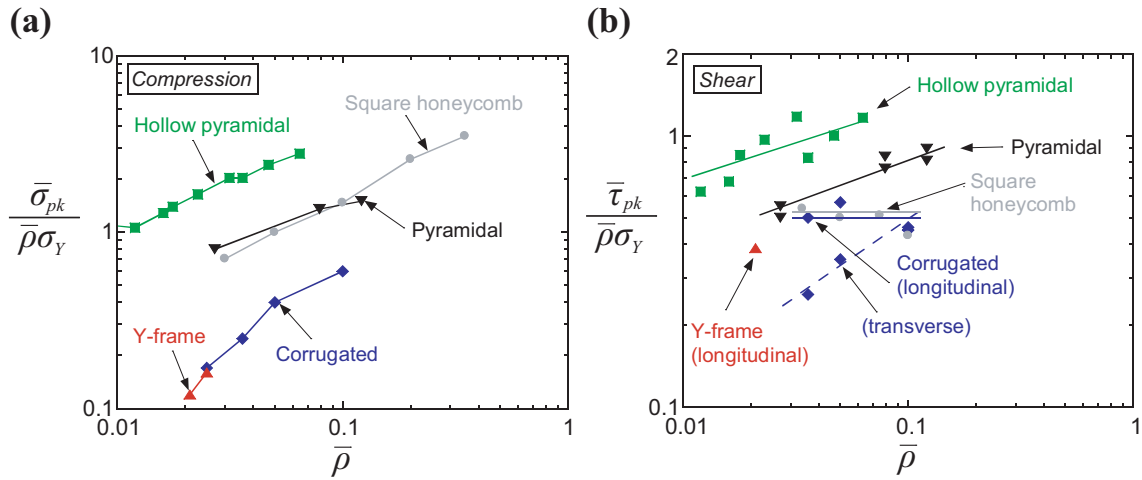


**Figure 2.7:** Measured normalised peak strength of stainless steel lattices loaded in (a) compression and (b) shear. The lattice compressive strength  $\bar{\sigma}_{pk}$  and shear strength  $\bar{\tau}_{pk}$  are normalised by the relative density  $\bar{\rho}$  and the yield strength of stainless steel  $\sigma_Y$ . Data taken from Côté et al. (2004); Côté et al. (2006); Queheillalt and Wadley (2011); Rubino et al. (2008a); Zok et al. (2004).

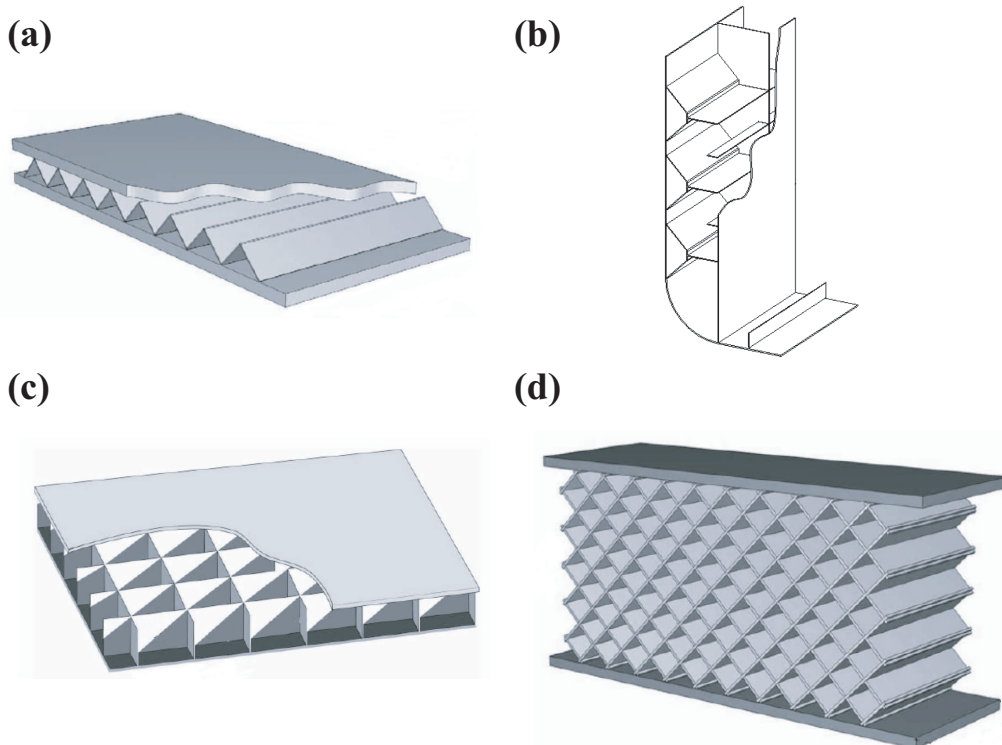


**Figure 2.8:** Examples of prismatic cores: (a) corrugated, (b) Y-frame, (c) square honeycomb and (d) diamond cores. Reproduced from Zok et al. (2005) and Côté et al. (2006).

they are more attractive for industrial applications. Square honeycomb and diamond cores can be assembled by cutting and slotting metal sheets, whereas corrugated and Y-frame cores require a folding operation. Finally, the sheets can be either brazed (for lab-scale specimens) or welded together (for industrial applications) to make a sandwich panel.

The compressive and shear strengths of the square honeycomb were measured by Côté et al. (2004) and its performances were found to be similar to those of the pyramidal core, see Fig. 2.7(a). On the other hand, the mechanical properties of corrugated and diamond cores were measured by Côté et al. (2006). The compressive and transverse shear strengths of the corrugated core are inferior to those of the square honeycomb, see Fig. 2.7. In contrast, the longitudinal shear strength of the corrugated core is similar to that of the square honeycomb (see Fig. 2.7(b)), making the corrugated core a promising topology for sandwich panels.

The compressive response of the Y-frame core was studied numerically by Pedersen et al. (2006). They found that the introduction of a horizontal flange between the upper and lower sections of the Y-frame changed its behaviour from a stretching-dominated to a bending-dominated structure. This reduces the compressive strength of the Y-frame core, but increases its energy absorption capacities. The compressive and shear strengths of the Y-frame core were measured by Rubino et al. (2008a) and they were found to be similar to those of the corrugated core, as shown in Fig. 2.7.

### 2.1.4 Hierarchical topologies

At high relative densities, the compressive strength of prismatic and truss cores is governed by yielding or plastic buckling of the core members. However, at low relative densities, the core members are slender and collapse by elastic buckling. This change in collapse mechanism reduces significantly the compressive strength of the core. To increase the elastic buckling strength of the core members it is possible to fabricate hierarchical cores, where the core members are made from a sandwich construction of a smaller scale (Fleck et al., 2010).

This principle was investigated experimentally by Kooistra et al. (2007) who fabricated a second order corrugated core with a relative density  $\bar{\rho} = 0.02$ , as shown in Fig. 2.9(a). A comparison with a first order corrugated core of equal relative density (Fig. 2.9(b)) revealed that the compressive strength of the hierarchical core was

about ten times stronger. However, the second order construction is only beneficial for low values of relative density,  $\bar{\rho} < 0.05$ .

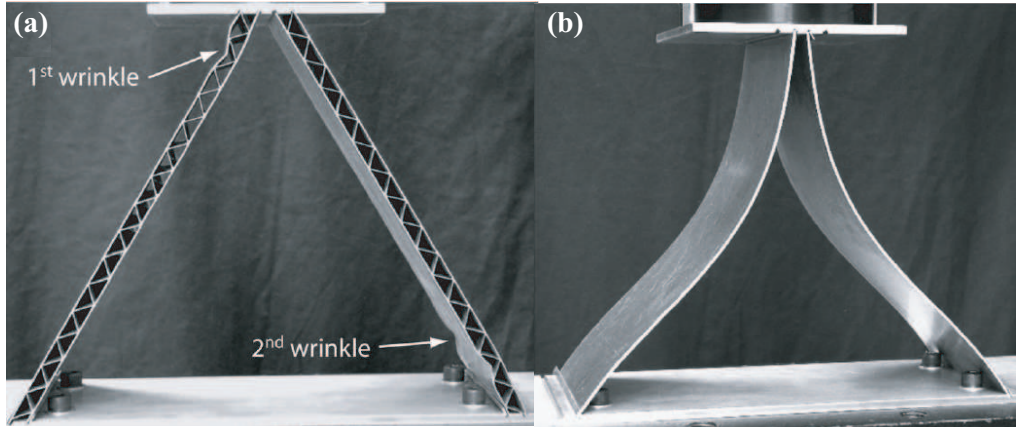


**Figure 2.9:** Photographs showing the collapse mechanisms of (a) second order and (b) first order corrugated cores, both with a relative density  $\bar{\rho} = 0.02$ . Reproduced from Kooistra et al. (2007).

### 2.1.5 Multifunctionality

In previous sections, lattice materials were presented with a strong emphasis on their compressive and shear strengths. However, the advantages of lattice materials are not limited only to their structural performances. For example, closed-cell foams can provide thermal and sound insulations (Gibson and Ashby, 1997; Ashby et al., 2000). On the other hand, open-cell foams can be used as heat exchangers by pumping a fluid through the foam pores (Lu et al., 1998; Evans et al., 2001). Prismatic and truss cores can also be used as heat exchangers and, depending on the application, they usually outperform metal foams (Lu et al., 2005; Valdevit et al., 2006a).

Truss cores, such as the Kagomé lattice, have the potential to be actuated by elongating or contracting the core members (Hutchinson et al., 2003; Symons et al., 2005a,b). This work on the actuated Kagomé lattice was extended to other core topologies by Mai and Fleck (2009). Finally, another advantage of lattice materials is their use as the core of sandwich structures, and this is covered in the next section.

## 2.2 Sandwich structures under quasi-static three-point bending

Three families of lattice materials were introduced in the previous section: metal foams, truss and prismatic cores. Their high compressive and shear strengths at low densities make them ideal candidates for the core of sandwich structures. In this section, the collapse mechanisms applicable to metallic sandwich structures loaded in three-point bending are introduced along with simple analytical formulae to predict their collapse strength. Subsequently, the research conducted on sandwich beams with either a metal foam core, a truss core, or a prismatic core will be presented in turn. For an extensive coverage of the design and the mechanics of sandwich structures the reader is referred to the classic textbooks of Plantema (1966), Allen (1969) and Zenkert (1995).

### 2.2.1 Collapse mechanisms

A sandwich panel loaded in three-point bending can collapse in different ways – referred to as collapse mechanisms – depending on its geometry and material properties. The relevant collapse mechanisms for metallic sandwich panels are: face yield, core shear and indentation (Ashby et al., 2000). These three collapse mechanisms are illustrated in Fig. 2.10 for a sandwich beam with a metal foam core. For each collapse mechanism, simply supported and clamped sandwich beams are compared to show the effect of the boundary conditions. Analytical predictions for each of the three collapse mechanisms are presented below.

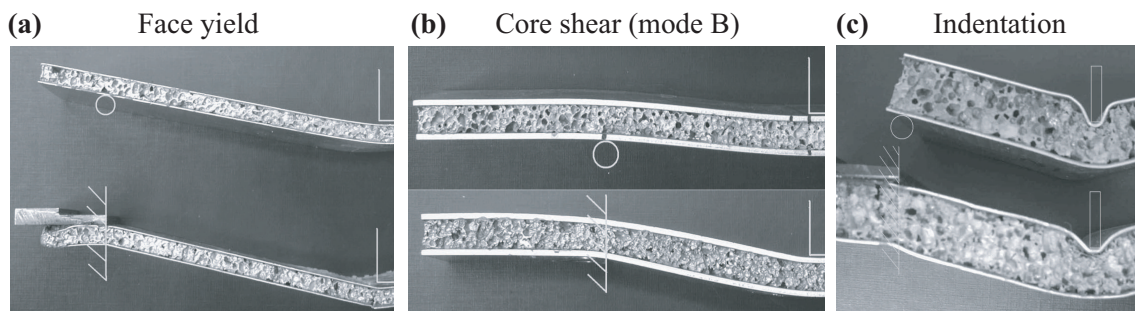


**Figure 2.10:** A sandwich beam with a metal foam core loaded in three-point bending that collapsed by (a) face yield, (b) core shear (mode B) and (c) indentation. For each collapse mechanism, simply supported and clamped sandwich beams are shown. Reproduced from Tagarielli and Fleck (2005).

## 2.2 Sandwich structures under quasi-static three-point bending

Consider the simply supported and clamped sandwich panels loaded in three-point bending and illustrated in Fig. 2.11(a) and (b), respectively. The geometry of the panel is defined by: the span  $2L$ , the overhang  $H$ , the face-sheet thickness  $t$ , the core thickness  $c$  and the width  $b$  (normal to the plane). The core and face-sheets are made from rigid perfectly plastic solids with a yield strength  $\sigma_Y^c$  and  $\sigma_Y^f$ , respectively. In addition, the core is assumed to have a shear strength  $\tau_Y^c$ .

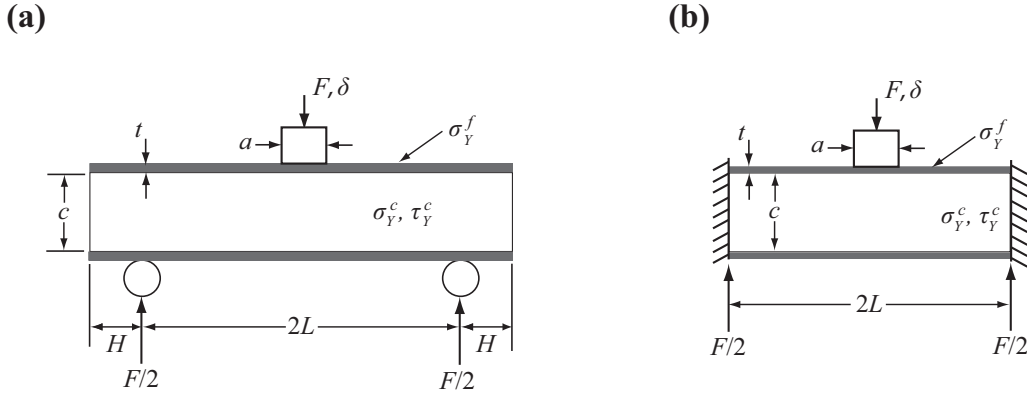


**Figure 2.11:** (a) Simply supported and (b) clamped sandwich panels loaded in three-point bending.

### Face yield

Slender sandwich panels can collapse by face yield, see Fig. 2.10(a). Assuming the formation of two global plastic hinges on each side of the indenter, see Fig. 2.12(a), the collapse load for a simply supported panel is given by (Ashby et al., 2000):

$$F_{fy} = \frac{2bt(c+t)}{L} \sigma_Y^f + \frac{bc^2}{2L} \sigma_Y^c \quad . \quad (2.1)$$

For clamped beams, two additional plastic hinges are forming at the fixed ends, see Fig. 2.12(b), which doubles the collapse load (Tagarielli and Fleck, 2005). Equation (2.1) assumes that the face-sheets and core yields simultaneously; however, other models proposed by Triantafillou and Gibson (1987a) and McCormack et al. (2001) have neglected the contribution of the core in their estimation of the face yield collapse load by setting  $\sigma_Y^c = 0$  in Eq. (2.1).

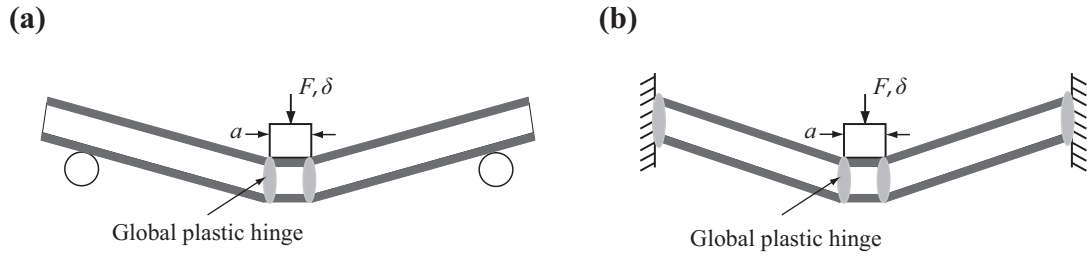


**Figure 2.12:** Face yield collapse mechanism for (a) simply supported and (b) clamped sandwich panels.

### Core shear

When a sandwich panel is loaded in three-point bending, the transverse shear force is carried mostly by the core and consequently the panel can collapse by core shear. Two modes of core shear are possible for simply supported panels and they are illustrated in Fig. 2.13. Mode A assumes the formation of four plastic hinges in the face-sheets and shearing of the core over a length  $2(L + H)$ . The collapse load for mode A is given by (Ashby et al., 2000):

$$F_A = \frac{bt^2}{L}\sigma_Y^f + 2bc\tau_Y^c \left(1 + \frac{H}{L}\right) \quad . \quad (2.2)$$

On the other hand, mode B assumes four additional plastic hinges at the supported ends and shearing of the core over a length  $2L$ . The collapse load for mode B is given by (Ashby et al., 2000):

$$F_B = \frac{2bt^2}{L}\sigma_Y^f + 2bc\tau_Y^c \quad . \quad (2.3)$$

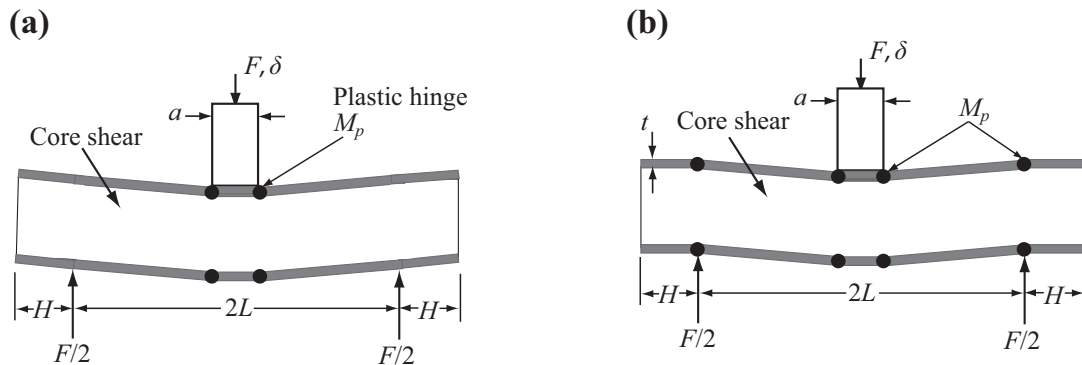


**Figure 2.13:** Core shear collapse mechanisms: (a) mode A and (b) mode B.

## 2.2 Sandwich structures under quasi-static three-point bending

---

The operative mode is the one associated with the lowest collapse load; mode A is operative for short overhangs  $H$ , whereas mode B is active for large values of  $H$ . The transition between the two modes occurs at an overhang  $H_t$  given by:

$$H_t = \frac{t^2 \sigma_Y^f}{2c\tau_Y^c} . \quad (2.4)$$

Tagarielli and Fleck (2005) noted that only mode B is applicable for clamped boundary conditions, see Fig. 2.10(b). Core shear can also occur while the face-sheets are loaded elastically (Chiras et al., 2002), in these cases, the contribution of the faces can be neglected by setting  $\sigma_Y^f = 0$  in Eq. (2.2) and (2.3).

### Indentation

The indentation collapse mechanism consists of a localised failure of the core underneath the mid-span indenter, see Fig. 2.10(c). Assuming the formation of four plastic hinges in the front face and yielding of the core in compression, as shown in Fig. 2.14, the collapse load can be obtained with an upper bound calculation (Ashby et al., 2000):

$$F = \frac{4M_p}{\lambda} + (a + \lambda)b\sigma_Y^c , \quad (2.5)$$

where the full plastic moment of the face-sheet is  $M_p = \sigma_Y^f bt^2/4$ . Minimising  $F$  with respect to  $\lambda$  gives the collapse load:

$$F_I = 2tb\sqrt{\sigma_Y^f \sigma_Y^c} + ab\sigma_Y^c , \quad (2.6)$$

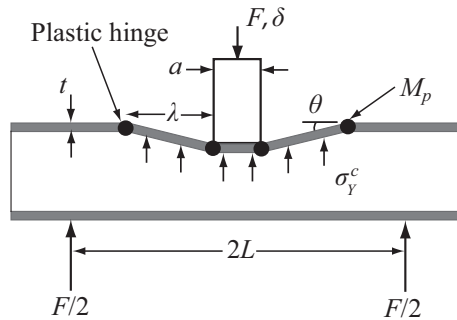


**Figure 2.14:** Indentation collapse mechanism.

where  $\lambda = t\sqrt{\sigma_Y^f/\sigma_Y^c}$ . Note that a lower bound calculation gives the same collapse load; therefore it can be concluded that Eq. (2.6) gives the exact solution for rigid perfectly plastic materials. It is interesting to note that the indentation collapse load is independent of the span  $2L$  and of the boundary conditions.

The analysis above assumes that the front face and core both yield plastically. Additional models have been developed in which the core yields plastically, but the front face is loaded elastically, see for example Soden (1996), Shuaeib and Soden (1997) and Steeves and Fleck (2004). In all studies cited above, the compressive strength of the core is considered, but its longitudinal shear strength is neglected. This assumption is not adequate for cores with a longitudinal shear strength comparable to their compressive strength, such as the corrugated and Y-frame cores. To account for this, an analytical indentation model incorporating the longitudinal shear strength of the core has been developed by Rubino et al. (2008a, 2010).

### Collapse mechanism maps

The operative collapse mechanism is the one associated with the lowest collapse load. Collapse mechanism maps provide a graphical representation of the operative collapse mechanism and associated collapse load as a function of two design parameters. An example is given in Fig. 2.15(a) where the collapse mechanism and contours of normalised collapse load  $\bar{F} = F/(2bL\sigma_Y^f)$  are plotted as a function of  $t/c$  and  $c/(2L)$ . Those results were obtained for a normalised indenter size  $a/(2L) = 0.1$  and the following material properties:  $\sigma_Y^c/\sigma_Y^f = 0.005$  and  $\tau_Y^c/\sigma_Y^f = 0.005$ .

The normalised indenter size has a strong effect upon the collapse mechanism map; reducing  $a/(2L)$  expands the indentation regime as shown in Fig. 2.15(b). The map is also sensitive to the boundary conditions; the face yield domain decreases when the boundary conditions are changed from simple support to fully-clamped (Tagarielli and Fleck, 2005).

Collapse mechanism maps were developed for different core topologies including: metal foams (McCormack et al., 2001; Bart-Smith et al., 2001), the tetrahedral core (Deshpande and Fleck, 2001), the pyramidal core (Zok et al., 2004; Côté et al., 2007), the square honeycomb core (Zok et al., 2005) and the corrugated core (Valdevit et al., 2006a). The research done on each of these core topologies will be presented below in more details.

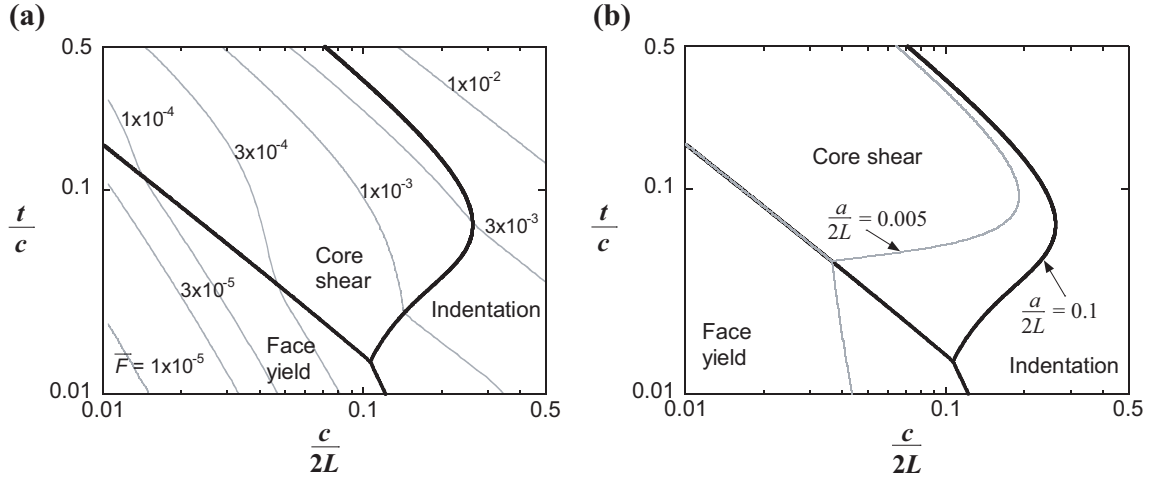


**Figure 2.15:** Collapse mechanism maps for a simply supported sandwich panel: (a) contours of normalised collapse load  $\bar{F} = F/(2bL\sigma_Y^f)$  for  $a/(2L) = 0.1$  and (b) influence of the normalised indenter size  $a/(2L)$  upon the operative collapse mechanism. In both cases,  $\sigma_Y^c/\sigma_Y^f = 0.005$  and  $\tau_Y^c/\sigma_Y^f = 0.005$ . Adapted from Ashby et al. (2000).

### 2.2.2 Sandwich beams with a metal foam core

The three-point bending response of simply supported sandwich beams with a metal foam core was investigated by Triantafyllou and Gibson (1987b), McCormack et al. (2001) and Bart-Smith et al. (2001). Chen et al. (2001) extended this work to simply supported beams loaded in four-point bending whereas Tagarielli and Fleck (2005) investigated the influence of the boundary conditions by comparing the responses of simply supported and clamped beams. These studies revealed that the analytical formulae presented in Section 2.2.1 gave an accurate prediction of the measured collapse load. The measurements were also in good agreement with finite element predictions, in which the metal foam core was treated as a homogeneous solid using the constitutive model of Deshpande and Fleck (2000a).

### 2.2.3 Sandwich beams with a truss core

Sandwich beams with a tetrahedral core were first manufactured by investment casting of an aluminium-silicon alloy (Deshpande and Fleck, 2001) or a beryllium-copper alloy (Chiras et al., 2002). Subsequently, the technique illustrated in Fig. 2.5(a) was employed by Rathbun et al. (2004) to fabricate sandwich beams made from stainless steel. In these three studies, the beams were tested under simply supported boundary conditions and all geometries considered were found to collapse

by core shear. The measured collapse loads were also found to be in good agreement with the analytical predictions of Wicks and Hutchinson (2001, 2004).

Stainless steel sandwich beams with a pyramidal core were tested by Zok et al. (2004) and Côté et al. (2007). Zok et al. (2004) tested both simply supported and clamped beams and proposed an orthotropic constitutive law to model the behaviour of the pyramidal core. On the other hand, Côté et al. (2007) tested simply supported beams only, but focused on their resistance to fatigue.

Sandwich beams with a truss core made from stainless steel tubes, as shown in Fig. 2.6, were tested by Rathbun et al. (2006b) under simply supported and clamped boundary conditions. For both end conditions, the collapse load measured with the diamond orientation (see Fig. 2.6) exceeded the one measured with the square orientation. This is due to the fact that the longitudinal shear strength of the core is greater in the diamond orientation than in the square orientation.

### 2.2.4 Sandwich beams with a prismatic core

Stainless steel sandwich beams with a square honeycomb core were tested by Zok et al. (2005) under simply supported and clamped boundary conditions. The beams collapsed by core shear or face yield depending upon their geometry, and the measured responses were used to calibrate an orthotropic constitutive law for the core.

Simply supported sandwich beams with a corrugated core were tested by Valdevit et al. (2006a) and the measured collapse loads were found to be in good agreement with analytical predictions. This work was extended by Rubino et al. (2010) who compared the three-point bending strength of sandwich beams with a corrugated core to those with a Y-frame core for both simply supported and clamped boundary conditions. Both core topologies were found to have a similar three-point bending strength. In all cases, the sandwich beams collapsed by indentation, and the measurements were found to be in good agreement with finite element simulations, as shown in Fig. 2.16.

### 2.2.5 Optimisation studies

The studies reported above have investigated the three-point bending response of sandwich beams with different core topologies. However, one fundamental question

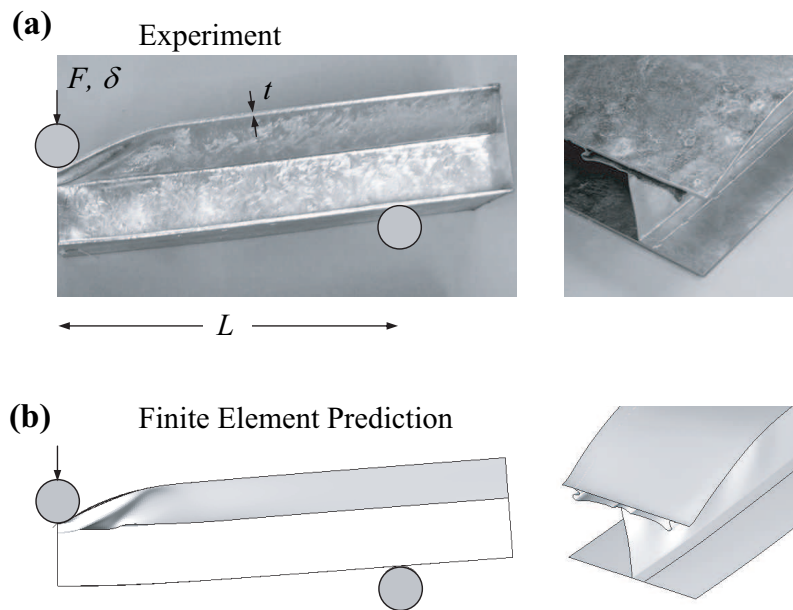


**Figure 2.16:** A simply supported sandwich beam with a Y-frame core loaded in three-point bending and collapsing by indentation: (a) experiment and (b) finite element prediction. A side view showing half the beam (left) and a view of the core deformation obtained by sectioning the beam at mid-span (right) are included. Reproduced from Rubino et al. (2010).

is left unanswered: for a given load, which core topology provides the lightest sandwich panel? This optimisation problem was investigated analytically by Valdevit et al. (2004), Rathbun et al. (2005) and Wei et al. (2006). These studies revealed that the differences between the mass of the optimised sandwich panels are very small; about 15% variations between the different core topologies considered. Consequently, the authors suggest that the choice of core topology should be based on considerations other than strength, such as manufacturing costs and the potential for multifunctionality (Rathbun et al., 2005).

## 2.3 Lattice materials and sandwich structures under dynamic loading

So far, the behaviour of lattice materials and sandwich structures has been examined for quasi-static loading only. In this section, their behaviour under dynamic loading will be addressed. The dynamic collapse response of a structure can be significantly different from its quasi-static response because of three effects described below:

**Material strain-rate sensitivity.** The yield strength of several alloys, such as mild steel, increases with increasing strain-rate (Jones, 1989; Stout and Follansbee, 1986).

**Inertia stabilisation.** Take for example a column loaded dynamically in compression; its lateral inertia will stabilise it against buckling. This effect can be important at low impact velocities for which wave propagation effects are negligible (Calladine and English, 1984; Karagiozova and Jones, 1996).

**Wave propagation.** As the impact velocity is increased, wave propagation effects become important. Again, consider a column loaded dynamically in compression. An axial plastic wave propagates along the column and only the portion of material engulfed by the plastic wave buckles (Vaughn et al., 2005; Vaughn and Hutchinson, 2006). If the impact velocity is greater than the plastic wave speed, the column does not buckle and material accumulates at the impacted end (Taylor, 1948; McShane, 2007).

Three topics will be covered in this section. First, the literature on the dynamic compressive response of lattice materials is reviewed. Second, the low-velocity impact response of sandwich structures is presented, and finally, the use of sandwich panels for blast protection is covered.

### 2.3.1 Dynamic compressive response of lattice materials

When a sandwich panel is loaded dynamically, some energy is absorbed by crushing of the core. Consequently, the dynamic performances of sandwich panels are highly dependent on the compressive response of the core (Liang et al., 2007; McShane et al., 2007). The dynamic compressive response of a lattice material can be measured using a strain-gauged Kolsky bar, as shown in Fig. 2.17. The stresses on front and back faces can be obtained from two independent tests. In the front face configuration, the specimen is fixed to the striker and they are both fired on the Kolsky bar. Alternatively, in the back face configuration, the specimen is fixed on the stationary Kolsky bar and impacted by the striker.

This method was used by Deshpande and Fleck (2000b) to measure the dynamic compressive response of closed-cell and open-cell aluminium foams, and their dynamic responses were found to be relatively similar to their quasi-static responses. The same method was used to test truss and prismatic cores made from stainless

## 2.3 Lattice materials and sandwich structures under dynamic loading

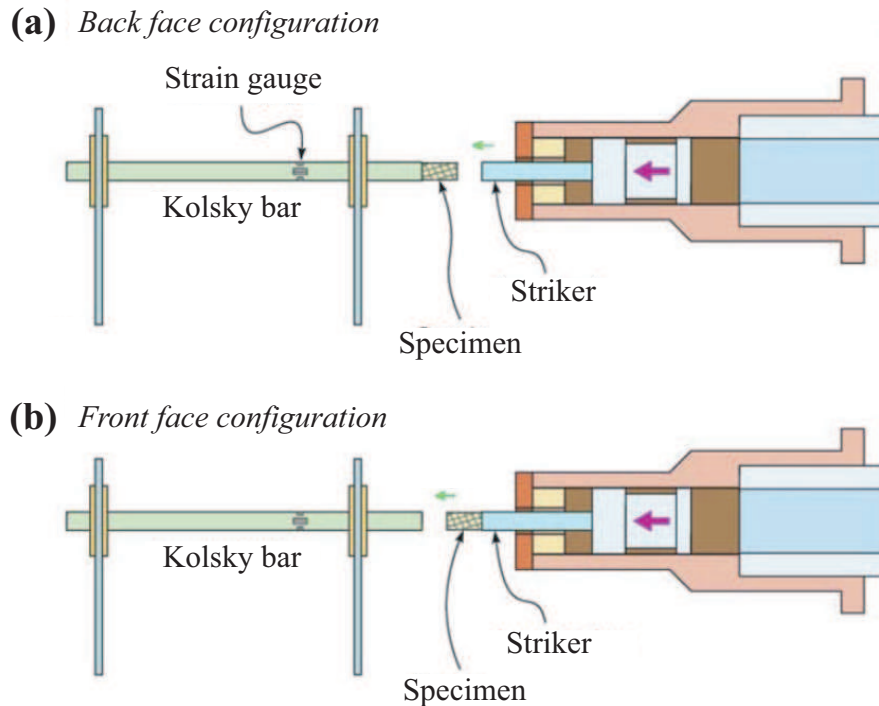


**Figure 2.17:** Direct impact Kolsky bar setup in (a) back face and (b) front face configurations. Adapted from Lee et al. (2006).

steel, such as the square honeycomb core (Radford et al., 2007); the corrugated and Y-frame cores (Tilbrook et al., 2007); the I-core (Ferri et al., 2006) and the pyramidal core (Lee et al., 2006). The measured dynamic compressive response of truss and prismatic cores was stronger than its quasi-static response. This strengthening is attributed to the three factors introduced above: (i) material strain-rate sensitivity, (ii) inertia stabilisation of the core members against buckling and (iii) wave propagation effects. In general, material strain-rate effects were found to have a small influence on the results. On the other hand, inertia stabilisation effects were predominant at low velocities (less than approximately 50 m/s, depending on the lattice) whereas wave propagation effects appeared at high impact velocities.

In most practical engineering applications, a sandwich panel is not loaded in uniform compression. For example, during a ship collision, a sandwich hull structure deforms by indentation. What will be the importance of the three dynamic strengthening effects mentioned above if the loading is changed from uniform compression to localised indentation? This question will be addressed in Chapter 6.

### 2.3.2 Sandwich structures subjected to a low-velocity impact

Sandwich structures used in aerospace, automotive and marine applications are exposed to low-velocity impacts (below 10 m/s). These can be replicated in laboratory using a drop weight apparatus. The literature on the low-velocity impact response of sandwich structures is vast and can be divided in two categories aiming at:

1. quantifying the damage caused by a localised impact on a sandwich panel or
2. comparing the quasi-static and low-velocity responses of a sandwich structure.

The first category regroups most of the literature on low-velocity impacts and is primarily interested in composite sandwich panels used in the aerospace industry. These structures often have a Nomex or aluminium honeycomb core, which is glued to the face-sheets that can be made from graphite, glass or carbon fibre reinforced polymers. When these panels are subjected to a localised impact, delamination, core crushing and debonding of the core and faces can occur. Several studies have proposed methods to quantify and measure the damage inferred to the sandwich panel (Hazizan and Cantwell, 2003; Meo et al., 2005; Castanié et al., 2008; Park et al., 2008; Shin et al., 2008). These studies are not of primary interest in this thesis; the second category is more relevant.

The second category includes a few papers only. The quasi-static and low-velocity impact responses of simply supported sandwich beams with a metal foam core were investigated by Yu et al. (2008). The authors showed that the collapse mechanism obtained during drop weight tests at 5 m/s is the same as the one observed quasi-statically. This finding was corroborated by other experimental studies on sandwich beams with a metal foam core (Yu et al., 2003; Crupi and Montanini, 2007) or a honeycomb core (Crupi et al., 2012).

The low-velocity impact response of sandwich beams with a corrugated core or a Y-frame core will be investigated experimentally and numerically in Chapter 5. The objective is to determine whether the collapse mechanism observed during a ship collision at 5 m/s is the same as the one observed under quasi-static loading.

### 2.3.3 Sandwich structures subjected to blast loading

Most of the literature on dynamic loading of metallic sandwich structures focuses on their use for blast mitigation. Even though the emphasis of this thesis is on the quasi-static and low-velocity impact response of sandwich structures used in the construction of ship hulls, it is insightful to cover the blast response of sandwich structures to (i) determine the sensitivity of the dynamic response to the core topology and (ii) evaluate the accuracy of the finite element method to simulate the measured dynamic response.

#### Analytical and numerical studies

An analytical model was developed by Fleck and Deshpande (2004) to describe the structural response of a clamped sandwich beam subjected to a blast. Their model consists of three sequential stages:

**Stage I** is the one-dimensional fluid-structure interaction during which the front face acquires an uniform velocity.

**Stage II** involves compression of the core until the velocities of the front and back faces equalise.

**Stage III** is the dissipation of the beam's kinetic energy through plastic bending and stretching.

The analytical predictions of Fleck and Deshpande (2004) were found to be in good agreement with the finite element simulations of Qiu et al. (2003). In the simulations done by Qiu et al. (2003), the core was treated as a homogeneous solid based on the metal foam constitutive model of Deshpande and Fleck (2000a). Xue and Hutchinson (2004) performed finite element simulations on sandwich beams with three fully-meshed core topologies: a square honeycomb core, a corrugated core and a pyramidal core. The maximum back face deflection was used as a metric to compare the performances of sandwich plates to those of a monolithic plate of the same mass. The results are reproduced in Fig. 2.18 where the normalised maximum back face deflection  $w/L$  is plotted as a function of the normalised blast impulse  $I/M\sqrt{\sigma_Y/\rho_f}$  for both air and water blasts. Note that the blast impulse is  $I$ , the back face deflection is  $w$ , the beam has a span  $2L$ , an areal mass  $M$  and is made from a material with a yield strength  $\sigma_Y$  and a density  $\rho_f$ . The main findings are:

1. Sandwich beams outperform monolithic beams on an equal mass basis.
2. The advantage of sandwich structures is sensitive to the core topology; prismatic cores, such as the corrugated and square honeycomb cores, are preferable to truss cores because of their high longitudinal strength.
3. The benefit of using a sandwich construction is more important for a water blast than for an air blast because the impulse transmitted to the front face of the sandwich beam is lower than the one transmitted to a monolithic beam.

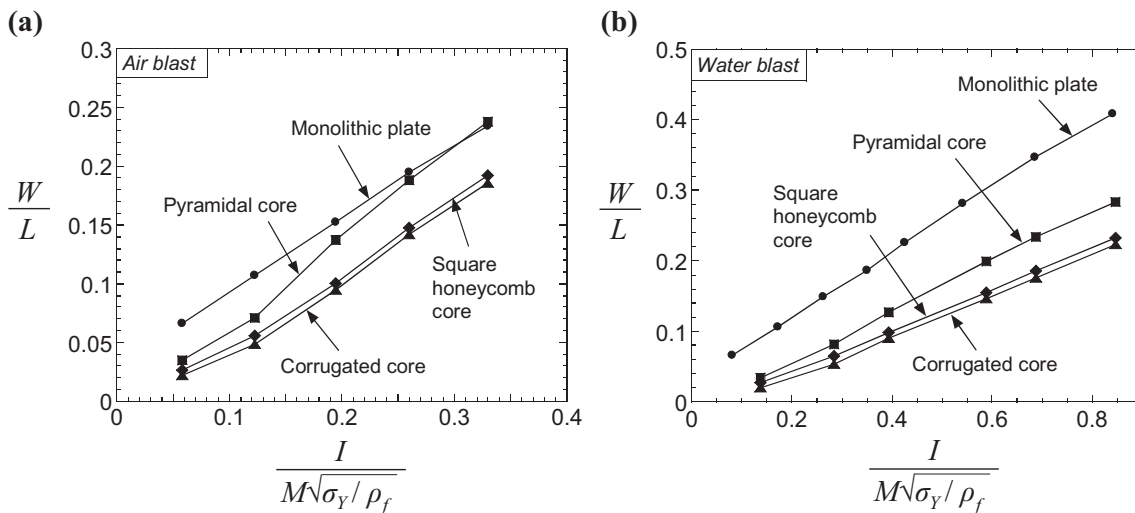


**Figure 2.18:** Normalised maximum back face deflection  $w/L$  as a function of the normalised blast impulse  $I/(M\sqrt{\sigma_Y/\rho_f})$ . Adapted from Rathbun et al. (2006a).

### Experimental studies

Radford et al. (2005) proposed to use metal foam projectiles to produce dynamic pressures representative of air and water blasts. This technique can generate peak pressures around 100 MPa over a duration of about 100  $\mu$ s. This approach was used by several authors (Rathbun et al., 2006a; Radford et al., 2006a; Rubino et al., 2008b) to compare, on an equal mass basis, the dynamic performances of clamped sandwich beams with different core topologies to that of monolithic beams. Similar work was done on circular plates (Radford et al., 2006b; McShane et al., 2006) and on rectangular plates (Rubino et al., 2009). All studies have shown that sandwich structures have a lower maximum back face deflection than their monolithic counterparts. In addition, a good correlation was found between experiments and finite element simulations; see for example Fig. 2.19 where the results of Rubino et al. (2009) are reproduced.

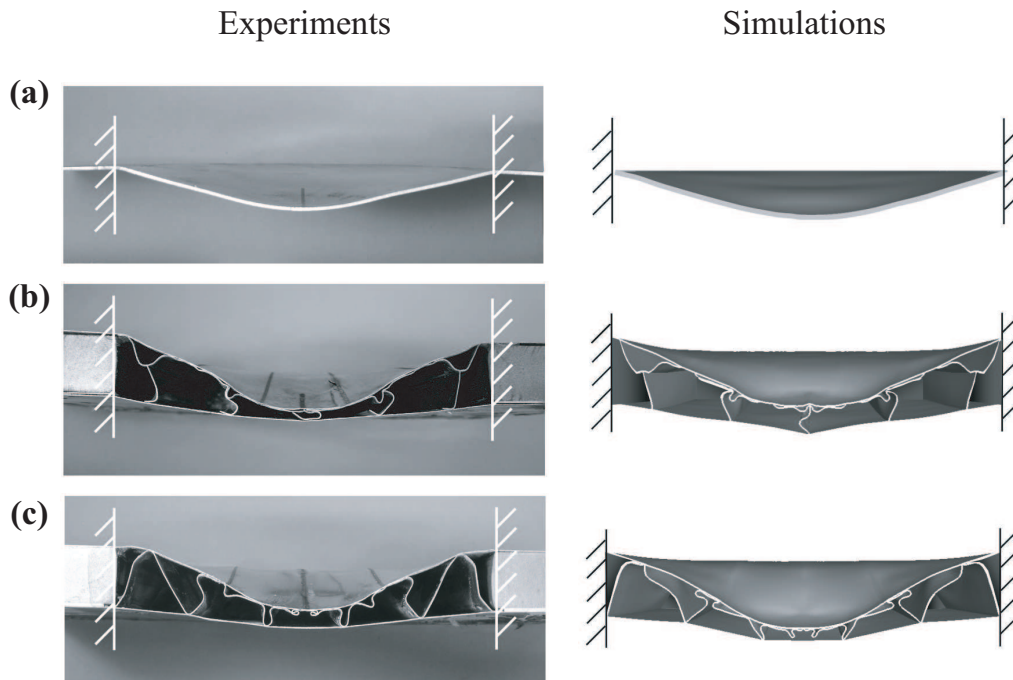


**Figure 2.19:** Photographs and finite element simulations of (a) monolithic, (b) Y-frame and (c) corrugated plates impacted by a metal foam projectile with a momentum of  $3 \text{ kNs/m}^2$ . All plates have the same mass. Reproduced from Rubino et al. (2009).

One disadvantage of using metal foam projectiles to simulate blast loading is that the pressure pulse is localised over a central patch whereas a real shock wave would spread over the entire front face. To address this issue, a few experiments have been performed on rectangular sandwich plates loaded by an explosive charge detonated in air (Dharmasena et al., 2008, 2011). Again, sandwich panels were found to have lower back face deflections than monolithic plates.

## 2.4 Ship hull design

Commercial vessels need to resist accidental loads such as ship collisions and groundings (when a ship hits the seabed). Recently, the growing threat of terrorist attacks and the impressive growth of offshore oil and gas extraction systems have forced commercial shipbuilders to also consider explosions as a potential accident scenario (ISSC, 2006b). In this section, design strategies to minimise the consequences of such accidents are presented with a focus on ship collisions and groundings. These two accident scenarios are more likely to occur than explosions and are also more relevant to this thesis.

### 2.4.1 Regulations

The design of ship hulls was influenced by major pollution catastrophes such as the grounding of the Exxon Valdez of the coast of Alaska in 1989. When the single hull construction of the tanker was breached, over ten million gallons of crude oil flooded into a sensitive ecosystem within the first five hours only (Skinner and Reilly, 1989). The environmental consequences of the oil spill attracted the public's attention and forced the political power to legislate on the maritime transport of oil and other hazardous chemical products. The United States introduced the Oil Pollution Act in 1990 (OPA 90) and the International Maritime Organization (IMO) followed with a similar legislation in 1992. One important aspect of this legislation was that all new tankers should be built with a double hull construction.

The OPA 90 and IMO regulations offer design guidelines for the construction of double hull vessels; the plate thickness and the spacing between inner and outer hulls are given as a function of the overall ship dimensions. From a structural point of view, these design requirements are sub-optimal. However, the IMO regulations allow shipbuilders to propose alternative designs as long as their crashworthiness is proven to be equal or superior to that of a conventional double hull construction. Only the ADNR regulations, regarding navigation on the Rhine River, quantify the energy absorption capacity of a ship hull; the side structure must absorb 22 MJ if the design differs from a conventional construction.

### 2.4.2 Evaluating the resistance of ship hulls

The issue of ship collisions and grounding events can be tackled from two different angles. The first angle is to investigate how and why accidents occur. This leads to the development of risk assessment methods to quantify the probability and severity of different accident scenarios, see for example the work of Pedersen (2002) and Friis-Hansen and Simonsen (2002).

The second perspective is more relevant to this thesis and examines the response of the ship structure during an accident. Different methods have been developed to evaluate the structural damage occurred during a ship collision or a grounding event. Those methods can be divided in four categories: (i) empirical methods, (ii) simplified analytical methods, (iii) finite element simulations and (iv) experimental tests on full-scale and/or lab-scale structures.

The most famous empirical method is certainly the one developed by Minorsky (1959). By analysing several accidents, the author suggested that the energy absorbed by the ship structure  $E$  during an accident is given by:

$$E(MJ) = 47.2R_T(m^3) + 32.7 \quad , \quad (2.7)$$

where  $R_T$  is the volume of deformed material. This empirical formula neglects several parameters such the vessel speed, the structural arrangements and the material properties. Several authors have proposed revised Minorsky formulae, for example Pedersen and Zhang (2000).

Simplified analytical methods allow to study the motion of ships during a collision (external dynamics) as well as the deformation of the structural components (internal dynamics). The effect of the surrounding water, vessel speed and collision angle can be used to estimate the contact forces (Simonsen, 1997; Pedersen and Zhang, 1998; Zhang, 1999; Tabri et al., 2009).

Finite element simulations can capture accurately the deformation of a ship hull under different loading scenarios. The method takes into account large deformations, contact friction, non-linear material properties and even fracture. However, the definition of an adequate fracture criterion is problematic due to the large mesh size used to discretise the ship structure (Urban, 2002; Törnqvist, 2003; Simonsen and Törnqvist, 2004).

Experimental tests are useful to validate the results of finite element simulations but they are expensive when performed on full-scale structures. Tests on lab-scale structures are less expensive, but present scaling issues (Jones, 1979). See Pedersen et al. (1993) and Wang et al. (2000) for a review of full-scale and lab-scale experiments, respectively.

### 2.4.3 Design against collision and grounding

The regulations mentioned above have forced shipbuilders to migrate from a single hull to a double hull construction. A double hull structure can absorb more energy than a single hull construction of the same mass and overall dimensions (Ozguc et al., 2005). The energy absorption capacity of a ship structure can also be increased by using a high strength steel instead of traditional mild steel in its fabri-

cation (Lehmann and Peschmann, 2005). Recently, Paik (2003) proposed structural design alternatives to increase the resistance of ship structures against collisions and grounding events. A few examples are given here:

**Soft bow.** During a ship collision, the rigid bulbous bow of the striking ship can penetrate the side of the struck vessel. To limit the damage induced to the struck ship, soft buffer bows can be designed to absorb a part of the collision energy (Endo et al., 2004; Yamada and Endo, 2004).

**Variable bottom height.** About 65% of grounding accidents involve the front part of the vessel. To account for this risk, the spacing between the inner and outer hulls can be varied along the length of the ship to offer a better protection of the inner hull (LR, 1991; Amdahl and Kavlie, 1995).

**Mid-deck tanker.** The mid-deck construction has double hull sides, but a single hull bottom with a deck at mid-height. In the event of a side collision, the mid-deck provides structural reinforcement to the side panels. On the other hand, in the event of grounding, the design allows the oil to flow upward in the mid-deck since the density of sea water is superior to the density of oil. See Kawaichi et al. (1995) for more details.

**Sandwich construction.** The inner and outer hulls can be connected with a light core to increase the structural performances of the ship hull. This concept was proposed by Jones (1976), but it has been adopted by shipbuilders only recently. Examples of core topologies considered for ship hulls include the X-core (Törnqvist, 2003; Törnqvist and Simonsen, 2004) and the Y-core (Ludolph, 2001; Konter et al., 2004). The Y-frame core is of particular interest in this thesis and its development is reported in the next section.

### 2.4.4 Development of the Y-frame sandwich hull design

Full-scale collision tests were performed by Damen Schelde Naval Shipbuilding to compare the resistance of different conventional and innovative hull designs. Four structures were considered: (i) a conventional single hull, (ii) a conventional double hull, (iii) a double hull with a Y-frame core and (iv) a double hull made from two corrugated panels. These designs are illustrated in Fig. 2.20. The results were striking; all structures were perforated except the Y-frame double hull, which showed only a small dent after not only one, but two successive impacts, see Fig.

2.21 (Wevers and Vredeveldt, 1999). Those experimental results were also supported by finite element simulations, which revealed that the Y-frame double hull design can absorb two times more energy than a conventional double hull before perforation of the outer hull (Naar et al., 2002).

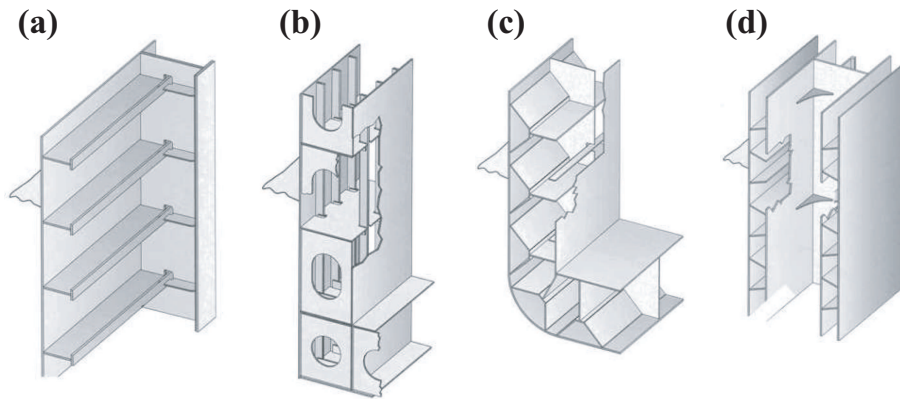


**Figure 2.20:** Four hull designs considered in full-scale collision tests: (a) a conventional single hull, (b) a conventional double hull, (c) a double hull with a Y-frame core and (d) a double hull made from two corrugated panels. Adapted from ISSC (2006a).



**Figure 2.21:** Photographs of full-scale collision tests performed on the Y-frame double hull structure. Adapted from Konter et al. (2004) and Wevers and Vredeveldt (1999).

The examination of the Y-frame double hull structure after the full-scale collision tests revealed that the inner hull played a minor role and underwent no visible plastic deformation (Wevers and Vredeveldt, 1999). This motivated Damen Schelde Naval Shipbuilding to develop a Y-frame single hull design where the Y-frame stiffeners are fixed to the bulkhead with the back face absent. Full-scale collision tests were also performed on this Y-frame single hull structure and it was found to be as resistant as the Y-frame double hull design. However, the results did not allow a direct comparison between the Y-frame single and double hull constructions; the two designs had a slightly different geometry and a different mass. The strength of

Y-frame single and double hull designs will be compared on an equal mass basis in Chapter 4.

The Y-frame single hull was approved by the classification society Germanischer Lloyd and it is now a patented design<sup>1</sup>. So far, 24 inland waterway tankers have been manufactured with the Y-frame single hull design. The Y-frame profile is obtained by welding together folded mild steel plates, see Fig. 2.22 (Graaf et al., 2004). The superior crashworthiness of the Y-frame single hull design (compared to a conventional double hull design) allows Damen Schelde Naval Shipbuilding to build the inline waterway tankers with four tanks of 550 m<sup>3</sup> instead of six tanks of 380 m<sup>3</sup> as usually required by the ADNR regulations (Vredeveldt and Roeters, 2004). Using four tanks instead of six is a considerable competitive advantage for Damen Schelde Naval Shipbuilding as it reduces the cost of piping equipment.



**Figure 2.22:** Construction of inland waterway tankers with a Y-frame single hull structure. Adapted from Graaf et al. (2004) and Vredeveldt and Roeters (2004).

## 2.5 Concluding remarks

Metallic lattice materials have been introduced in this chapter and classified in three families: foams, truss and prismatic lattices. They were shown to be ideal candidates for sandwich cores on the account of their high strength and low density. Of all stainless steel lattice materials tested, the pyramidal lattice made from hollow tubes offered the highest compressive strength. The potential of using a surface treatment to increase the strength of this lattice will be the subject of the next chapter.

Prismatic lattices, like the corrugated and Y-frame cores, are easier to manufacture than truss lattices. Consequently they are more attractive for industrial applications such as the construction of ship hulls. Extensive research has been conducted on the

---

<sup>1</sup>International Patent Application No.PCT/NL99/00757 with Publication No.WO 00/35746

quasi-static and the blast responses of both the corrugated core and the Y-frame core. However, some aspects regarding their use in sandwich ship hulls remain unclear and will be addressed in Chapters 4, 5 and 6. A comparison between the strength of single and double hull designs will be presented in Chapter 4 for quasi-static loading. Then, the response of a sandwich hull construction to a ship collision at 5 m/s is compared to its quasi-static response in Chapter 5. Finally, the influence of the loading velocity upon the indentation response of a sandwich ship hull is addressed in Chapter 6.



## Chapter 3

# Compressive response of a carburised pyramidal lattice

### Summary

The finite element method was used to simulate the compressive response of a pyramidal lattice made from inclined tubes or solid struts. First, the response of both lattices was compared for two levels of material strain hardening: (i) a perfectly plastic solid and (ii) a strain hardening solid representative of stainless steel. The compressive collapse mode of the lattice was relatively insensitive to the level of strain hardening. In contrast, strain hardening increased the peak compressive strength of both inclined tubes and struts with a slenderness ratio inferior to ten. Second, the response of a carburised pyramidal lattice was simulated. Carburisation increases the yield strength of the parent material and influences the collapse mode of the lattice; the transition between plastic and elastic buckling occurred at a smaller slenderness ratio when the lattice was carburised. Carburisation also increased the peak compressive strength of the lattice, except for those collapsing by elastic buckling. Finally, a comparison with other lattice materials revealed that the pyramidal lattice made from carburised tubes is stronger than aluminium or titanium lattices and as strong as those made from carbon fibre reinforced polymers.

### 3.1 Introduction

Lightweight metallic sandwich panels comprise of two face-sheets separated by a low density core (Zenkert, 1995). The core has to be light but also strong as its compressive and shear strengths have a significant influence on the overall bending strength of the sandwich panel. The compressive and shear strengths of the core depend on three parameters: (i) the topology, (ii) the relative density and (iii) the mechanical properties of the material from which the core is made (Ashby, 2006). Over the last decade, several different core topologies have been manufactured from type 304 stainless steel, for example: the corrugated core (Côté et al., 2006), the square honeycomb core (Côté et al., 2004) and the pyramidal core made from solid struts (Zok et al., 2004) or hollow tubes (Queheillalt and Wadley, 2005b, 2011). The measured compressive strength  $\bar{\sigma}_{pk}$  of each core topology is plotted in Fig. 2.7(a) (on page 13) as a function of the relative density  $\bar{\rho}$ . The results indicate clearly that the hollow pyramidal core is stronger than other core topologies, especially for low values of relative density.

The unit cell of a hollow pyramidal lattice is shown in Fig. 3.1(a); its geometry is defined by the inclination angle  $\omega$ , the tube length  $l$ , the tube outside diameter  $d$  and the wall thickness  $t$ . Pingle et al. (2011a) used the finite element method to examine the influence of the tube geometry upon the collapse mode of a hollow pyramidal lattice with  $\omega = 55^\circ$ . Their results are presented in the form of a collapse mechanism map<sup>1</sup> reproduced in Fig. 3.2. Six collapse modes are identified dependent upon the tube slenderness ratio  $l/d$  and the normalised wall thickness  $t/d$ . This map was developed for a hollow pyramidal lattice made from stainless steel, which possesses an important strain hardening capacity.

In the first part of this study, the effect of strain hardening upon the collapse mode and upon the compressive strength of a hollow pyramidal lattice will be evaluated. In the second part, the effect of carburisation will be investigated. Carburisation is a heat treatment process that hardens the surface of a metal. A low temperature carburisation treatment has been developed recently for stainless steel and, depending on the duration of the treatment, carburisation depths of 25-70  $\mu\text{m}$  can be achieved (Cao et al., 2003; Michal et al., 2006). In this study, the effect of carburisation upon the collapse mode and upon the compressive strength of a hollow pyramidal lattice will be examined. The potential of carburisation to increase the strength of lattice

---

<sup>1</sup>Similar collapse mechanism maps were developed for vertical tubes made from aluminium by Andrews et al. (1983) and Guillow et al. (2001).

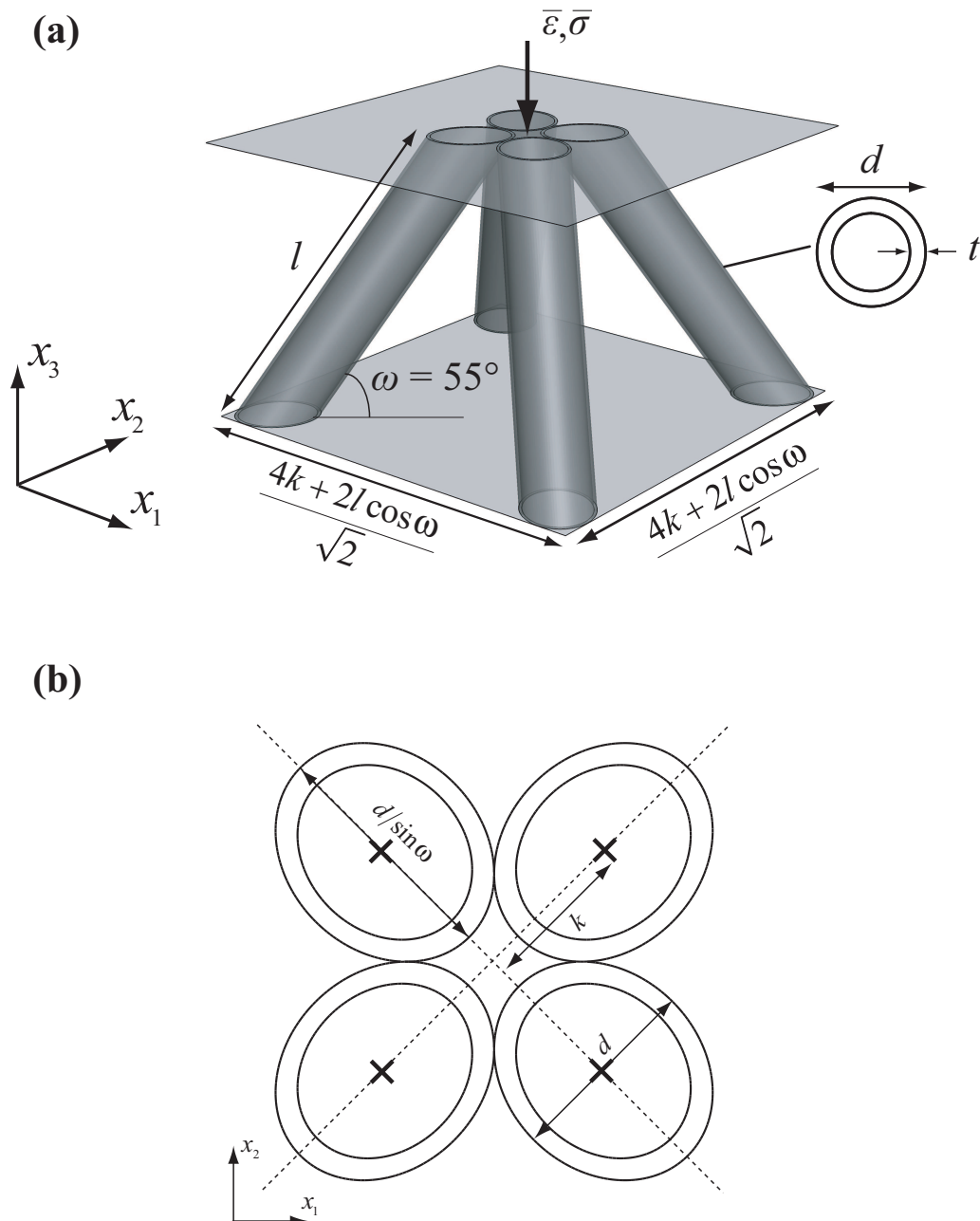
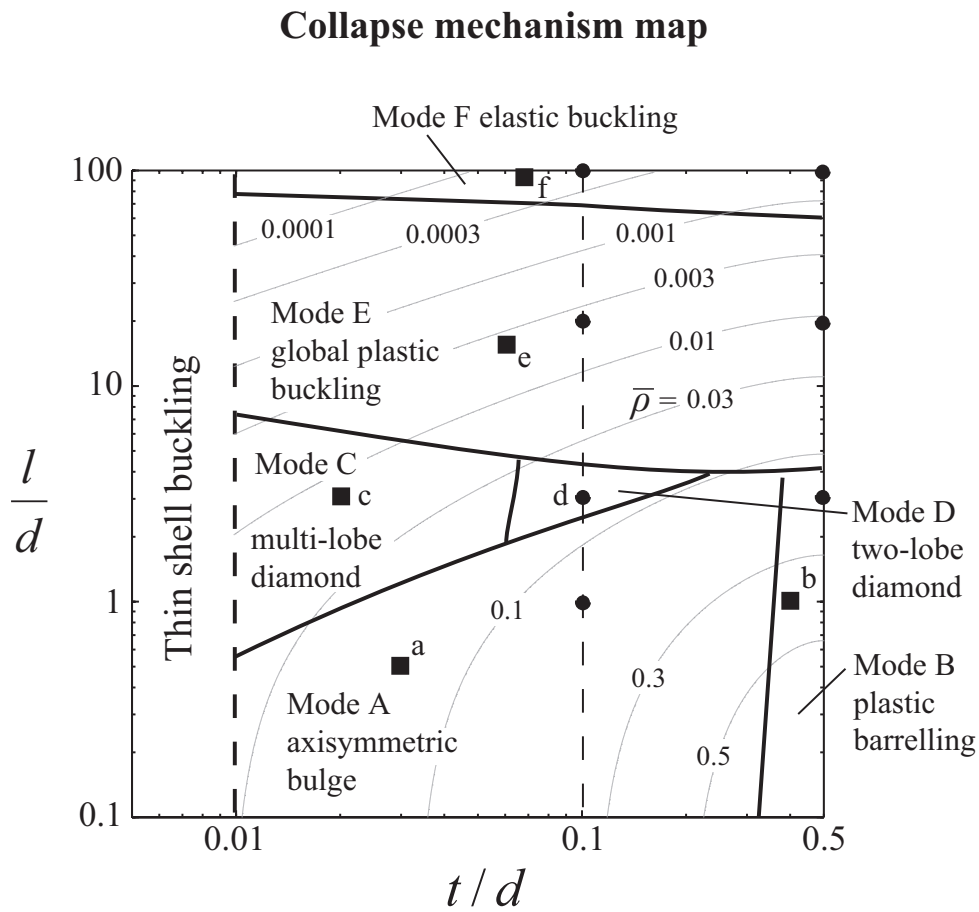


**Figure 3.1:** (a) Unit cell of the hollow pyramidal lattice. (b) Top view of the lattice.



### Collapse modes

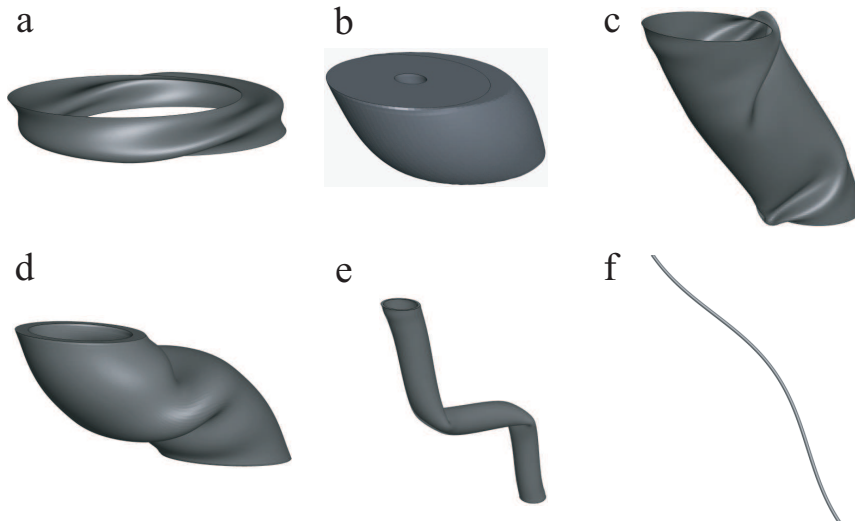


**Figure 3.2:** Collapse mechanism map for a hollow pyramidal lattice made from AISI 304 stainless steel. Examples of the six collapse modes (A-F) are also included. Representative geometries considered in this study are indicated by filled black circles and contours of relative density  $\bar{\rho}$  are plotted as grey lines. Adapted from Pingle et al. (2011a).

## 3.2 Geometry and analytical collapse load of the pyramidal lattice

---

materials made from stainless steel has not been investigated before; however, other surface treatments, such as plasma electrolytic oxidation and electrochemical anodizing, have been used recently to increase the compressive strength of aluminium metal foams (Abdulla et al., 2011; Bele et al., 2011; Dunleavy et al., 2011).

The effect of strain hardening and carburisation will be studied using the finite element method. The study will focus on two trajectories on the collapse mechanism map shown in Fig. 3.2. The first trajectory is indicated by a dashed line and represents tubes with a normalised wall thickness  $t/d = 0.1$ . The second trajectory is the right hand side of the map and represents pyramidal lattices made from solid struts,  $t/d = 0.5$ . For both trajectories, the slenderness ratio  $l/d$  will be varied from 1 to 100.

This chapter is organised as follows. First, the geometry and the analytical collapse load of the hollow pyramidal lattice are presented in Section 3.2. Second, the effect of strain hardening is addressed in Section 3.3 and then, the effect of carburisation is analysed in Section 3.4. Both Sections 3.3 and 3.4 include a description of the finite element models, an analysis of the compressive responses and a comparison between the compressive strength of inclined tubes and solid struts.

## 3.2 Geometry and analytical collapse load of the pyramidal lattice

### 3.2.1 Relative density

The unit cell of a hollow pyramidal lattice is shown in Fig. 3.1(a). Its geometry is defined by the tube length  $l$ , the outside diameter  $d$ , the wall thickness  $t$  and the inclination  $\omega$ . A top view of the lattice, see Fig. 3.1(b), reveals that the tube centres are offset by a distance  $k$  from the centre of the pyramid. The distance  $k$  is constrained such that:

$$k \geq k_{min} = \frac{d\sqrt{1 + \sin^2 \omega}}{2 \sin \omega} . \quad (3.1)$$

The tubes are touching each other at the face-sheets when  $k = k_{min}$ . The relative density of the hollow pyramidal lattice is given by:

$$\bar{\rho} = \frac{2\pi (d^2 - (d - 2t)^2)}{(4k + 2l \cos \omega)^2 \sin \omega} = \frac{2\pi \frac{t}{d} \left(1 - \frac{t}{d}\right)}{\left(2\gamma + \frac{l}{d} \cos \omega\right)^2 \sin \omega} \quad , \quad (3.2)$$

where  $\gamma$  is a function of the inclination  $\omega$  and is given by:

$$\gamma = \frac{\sqrt{1 + \sin^2 \omega}}{2 \sin \omega} \quad . \quad (3.3)$$

In this study, the tube spacing  $k = k_{min}$  and the inclination angle  $\omega = 55^\circ$  in all cases. With these two parameters fixed, Eq. (3.2) is used to plot contours of relative density  $\bar{\rho}$  on the collapse mechanism map shown in Fig. 3.2.

### 3.2.2 Analytical collapse load

When the hollow pyramidal lattice is compressed by a downward displacement  $\delta$ , a vertical force  $P$  develops in each tube of the lattice. The nominal compressive stress  $\bar{\sigma}$  on the front face-sheet can be expressed as:

$$\bar{\sigma} = \frac{8P}{(4k + 2l \cos \omega)^2} \quad , \quad (3.4)$$

and the corresponding nominal compressive strain is:

$$\bar{\epsilon} = \frac{\delta}{l \sin \omega} \quad . \quad (3.5)$$

Assuming that the lattice is made from an elastic perfectly plastic solid, two collapse modes can be anticipated: (i) plastic collapse or (ii) elastic buckling. An analytical expression for the plastic collapse load can be obtained by setting:

$$P_{pl} = \sigma_Y \frac{\pi}{4} \left(d^2 - (d - 2t)^2\right) \sin \omega \quad , \quad (3.6)$$

where the yield strength of the material is  $\sigma_Y$ . Substituting Eq. (3.6) in Eq. (3.4) returns the plastic collapse stress of the lattice:

$$\bar{\sigma}_{pl} = \bar{\rho} \sigma_Y \sin^2 \omega \quad . \quad (3.7)$$

Alternatively, an expression for the elastic buckling load can be obtained with:

$$P_{el} = \frac{4\pi^2 EI}{l^2} \sin \omega \quad , \quad (3.8)$$

where the Young's modulus of the material is  $E$  and the second moment of area of the tube is  $I = \frac{\pi}{64}(d^4 - (d - 2t)^4)$ . Equation (3.8) assumes that the inclined tube has both ends built in (Timoshenko and Gere, 1963). Substituting Eq. (3.8) in Eq. (3.4) returns the elastic buckling stress of the lattice:

$$\bar{\sigma}_{el} = \frac{\pi^3 E \frac{t}{d} \left( 1 - 3\frac{t}{d} + 4\left(\frac{t}{d}\right)^2 - 2\left(\frac{t}{d}\right)^3 \right)}{\left( \frac{l}{d} \left( 2\gamma + \frac{l}{d} \cos \omega \right) \right)^2} \sin \omega \quad . \quad (3.9)$$

Finally, the transition from plastic collapse to elastic buckling can be obtained by setting  $P_{el} = P_{pl}$ . This transition occurs at a slenderness ratio:

$$\frac{l}{d} = \sqrt{\frac{\pi^2 E}{2\sigma_Y} \left( 1 - 2\frac{t}{d} + 2\left(\frac{t}{d}\right)^2 \right)} \quad . \quad (3.10)$$

## 3.3 Influence of strain hardening

### 3.3.1 Description of the finite element models

All simulations were performed with the implicit solver of the commercially available finite element software Abaqus (version 6.10). The boundary conditions, mesh, geometric imperfections, material properties and dimensions employed are detailed below.

#### Boundary conditions

It is sufficient to consider only one inclined tube to capture the compressive response of the hollow pyramidal lattice. The boundary conditions employed in the finite element simulations are illustrated in Fig. 3.3. Front and back face-sheets were modelled as rigid surfaces and a perfect bonding was assumed between the inclined tube and the face-sheets. The back face was clamped against translational

and rotational displacements whereas the front face had a prescribed downward displacement  $\delta$ , see Fig. Fig. 3.3. No lateral motion (in the  $x_1$  and  $x_2$  directions) and no rotation were allowed for the front face. A hard frictionless contact was defined between all surfaces of the model allowing the lattice to densify at large values of nominal compressive strain  $\bar{\epsilon}$ .

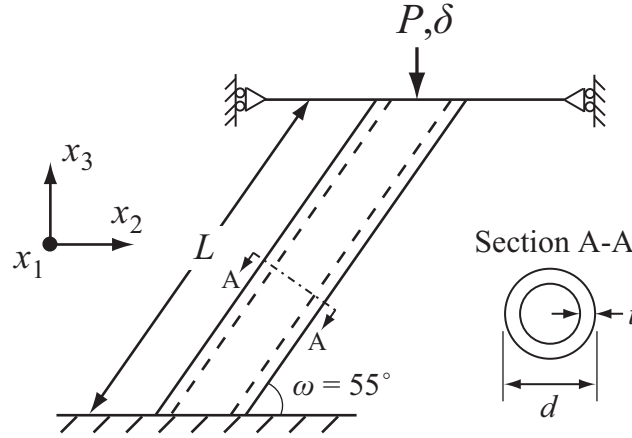


**Figure 3.3:** Finite element model used to simulate the compressive response of an inclined tube.

### Mesh and geometric imperfections

The inclined tubes were meshed using three-dimensional hexahedral elements (C3D8R in Abaqus notation) with at least five elements through the wall thickness. A small geometric imperfection was included in all simulations. The imperfection had the shape of the first buckling mode with an amplitude  $\zeta = 0.05t$ . The sensitivity of the compressive response upon the choice of imperfection is discussed in Appendix 3.A.

### Material properties

The material properties were chosen to be representative of AISI 304 stainless steel. This material was used in previous experimental and numerical studies on the hollow pyramidal lattice (Queheillalt and Wadley, 2005b, 2011; Pingle et al., 2011a,b). The parent material of the lattice was modelled as a rate-independent elastic-plastic solid in accordance with J2-flow theory. The elastic regime was linear and isotropic, as characterised by a Young's modulus  $E = 200$  GPa and a Poisson's ratio  $\nu = 0.3$ . The yield strength of the material was set to  $\sigma_Y^A = 200$  MPa. In this section, two levels of strain hardening are compared: (i)  $E_t = 0$ , representing a perfectly plastic

solid and (ii)  $E_t = 2$  GPa, a realistic value for stainless steel. The uniaxial tensile responses of these two material models are compared in Fig. 3.4.

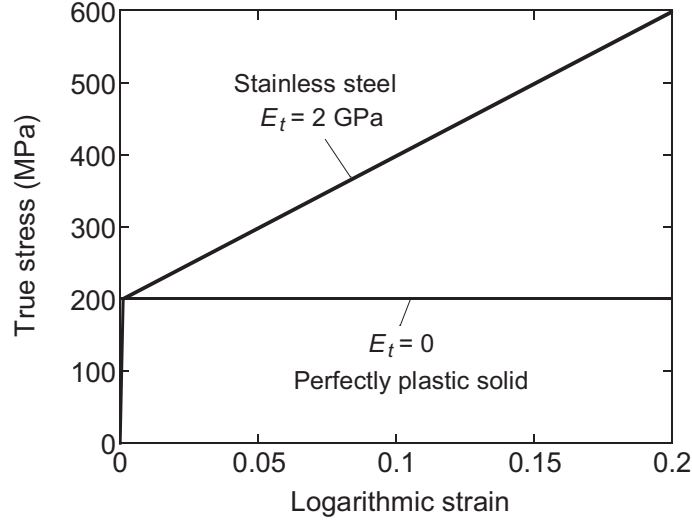


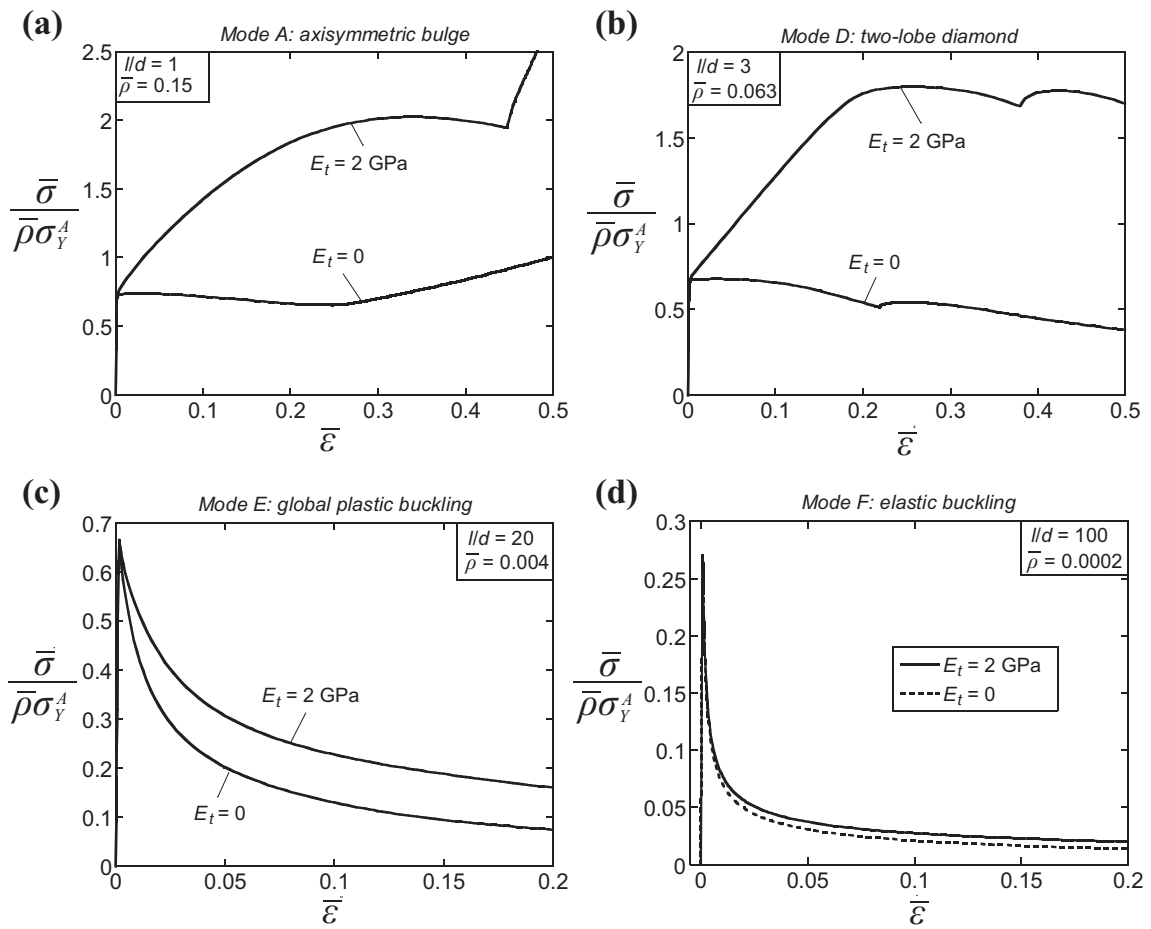
**Figure 3.4:** Uniaxial tensile responses of the two material models employed in the finite element simulations analysing the influence of strain hardening.

#### Dimensions analysed

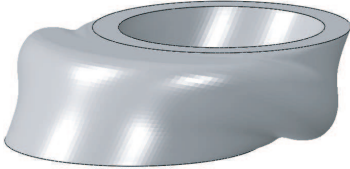
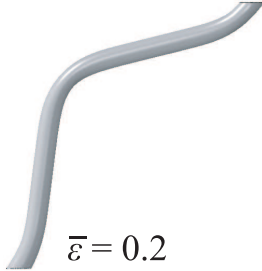
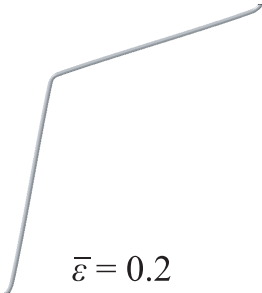
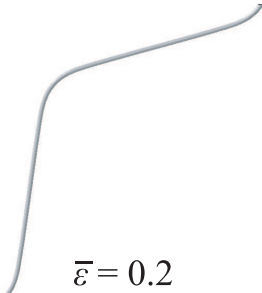
In this study, the inclination angle was kept fixed at  $\omega = 55^\circ$  and two different cross-sections were considered: (i) a tube with  $t/d = 0.1$  and (ii) a solid strut corresponding to  $t/d = 0.5$ . For these two values of  $t/d$ , the slenderness ratio  $l/d$  was varied from 1 to 100.

#### 3.3.2 Results for an inclined tube

The collapse of an inclined stainless steel tube with  $t/d = 0.1$  can be catalogued into four distinct modes (A, D, E and F) depending on the slenderness ratio  $l/d$ , see Fig. 3.2. Four selected geometries with  $l/d = 1, 3, 20$  and  $100$  that collapse in mode A, D, E and F, respectively, are marked on the map in Fig. 3.2 and their compressive responses are shown in Fig. 3.5. The responses are plotted in terms of the nominal compressive stress  $\bar{\sigma}$ , normalised by the relative density  $\bar{\rho}$  and the yield strength  $\sigma_Y^A$ , versus the nominal compressive strain  $\bar{\epsilon}$ . For each geometry, the compressive response is given for two strain hardening moduli: (i)  $E_t = 0$  and (ii)  $E_t = 2$  GPa. The deformed meshes corresponding to these responses are given in Table 3.1 to exemplify the four collapse modes of the inclined tube.



**Figure 3.5:** Influence of the strain hardening modulus  $E_t$  on the compressive response of an inclined tube  $t/d = 0.1$ . Results are given for (a)  $l/d = 1$ , (b)  $l/d = 3$ , (c)  $l/d = 20$  (d)  $l/d = 100$ .

Geometry	$E_t = 0$	$E_t = 2 \text{ GPa}$
Mode A $l/d = 1$ $\bar{\rho} = 0.15$	 $\bar{\varepsilon} = 0.5$	 $\bar{\varepsilon} = 0.5$
Mode D $l/d = 3$ $\bar{\rho} = 0.064$	 $\bar{\varepsilon} = 0.5$	 $\bar{\varepsilon} = 0.5$
Mode E $l/d = 20$ $\bar{\rho} = 0.004$	 $\bar{\varepsilon} = 0.2$	 $\bar{\varepsilon} = 0.2$
Mode F $l/d = 100$ $\bar{\rho} = 0.0002$	 $\bar{\varepsilon} = 0.2$	 $\bar{\varepsilon} = 0.2$

**Table 3.1:** Influence of the strain hardening modulus  $E_t$  on the deformed meshes of an inclined tube  $t/d = 0.1$ . Results are given for selected values of  $l/d$ .

All compressive responses shown in Fig. 3.5 exhibit a peak stress  $\bar{\sigma}_{pk}$ . The axial compressive stress in the tube reaches the yield strength when  $\bar{\sigma}/(\bar{\rho}\sigma_Y^A) = \sin^2 \omega \approx 0.67$ , see Eq. (3.7). Of the four collapse modes shown in Fig. 3.5, only mode F: elastic buckling has a peak stress inferior to the yield limit. The influence of strain hardening will be discussed below for each collapse mode.

Mode A: axisymmetric bulge is the collapse mode for  $l/d = 1$ , see Fig. 3.5(a). Material strain hardening has a significant influence on the compressive response for this collapse mode; the peak stress increases by a factor of three when  $E_t$  is increased from 0 to 2 GPa.

An inclined tube with  $l/d = 3$  collapses by Mode D: two-lobe diamond, see Fig. 3.5(b). The two “bumps” in the compressive response represent the formation of the two lobes. Again, material strain hardening increases the peak stress, but the increase is slightly less than for  $l/d = 1$ .

Mode E: global plastic buckling is the operative collapse mode for an inclined tube with  $l/d = 20$  and its compressive response is shown in Fig. 3.5(c). Note that strain hardening has no influence on the peak stress; in both cases the axial compressive stress in the tube reaches the yield strength  $\bar{\sigma}/(\bar{\rho}\sigma_Y^A) \approx 0.67$ , then the tube buckles and forms a plastic hinge at mid-length. However, the post-peak response is stronger for  $E_t = 2$  GPa than for  $E_t = 0$ .

Finally, an inclined tube with a slenderness ratio  $l/d = 100$  collapses by Mode F: elastic buckling, see Fig. 3.5(d). As expected, strain hardening has no influence on the peak stress for this collapse mode. The stress drops sharply after the peak due to the development of a plastic hinge at mid-length. Despite the formation of a plastic hinge, strain hardening has a negligible effect on the post-peak response.

The deformed meshes, corresponding to the responses given in Fig. 3.5, are shown in Table 3.1. The deformed meshes of simulations with a strain hardening solid ( $E_t = 2$  GPa) have more diffuse plastic hinges than those obtained with a perfectly plastic solid ( $E_t = 0$ ). Nevertheless, the collapse mode appears to be insensitive to the strain hardening modulus.

### 3.3.3 Results for an inclined solid strut

The map in Fig. 3.2 indicates that the collapse of an inclined solid strut ( $t/d = 0.5$ ) made from stainless steel can be catalogued into three distinct modes (B, E and F)

depending on the slenderness ratio  $l/d$ . As marked in Fig. 3.2, one geometry was selected in each of the three collapse modes:  $l/d = 3$  for mode B,  $l/d = 20$  for mode E and  $l/d = 100$  for mode F. The compressive responses of these three selected geometries are shown in Fig. 3.6. In each plot, results are given for  $E_t = 0$  and  $E_t = 2$  GPa. In addition, the deformed meshes corresponding to these compressive responses are shown in Table 3.2.

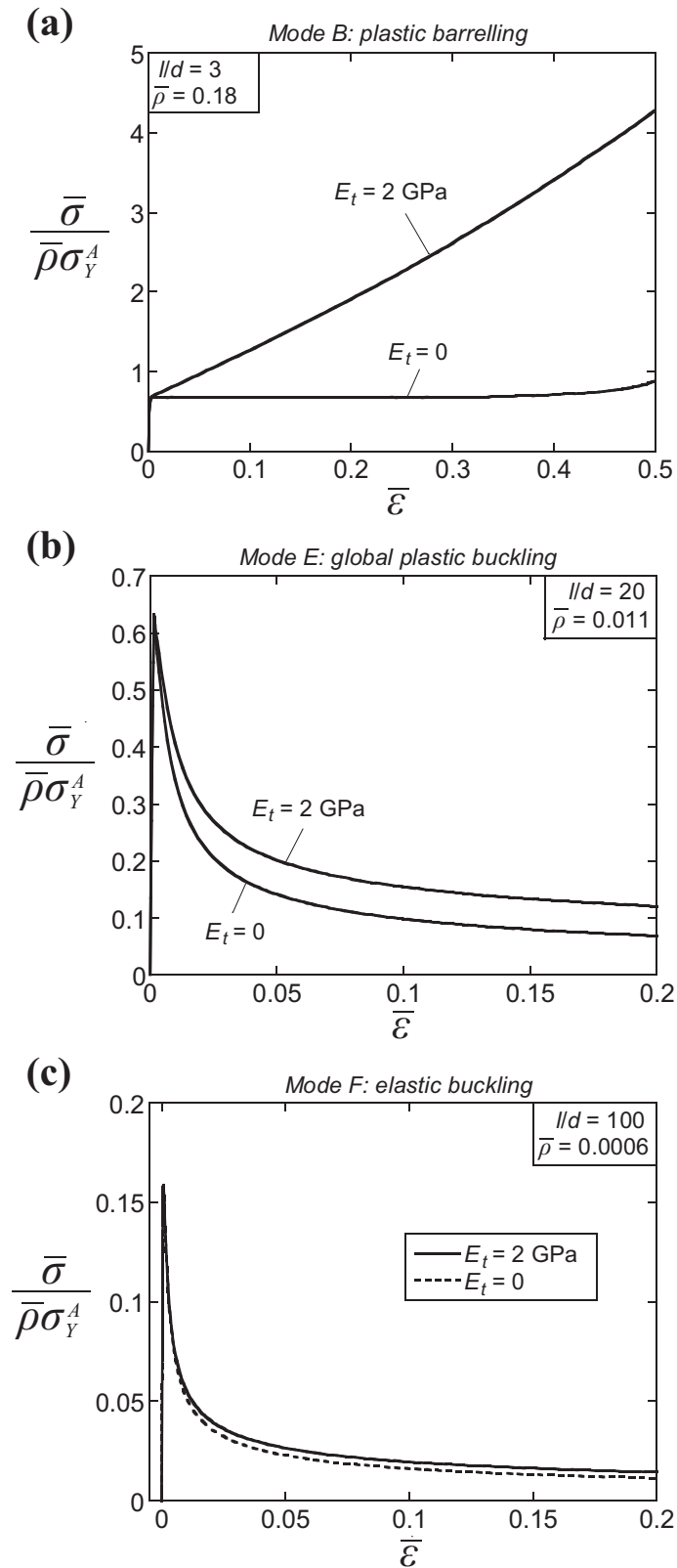
An inclined solid strut with  $l/d = 3$  collapses by mode B: plastic barrelling and its compressive response is particularly sensitive to strain hardening, see Fig. 3.6(a). Note that the response for this collapse mode does not exhibit a peak stress (below  $\bar{\epsilon} = 0.5$ ). For this particular case, the peak stress  $\bar{\sigma}_{pk}$  will be defined as the stress at a nominal compressive strain  $\bar{\epsilon} = 0.5$ . The same definition was adopted by Pingle et al. (2011a).

As the slenderness ratio of the inclined solid strut is increased, the collapse mode changes to mode E: global plastic buckling, see Fig. 3.6(b), and subsequently to mode F: elastic buckling, see Fig. 3.6(c). The influence of strain hardening on the responses of these two collapse modes was discussed above for inclined tubes, and the results for inclined struts are similar: (i) the peak stress for  $l/d = 20$  and 100 is insensitive to  $E_t$  and (ii) strain hardening strengthens the post-peak response when  $l/d = 20$ , but has minimal effect when  $l/d = 100$ .

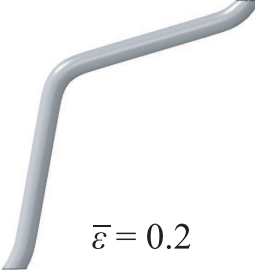
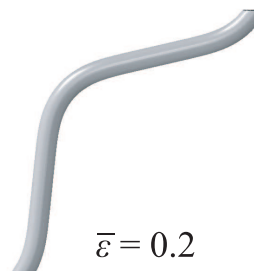
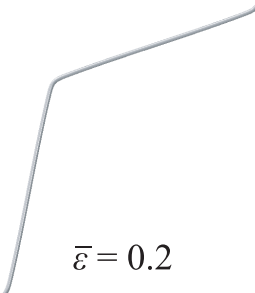
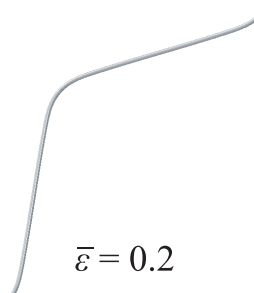
The deformed meshes shown in Table 3.2 for inclined solid struts confirm the observations made above for inclined tubes: strain hardening results in more diffuse plastic hinges, but the collapse mode is insensitive to  $E_t$ . For the tube and the solid strut, our simulations indicate that the collapse mechanism map shown in Fig. 3.2 is relatively insensitive to the strain hardening modulus, at least for the two values of  $E_t$  considered in this study.

#### 3.3.4 Comparison between tube and solid strut

Above, the compressive responses of inclined tubes and solid struts were presented separately for selected values of slenderness ratio  $l/d$ . To summarise these results, the normalised peak stress  $\bar{\sigma}_{pk}/(\bar{\rho}\sigma_Y^A)$  is plotted in Fig. 3.7 as a function of the relative density  $\bar{\rho}$  for both inclined tubes ( $t/d = 0.1$ ) and solid struts ( $t/d = 0.5$ ). For both values of  $t/d$ , the collapse modes are identified and results are given for  $E_t = 0$  and  $E_t = 2$  GPa. Three regimes can be identified in Fig. 3.7:



**Figure 3.6:** Influence of the strain hardening modulus  $E_t$  on the compressive response of an inclined solid strut  $t/d = 0.5$ . Results are given for (a)  $l/d = 3$ , (b)  $l/d = 20$  and (c)  $l/d = 100$ .

Geometry	$E_t = 0$	$E_t = 2 \text{ GPa}$
Mode B $l/d = 3$ $\bar{\rho} = 0.18$	 $\bar{\varepsilon} = 0.4$	 $\bar{\varepsilon} = 0.4$
Mode E $l/d = 20$ $\bar{\rho} = 0.011$	 $\bar{\varepsilon} = 0.2$	 $\bar{\varepsilon} = 0.2$
Mode F $l/d = 100$ $\bar{\rho} = 0.0006$	 $\bar{\varepsilon} = 0.2$	 $\bar{\varepsilon} = 0.2$

**Table 3.2:** Influence of the strain hardening modulus  $E_t$  on the deformed meshes of an inclined solid strut  $t/d = 0.5$ . Results are given for selected values of  $l/d$ .

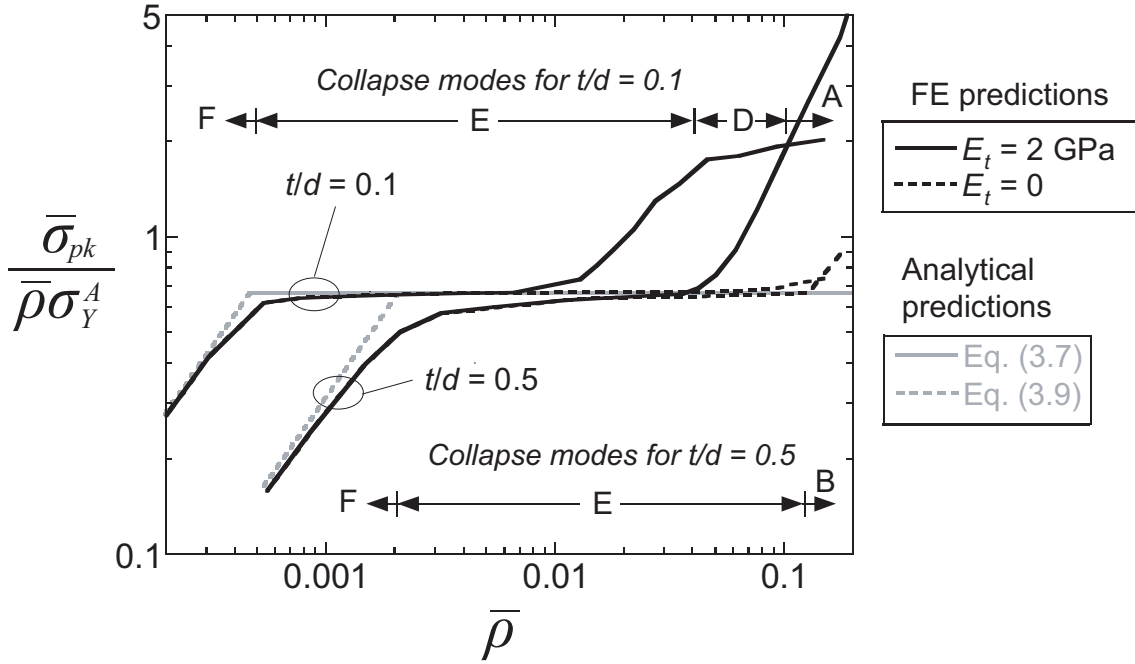


**Figure 3.7:** Influence of the strain hardening modulus  $E_t$  on the compressive strength of an inclined tube  $t/d = 0.1$  and an inclined solid strut  $t/d = 0.5$ .

1. The inclined tube with  $\bar{\rho} < 0.0005$  and the inclined solid strut with  $\bar{\rho} < 0.002$  both collapse by Mode F: elastic buckling. For this collapse mode, the normalised peak stress increases with increasing relative density as suggested by the analytical expression for elastic buckling, Eq. (3.9). This equation is also plotted in Fig. 3.7 and is in excellent agreement with the simulations, for both the tube and the solid strut. As mentioned above, strain hardening has no influence on the peak stress for this collapse mode.
2. When the relative density of the inclined tube is in the range  $0.0005 \leq \bar{\rho} \leq 0.01$ , the collapse mode is E: global plastic buckling. The same collapse mode is operative for inclined solid struts with relative densities  $0.002 \leq \bar{\rho} \leq 0.04$ . Equation (3.7) predicting the plastic collapse of the lattice is also included in Fig. 3.7; there is a good agreement between the analytical formula and the simulations. Again, for those intervals of relative density, the peak stress is insensitive to the level of strain hardening.
3. Finally, when  $\bar{\rho} > 0.01$  for the inclined tube and when  $\bar{\rho} > 0.04$  for the inclined solid strut, the peak stress becomes sensitive to strain hardening; values of  $\bar{\sigma}_{pk}/(\bar{\rho}\sigma_Y^A)$  obtained with  $E_t = 2$  GPa exceed those obtained with  $E_t = 0$ . Note that an inclined tube with  $\bar{\rho} = 0.01$  and a solid strut with  $\bar{\rho} = 0.04$  both

correspond to a slenderness ratio  $l/d = 10$ , see Fig. 3.2 or refer to Eq. (3.2).

It is clear from Fig. 3.7 that the tube outperforms the solid strut for low values of relative density,  $\bar{\rho} < 0.002$ . This is because the transition from global plastic buckling (Mode E) to elastic buckling (Mode F) occurs at a lower value of relative density for the tube than for the solid strut. In contrast, at high values of relative density,  $\bar{\rho} > 0.1$ , the solid strut collapses by plastic barrelling (Mode B) and outperforms the tube, especially for  $E_t = 2$  GPa.

### 3.4 Influence of carburisation

Carburisation is a heat treatment process during which carbon is absorbed by a metallic part making its surface harder. Different carburisation depths can be achieved depending upon the duration and temperature of the heat treatment. The cross-sections of a carburised tube and a carburised solid strut are illustrated in Fig. 3.8. The carburisation depth  $h$  adds a third non-dimensional parameter to the analysis; the compressive strength of the pyramidal lattice is now governed by  $l/d$ ,  $t/d$  and  $h/d$  (recall that the inclination angle is fixed at  $\omega = 55^\circ$ ).

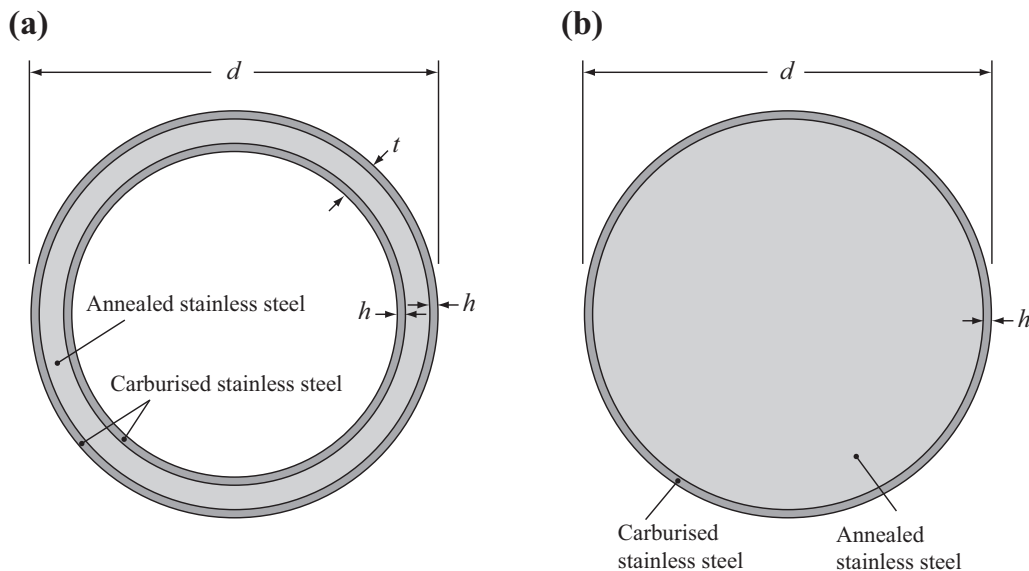


**Figure 3.8:** Cross-sections of a carburised (a) tube and (b) solid strut.

### 3.4.1 Description of the finite element models

The boundary conditions, the mesh details and the geometric imperfections used in this section were the same as those used previously, see Section 3.3.1.

#### Material properties

Both annealed and carburised stainless steels were modelled as rate-independent elastic-plastic solids in accordance with J2-flow theory. The elastic regime of both materials was linear and isotropic, as characterised by a Young's modulus  $E = 200$  GPa and a Poisson's ratio  $\nu = 0.3$ . Each material had a different plastic behaviour. Annealed stainless steel had a yield strength  $\sigma_Y^A = 200$  MPa and a linear strain hardening response with a tangent modulus  $E_t = 2$  GPa. In contrast, carburised stainless steel was considered to be perfectly plastic ( $E_t = 0$ ) with a yield strength  $\sigma_Y^C = 2$  GPa. The yield strength of carburised stainless steel is estimated from a hardness test reported by Michal et al. (2006). The uniaxial tensile responses of annealed and carburised stainless steels are compared in Fig. 3.9.

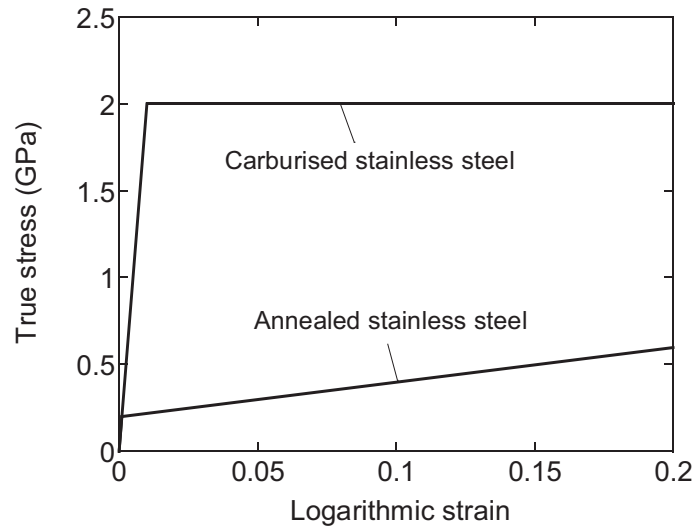


**Figure 3.9:** Uniaxial tensile responses of annealed and carburised stainless steels employed in the finite element simulations analysing the influence of carburisation.

#### Dimensions analysed

Again, the slenderness ratio  $l/d$  was varied from 1 to 100 for both the inclined tube ( $t/d = 0.1$ ) and the inclined solid strut ( $t/d = 0.5$ ). Four values of normalised

carburisation depth were considered  $h/d = 0, 0.02, 0.04$  and  $0.05$ . Note that for  $h/d = 0.05$ , the entire cross-section of the tube ( $t/d = 0.1$ ) is carburised.

### 3.4.2 Results for an inclined tube

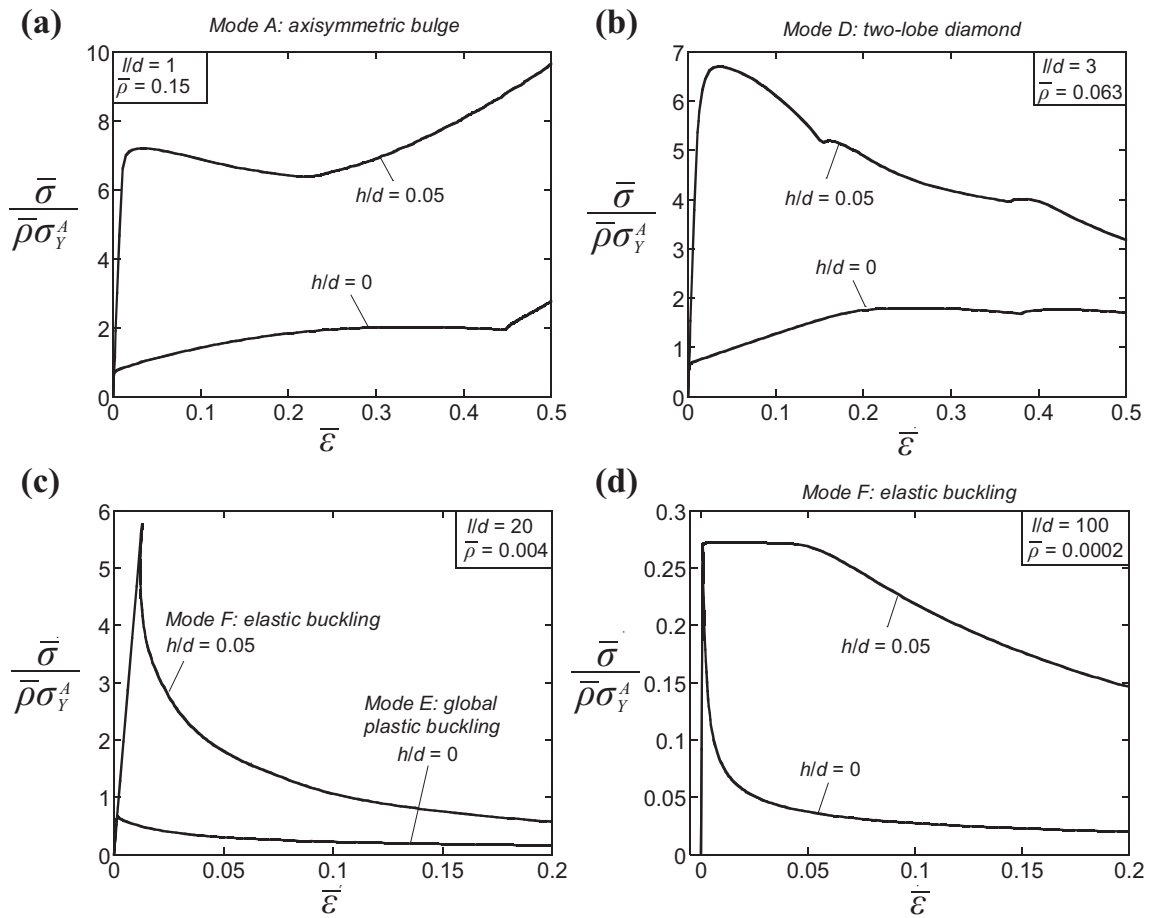
The influence of carburisation upon the compressive response of an inclined tube with  $t/d = 0.1$  is shown in Fig. 3.10 for the four selected geometries identified in Section 3.3.2. For each geometry, the results are given for a non-carburised tube,  $h/d = 0$ , and for a tube with a normalised carburisation depth  $h/d = 0.05$ . The deformed meshes corresponding to these responses are given in Table 3.3.

Carburisation significantly increases the peak compressive stress  $\bar{\sigma}_{pk}$  of short inclined tubes with  $l/d = 1$  and  $3$ , see Fig. 3.10(a) and (b), respectively. Note that both carburised tubes ( $h/d = 0.05$ ) have the same peak stress  $\bar{\sigma}_{pk} = 6.7\bar{\rho}\sigma_Y^A$ , which corresponds to the plastic collapse stress evaluated by Eq. (3.7) by setting the yield strength to  $\sigma_Y^C = 10\sigma_Y^A = 2$  GPa (recall that for  $h/d = 0.05$  the entire cross-section of the tube is carburised). In addition, the peak stress occurs at a larger value of nominal compressive strain for non-carburised tubes than for carburised ones. Annealed stainless steel has a tangent modulus  $E_t = 2$  GPa and the response of non-carburised tubes display a significant amount of plastic hardening before reaching the peak stress. On the other hand, carburised stainless steel is modelled as a perfectly plastic solid and consequently the response of carburised tubes do not display any plastic hardening.

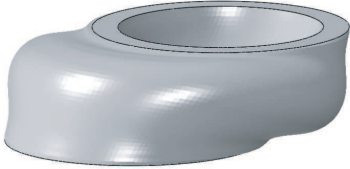
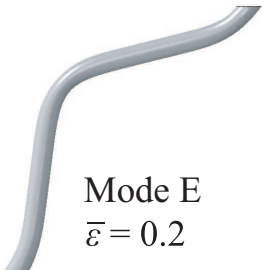
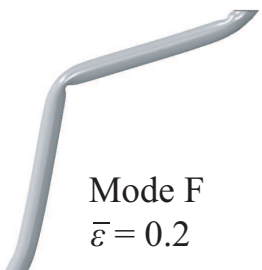
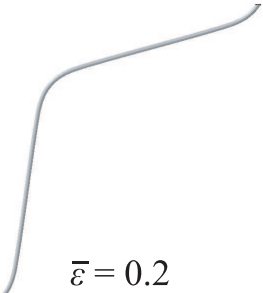
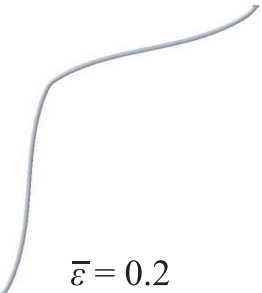
The non-carburised inclined tube with a slenderness ratio  $l/d = 20$  collapses by mode E: global plastic buckling and has a peak stress  $\bar{\sigma}_{pk} = 0.67\bar{\rho}\sigma_Y^A$ , see Fig 3.10(c). Carburising this tube increases the peak stress to  $\bar{\sigma}_{pk} = 5.7\bar{\rho}\sigma_Y^A$ , which is inferior to the plastic collapse load  $\bar{\sigma}_{pl} = 6.7\bar{\rho}\sigma_Y^A$  prescribed by Eq. (3.7). Thus, carburisation increases the peak stress, but also changes the collapse mode from mode E: plastic buckling to mode F: elastic buckling.

The peak stress of long inclined tubes collapsing by mode F: elastic buckling is insensitive to carburisation, see Fig. 3.10(d). This result was expected as both annealed and carburised stainless steels have the same Young's modulus  $E = 200$  GPa. On the other hand, the post-peak response is sensitive to carburisation; the carburised tube is significantly stronger than the non-carburised one.

Finally, the deformed meshes of non-carburised tubes ( $h/d = 0$ ) are compared to



**Figure 3.10:** Influence of the carburisation depth  $h/d$  on the compressive response of an inclined tube  $t/d = 0.1$ . Results are given for (a)  $l/d = 1$ , (b)  $l/d = 3$ , (c)  $l/d = 20$  (d)  $l/d = 100$ .

Geometry	$h/d = 0$	$h/d = 0.05$
Mode A $l/d = 1$ $\bar{\rho} = 0.15$	 $\bar{\varepsilon} = 0.5$	 $\bar{\varepsilon} = 0.5$
Mode D $l/d = 3$ $\bar{\rho} = 0.063$	 $\bar{\varepsilon} = 0.5$	 $\bar{\varepsilon} = 0.5$
$l/d = 20$ $\bar{\rho} = 0.004$	Mode E $\bar{\varepsilon} = 0.2$ 	Mode F $\bar{\varepsilon} = 0.2$ 
Mode F $l/d = 100$ $\bar{\rho} = 0.0002$	$\bar{\varepsilon} = 0.2$ 	$\bar{\varepsilon} = 0.2$ 

**Table 3.3:** Influence of the carburisation depth  $h/d$  on the deformed meshes of an inclined tube  $t/d = 0.1$ . Results are given for selected values of  $l/d$ .

those of carburised tubes ( $h/d = 0.05$ ) in Table 3.3. In general, carburisation has a relatively small effect on the deformed meshes.

### 3.4.3 Results for an inclined solid strut

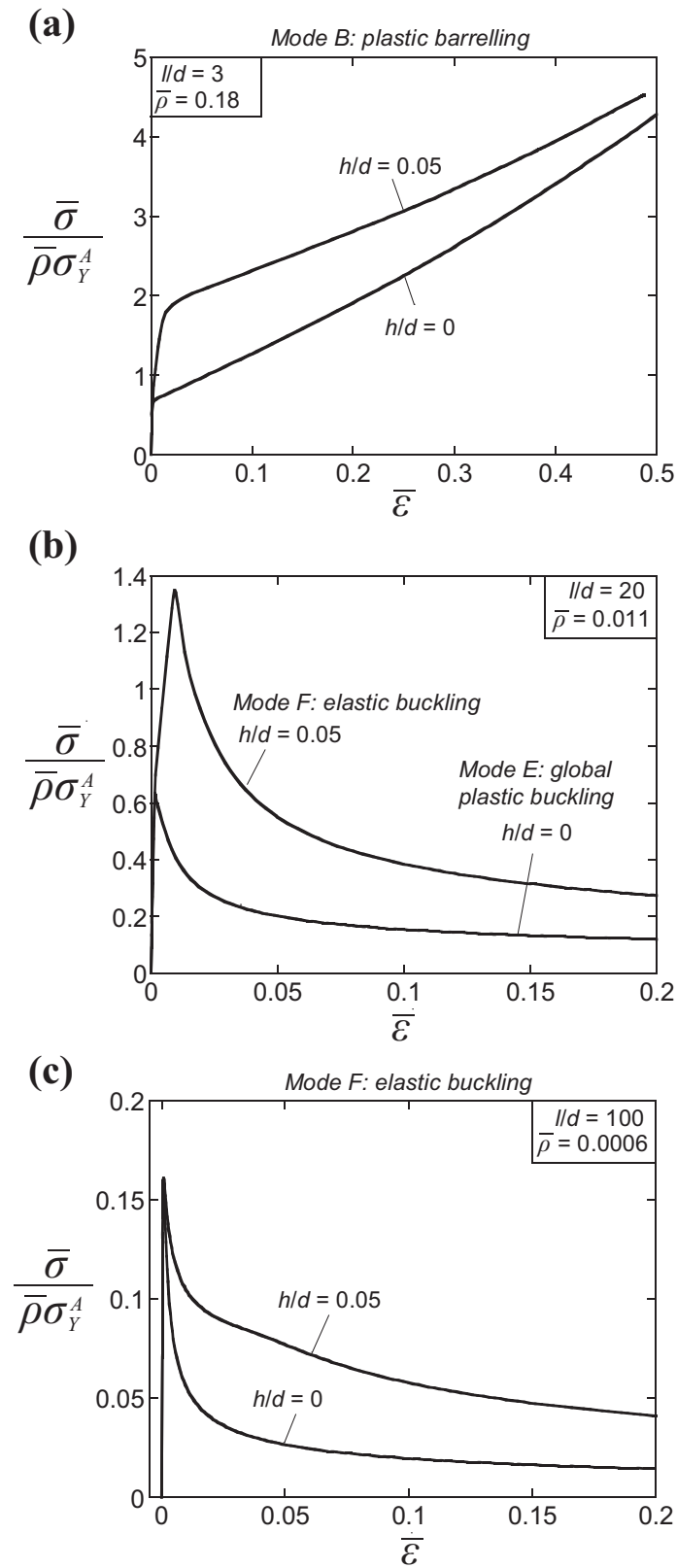
The compressive response of an inclined solid strut ( $t/d = 0.5$ ) is shown in Fig. 3.11 for the three selected geometries identified in Section 3.3.3. For each geometry, the response of a non-carburised strut,  $h/d = 0$ , is compared to that of a carburised strut with  $h/d = 0.05$ . For completeness, the deformed meshes corresponding to these responses are displayed in Table 3.4. In contrast with the carburised tube analysed in the previous section, the cross-section of the carburised strut with  $h/d = 0.05$  is not entirely carburised; it has an outside layer of carburised stainless steel with an inside core of annealed stainless steel.

The compressive response of a strut with  $l/d = 3$ , which collapses by mode B: plastic barrelling, is shown in Fig. 3.11(a). Carburisation clearly increases the yield stress of the lattice from  $0.67\bar{\rho}\sigma_Y^A$  to approximately  $1.8\bar{\rho}\sigma_Y^A$ . However, the slope of the plastic hardening response, which is characteristic of plastic barrelling, is less for carburised struts than for non-carburised ones. This can be explained by the level of strain hardening of the two materials: carburised stainless steel is modelled as a perfectly plastic solid ( $E_t = 0$ ) whereas annealed stainless steel has a strain hardening modulus  $E_t = 2$  GPa.

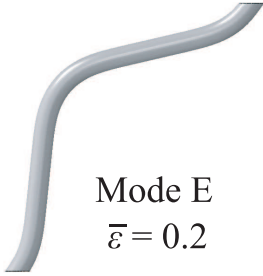
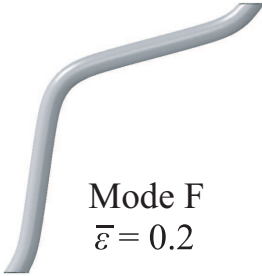
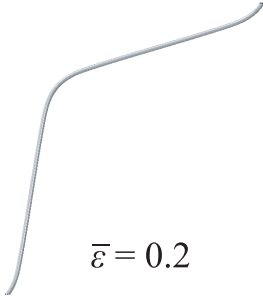
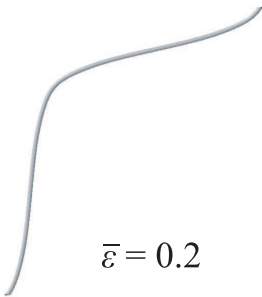
Carburisation significantly increases the peak stress of an inclined strut with  $l/d = 20$ , see Fig. 3.11(b). The collapse mode of the carburised strut ( $h/d = 0.05$ ) is classified as mode F: elastic buckling because at  $\bar{\sigma}_{pk}$ , the axial compressive stress in the strut is inferior to the yield strength of carburised stainless steel (but greater than the yield strength of annealed stainless steel). A similar change in collapse mechanism was observed in the previous section for an inclined tube with the same slenderness ratio.

Similarly to the inclined tube analysed in the previous section, the peak stress of a long inclined strut with  $l/d = 100$ , which collapses by mode F: elastic buckling, is insensitive to carburisation, see Fig. 3.11(c). Nevertheless, carburisation strengthens the post-peak response.

Finally, the deformed meshes of non-carburised struts ( $h/d = 0$ ) are compared to those of carburised struts ( $h/d = 0.05$ ) in Table 3.4. It is clear from Table 3.4 that



**Figure 3.11:** Influence of the carburisation depth  $h/d$  on the compressive response of an inclined solid strut  $t/d = 0.5$ . Results are given for (a)  $l/d = 3$ , (b)  $l/d = 20$  and (c)  $l/d = 100$ .

Geometry	$h/d = 0$	$h/d = 0.05$
Mode B $l/d = 3$ $\bar{\rho} = 0.18$	 $\bar{\varepsilon} = 0.4$	 $\bar{\varepsilon} = 0.4$
$l/d = 20$ $\bar{\rho} = 0.011$	Mode E $\bar{\varepsilon} = 0.2$ 	Mode F $\bar{\varepsilon} = 0.2$ 
Mode F $l/d = 100$ $\bar{\rho} = 0.0006$	$\bar{\varepsilon} = 0.2$ 	$\bar{\varepsilon} = 0.2$ 

**Table 3.4:** Influence of the carburisation depth  $h/d$  on the deformed meshes of an inclined solid strut  $t/d = 0.5$ . Results are given for selected values of  $l/d$ .

carburisation has only a small effect on the deformed meshes.

### 3.4.4 Comparison between tube and solid strut

The normalised peak stress  $\bar{\sigma}_{pk}/(\bar{\rho}\sigma_Y^A)$ , for both  $t/d = 0.1$  and  $0.5$ , is plotted as a function of relative density in Fig. 3.12. The results are shown for four selected values of normalised carburisation depth  $h/d$  ranging from 0 to 0.05. In addition, the collapse modes are identified for both the tube and the solid strut. Note that the collapse modes are different for non-carburised ( $h/d = 0$ ) and carburised ( $h/d > 0$ ) lattices. Four regimes can be identified in Fig. 3.12:

1. Inclined tubes with  $\bar{\rho} < 0.0005$  and inclined solid struts with  $\bar{\rho} < 0.002$  both collapse by mode F: elastic buckling. It is clear from Fig. 3.12 that carburisation has no effect on the peak stress for this particular collapse mode.
2. When the relative density of the inclined tube is in the range  $0.0005 \leq \bar{\rho} < 0.004$  and that of the inclined strut is between  $0.002 \leq \bar{\rho} < 0.02$ , the non-

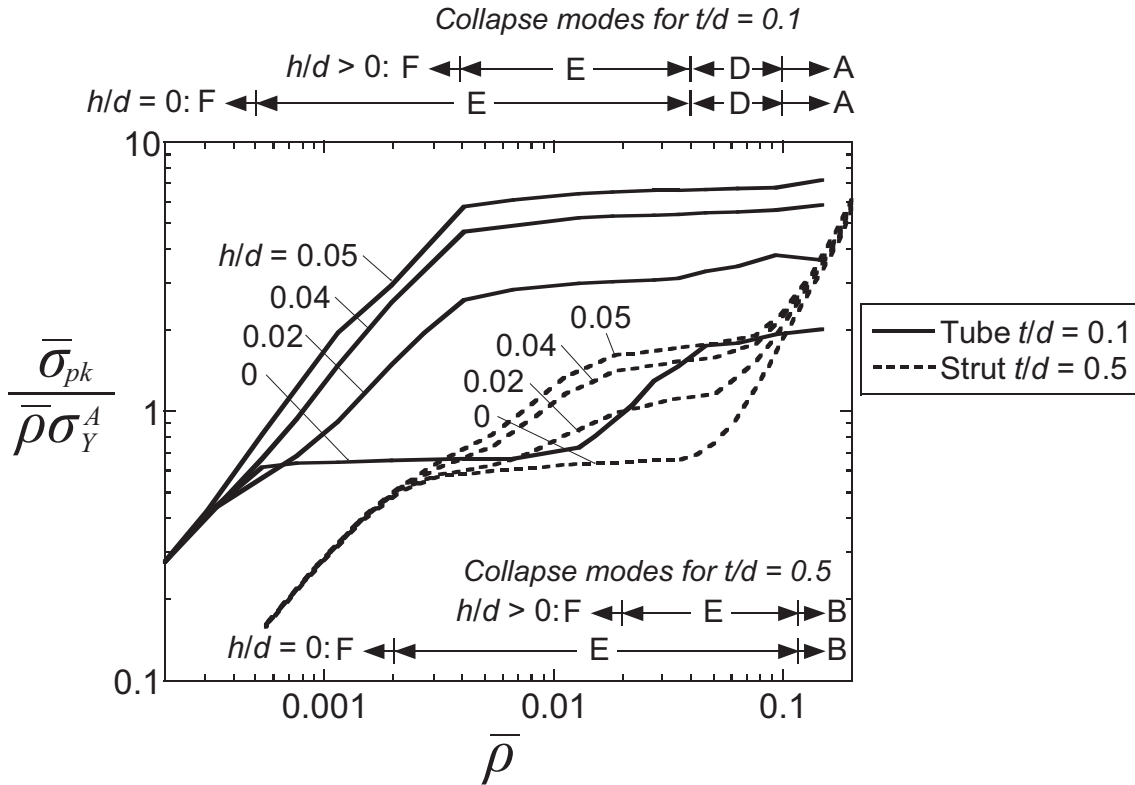


**Figure 3.12:** Influence of the carburisation depth  $h/d$  on the compressive strength of an inclined tube  $t/d = 0.1$  and an inclined solid strut  $t/d = 0.5$ .

carburised lattices collapse by mode E: global plastic buckling whereas the carburised ones collapse by mode F: elastic buckling. In this regime, carburisation increases the peak stress of the lattice and this increase is more important for the tube than for the strut.

3. The peak stress of inclined tubes with  $\bar{\rho} > 0.004$  has reached the yield strength of the material. Carburisation increases the peak stress of the lattice, but does not change the transition between the plastic collapse modes A, D and E. There is a similar regime for inclined struts with  $0.02 \leq \bar{\rho} < 0.1$ , but it covers only mode E: global plastic buckling.
4. This regime is specific to inclined struts with  $\bar{\rho} \geq 0.1$ , which collapse by Mode B: plastic barrelling. Recall that the response for this collapse mode does not exhibit a peak stress, see Fig. 3.11(a), and  $\bar{\sigma}_{pk}$  was defined as the stress at a nominal compressive strain  $\bar{\epsilon} = 0.5$ . Based on this definition, the normalised peak stress appears to be insensitive to carburisation, but this result is dependent upon the definition of  $\bar{\sigma}_{pk}$ .

### 3.4.5 Position of carburised lattices on the strength-density chart

A material property chart allows us to position different materials on a figure where each axis is a material property (Ashby, 2010). A chart of strength versus density is presented in Fig. 3.13. The chart was generated using the software CES EduPack 2010<sup>2</sup>. The strength of fully-dense materials such as metals, ceramics, composites and polymers is compared to that of lattice materials such as metal and polymer foams, tetrahedral lattices made from aluminium (Al) and pyramidal lattices made from titanium (Ti) and carbon fibre reinforced polymer (CRFP). For comparison purposes, the results of the finite element simulations for an inclined tube ( $t/d = 0.1$ ) with a normalised carburisation depth  $h/d = 0.05$  are also plotted in Fig. 3.13. Carburised stainless steel was assumed to have a density  $\rho_s = 8000 \text{ kg/m}^3$ , hence the density of a carburised stainless steel lattice is given by  $\rho_l = \bar{\rho}\rho_s$ .

The results indicate that carburised pyramidal lattices are stronger than their metallic counterparts made from aluminium or titanium. For densities below  $0.1 \text{ Mg/m}^3$ , the carburised pyramidal lattices are positioned at the frontier of material space,

---

<sup>2</sup>Granta Design Limited, Rustat House, 62 Clifton Road, Cambridge, CB1 7EG, UK.

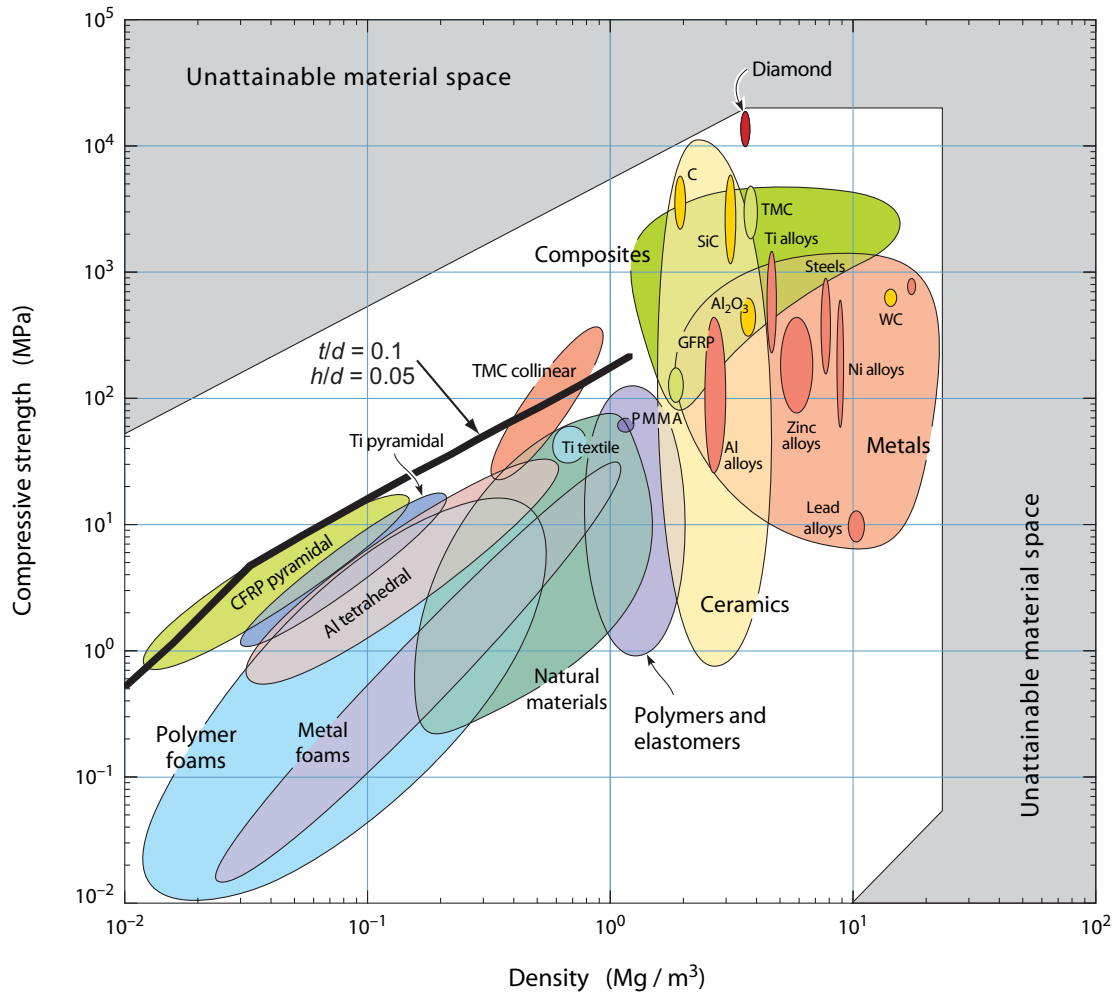


**Figure 3.13:** Strength versus density material chart. The simulated compressive strength of a pyramidal lattice made from carburised tubes ( $t/d = 0.1$ ,  $h/d = 0.05$ ) is also included. Al, aluminium; CRFP, carbon fibre reinforced polymers; Ti, titanium; TMC, titanium matrix composites.

performing as well as the strongest pyramidal lattices made from carbon fibre reinforced polymer. Recall that carburised stainless steel was assumed to possess a yield strength  $\sigma_Y^C = 2$  GPa in this study. If carburisation (or another heat treatment) is able to increase the yield strength above 2 GPa, this would expand the current material space.

### 3.5 Concluding remarks

The finite element method was used to simulate the compressive response of a pyramidal lattice made from tubes ( $t/d = 0.1$ ) or solid struts ( $t/d = 0.5$ ), both with an

inclination angle  $\omega = 55^\circ$ . First, the effect of material strain hardening was examined by comparing the compressive response of a lattice made from stainless steel to that of a lattice made from a perfectly plastic solid. Strain hardening was found to increase the compressive strength of lattices with a slenderness ratio  $l/d$  inferior to ten, but had no influence on the compressive strength of lattices with  $l/d > 10$ . Furthermore, strain hardening had a negligible effect on the collapse mode of the pyramidal lattice. This holds true for both lattices made from tubes and those made from solid struts.

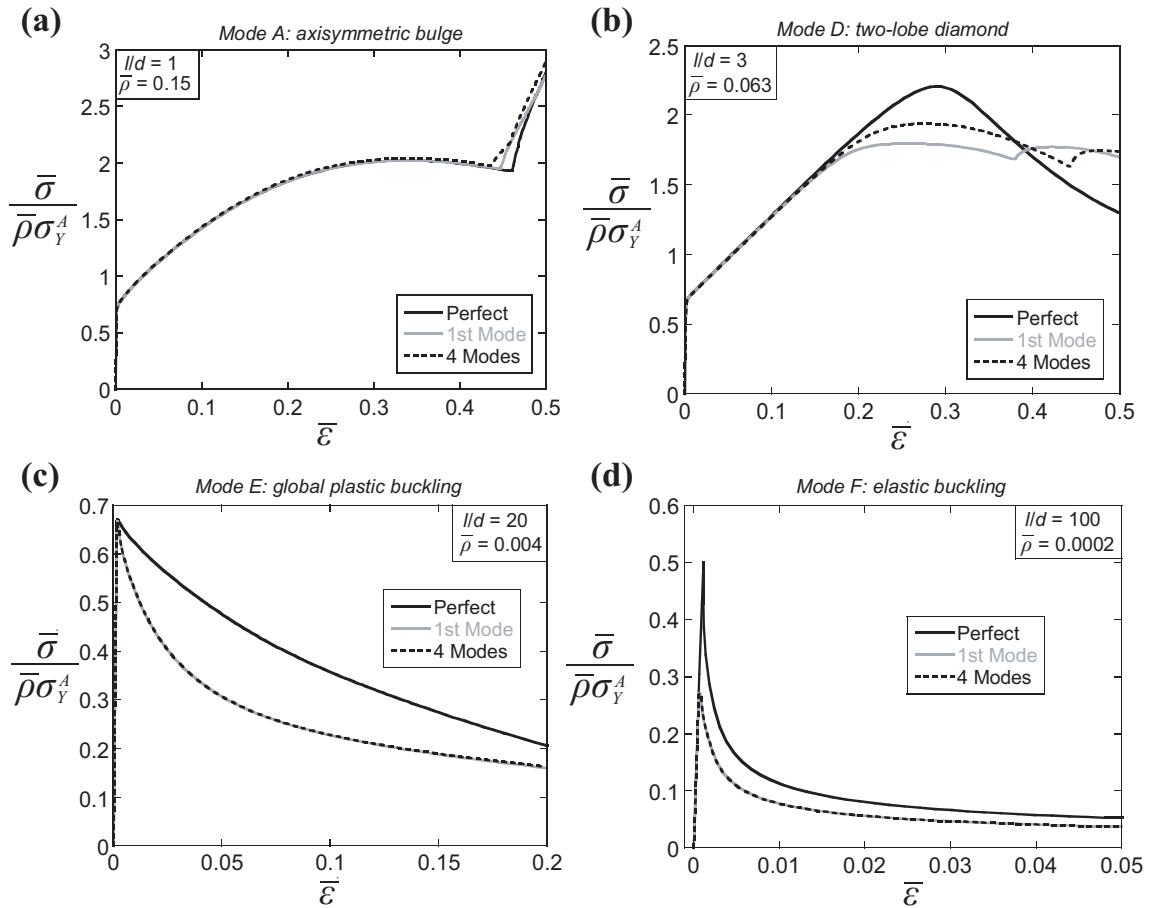
Then, the influence of carburisation upon the compressive response of a pyramidal lattice was analysed. The slenderness ratio  $l/d$  at which the collapse mode changes from plastic to elastic buckling was less for carburised lattices than for their non-carburised counterparts. Carburisation also increased the peak stress of the lattice, except for geometries that collapse by elastic buckling. This increase of the peak stress was more important for a lattice made from tubes than for one made from solid struts. Finally, the performances of the pyramidal lattice made from carburised tubes were compared to other engineering materials and lattices on a chart of strength versus density. The carburised lattice is stronger than other metallic lattices made from aluminium or titanium and offers similar performances to pyramidal lattices made from carbon fibre reinforced polymers. The simulations presented in this chapter suggest that the carburisation surface treatment can significantly enhance the strength of lattice materials, and this combination has the potential to expand the current material space. However, the embrittlement that may be caused by the carburisation surface treatment was neglected in the simulations presented above, and experimental tests are necessary to validate this assumption and to evaluate the accuracy of the finite element predictions.

### 3.A Influence of geometric imperfections

In this appendix, the sensitivity of the compressive response to the choice of geometric imperfection is explored. The imperfection consists of one or multiple elastic buckling modes, which can have different amplitudes. The effect of the number of modes superimposed and the effect of amplitude will be addressed below. The simulations were done for an inclined tube  $t/d = 0.1$  made from annealed stainless steel ( $\sigma_Y^A = 200$  MPa and  $E_t = 2$  GPa).

## 3.A.1 Influence of the number of superimposed modes

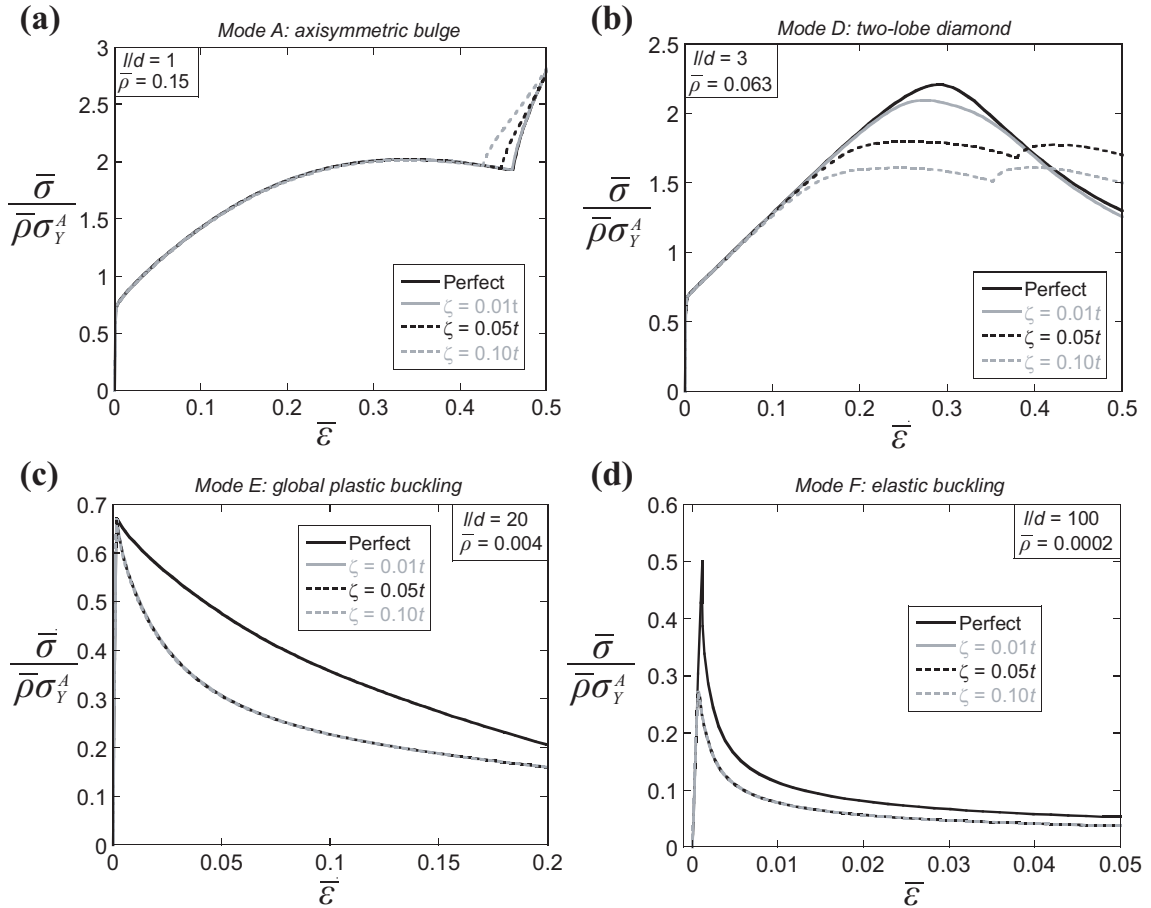
The effect of the number of modes superimposed upon the compressive response of an inclined tube with  $t/d = 0.1$  is shown in Fig. 3.14 for selected values of slenderness ratio  $l/d$ . In each plot, three cases are compared: (i) a perfect structure (no imperfection), (ii) an imperfection of amplitude  $\zeta = 0.05t$  in the form of the first buckling mode and (iii) an imperfection of amplitude  $\zeta = 0.05t$  in the form of the first four buckling modes superimposed. Except for the case of  $l/d = 1$ , the compressive response of an inclined tube is imperfection sensitive; case (i) differs from cases (ii) and (iii). However, the results indicate that the compressive response is relatively insensitive to the number of modes superimposed; cases (ii) and (iii) are similar. For this reason, an imperfection in the shape of the first buckling mode only was included in all simulations.



**Figure 3.14:** Influence of imperfection shape on the compressive response of an inclined tube  $t/d = 0.1$ . In all cases, the imperfection amplitude is  $\zeta = 0.05t$ . Results are given for (a)  $l/d = 1$ , (b)  $l/d = 3$ , (c)  $l/d = 20$  (d)  $l/d = 100$ .

## 3.A.2 Influence of amplitude

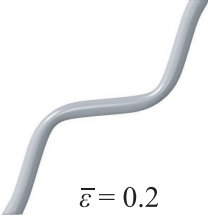
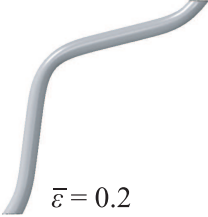
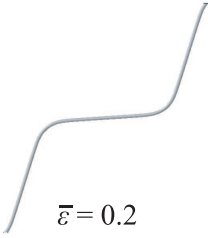
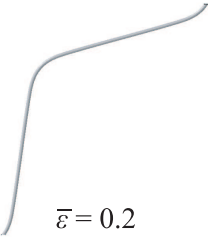
The effect of imperfection amplitude upon the compressive response of an inclined tube with  $t/d = 0.1$  is shown in Fig. 3.15 for selected values of  $l/d$ . In each plot, results are given for a perfect structure (no imperfection) and for an imperfection in the form of the first buckling mode with three different amplitudes  $\zeta = 0.01t$ ,  $0.05t$  and  $0.1t$ . Except for the case of  $l/d = 3$ , the compressive response of an inclined tube is insensitive to the imperfection amplitude in the range  $\zeta = 0.01t - 0.1t$ . Based on the results of Fig. 3.15, an imperfection amplitude  $\zeta = 0.05t$  was used in all simulations.



**Figure 3.15:** Influence of imperfection amplitude on the compressive response of an inclined tube  $t/d = 0.1$ . In all cases, the imperfection shape is in the form of the 1<sup>st</sup> buckling mode. Results are given for (a)  $l/d = 1$ , (b)  $l/d = 3$ , (c)  $l/d = 20$  (d)  $l/d = 100$ .

3.A.3 Influence of imperfection on the deformed meshes

The effect of including a geometric imperfection on the deformed meshes of an inclined tube with  $t/d = 0.1$  is shown in Table 3.5 for selected values of  $l/d$ . Results are shown for a perfect structure (no imperfection) and for simulations with an imperfection in the form of the first buckling mode with an amplitude  $\zeta = 0.05t$ . For  $l/d = 1$ , the deformed meshes are imperfection insensitive. In contrast, introducing an imperfection has a strong influence on the deformed meshes of inclined tubes with  $l/d \geq 3$ . Note that for  $l/d = 20$  and  $100$ , a higher order buckling mode is obtained when no imperfections are included.

Geometry	Perfect	First mode $\zeta = 0.05t$
Mode A $l/d = 1$ $\bar{\rho} = 0.15$	 $\bar{\epsilon} = 0.5$	 $\bar{\epsilon} = 0.5$
Mode D $l/d = 3$ $\bar{\rho} = 0.064$	 $\bar{\epsilon} = 0.5$	 $\bar{\epsilon} = 0.5$
Mode E $l/d = 20$ $\bar{\rho} = 0.004$	 $\bar{\epsilon} = 0.2$	 $\bar{\epsilon} = 0.2$
Mode F $l/d = 100$ $\bar{\rho} = 0.0002$	 $\bar{\epsilon} = 0.2$	 $\bar{\epsilon} = 0.2$

**Table 3.5:** Influence of a geometric imperfection on the deformed meshes of an inclined tube  $t/d = 0.1$ . Results are given for selected values of  $l/d$ .



## Chapter 4

# The influence of the back face on the bending response of prismatic sandwich beams

### Summary

Stainless steel sandwich beams with a corrugated core or a Y-frame core have been tested in three-point bending and the role of the face-sheets has been assessed by considering beams with (i) front-and-back faces present, and (ii) front face present but back face absent. These competing beam designs were compared on an equal mass basis by doubling the front face thickness when the back face is absent. The quasi-static, three-point bending responses were measured under simply supported and clamped boundary conditions. For both end conditions and for both core topologies, the beams containing front-and-back faces underwent indentation beneath the mid-span roller whereas Brazier plastic buckling was responsible for the collapse of beams without a back face. Three-dimensional finite element predictions were in good agreement with the measurements and gave additional insight into the deformation modes. The finite element method was also used to study the effect of (i) mass distribution between core and face-sheets and (ii) beam span upon the collapse response of a simply supported sandwich panel. Panels of short span are plastically indented by the mid-span roller and the panels without a back face are stronger than those with front-and-back faces present. In contrast, panels of long span undergo Brazier plastic buckling, and the presence of a back face strengthens the panel.

## 4.1 Introduction

Oil tanker spills pose a significant environmental threat to the oceans and coastlines of the world: 60% of worldwide oil transportation is by tankers and many heavily trafficked routes pass through regions of high marine biodiversity (Burgherr, 2007). The conventional double hull design, with minimal mechanical coupling between inner and outer hulls, is commonly used to safeguard oil tankers against spills. Recently, design alternatives have been proposed to improve the structural performances of ship hulls over those normally achieved with a conventional double hull construction, see for example the review by Paik (2003). One such alternative is to employ a sandwich construction to increase the stiffness, strength and energy absorption of the hull.

An example of sandwich construction is the Y-frame double hull design, as proposed by Damen Schelde Naval Shipbuilding<sup>1</sup> and as illustrated in Fig. 4.1(a). Full-scale collision tests have been performed on this structure and its resistance to tearing was found to exceed that of a conventional double hull design (Wevers and Vredeveltdt, 1999). In these collision trials, the inner hull played a minor role and underwent negligible plastic deformation. This motivated the development of a single hull structure where the Y-frame stiffeners are welded directly to the bulkheads as shown in Fig. 4.1(b). Full-scale collision tests have also been performed on this single hull Y-frame structure. It has similar crashworthiness to the Y-frame double hull design, but it is significantly simpler and cheaper to manufacture. Several inland waterway tankers have been manufactured using the Y-frame single hull design (Graaf et al., 2004). The corrugated core, under the trade-name Navtruss<sup>2</sup>, is a competing design to the Y-frame. No large-scale collision tests on the Navtruss design have been reported in the open literature, and little is known about its crashworthiness relative to that of the Y-frame core.

The relative performance of corrugated and Y-frame cores has been explored recently for a range of loadings in a laboratory setting. For example, the out-of-plane compressive strength and longitudinal shear strength of the Y-frame core and corrugated core have been investigated by Rubino et al. (2008a) and Côté et al. (2006), respectively. The three-point bending response of sandwich beams with a corrugated core was studied by Valdevit et al. (2006a); they proposed failure maps for simply supported beams. This work was extended by Rubino et al. (2010) who compared

---

<sup>1</sup>Damen Schelde Naval Shipbuilding, Glacisstraat 165, 4381 SE Vlissingen, The Netherlands.

<sup>2</sup>Astech Engineering Products Inc., 3030 Red Hill Ave., Santa Ana, CA 92705, USA.

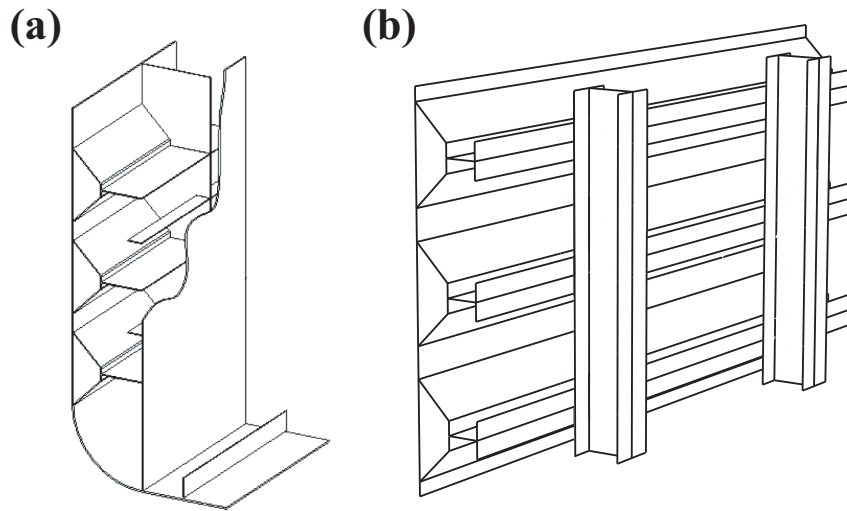


**Figure 4.1:** The Y-frame sandwich core in (a) double hull and (b) single hull designs.

the three-point bending responses of sandwich beams with a corrugated core and a Y-frame core under both simply supported and clamped boundary conditions. It was found that sandwich beams with a corrugated core or a Y-frame core have comparable responses on an equal mass basis. However, these studies have been limited to sandwich beams with identical front-and-back faces.

The objective of this chapter is to explore the sensitivity of the three-point bending response of a sandwich beam to the relative placement of material in the core, front face and back face. The relative allocation of material can be represented in a diagram resembling a triple phase diagram, as shown in Fig. 4.2. Any point on this diagram corresponds to a sandwich structure of total areal mass  $m$ , with fraction  $(m_c/m)$  in the core,  $(m_f/m)$  in the front face and  $(m_b/m) = 1 - (m_f/m) - (m_c/m)$  in the back face.

This study focuses on two trajectories in the design space of Fig. 4.2. The first one is indicated by the vertical dashed line and includes all sandwich beams with identical front-and-back faces,  $m_f = m_b$ . The second trajectory is the left-hand edge of the triangle and denotes all sandwich beams without a back face,  $m_b = 0$ .

The three-point bending response of sandwich panels of geometry along these two trajectories will be compared on an equal mass basis. Consider, as the reference design, a sandwich panel with identical front-and-back faces. If the back face material is relocated to the front face or to the core, will the three-point bending strength increase or decrease? This question will be addressed for a corrugated core and a Y-frame core, and for both simply supported and clamped boundary conditions.

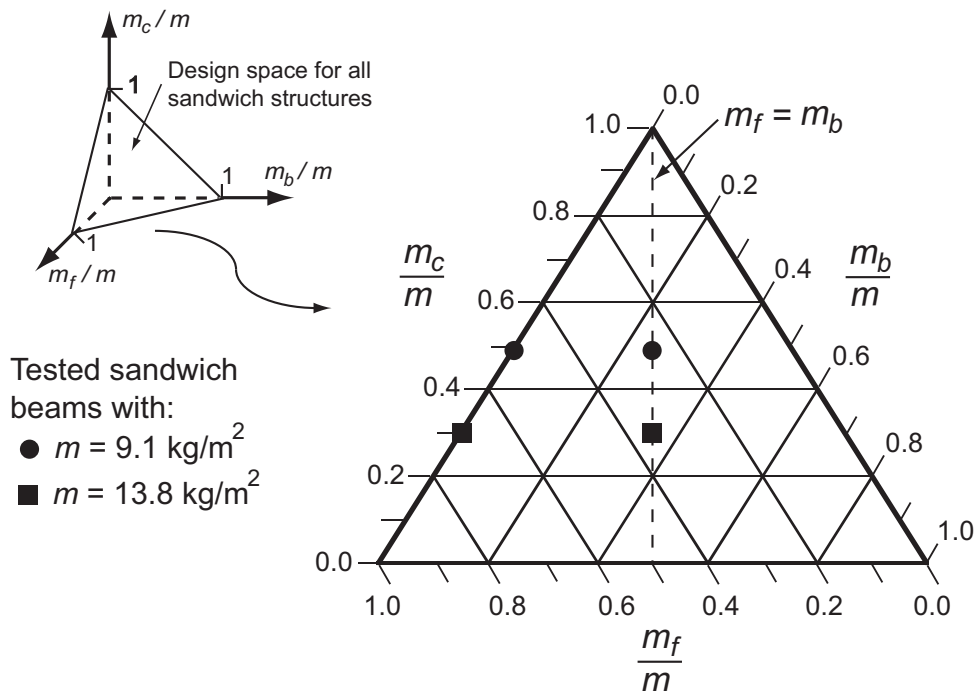


**Figure 4.2:** The design space for mass distribution within a sandwich panel of areal mass  $m$ . The proportion of mass in the core, in the front face and in the back face are denoted by  $m_c/m$ ,  $m_f/m$  and  $m_b/m$ , respectively. The mass distribution of the test geometries is indicated for two choices of areal mass.

#### 4.1.1 Choice of test material

There is a need to select a pertinent test material, which in the as-manufactured state has similar properties to that of commercial shipbuilding steel, such as Lloyd's Grade A steel. The uniaxial tensile response of Lloyd's Grade A steel has been measured by Broekhuijsen (2003) and is shown in Fig. 4.3. It is used by Damen Schelde Naval Shipbuilding in the construction of tankers with a Y-frame sandwich core.

In previous laboratory studies (Côté et al., 2006; Valdevit et al., 2006b; Rubino et al., 2008a, 2010) corrugated cores and Y-frame cores have been manufactured by brazing together AISI 304 stainless steel sheets. In order to compare the uniaxial properties of this material with those of Lloyd's Grade A steel, preliminary uniaxial tests have been performed on dog-bone specimens cut from as-received AISI 304 stainless steel sheets; these were subjected to the same braze cycle as that used in the manufacture of sandwich beams (see Section 4.2.1). The uniaxial tensile response of the brazed 304 material, at an applied strain rate of  $10^{-3} \text{ s}^{-1}$ , is included in Fig. 4.3. The measured Young's modulus  $E$  and 0.2% offset yield strength  $\sigma_Y$  are 210 GPa and

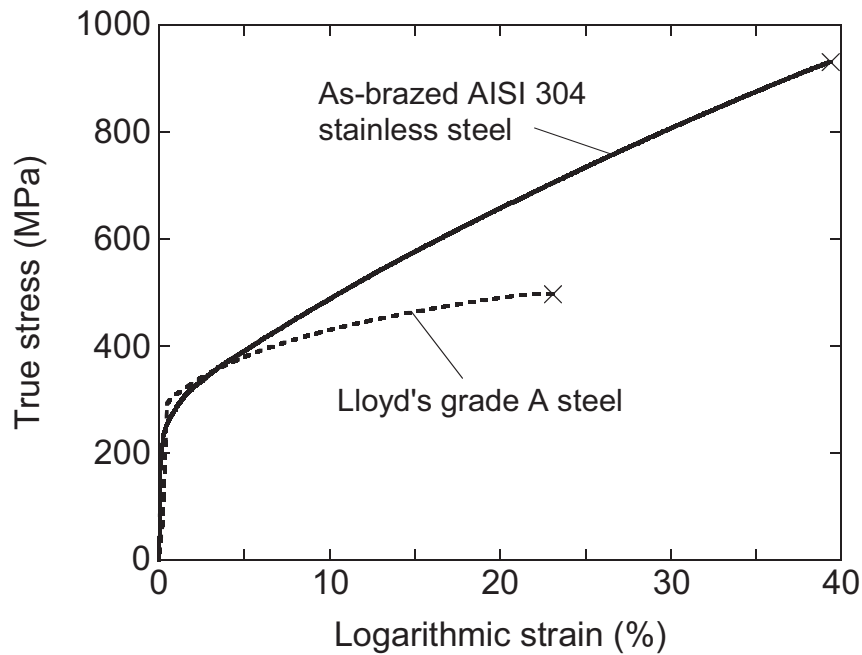


**Figure 4.3:** Measured uniaxial tensile responses of as-brazed AISI 304 stainless steel and Lloyd's Grade A steel, at a strain rate of  $10^{-3} \text{ s}^{-1}$ .

210 MPa, respectively. The observed strain hardening response is close to linear, with a tangent modulus of  $E_t = 2.1 \text{ GPa}$ . Lloyd's Grade A steel has a slightly higher yield strength of 280 MPa and a somewhat reduced ductility and strain hardening capacity. In broad terms, however, the as-brazed stainless steel is representative of Lloyd's grade A steel at strain levels below 10%. To confirm this, a limited set of finite element simulations have been performed on the three-point bending response of sandwich beams made from as-brazed stainless steel and Lloyd's grade A steel, as summarised in Appendix 4.A. The simulations confirm that sandwich beams made from as-brazed stainless steel or from Grade A steel have similar responses. Based upon these exploratory findings, the sandwich beams of the present study were manufactured by brazing together type 304 stainless steel sheets.

#### 4.1.2 Scope of study

First, the methodology used to manufacture and test the sandwich beams is reported along with a description of the finite element models. Second, the measured three-point bending responses of sandwich beams, with and without a back face, are compared for simply supported and clamped boundary conditions. Then, to gain additional insight into the collapse mechanisms, the beam responses are simulated

by three-dimensional finite element simulations. Finally, the three-point bending response of simply supported sandwich panels is explored numerically as a function of span and of relative proportion of material in the core and face-sheets. The two asymptotic responses of indentation at short span and a bending instability at long span are analysed and used to determine the collapse load as a function of span.

## 4.2 Methodology

### 4.2.1 Specimen manufacture

Corrugated and Y-frame cores, of cross-section shown in Fig. 4.4, were used to construct prismatic sandwich beams. These cores are approximately 1:20 scale models of the cores used in a ship hull and had a relative density of 2.5%. Both cores were made from AISI 304 stainless steel sheets of thickness 0.3 mm and density  $\rho = 7900$  kg/m<sup>3</sup>.

The corrugated core was manufactured by alternately folding stainless steel sheets at  $\pm 60^\circ$  under computer-numerical-control (CNC). In contrast, the Y-frame core was manufactured by CNC folding of stainless steel sheets and then assembling two sections: the  $\pm 45^\circ$  upper part of the Y-frame and the Y-frame leg. Slots were cut periodically into the central flange of the upper part of the Y-frame and a matching set of keys were cut into the top of the Y-frame leg to facilitate assembly, as described by Rubino et al. (2008a).

Stainless steel face-sheets were brazed to the cores to produce two classes of sandwich beam:

1. a beam, with front-and-back faces of thickness  $t$  and
2. a beam, with only a front face of thickness  $2t$ .

Two different values of thickness  $t$  were considered, 0.3 mm and 0.6 mm, giving sandwich beams of areal mass  $m = 9.1$  and  $13.8$  kg/m<sup>2</sup>, respectively, as shown in Fig. 4.4(c). These test geometries are also included in the design space of Fig. 4.2. The proportion of mass in the core  $m_c/m$  is 0.48 and 0.31 for sandwich beams with an areal mass  $m$  of 9.1 and 13.8 kg/m<sup>2</sup>, respectively.

The sandwich beams were assembled as follows. First, the face-sheets were spot-

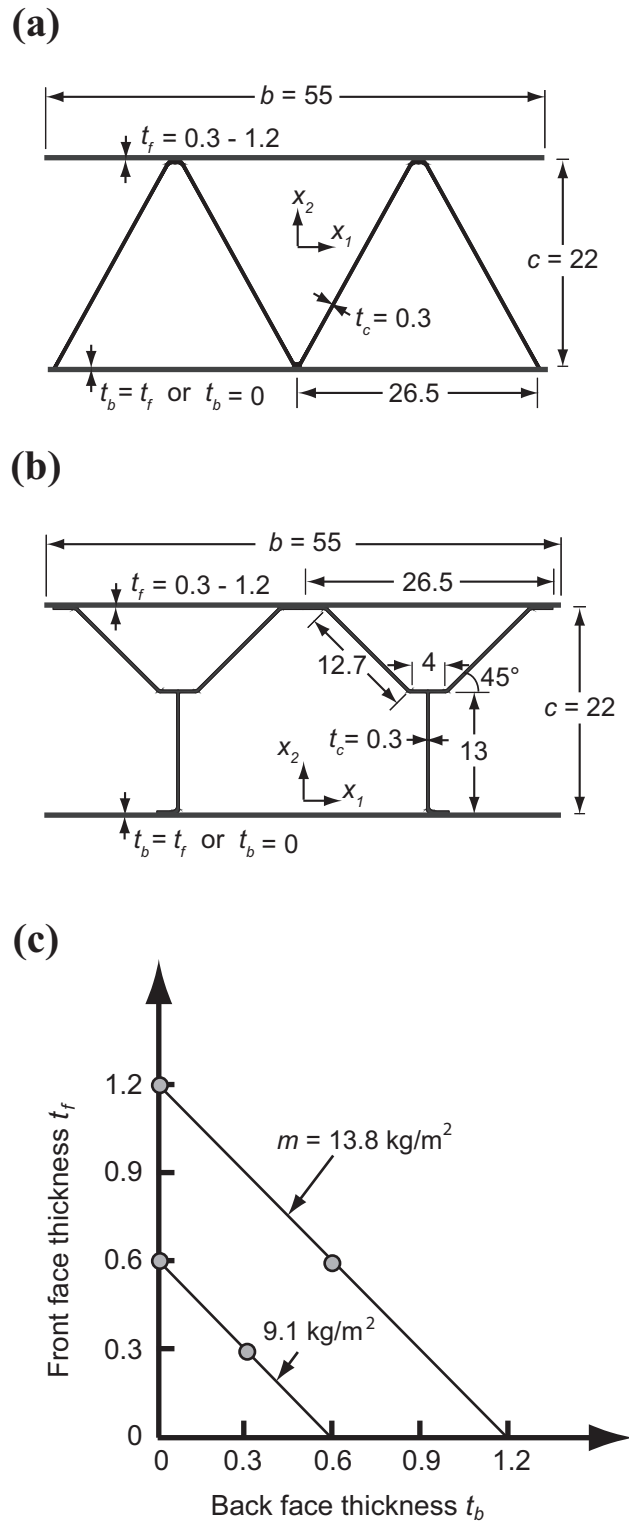


**Figure 4.4:** Cross-sectional dimensions of the sandwich beams: (a) corrugated core and (b) Y-frame core. (c) The chosen values of face-sheet thickness used in the experimental study. All dimensions are in mm.

welded to the core, and second, a thin layer (of thickness  $10\ \mu\text{m}$ ) of Ni-CR 25-P10 (wt.%) braze powder was applied over all sheets of the assembly. Third, brazing was performed in a vacuum furnace (at 0.03-0.1 mbar) using a dry argon atmosphere at  $1075^\circ\text{C}$  for one hour, followed by a slow furnace cool.

### 4.2.2 Geometry of the three-point bending tests

Simply supported and clamped sandwich beams were tested and their dimensions are shown in Fig. 4.5. In all cases, the prismatic axis of the core was aligned with the longitudinal direction of the beam ( $x_3$ -axis). The span of the beams was held fixed at  $2L = 250\ \text{mm}$  and load introduction at mid-span was via a steel roller of diameter  $D = 9\ \text{mm}$ .

#### Simply supported beams

Steel rollers of diameter  $D = 9\ \text{mm}$  were also used to provide simple outer support to the sandwich beams, see Fig. 4.5(a). For those specimens without a back face, preliminary tests revealed that the core crushed and splayed out-of-plane (in the  $x_1$ -direction) at the outer supports. To prevent this mode of collapse, short sections of back face were brazed to the core at both ends of the beam, see Fig. 4.5(a). These additional face plates had the same thickness as that of the front face-sheet. No such reinforcement was required for the sandwich beams with front-and-back faces.

#### Clamped beams

To achieve a fully-clamped boundary condition, the ends of the sandwich beams were filled with an epoxy resin to make the core fully dense. Then, the end portions of the sandwich beams were bolted to the test rig using steel clamping plates and M6 bolts, as shown in Fig. 4.5(b). For those specimens without a back face, local reinforcement was again achieved by brazing short sections of back face to the core at each end of the beam.

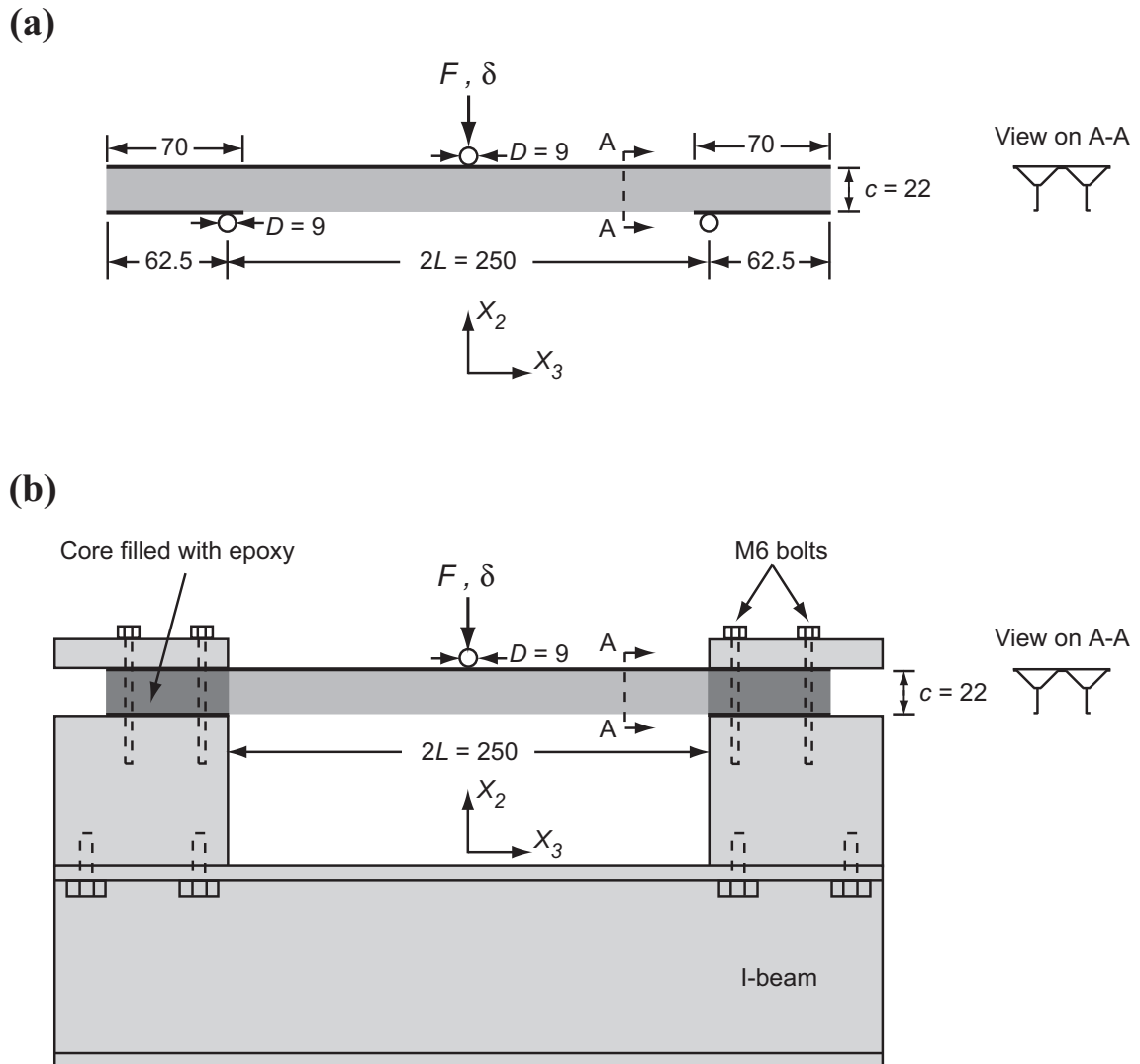


**Figure 4.5:** The test fixtures used for (a) simply supported and (b) clamped beams. A sandwich beam with a Y-frame core and without a back face is shown. All dimensions are in mm.

### 4.2.3 Finite element models

The commercial software Abaqus was used to develop three-dimensional finite element (FE) models for all sandwich beams tested. The geometries used in the simulations were identical to those employed in the experimental investigation, recall Fig. 4.4 and 4.5. Perfect bonding between core and face-sheets was assumed in all cases. Four noded, linear shell elements with reduced integration (S4R in Abaqus notation) were used to discretise the sandwich beams using a mesh size of 0.5 mm. A convergence study showed that further mesh refinement did not improve significantly the accuracy of the simulations.

#### Boundary conditions

Only one quarter of the sandwich beam was modelled in the simulations, with symmetric boundary conditions at mid-span ( $x_3 = 0$ ) and at mid-plane ( $x_1 = 0$ ). The mid-span roller was modelled as a rigid body in the FE simulations and its displacement was prescribed during the analysis. A frictionless hard contact condition was used to model the interaction between the roller and front face. The same contact properties were used between all potentially contacting surfaces of the sandwich beam.

The overhang of the simply supported sandwich beams beyond the outer rollers was included in the FE analysis. Alternatively, the clamped boundary condition was enforced by imposing zero displacement on the nodes of the end face of the sandwich beam ( $x_3 = L$ ).

#### Material properties

The as-brazed AISI 304 stainless steel was modelled as a rate-independent, elastic-plastic solid in accordance with J2-flow theory. The elastic branch was linear and isotropic, as characterised by a Young's modulus  $E = 210$  GPa and a Poisson's ratio  $\nu = 0.3$ . The uniaxial yield strength was  $\sigma_Y = 210$  MPa, and the hardening response was tabulated in Abaqus from the plot in Fig. 4.3.

## 4.3 Experimental results

The three-point bending tests were conducted using a 100 kN screw driven test machine with a constant cross-head velocity of  $\dot{\delta} = 5 \times 10^{-3}$  mm/s. The load  $F$  applied to the specimen was measured by the load cell of the test machine and the mid-span roller displacement  $\delta$  was measured via a laser extensometer.

The three-point bending responses of all sandwich beams tested are given in Fig. 4.6 and 4.7 for simply supported and clamped boundary conditions, respectively. In each figure, results are shown for sandwich beams with a corrugated core and a Y-frame core, and for an areal mass  $m = 9.1$  and  $13.8$  kg/m<sup>2</sup>. The mid-span roller displacement  $\delta$  is normalised by the beam half-span  $L = 125$  mm whereas the load  $F$  is normalised by  $\sigma_Y bc$ , where the yield strength is  $\sigma_Y = 210$  MPa, the width of the sandwich beams is  $b = 55$  mm and the core thickness is  $c = 22$  mm.

### 4.3.1 Simply supported beams

The simply supported beam response is shown in Fig. 4.6(a) for the corrugated core and in Fig. 4.6(b) for the Y-frame core, both at  $m = 9.1$  kg/m<sup>2</sup>. Likewise, the response is given in Fig. 4.6(c) and (d) for the corrugated core and Y-frame core, respectively, at  $m = 13.8$  kg/m<sup>2</sup>. In each plot, results are shown for sandwich beams with both faces present and for sandwich beams with the back face absent.

All simply supported sandwich beams have an initial elastic regime. The elastic stiffness is, however, sensitive to the distribution of face-sheet material: beams containing both front-and-back faces are at least 40% stiffer than those with the back face absent. In contrast, the peak load reduces by less than 20% when the back face material is relocated onto the front face.

The peak load for sandwich beams with a corrugated core exceeds that of beams with a Y-frame core by 15-25%. In all cases, the peak load is followed by a softening response, with more pronounced softening for the corrugated core than for the Y-frame core: the load drops to less than 35% of the peak load for sandwich beams with a corrugated core when  $\delta/L$  is increased to 0.15. In contrast, for the Y-frame core the load at  $\delta/L = 0.15$  exceeds 55% of the peak load.

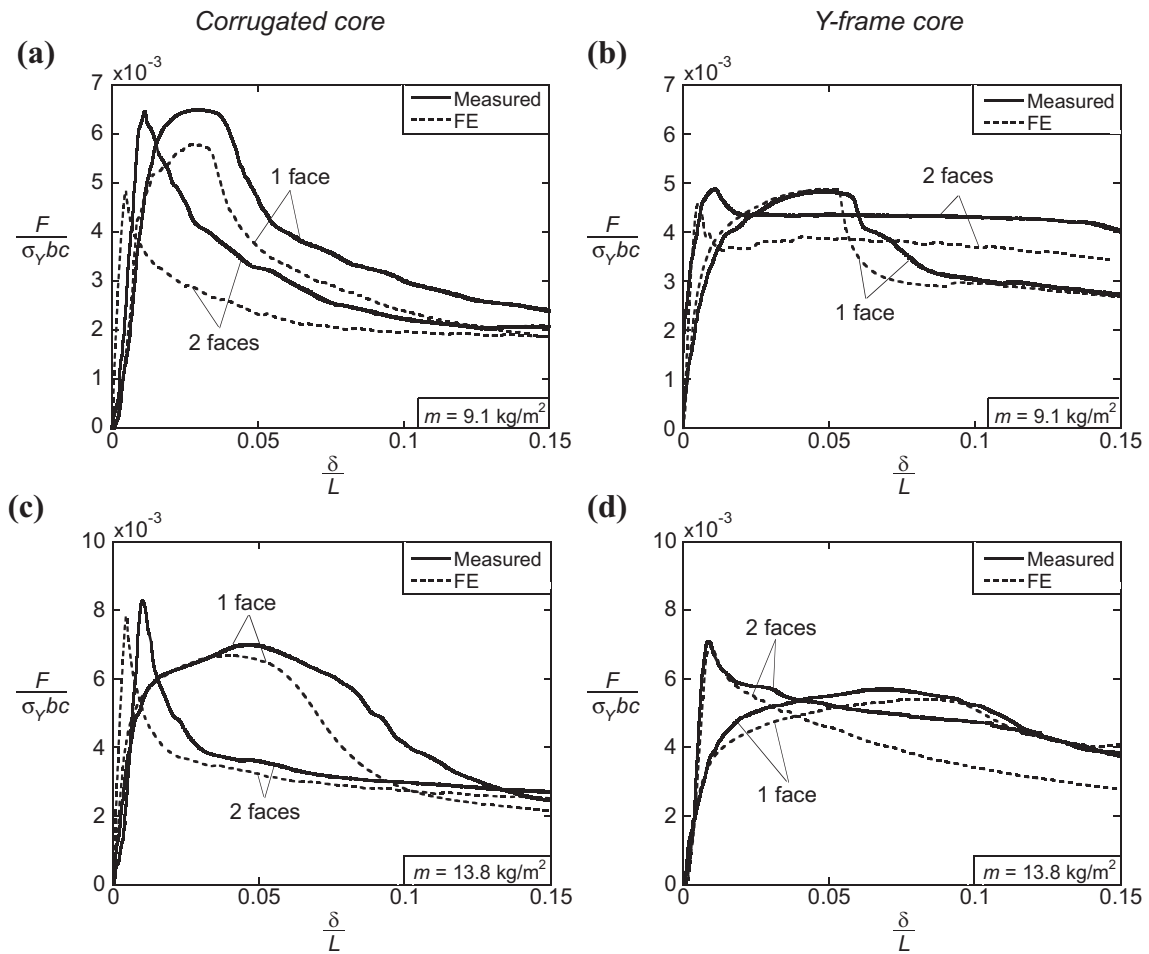


**Figure 4.6:** Three-point bending responses of simply supported sandwich beams. Sandwich beams with an areal mass  $m = 9.1 \text{ kg/m}^2$  are shown with (a) a corrugated core and (b) a Y-frame core. Likewise, sandwich beams with an areal mass  $m = 13.8 \text{ kg/m}^2$  are shown with (c) a corrugated core and (d) a Y-frame core.

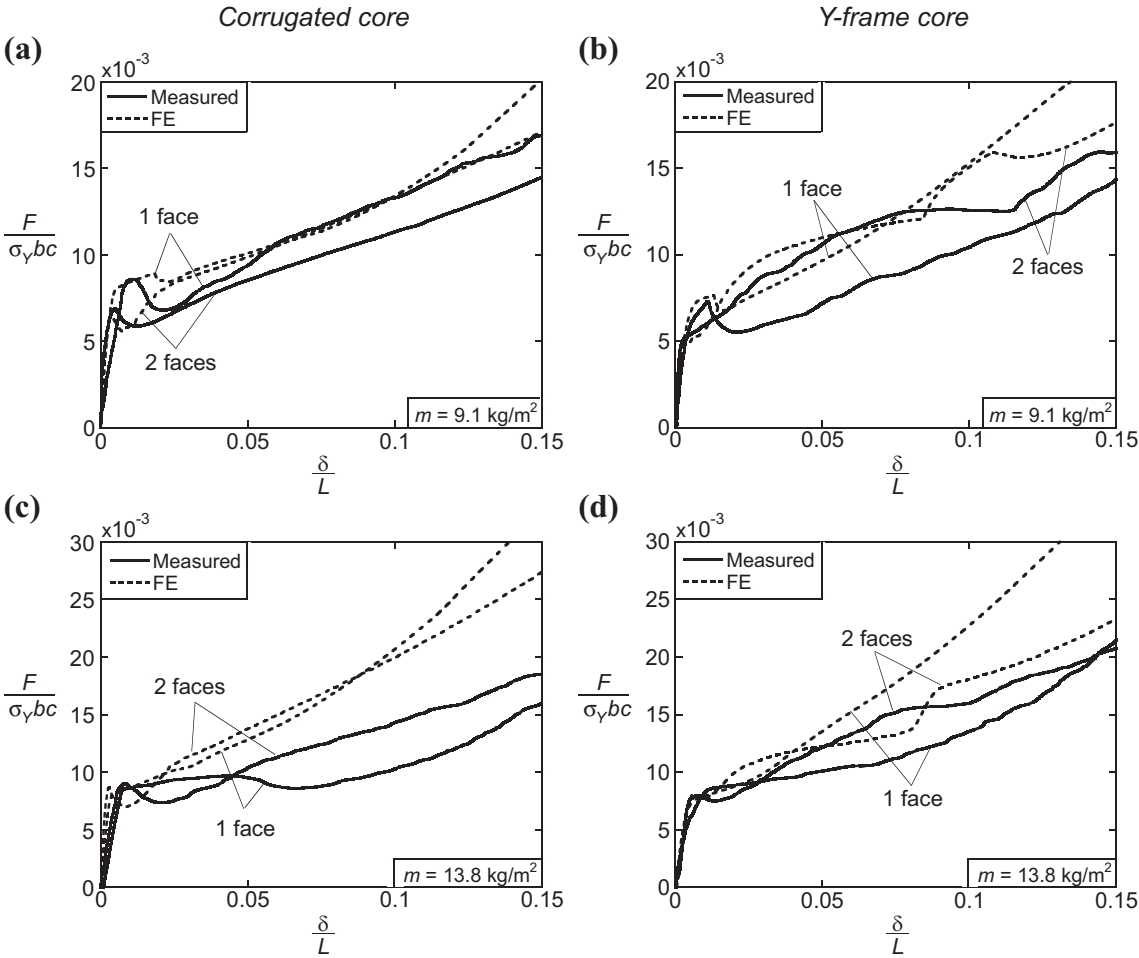


**Figure 4.7:** Three-point bending responses of clamped sandwich beams. Sandwich beams with an areal mass  $m = 9.1 \text{ kg/m}^2$  are shown with (a) a corrugated core and (b) a Y-frame core. Likewise, sandwich beams with an areal mass  $m = 13.8 \text{ kg/m}^2$  are shown with (c) a corrugated core and (d) a Y-frame core.

### 4.3.2 Clamped beams

The measured three-point bending responses of clamped sandwich beams are shown in Fig. 4.7. The layout of Fig. 4.7 is the same as that in Fig. 4.6: structures with a corrugated core and a Y-frame core are shown in Fig. 4.7(a) and (b), respectively, for an areal mass  $m = 9.1 \text{ kg/m}^2$ . Likewise, the responses for  $m = 13.8 \text{ kg/m}^2$  are given in Fig. 4.7(c) and (d) for the corrugated core and Y-frame core, respectively. In each plot, the response of a sandwich beam with front-and-back faces present is compared to that of a sandwich beam without a back face.

In all cases, an initial elastic regime is followed by a peak load  $F_{pk}$ . Subsequently, the clamped beams soften and then re-harden due to longitudinal stretching of the beam. The core topology has a similar influence upon the initial peak load of clamped beams to that of the simply supported beams: sandwich structures with a corrugated core are 10-25% stronger than their counterparts with a Y-frame core. The initial peak load of sandwich beams with an areal mass  $m = 9.1 \text{ kg/m}^2$  is sensitive to the distribution of face-sheet material: beams without a back face are 25-35% stronger than those with front-and-back faces. In contrast, for  $m = 13.8 \text{ kg/m}^2$ , the sandwich beams with front-and-back faces present have comparable initial peak strengths to those without a back face. For all clamped beams considered, the load drop following the initial peak load  $F_{pk}$  is at most 20%. We note in passing that the simply supported Y-frame core shows load drop of this order, whereas the corrugated core exhibits much larger load drops, recall Fig. 4.6.

### 4.3.3 Collapse mechanisms

To gain additional insight into the collapse mechanisms, photographs of the deformed sandwich beams with an areal mass  $m = 13.8 \text{ kg/m}^2$  are shown in Fig. 4.8-4.11. Simply supported sandwich beams with a corrugated core and with a Y-frame core are given in Fig. 4.8 and 4.9, respectively. Likewise, photographs of clamped sandwich beams with a corrugated core and a Y-frame core are reported in Fig. 4.10 and 4.11, respectively. In part (a) of each figure, the deformed geometry is shown for front-and-back faces present, whereas in part (b) the images are for the back face absent. The photographs were taken after deforming the sandwich beam to  $\delta = 0.2L$  and then unloading. Two views are shown in the figures: on the left, a side view along the  $x_3$ -direction showing half of the sandwich beam and on the right, a view of the core deformation after sectioning of the beam at mid-span.

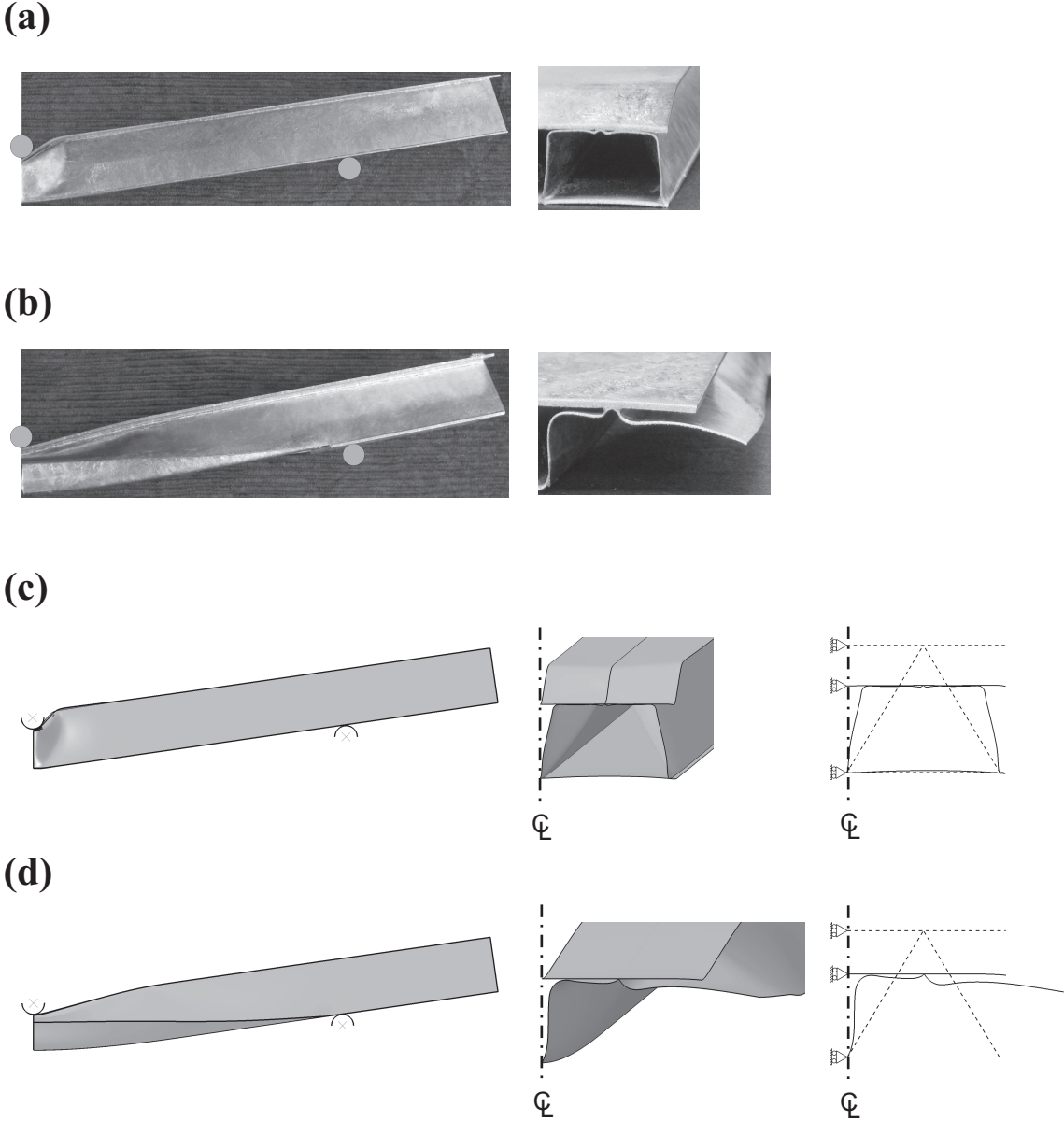


**Figure 4.8:** Photographs of the simply supported sandwich beams with a corrugated core ( $m = 13.8 \text{ kg/m}^2$ ) (a) with front-and-back faces and (b) without a back face. Deformed finite element meshes of the same sandwich beam (c) with front-and-back faces and (d) without a back face. A side view showing half of the beam and a view of the core deformation at mid-span are given. To clarify the predicted deformation modes, the undeformed (dashed line) and deformed (solid line) cross-sections at mid-span are included in (c) and (d). The images are for beams loaded to  $\delta = 0.2L$  and then unloaded.

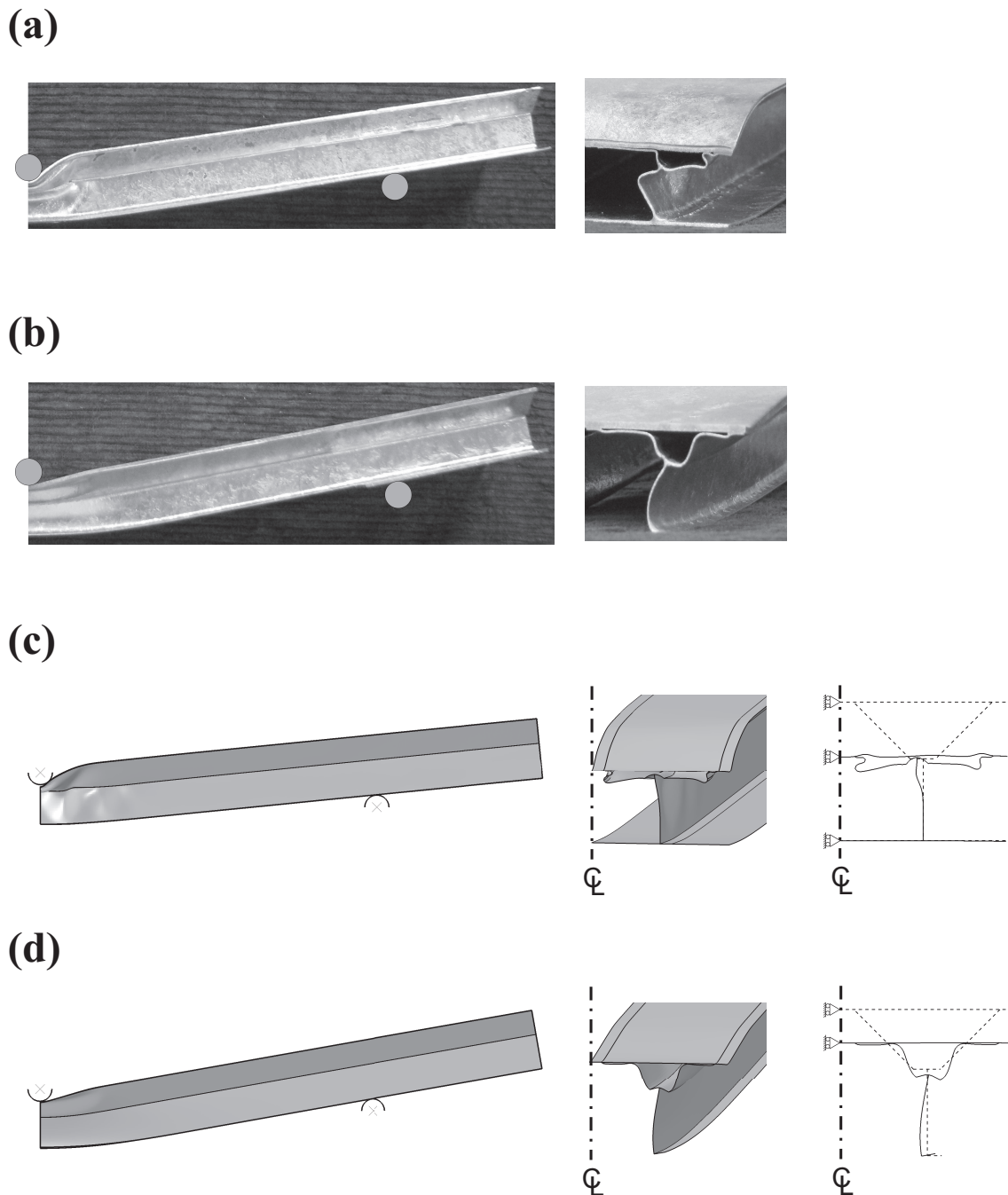


**Figure 4.9:** Photographs of the simply supported sandwich beams with a Y-frame core ( $m = 13.8 \text{ kg/m}^2$ ) (a) with front-and-back faces and (b) without a back face. Deformed finite element meshes of the same sandwich beam (c) with front-and-back faces and (d) without a back face. A side view showing half of the beam and a view of the core deformation at mid-span are given. To clarify the predicted deformation modes, the undeformed (dashed line) and deformed (solid line) cross-sections at mid-span are included in (c) and (d). The images are for beams loaded to  $\delta = 0.2L$  and then unloaded.

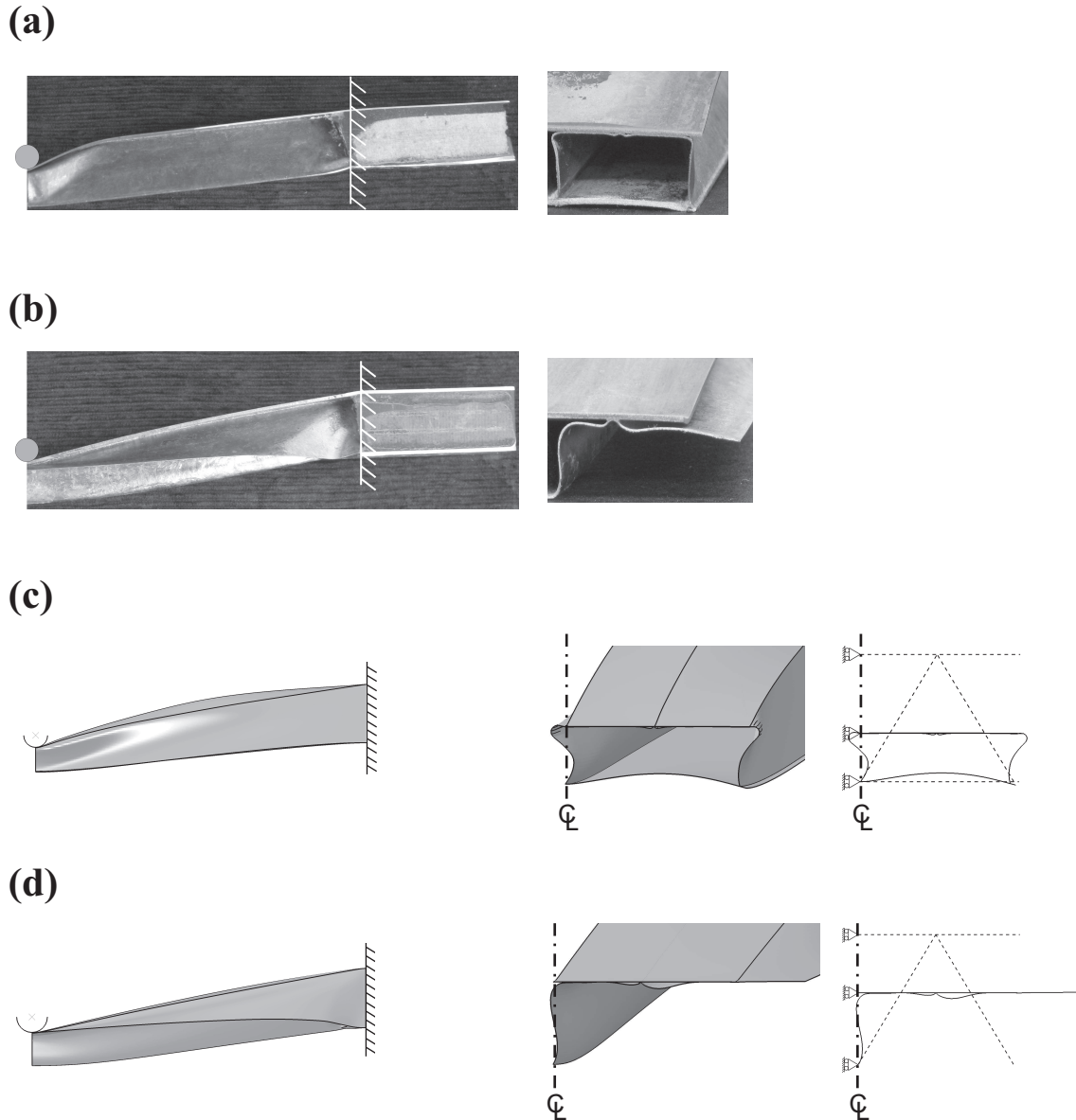
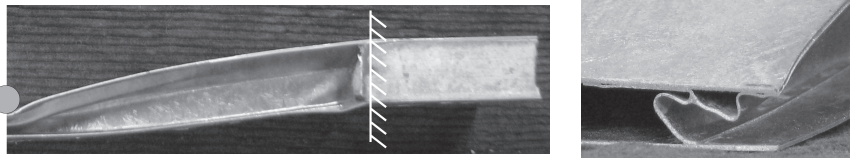
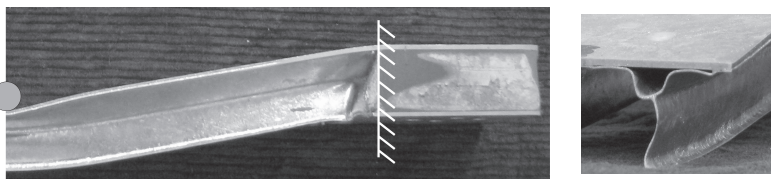


**Figure 4.10:** Photographs of the clamped sandwich beams with a corrugated core ( $m = 13.8 \text{ kg/m}^2$ ) (a) with front-and-back faces and (b) without a back face. Deformed finite element meshes of the same sandwich beam (c) with front-and-back faces and (d) without a back face. A side view showing half of the beam and a view of the core deformation at mid-span are given. To clarify the predicted deformation modes, the undeformed (dashed line) and deformed (solid line) cross-sections at mid-span are included in (c) and (d). The images are for beams loaded to  $\delta = 0.2L$  and then unloaded.

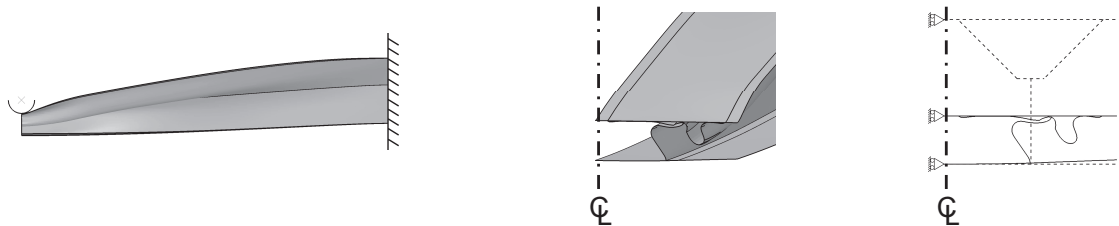
(a)



(b)



(c)



(d)

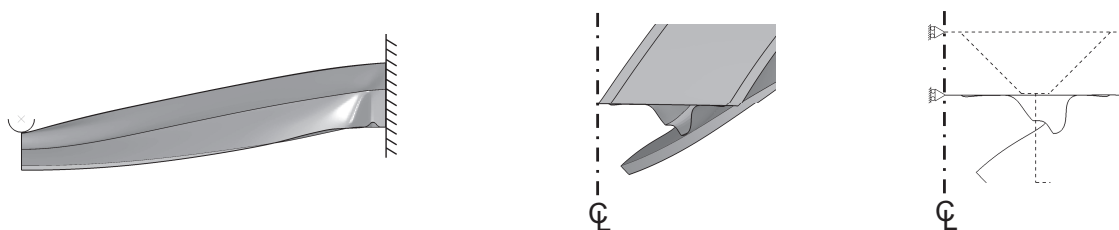


**Figure 4.11:** Photographs of the clamped sandwich beams with a Y-frame core ( $m = 13.8 \text{ kg/m}^2$ ) (a) with front-and-back faces and (b) without a back face. Deformed finite element meshes of the same sandwich beam (c) with front-and-back faces and (d) without a back face. A side view showing half of the beam and a view of the core deformation at mid-span are given. To clarify the predicted deformation modes, the undeformed (dashed line) and deformed (solid line) cross-sections at mid-span are included in (c) and (d). The images are for beams loaded to  $\delta = 0.2L$  and then unloaded.

The photographs of sandwich beams with front-and-back faces present, as shown in part (a) of Fig. 4.8-4.11, indicate that beam collapse is by indentation of the core beneath the mid-span roller. This holds true for both corrugated and Y-frame core topologies and for both simply supported and clamped beams. The normalised initial peak loads,  $\hat{F} = F_{pk}/(\sigma_Y bc)$ , for all sandwich beams tested are summarised in Table 4.1. It is clear from the table that the initial peak load for indentation of sandwich beams with both faces present has only minor sensitivity to the choice of boundary conditions.

The images shown in part (b) of Fig. 4.8-4.11 reveal that the beams without a back face collapse by plastic buckling at mid-span. This alternative mode is reminiscent of the buckling of circular tubes by ovalisation of their cross-section, as first identified by Brazier (1927). The progressive reduction of flexural plastic modulus of the sandwich beams in bending induces a Brazier-type instability, and we shall refer to this collapse mode by the generalised term *Brazier plastic buckling*. The mode of Brazier plastic buckling is more diffuse than the highly localised indentation mode beneath the central roller, compare the images as given in parts (a) and (b) of Fig. 4.8-4.11. For an introduction to Brazier buckling, see Calladine (1983).

Specimen				$\hat{F} = F_{pk}/(\sigma_Y bc)$ ( $10^{-3}$ )	
Boundary condition	Areal mass (kg/m <sup>2</sup> )	Core topology	Number of faces	Measured	FE
Simply supported	9.1	Corrugated	1	6.5	5.8
			2	6.5	4.9
		Y-frame	1	4.8	4.9
			2	4.9	4.6
	13.8	Corrugated	1	7.0	6.6
			2	8.3	7.8
		Y-frame	1	5.7	5.4
			2	7.1	7.4
Clamped	9.1	Corrugated	1	8.6	9.0
			2	6.8	6.4
		Y-frame	1	7.2	7.6
			2	5.2	5.3
	13.8	Corrugated	1	9.6	10.2
			2	9.0	8.7
		Y-frame	1	8.7	7.7
			2	8.0	8.3

**Table 4.1:** The measured and predicted values of normalised peak load  $\hat{F} = F_{pk}/(\sigma_Y bc)$ .

The peak load  $F_{pk}$  associated with Brazier plastic buckling occurs at a significantly larger value of  $\delta/L$  than the indentation mode for simply supported beams, recall Fig. 4.6. Also, the value of  $F_{pk}$  for Brazier plastic buckling is sensitive to the choice of boundary condition: clamped beams are 30-50% stronger than simply supported beams (see Table 4.1). This is consistent with the fact that for a given applied load  $F$ , the bending moment at mid-span of clamped beams is less than that for simply supported beams.

### 4.4 Finite element predictions

A Finite Element (FE) investigation of the three-point bending response of sandwich beams with corrugated and Y-frame cores has been conducted with the following objectives:

1. to obtain additional insight into the measured responses presented in Section 4.3,
2. to explore the influence of mass distribution between core and face-sheets upon the three-point bending response of a sandwich panel and
3. to analyse the effect of beam span upon the collapse mechanism.

All computations were performed using the commercial software Abaqus (version 6.9). Most simulations were done with the implicit solver, but the explicit solver was also used when convergence issues were encountered. The explicit solver can handle more easily the complex contact conditions that arise within the sandwich beam when the core is crushed beneath the mid-span roller. To ensure that a quasi-static solution was obtained with the explicit solver, the kinetic energy of the sandwich beam was monitored to ensure it never exceeds 10% of the strain energy, as suggested within the Abaqus documentation<sup>3</sup>.

#### 4.4.1 Comparison between measurements and simulations

The FE predictions for all sandwich beams tested are included in Fig. 4.6 and 4.7 for simply supported and clamped boundary conditions, respectively. In each figure,

---

<sup>3</sup>Dassault Systèmes Simulia Corp., *Abaqus analysis users manual*, version 6.9, Providence, RI, USA.

the simulated response of sandwich beams with a corrugated core (part (a)) and a Y-frame core (part (b)) is shown for  $m = 9.1 \text{ kg/m}^2$ . Likewise, the results for sandwich beams with  $m = 13.8 \text{ kg/m}^2$  are shown with a corrugated core (part (c)) and a Y-frame core (part (d)).

It is evident from Fig. 4.6 that the predicted peak loads of the simply supported beams slightly underestimate the measured peak loads. This is attributed to the fact that the FE analysis assumes frictionless contact between the sandwich beam and rollers, and neglects the strengthening due to the presence of the braze alloy over all surfaces of the sandwich beam. In contrast, the FE analysis somewhat overpredicts the strength of the fully-clamped beams following the initial peak load. This is traced to the fact that perfect clamping is assumed in the FE simulations whereas the test rig was unable to achieve this. The finite additional compliance of the test fixture is particularly significant for the sandwich beams of areal mass  $m = 13.8 \text{ kg/m}^2$  because the reaction force and moment at the supports is greater for these specimens.

The predicted shapes of deformed sandwich beams of areal mass  $m = 13.8 \text{ kg/m}^2$  are compared with photographs of the as-tested specimens in Fig. 4.8-4.11. Recall that simply supported beams with a corrugated core and a Y-frame core are shown in Fig. 4.8 and 4.9, respectively. Likewise, clamped beams with a corrugated core and a Y-frame core are given in Fig. 4.10 and 4.11, respectively. In each figure, beams with front-and-back faces present (part (c)) are compared with those without a back face (part (d)). Additional views are included in parts (c) and (d) to show the predicted cross-sections at mid-span.

The observed and predicted deformation of the sandwich beams with front-and-back faces present is by indentation beneath the central roller. In contrast, for the sandwich beams without a back face, the observed and predicted deformation mode is by Brazier plastic buckling at mid-span.

### 4.4.2 Sensitivity of the sandwich panel response to span and proportion of mass in the core

In the experimental investigation presented in Section 4.3, the proportion of mass in the core and the span of the sandwich beams were held fixed. The sensitivity of collapse strength to these geometric parameters is now explored using the FE

method. At this stage in the study, the perspective is changed from comparing FE predictions with the measured responses of sandwich *beams* to predicting the collapse response of sandwich *panels* in three-point bending. Sandwich panels are more commonly used in engineering practice (such as ship hulls) than sandwich beams, and it is of interest to evaluate the relative performance of corrugated cores and Y-frame cores in the sandwich panel configuration. We shall limit our attention to the simply supported case, and consider sandwich panels with identical front-and-back faces and panels with the back face absent. Results are presented in non-dimensional form so that they are applicable over a wide range of length scales; from laboratory test to industrial application.

The cross-sections of the sandwich panels are given in Fig. 4.12 for the corrugated core and Y-frame core. The panels are subjected to three-point bending, and are idealised by unit cells in the width-direction, as defined in Fig. 4.12. Under three-point bending, the panels will deform plastically over a limited portion along their length, and display negligible straining in the width direction,  $x_1$ . Consequently, the behaviour of a panel of large width is adequately captured by considering the response of a unit cell with symmetric boundary conditions imposed along the sides, as shown in Fig. 4.12.

### Dimensional analysis

In the simulations, the core shape is held fixed and parameterised in terms of the core thickness  $c$ , as shown in Fig. 4.12. The relative mass distribution between core and face-sheets is dictated by the thickness of the core members and of the face-sheets according to the following prescription.

The areal mass of the core  $m_c$  scales with the thickness of the core members  $t_c$  according to:

$$m_c = A\rho t_c \quad , \quad (4.1)$$

where the constant of proportionality is  $A = 1.843$  for both corrugated core and Y-frame core. Likewise, the areal mass of the sandwich panel  $m$  scales with the thickness of the face-sheets  $t_f$  according to:

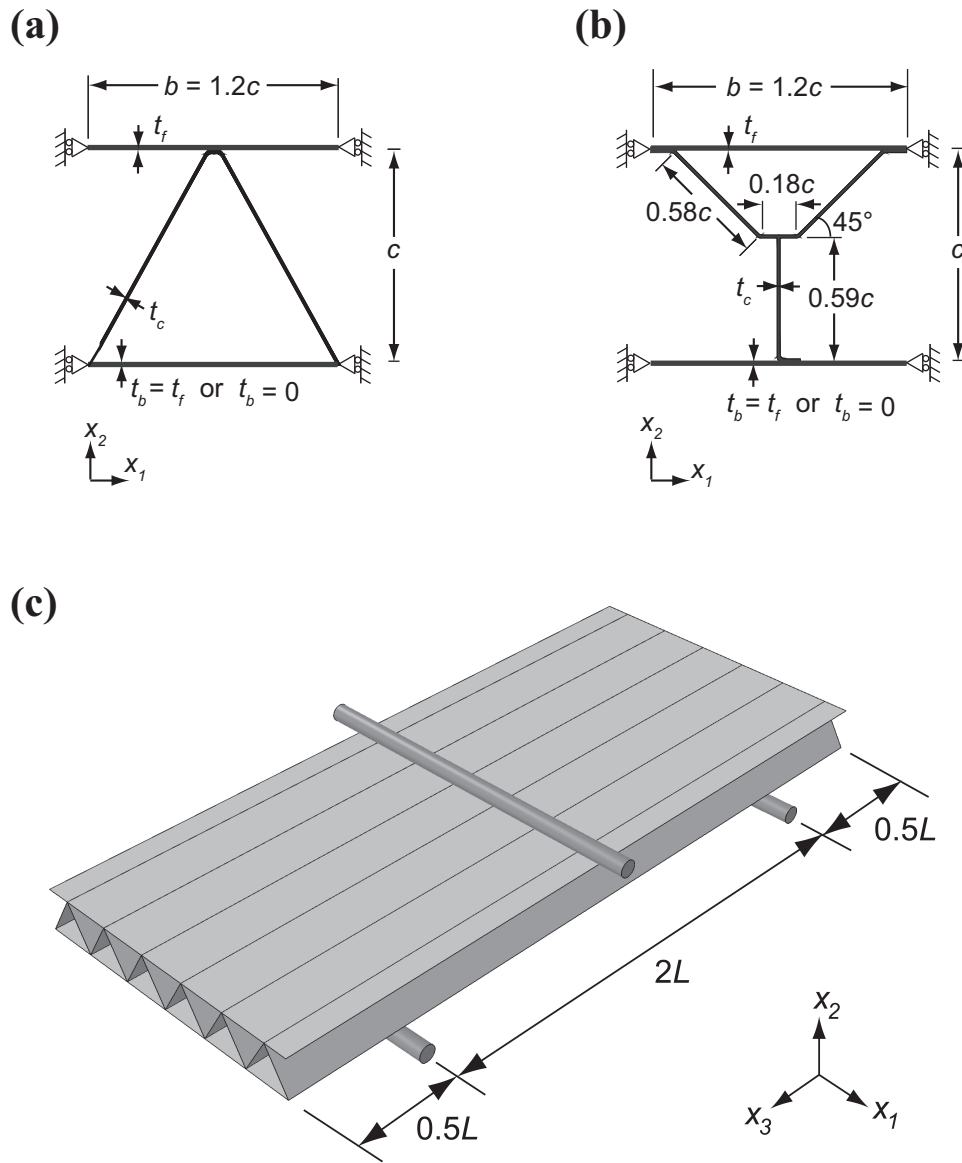


**Figure 4.12:** Cross-sectional dimensions of the sandwich panels considered in the numerical analysis: (a) corrugated core and (b) Y-frame core. (c) The sandwich panels, shown here with a corrugated core, are simply supported and loaded in three-point bending.

$$m = \rho t_f + m_c \quad , \quad (4.2)$$

when the back face is absent and as:

$$m = 2\rho t_f + m_c \quad , \quad (4.3)$$

when both front-and-back faces are present. Now, Eq. (4.1) can be rewritten in non-dimensional form as:

$$\frac{t_c}{c} = \frac{1}{A} \frac{m_c}{m} \frac{m}{\rho c} \quad , \quad (4.4)$$

and likewise Eq. (4.2) and (4.3) can be re-arranged to form:

$$\frac{t_f}{c} = \left(1 - \frac{m_c}{m}\right) \frac{m}{\rho c} \quad , \quad (4.5)$$

and

$$\frac{t_f}{c} = \frac{1}{2} \left(1 - \frac{m_c}{m}\right) \frac{m}{\rho c} \quad , \quad (4.6)$$

respectively. Thus, the sheet thickness of the core and face-sheets can be expressed directly in terms of the areal mass ratios  $m_c/m$  and  $m/(\rho c)$ .

The three-point bending strength of a simply supported sandwich panel of width  $b$ , core thickness  $c$  and span  $2L$  scales as:

$$F_{pk} = \frac{2M_p}{L} = \frac{2\sigma_Y b c t_f}{L} f_1(t_c, t_f, c) \quad , \quad (4.7)$$

where  $M_p$  is the plastic moment of the cross-section and  $f_1$  is a function of the cross-sectional geometry. Equation (4.7) can be rewritten in non-dimensional form as:

$$\hat{F} = \frac{F_{pk}}{\sigma_Y b c} = f_2\left(\frac{t_c}{c}, \frac{t_f}{c}, \frac{2L}{c}\right) \quad , \quad (4.8)$$

and using Eq. (4.4)-(4.6), the sheet thickness ratios can be expressed as areal mass ratios giving:

$$\hat{F} = \frac{F_{pk}}{\sigma_Y bc} = f_3 \left( \frac{m}{\rho c}, \frac{m_c}{m}, \frac{2L}{c} \right) \quad , \quad (4.9)$$

Therefore, the non-dimensional collapse load  $\hat{F}$  is a function of the normalised span  $2L/c$  and of the areal mass ratios  $m/(\rho c)$  and  $m_c/m$ .

In the experimental study, and associated numerical simulations reported above, the normalised span  $2L/c$  was held fixed at 11.4. The mass ratios were  $m/(\rho c) = 0.052$  and  $m_c/m = 0.48$  for sandwich beams of areal mass  $m = 9.1 \text{ kg/m}^2$ , and were  $m/(\rho c) = 0.079$  and  $m_c/m = 0.31$  for sandwich beams of areal mass  $m = 13.8 \text{ kg/m}^2$ .

We proceed by considering the sandwich panel response for corrugated cores and Y-frame cores, first with  $m/(\rho c)$  held fixed at 0.052 and second with varying mass ratio  $m/(\rho c)$ . The simulations with  $m/(\rho c) = 0.052$  represent the case considered in the above experimental study with  $m = 9.1 \text{ kg/m}^2$  and  $c = 22 \text{ mm}$ . Simulations were performed for selected values of  $m_c/m$  in the range 0.15 to 0.95 and of normalised spans  $2L/c$  in the range from 5 to 30. The overhang of the simply supported sandwich panels was  $0.5L$  and the length of the face-plates added to the extremities of the sandwich panels without a back face was  $0.56L$ : again, these values were equal to those used in the experimental investigation, recall Fig. 4.5(a). In all cases, the central and support rollers had a diameter  $D = 9 \text{ mm}$ , giving  $D/c = 0.41$ .

### Peak loads

The normalised peak load  $\hat{F} = F_{pk}/(\sigma_Y bc)$  is plotted in Fig. 4.13 as a function of normalised span  $2L/c$  for four selected values of  $m_c/m$ . The responses of sandwich panels with a corrugated core and a Y-frame core are shown in Fig. 4.13(a) and (b), respectively. In each plot, results are shown for sandwich panels with both faces present and for sandwich panels with the back face absent.

The peak load of all sandwich panels increases with increasing proportion of mass in the core,  $m_c/m$ . This increase in strength is more significant for short panels than for long panels. Also, with increasing  $m_c/m$ , the peak strength becomes less sensitive to whether the sandwich panel contains both face-sheets or only the front face-sheet: this is consistent with the fact that the peak strength is dominated by

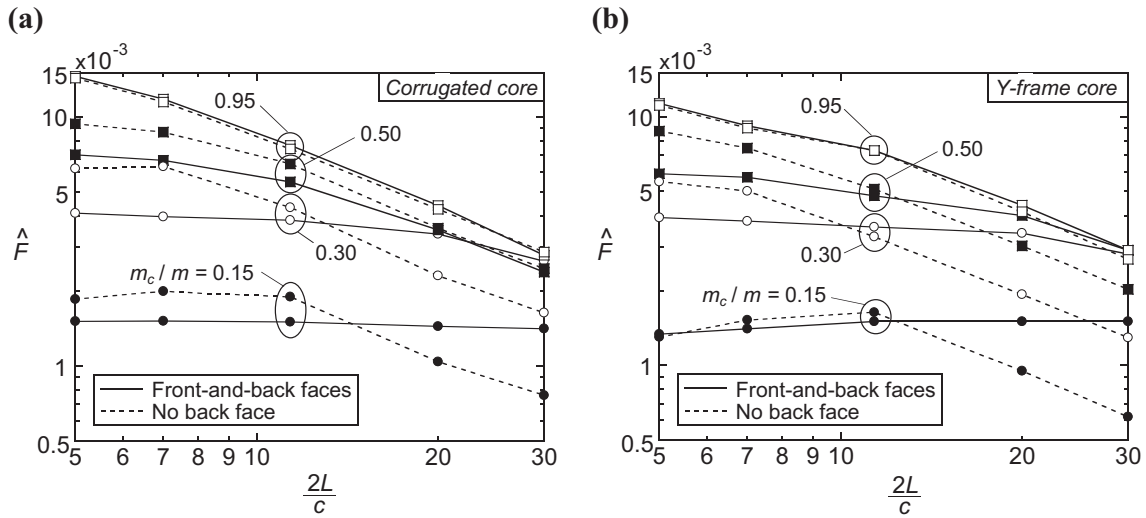


**Figure 4.13:** Normalised peak load  $\hat{F} = F_{pk}/(\sigma_Y bc)$  as a function of the normalised span  $2L/c$  for simply supported sandwich panels and selected values of  $m_c/m$  ( $m/(\rho c) = 0.052$ ). Results are shown for sandwich panels with (a) a corrugated core and (b) a Y-frame core.

the presence of the core rather than the relatively thin face-sheets at high  $m_c/m$ .

Next, consider the role of the back face upon the peak strength. For  $2L/c$  less than approximately 15, sandwich panels with a front face of double thickness but without a back face are stronger than those with front-and-back faces present. This is due to the fact that the thicker front face gives rise to a higher indentation strength. In contrast, sandwich panels with front-and-back faces have higher peak loads than panels without a back face for  $2L/c > 15$ ; this is consistent with the fact that the Brazier buckling load is reduced when the back face is removed.

In order to determine the degree to which sandwich panel collapse is dictated by core indentation or by Brazier buckling, a series of additional calculations have been performed to obtain the collapse strength due to each of these mechanisms acting in isolation. The details are as follows.

### Collapse mechanisms

**Indentation** The FE method was also used to obtain the indentation strength of the sandwich panels of geometry given in the previous section. To achieve this, the boundary conditions were changed such that the panel was adhered to a rigid foundation as shown in Fig. 4.14(a). This was achieved by constraining the translational degrees-of-freedom to zero along the bottom face of the panel.

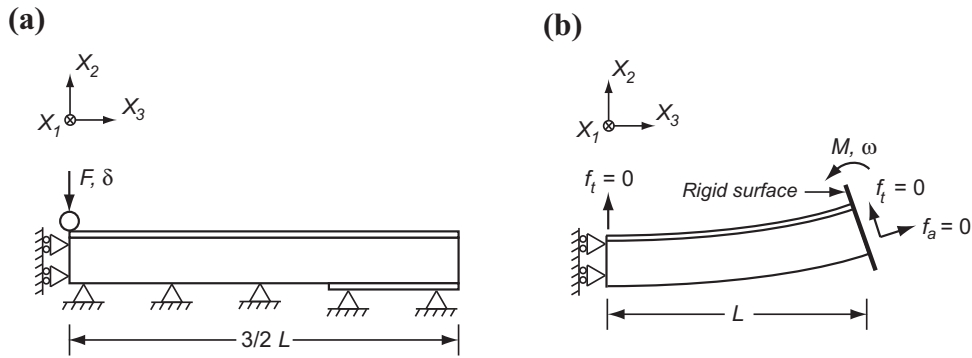


**Figure 4.14:** The boundary conditions on finite element models to simulate (a) indentation and (b) bending. A sandwich panel without a back face is shown.

Representative collapse responses of sandwich panels resting upon a rigid foundation are given in Fig. 4.15(a) for  $m/(\rho c) = 0.052$  and  $m_c/m = 0.5$ . The predictions of indentation strength are limited to  $2L/c = 11.4$ , as used in the experimental study on sandwich beams. Results are shown for corrugated and Y-frame cores, and for sandwich panels with and without a back face. The responses exhibit a peak load  $F_I$  at a roller displacement  $\delta$  of approximately 1% of the core thickness  $c$ . A small load drop ensues and subsequent deformation occurs at almost constant load. These simulations were repeated for other selected values of  $m_c/m$  and the results are summarised in Fig. 4.15(b): the normalised indentation strength  $\hat{F}_I$  is plotted as a function of the proportion of mass in the core.

For all sandwich panels analysed, the indentation strength increases with increasing

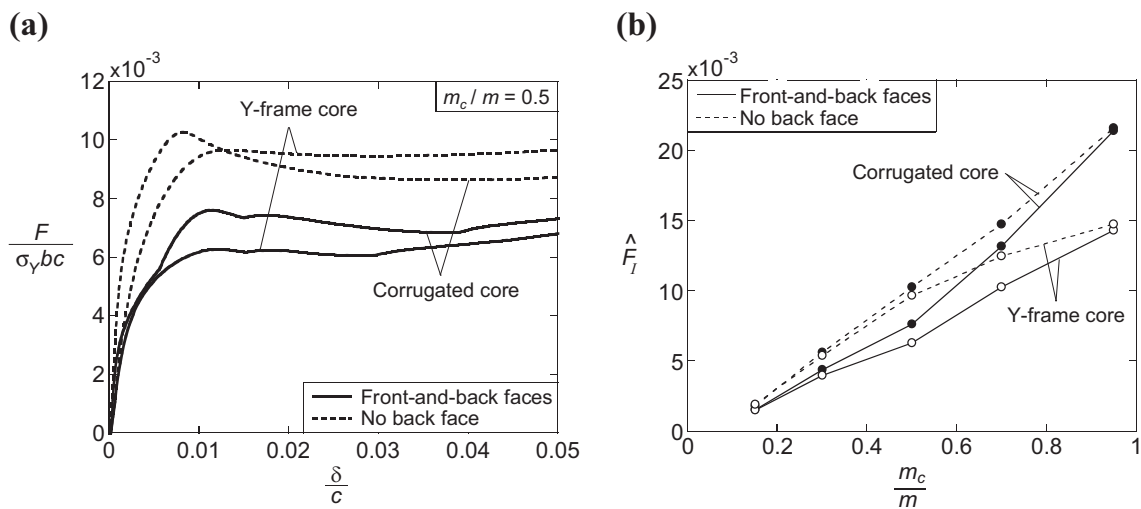


**Figure 4.15:** (a) The predicted indentation response of sandwich panels with  $m_c/m = 0.5$  resting on a rigid foundation. (b) Normalised indentation strength  $\hat{F}_I = F_I/(\sigma_Y bc)$  as a function of  $m_c/m$  ( $m/(\rho c) = 0.052$ ).

$m_c/m$ . The indentation strength is also sensitive to topology:

1. sandwich panels with a corrugated core have higher indentation strengths than their counterparts with a Y-frame core, and
2. the indentation strength of panels with a double thickness front face and without a back face exceeds that of sandwich panels with front-and-back faces present. These features have already been noted above in reference to Fig. 4.13.

**Brazier plastic buckling** The critical bending moment causing a sandwich panel to collapse by Brazier plastic buckling was also obtained with the FE method. For these simulations, all nodes (and corresponding degrees-of-freedom) at the right end of the panel were tied to a rigid surface as illustrated in Fig. 4.14(b). The rigid surface was rotated by an angle  $\omega$  about the  $x_1$ -axis, with the axis of rotation positioned at mid-height of the panel. Otherwise, the rigid surface was free to translate in the  $x_2$  and  $x_3$  directions to ensure that no axial or transverse forces were applied to the panel. To prevent rigid body motion, the  $x_2$ -component of nodal displacement was constrained to equal zero for one node of the front face ( $x_1 = 0$ ), at the left-hand end of the panel ( $x_3 = 0$ ).

The representative collapse response of sandwich panels with  $m/(\rho c) = 0.052$  and  $m_c/m = 0.5$  is given in Fig. 4.16(a). Results are shown for both corrugated and Y-frame core topologies and for sandwich panels with and without a back face. As the angular displacement  $\omega$  is increased, the reaction moment  $M$  increases up to a peak value  $M_B$  due to Brazier plastic buckling, and this is followed by a softening response. These simulations have been repeated for selected values of  $m_c/m$  and the normalised Brazier buckling moment  $\hat{M} = M_B/(\sigma_Y bc^2)$  is plotted in Fig. 4.16(b) as a function of the proportion of  $m_c/m$ , with  $m/(\rho c) = 0.052$ . The simulations are done for sandwich panels with  $2L/c = 11.4$ , but the peak moment is relatively insensitive to this ratio.

It is clear from Fig. 4.16(b) that the Brazier buckling moment for a sandwich panel without a back face increases with increasing  $m_c/m$ . For these structures, the position of the neutral axis is sensitive to the proportion of mass in the core; an increase in  $m_c/m$  moves the neutral axis closer to the centre of the core, increases the structural efficiency in plastic bending and leads to an increase in the Brazier buckling strength. In contrast, for sandwich panels with front-and-back faces present, the

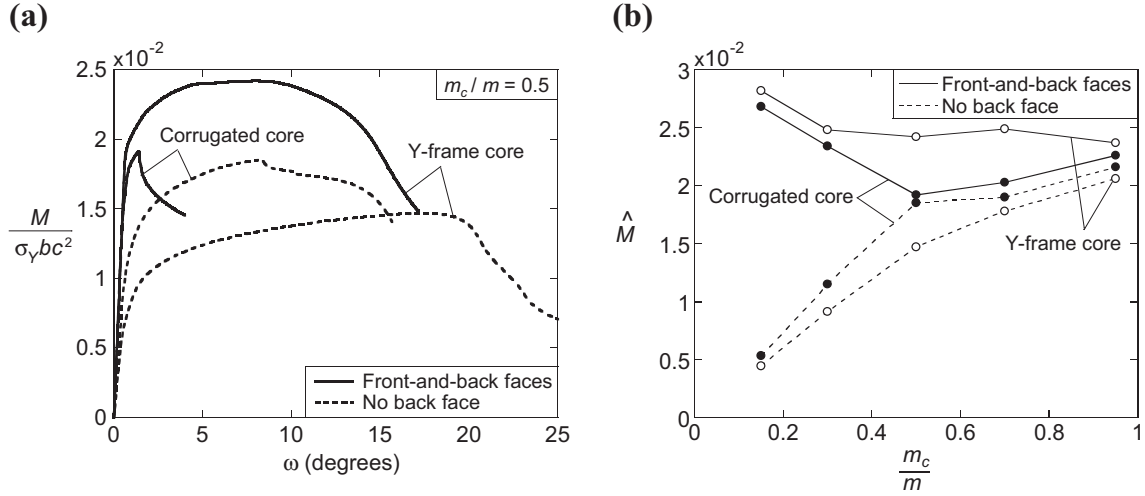


**Figure 4.16:** (a) The predicted bending response of sandwich panels with  $m_c/m = 0.5$ . (b) Normalised Brazier buckling moment  $\hat{M} = M_B/(\sigma_Y bc^2)$  as a function of  $m_c/m$  ( $m/(\rho c) = 0.052$ ).

position of the neutral axis is independent of the proportion of mass in the core and consequently  $\hat{M}$  is relatively insensitive to the value of  $m_c/m$ .

**Interpretation of the three-point bending strength in terms of indentation and Brazier buckling** We anticipate that, at a sufficiently short span  $2L$ , the three-point bending strength  $F_{pk}$  is approximated by the indentation strength  $F_I$  and is independent of span. In contrast, the three-point bending strength of long panels is dictated by Brazier plastic buckling; for a simply supported sandwich panel, the collapse load associated with Brazier plastic buckling scales with the panel length  $2L$  according to:

$$F_B = \frac{2M_B}{L} \quad . \quad (4.10)$$

The indentation load and Brazier buckling moment, as given in Fig. 4.15(b) and 4.16(b), are now used to estimate the collapse load of a panel in three-point bending. The lower value of  $F_I$  and  $F_B$  determines which collapse mechanism is active. These asymptotic predictions of collapse loads are compared with the three-point bending collapse loads in Fig. 4.17. Comparisons are made in Fig. 4.17(a) and (b) for sandwich panels with front-and-back faces present, and in Fig. 4.17(c) and (d) for sandwich panels with the back face absent.

In broad terms, there is excellent agreement between the predicted indentation load

and the three-point bending load at short spans, and between the predicted Brazier buckling load and the three-point bending load at long spans. The deformation mode of the panels in three-point bending confirms this (not shown). The switch in response from indentation to Brazier buckling occurs at a transition value of span  $2L_t/c$ . For sandwich panels containing front-and-back faces,  $2L_t/c$  decreases with increasing  $m_c/m$ . This is consistent with the feature that  $F_I$  increases with increasing  $m_c/m$  whereas  $M_B$  is relatively insensitive to  $m_c/m$  for panels containing front-and-back faces. In contrast, the transition span  $2L_t/c$  for sandwich panels with

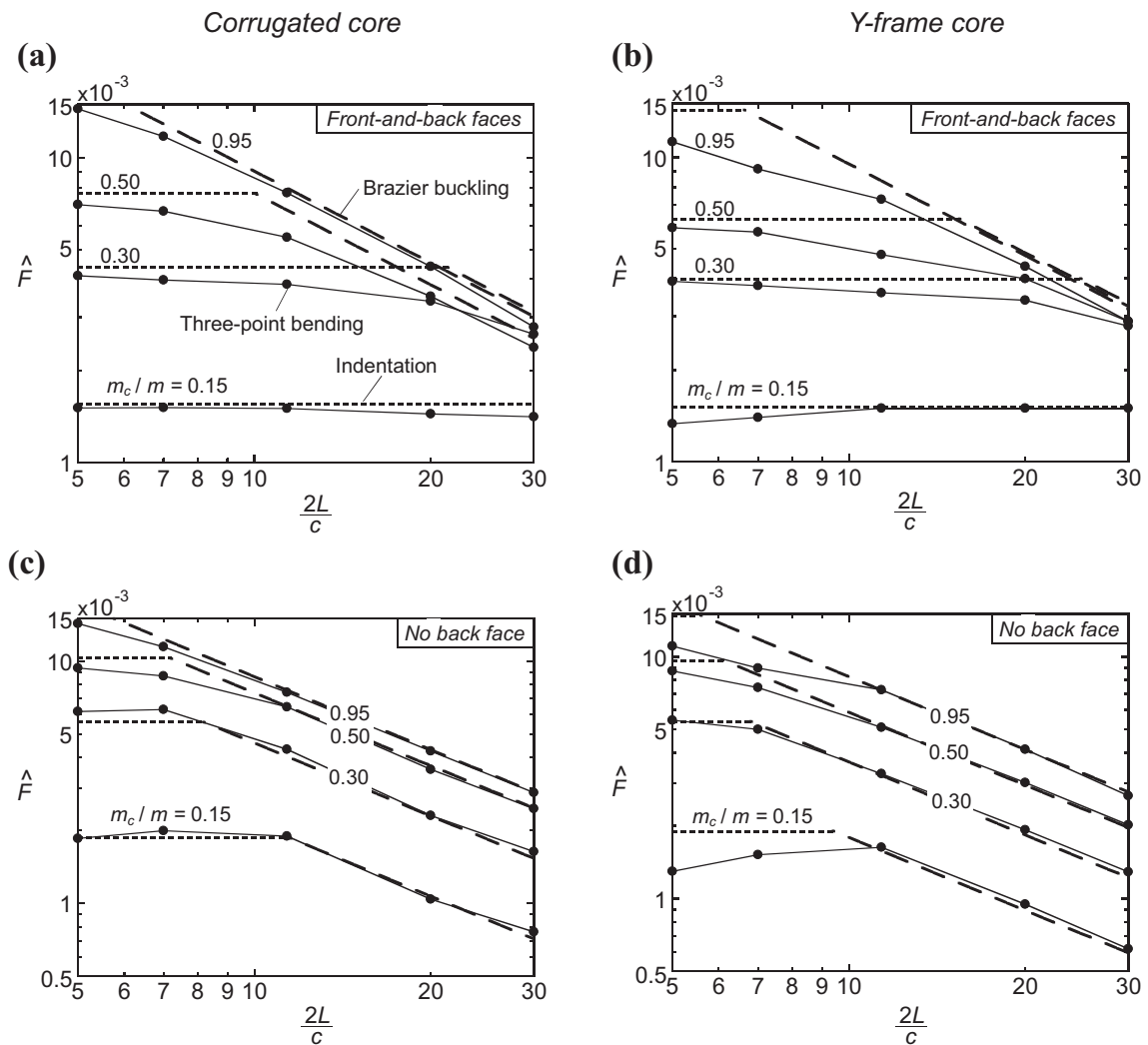


**Figure 4.17:** Normalised peak load  $\hat{F} = F_{pk}/(\sigma_Y bc)$  as a function of the normalised span  $2L/c$  for simply supported sandwich panels and selected values of  $m_c/m$  ( $m/(\rho c) = 0.052$ ). The three-point bending results are reproduced from Fig. 4.13. The indentation and Brazier buckling strengths are included as short and long dashed lines, respectively. Sandwich panels with front-and-back faces are shown with (a) a corrugated core and (b) a Y-frame core. Likewise, sandwich panels without a back face are shown with (c) a corrugated core and (d) a Y-frame core.

the back face absent is only mildly influenced by the value of  $m_c/m$ . This arises from the fact that  $F_I$  and  $M_B$  both increase with increasing  $m_c/m$  for sandwich panels without a back face.

### Sensitivity of the three-point bending strength to the value of $m/(\rho c)$

It has been demonstrated above that the three-point bending strength is adequately represented by the two asymptotic behaviours of core indentation and Brazier buckling, with the operative collapse mode dictated by the beam span. Here, the dependence of the indentation strength and the Brazier buckling strength upon  $m/\rho c$  is explored.

The indentation strength and Brazier buckling strength are plotted as a function of  $m_c/m$  in Fig. 4.18 and 4.19, respectively, for selected values of  $m/(\rho c)$  in the range of 0.015 and 0.15. Indentation strengths are shown in Fig. 4.18(a) for panels with a corrugated core and in Fig. 4.18(b) for panels with a Y-frame core; in each plot, results are given for panels with both faces present, and for panels with the back face absent. For all sandwich panels considered, the normalised indentation strength per unit mass  $\rho c \hat{F}_I/m$  increases with increasing value of  $m/(\rho c)$ . The observations made previously for sandwich panels with  $m/(\rho c) = 0.052$  also hold true for other values of  $m/(\rho c)$ :

1. sandwich panels with a corrugated core have higher indentation strengths than those with a Y-frame core and
2. relocating the back face material onto the front face increases the indentation strength of the sandwich panel.

The results for the Brazier buckling moment are given in Fig. 4.19(a) for panels with front-and-back faces present and in Fig. 4.19(b) for panels with the back face absent. In each plot, sandwich panels with a corrugated core are compared to those with a Y-frame core. The limit of  $m_c/m$  tending to zero is not included in Fig. 4.19(a) and (b) as this limit has no practical value and is not associated with a peak moment. It is clear from Fig. 4.19(a) that the Brazier buckling moment is relatively insensitive to  $m_c/m$  when front-and-back faces are present. In contrast, when the back face is absent, the Brazier buckling strength increases with increasing  $m_c/m$ . This was observed previously for sandwich panels with  $m/(\rho c) = 0.052$  (see Fig. 4.16(b)) but the results of Fig. 4.19 demonstrate that it holds true for other

selected values of  $m/(\rho c)$ . Now consider the effect of  $m/(\rho c)$  upon the normalised Brazier buckling strength per unit mass  $\rho c \hat{M}/m$ . Regardless of whether the back face is present or absent (and regardless of the core topology),  $\rho c \hat{M}/m$  increases by a factor of about 3 when  $m/(\rho c)$  is increased by a factor of 10 from 0.015 to 0.15.

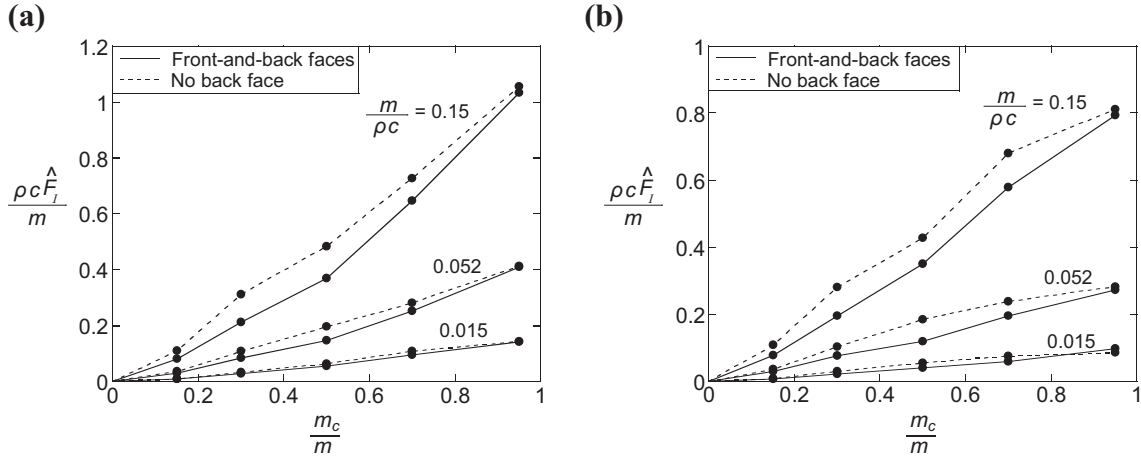


**Figure 4.18:** Normalised indentation strength per unit mass  $\rho c \hat{F}_I/m$  as a function of  $m_c/m$  for selected values of  $m/(\rho c)$ . Results are shown for sandwich panels with (a) a corrugated core and (b) a Y-frame core.

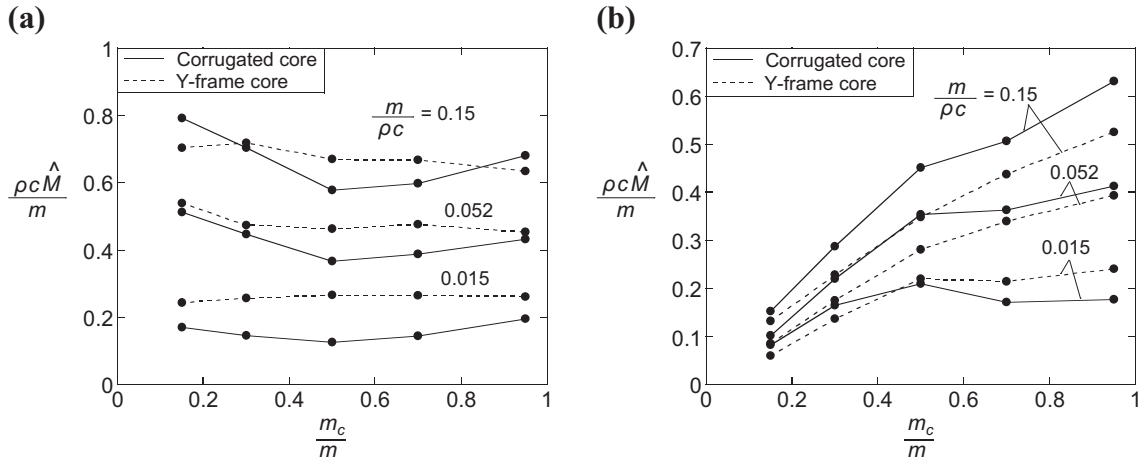


**Figure 4.19:** Normalised Brazier buckling moment per unit mass  $\rho c \hat{M}/m$  as a function of  $m_c/m$  for selected values of  $m/(\rho c)$ . Results are shown for sandwich panels (a) with front-and-back faces present and (b) without a back face.

## 4.5 Concluding remarks

Sandwich beams with corrugated and Y-frame cores have been manufactured by brazing together AISI 304 stainless steel sheets. The dimensions of the cores were

approximately 1:20 scale models of the cores used in a ship hull. In addition, the uniaxial tensile response of as-brazed stainless steel was found to be representative of shipbuilding steel up to strain levels of about 10%.

The three-point bending responses of sandwich beams with (i) front-and-back faces present and (ii) front face present, but back face absent have been measured and compared on an equal mass basis. The tests were done using simply supported and clamped boundary conditions, with the prismatic axis of the core aligned with the longitudinal axis of the beam. Sandwich beams with front-and-back faces present collapsed by indentation whereas beams without a back face collapsed by Brazier plastic buckling. Despite having different collapse mechanisms, sandwich beams with front-and-back faces and those without a back face had comparable three-point bending strengths for the choice of beam span employed.

Three-dimensional FE models were developed and the simulations were found to be in good agreement with the measured responses. The FE method was also used to study the influence of the mass distribution between the face-sheets and core. Upon concentrating the mass of the sandwich panel within the core the three-point bending strength of the structure increases. The analysis also showed the influence of the span upon the collapse response of a sandwich panel; short panels failed by indentation and long panels collapsed by Brazier plastic buckling. Sandwich panels with a corrugated core, and without a back face have the highest indentation strength and are thereby optimal for short spans, recall Fig. 4.18. In contrast, it is clear from Fig. 4.19 that panels with front-and-back faces have greater Brazier buckling strengths than their counterparts with the back face absent; consequently, panels with front-and-back faces are optimal for long spans. However, the choice of core topology plays only a minor role in the Brazier buckling regime: the corrugated core is either stronger or weaker than the Y-frame core depending upon the precise values of  $m/(\rho c)$  and of  $m_c/m$  and upon whether the sandwich panel has the back face present or absent.

## 4.A Influence of parent material

The influence of the parent material on the three-point bending responses of simply supported and clamped sandwich beams was investigated using the finite element method. The models used to simulate the experiments (see Section 4.2.3) were used

for this analysis, except that the material properties of as-brazed stainless steel were replaced by the ones of Lloyd's grade A steel. The yield strength was taken to be  $\sigma_Y = 280$  MPa and the hardening response of the material was tabulated in Abaqus from the plot given in Fig. 4.3. Both grades of steel have a Young's modulus of  $E = 210$  GPa and a Poisson's ratio of  $\nu = 0.3$ .

The three-point bending responses of beams with a Y-frame core are compared in Fig. 4.20 for the two choices of material. The responses of sandwich beams with front-and-back faces are shown in Fig. 4.20(a) whereas their counterparts without a back face are shown in Fig. 4.20(b). In each figure, results are shown for both simply supported and clamped boundary conditions, and the load  $F$  has been normalised by the yield strength of the as-brazed stainless steel,  $\sigma_Y = 210$  MPa. The peak load of sandwich beams made from as-brazed stainless steel are within 12% of those made from grade A steel. In general, the results in Fig. 4.20 indicate that the three-point bending response of a sandwich beam made from as-brazed stainless steel is representative of one made from Lloyds grade A steel.

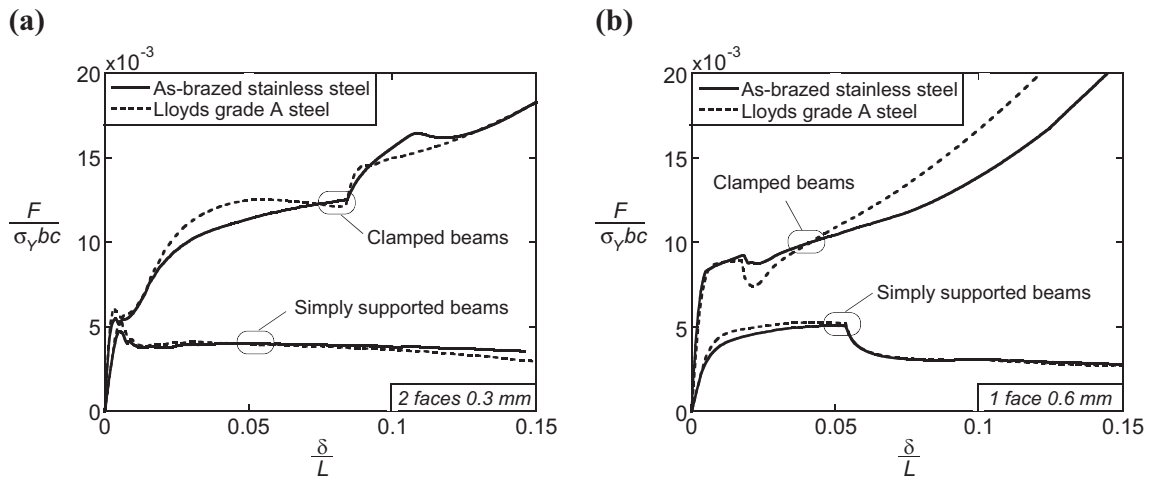


**Figure 4.20:** Sensitivity of the three-point bending response of a sandwich beam with a Y-frame core to the choice of material. (a) Front-and-back faces are present and (b) the back face is absent.

# Chapter 5

## Drop weight tests on prismatic sandwich beams

### Summary

To mimic the response of a sandwich hull design to a ship collision, drop weight tests with an impact velocity of 5 m/s were performed on stainless steel sandwich beams with a corrugated core or a Y-frame core. These tests were conducted on both simply supported and clamped beams, and the responses measured dynamically were compared to those measured quasi-statically. The dynamic peak load of the beams could not be measured accurately due to an artifact of the experimental setup; however, the instrumentation was able to capture precisely the post-peak response of the beams. The post-peak response at 5 m/s was slightly stronger than the one measured quasi-statically. Three-dimensional finite element simulations were found to be in reasonable agreement with the measurements and gave additional insight into the experiments. The finite element method was also used to investigate whether the peak load and collapse mechanism at 5 m/s are different from those obtained under quasi-static loading. The predictions indicated that sandwich beams which collapse quasi-statically by indentation also fail by indentation at 5 m/s. In contrast, the simulations for beams that fail by Brazier plastic buckling under quasi-static loading indicated that they collapse by indentation at 5 m/s. Finally, for all sandwich beams considered in the simulations, the dynamic peak load was found to be higher than its quasi-static value, and the mass of the front face was found to be an important factor contributing to this increase.

### 5.1 Introduction

More than 200 maritime accidents were recorded in the Gulf of Finland from 1997 to 2006 (Kujala et al., 2009). About 50% of those accidents were groundings and another 20% were ship-ship collisions. For large vessels such as oil and chemical tankers, ship collisions and groundings occur at low speeds, approximately 5 m/s<sup>1</sup>. These accidents are in general considered as quasi-static loading scenarios (ISSC, 2006c). This assumption seems reasonable for vessels with a conventional hull design which can absorb energy only by bending and stretching of the outer hull. The validity of this assumption is questionable for vessels with a sandwich hull construction because additional energy is absorbed by crushing of the core, and the crushing response of most core topologies is very sensitive to velocity. For example, Tilbrook et al. (2007) have shown that when the corrugated core or the Y-frame core are crushed dynamically, their dynamic strength is superior to their quasi-static strength due to inertia stabilisation effects, even at low velocities between 1-10 m/s. This strengthening effect was observed in compression by Tilbrook et al. (2007) and here, its influence on the dynamic bending response will be investigated.

The objective of this chapter is to compare the dynamic response of sandwich beams impacted at 5 m/s to their quasi-static response. Sandwich beams with a corrugated core and a Y-frame core will be considered under simply supported and clamped boundary conditions. Recall that their quasi-static responses have been measured previously in Chapter 4, and two collapse mechanisms were identified: indentation and Brazier plastic buckling. Will these collapse mechanisms change at 5 m/s? This question will be addressed below via experiments and simulations.

A drop weight apparatus will be used to impact the sandwich beams at 5 m/s. Similar tests were performed on aluminium sandwich beams with a metal foam core (Crupi and Montanini, 2007; Yu et al., 2003, 2008) and more recently on aluminium sandwich panels with a honeycomb core (Crupi et al., 2012). In both cases, the responses measured dynamically were similar to those measured quasi-statically, and no change in the collapse mechanism was observed when comparing the quasi-static and dynamic deformation modes. No drop weight tests have been performed on metallic sandwich beams with a corrugated core or a Y-frame core; hence, the motivation for this chapter.

---

<sup>1</sup>This collision speed is based on discussions with Mr. Joep Broekhuijsen, research coordinator at Damen Schelde Naval Shipbuilding.

This chapter is organised as follows. First, the drop weight apparatus and the dimensions of the tested sandwich beams are presented along with a description of the finite element models. Second, the measured dynamic responses are compared to the quasi-static responses for both simply supported and clamped sandwich beams. Third, finite element predictions are compared to the experiments and finally, the finite element method is used to explore if the quasi-static peak load and collapse mechanism of a sandwich beam are different during an impact at 5 m/s.

## 5.2 Methodology

### 5.2.1 Geometry of the tested sandwich beams

Sandwich beams with a corrugated core and a Y-frame core were tested and their cross-sectional dimensions are given in Fig. 5.1. The core and face-sheets were made from AISI 304 stainless steel sheets of thickness  $t = 0.3$  mm and density  $\rho = 7900$  kg/m<sup>3</sup>. Both corrugated and Y-frame cores had a relative density  $\bar{\rho} = 0.025$  and a core thickness  $c = 22$  mm. The face-sheets were brazed to the core to produce a sandwich beam of areal mass  $m = \rho(2t + \bar{\rho}c) = 9.1$  kg/m<sup>2</sup>. The brazing cycle used to manufacture the sandwich beams was detailed previously in Section 4.2.1.

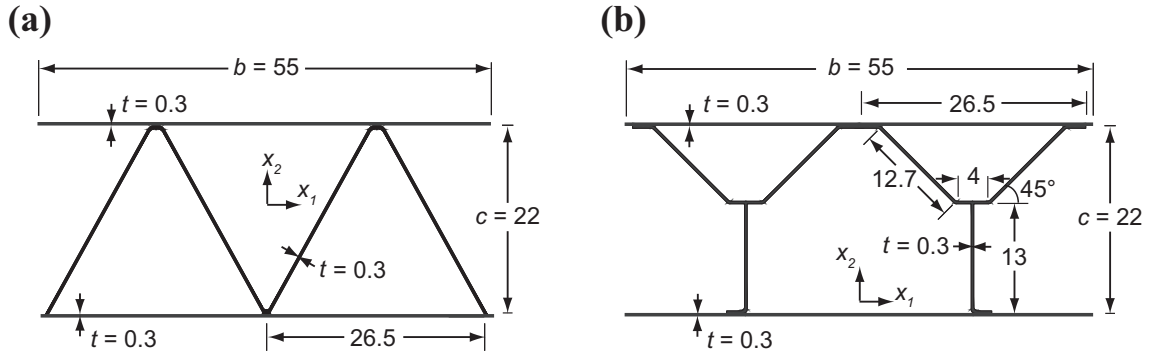


**Figure 5.1:** Cross-sectional dimensions of the tested sandwich beams with (a) a corrugated core and (b) a Y-frame core. All dimensions are in mm.

Simply supported and clamped sandwich beams were tested, both with a span  $2L = 250$  mm. In all cases, the prismatic axis of the core was aligned with the longitudinal direction of the beam ( $x_3$ -axis). Steel rollers of diameter  $D = 9$  mm were used to provide simple support to the sandwich beams, see Fig. 5.2(a). On the other hand, the fully-clamped boundary condition was achieved in two steps. First, the ends of

the sandwich beams were filled with an epoxy resin to make the core fully dense. Second, the end portions of the sandwich beams were bolted to the testing rig using steel clamping plates and M6 bolts, see Fig. 5.2(b).

### 5.2.2 Drop weight apparatus

The sandwich beams were impacted using a drop weight apparatus illustrated in Fig. 5.2. A projectile of mass  $M$  was dropped from 1.3 m to achieve an impact velocity of 5 m/s. The mass  $M$  was varied depending on the boundary conditions: 2 kg was used for simply supported beams whereas clamped beams were tested with 3 kg. Consequently, the kinetic energy of the projectile is 25 J for simply supported beams and 37.5 J for clamped beams.

The contact force was measured by a piezoelectric load cell (PCB model 218C). The load cell was mounted on a roller of diameter  $2R = 20$  mm. This assembly was placed stationary at mid-span on the sandwich beam to be tested. During the test, the projectile hits the load cell and the roller transfers the kinetic energy of the projectile to the sandwich beam. To reduce ringing in the load cell, a rubber pad of thickness  $t_r = 1.5$  mm, was added to the bottom surface of the projectile, see Fig. 5.2.

High-speed photography was used to capture the experiments with 10,000 frames per second. The displacement of the mid-span roller as a function of time was inferred from those images. For both simply supported and clamped beams, the duration of the first impact was 8-10 ms. The first impact was followed by a succession of rebounds and elastic impacts. The energy involved in these rebounds is negligible, approximately 1 J or less, as estimated from the rebound height of the projectile.

### 5.2.3 Finite element models

Three-dimensional Finite Element (FE) models were developed to simulate the dynamic response of all sandwich beams tested. All simulations were done with the explicit solver of the commercial software Abaqus (version 6.9).

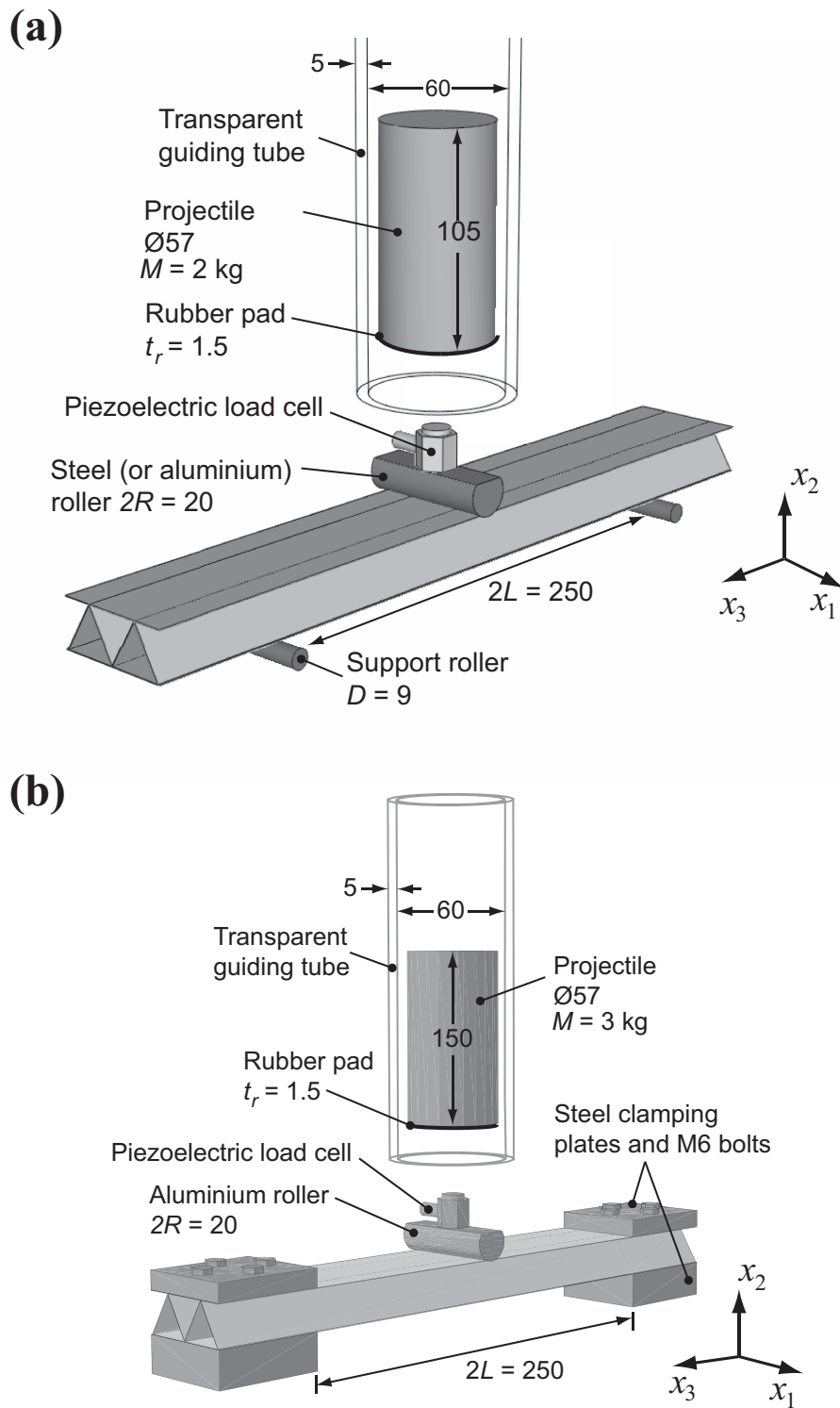


**Figure 5.2:** Experimental setup used to perform drop weight tests at 5 m/s on (a) simply supported and (b) clamped sandwich beams. A sandwich beam with a corrugated core is shown. All dimensions are in mm.

### Rigid mid-span roller

The FE simulations do not model the impact between the projectile and the assembly of the mid-span roller and load cell. To simplify the analysis, only the contact between the mid-span roller and the sandwich beam is simulated, see Fig. 5.3. The mid-span roller is modelled as a rigid body in the simulations. It is given an initial velocity  $v_i = 5$  m/s and then progressively slows down. The rigid mid-span roller is also given a mass in the simulations corresponding to the mass of the projectile used in the experiments. This ensures that the initial kinetic energy in the simulations is the same as that in the experiments. The interaction between the rigid mid-span roller and the front face of the sandwich beam was modelled as a hard frictionless contact.

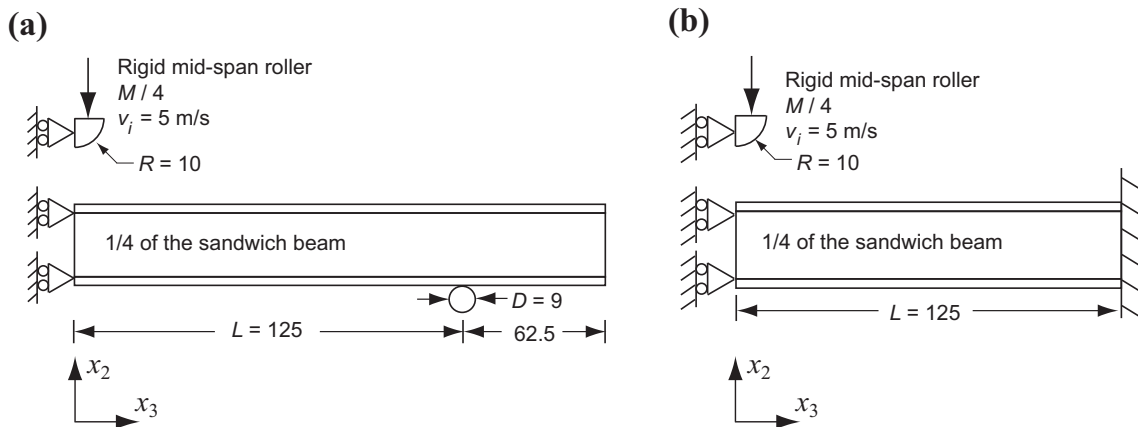


**Figure 5.3:** Finite element models used to simulate the drop weight tests on (a) simply supported and (b) clamped sandwich beams. All dimensions are in mm.

### Geometry and mesh of the sandwich beams

The geometry of the sandwich beams used in the simulations was identical to those employed in the experimental investigation, see Fig. 5.1. In all cases, the face-sheets were assumed to be perfectly bonded to the core. The sandwich beams were discretised using four noded linear shell elements (S4R in Abaqus notation) with an average mesh size of 0.5 mm. Numerical experimentation revealed that further mesh refinement did not improve significantly the accuracy of the calculations.

## Boundary conditions

It is sufficient to model only one quarter of the sandwich beam in the simulations, applying symmetric boundary conditions at mid-span ( $x_3 = 0$ ) and at mid-plane ( $x_1 = 0$ ). The overhang of simply supported beams beyond the outer rollers was included in the simulations. Simply supported boundary conditions were modelled by placing the sandwich beam on a rigid cylindrical roller with the same contact properties as those mentioned above. On the other hand, clamped boundary conditions were enforced by constraining to zero all degrees-of-freedom on the nodes of the end face of the sandwich beam ( $x_3 = L$ ).

## Material properties

The uniaxial tensile response of as-brazed AISI 304 stainless steel was measured in Chapter 4 at a nominal strain-rate of  $10^{-3} \text{ s}^{-1}$  and is reproduced in Fig. 5.4(a). In the simulations, the material was modelled as a rate-dependent, elastic-plastic solid in accordance with J2-flow theory. The material has a density  $\rho = 7900 \text{ kg/m}^3$ , a Young's modulus  $E = 210 \text{ GPa}$ , a Poisson's ratio  $\nu = 0.3$  and a quasi-static ( $10^{-3} \text{ s}^{-1}$ ) yield strength  $\sigma_Y = 210 \text{ MPa}$ . The hardening plastic behaviour was tabulated in Abaqus from the data shown in Fig. 5.4(a).

The strain-rate sensitivity of stainless steel was investigated by Stout and Follansbee

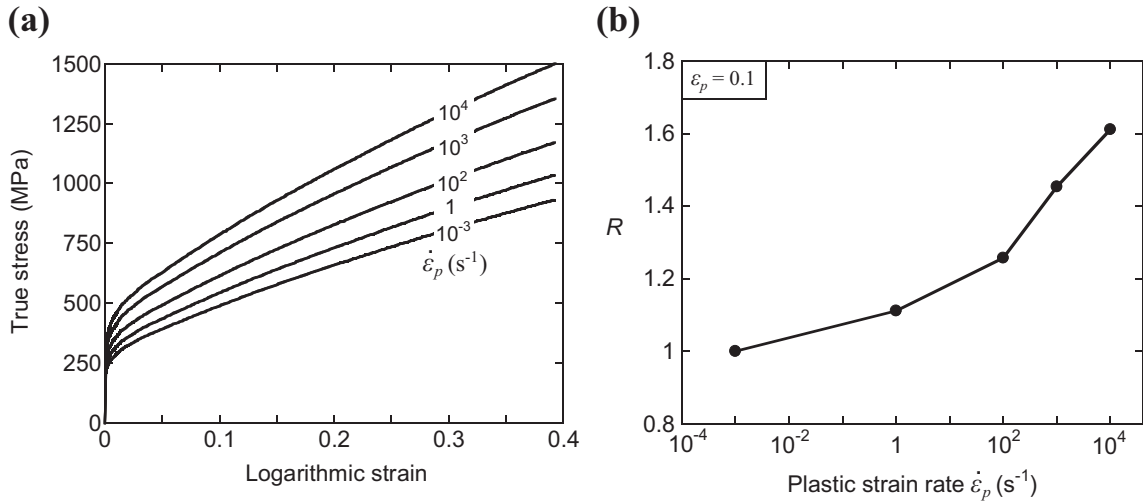


**Figure 5.4:** (a) The quasi-static ( $\dot{\epsilon}_p = 10^{-3} \text{ s}^{-1}$ ) uniaxial tensile response of AISI 304 stainless steel and the estimated high strain-rate responses based on the data of Stout and Follansbee (1986). (b) Dynamic strengthening ratio  $R$  as a function of plastic strain rate  $\dot{\epsilon}_p$ .

(1986) for strain-rates in the range  $10^{-4} \text{ s}^{-1} \leq \dot{\epsilon} \leq 10^4 \text{ s}^{-1}$ . Their results are reproduced in Fig. 5.4(b), where the dynamic strengthening ratio  $R$  is plotted as a function of the plastic strain rate  $\dot{\epsilon}_p$ . The ratio  $R$  is defined as the dynamic stress  $\sigma^d(\epsilon_p = 0.1)$  at an applied strain-rate  $\dot{\epsilon}_p$  divided by the corresponding quasi-static stress  $\sigma^{qs}(\epsilon_p = 0.1)$  at  $\dot{\epsilon}_p = 10^{-3} \text{ s}^{-1}$ . Stout and Follansbee (1986) also mentioned that the ratio  $R$  is reasonably independent of  $\epsilon_p$ . Consequently, the dynamic stress  $\sigma^d$  versus plastic strain  $\epsilon_p$  response can be expressed as:

$$\sigma^d(\epsilon_p, \dot{\epsilon}_p) = R(\dot{\epsilon}_p)\sigma^{qs}(\epsilon_p) \quad , \quad (5.1)$$

where  $R$  is given in Fig. 5.4(b). This prescription was employed in all simulations with  $\sigma^{qs}(\epsilon_p)$  given by the measured quasi-static response shown in Fig. 5.4(a). To illustrate the influence of material strain-rate sensitivity, the estimated uniaxial tensile responses of type 304 stainless steel at four selected additional values of strain-rate are given in Fig. 5.4(a).

## 5.3 Experimental results

The dynamic responses at 5 m/s for all sandwich beams tested are given in Fig. 5.5 for simply supported beams and in Fig. 5.7 for clamped beams. In each figure, results are shown for sandwich beams with a corrugated core and a Y-frame core. For each beam, the dynamic response is compared to the quasi-static response measured previously in Chapter 4. In each plot, the mid-span roller displacement  $\delta$  is normalised by the beam half-span  $L = 125 \text{ mm}$  whereas the load applied at mid-span  $F$  is normalised by  $\sigma_Y bc$ , where the quasi-static yield strength is  $\sigma_Y = 210 \text{ MPa}$ , the width of the sandwich beams is  $b = 55 \text{ mm}$  and the core thickness is  $c = 22 \text{ mm}$ .

### 5.3.1 Simply supported beams

The quasi-static and 5 m/s responses of simply supported sandwich beams are given in Fig. 5.5(a) for the corrugated core and in Fig. 5.5(b) for the Y-frame core. All simply supported beams have an initial elastic regime up to a peak load, which is followed by a softening response. For both core topologies, the dynamic peak load is significantly higher than its quasi-static peak load. In contrast, the post-peak

response at 5 m/s is only slightly stronger than that under quasi-static loading. The energy absorbed by the beams at 5 m/s is 24 and 25 J for the tests on the corrugated core and on the Y-frame core, respectively. These values are in excellent agreement with the kinetic energy of the projectile, which is 25 J.

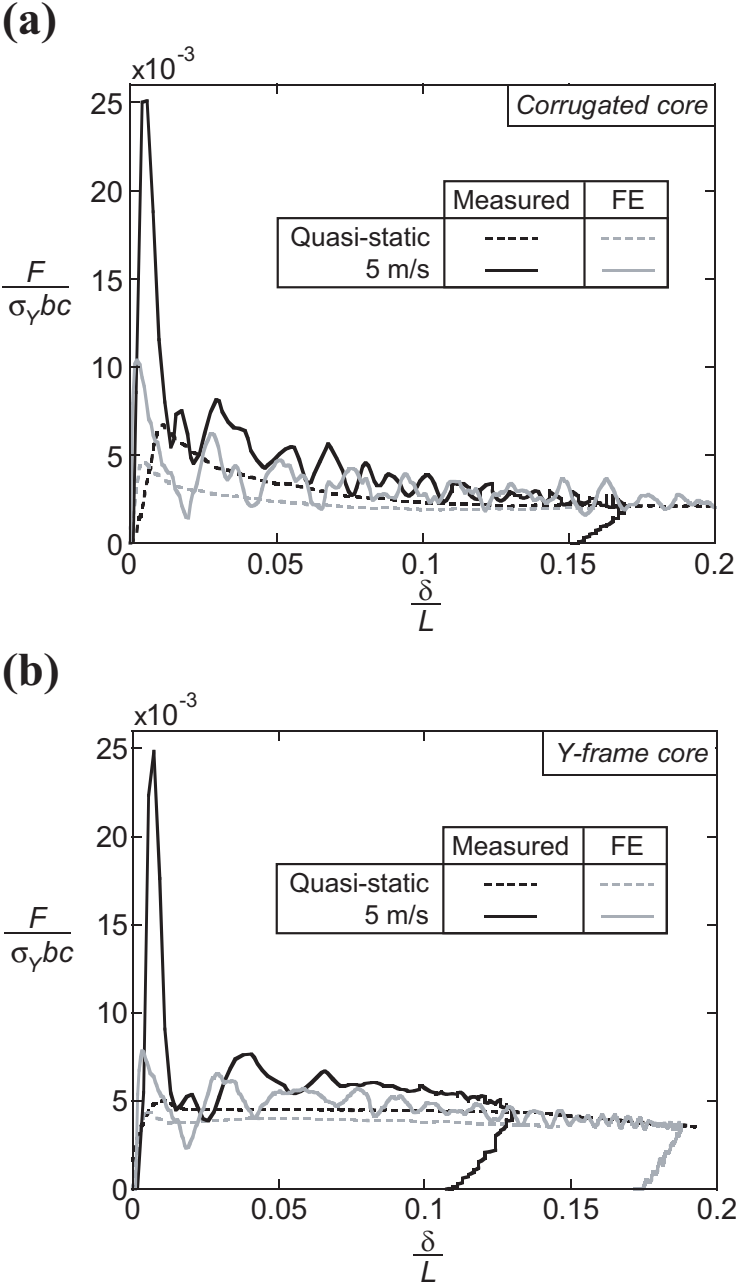


**Figure 5.5:** Quasi-static and 5 m/s responses of simply supported sandwich beams with (a) a corrugated core and (b) a Y-frame core.

One surprising result in Fig. 5.5 is that both core topologies have the same peak loads at 5 m/s whereas their quasi-static peak loads are different. We anticipate

that the peak load measured during the drop weight tests is influenced by the mass of the load cell and steel roller that are placed on the sandwich beam. To test this hypothesis, an additional drop weight test was performed using aluminium roller instead of a steel roller, and the influence on the measured response is shown in Fig. 5.6 for a simply supported sandwich beam with a Y-frame core. Note that a simply supported sandwich beam has a total mass of approximately 200 g. In contrast, the steel roller and load cell have a combined mass of 146 g, and replacing the steel roller by an aluminium roller reduces the mass of this assembly to 64 g.

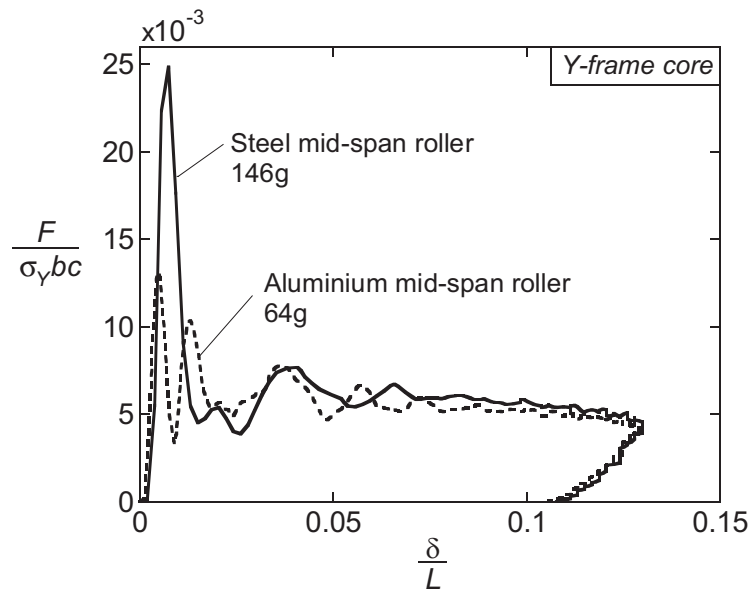


**Figure 5.6:** Influence of the mid-span roller mass upon the measured 5 m/s response of a simply supported sandwich beam with a Y-frame core. The measured response with a steel mid-span roller is reproduced from Fig. 5.5(b).

It is clear from Fig. 5.6 that the mass of the mid-span roller has a strong influence on the peak load measured at 5 m/s. Replacing the steel roller by an aluminium roller reduces the mass of this component by about 50% and accordingly, the peak load is also reduced by the same proportion. To minimise the effect of the mid-span roller upon the measured dynamic peak load, the aluminium roller was used for the tests on clamped beams, which are presented below.

### 5.3.2 Clamped beams

The responses of clamped sandwich beams are given in Fig. 5.7(a) and (b) for the corrugated core and the Y-frame core, respectively. In each plot, the quasi-static response is compared to the one measured at 5 m/s. All clamped sandwich beams

have an initial elastic regime followed by a peak load. This peak load is often followed by a small load drop, and then the beam hardens due to longitudinal stretching. The measured energy absorbed by clamped beams at 5 m/s is 34 J for the corrugated core and 33 J for the Y-frame core. These values are slightly inferior to the kinetic energy of the projectile, which is equal to 37.5 J.

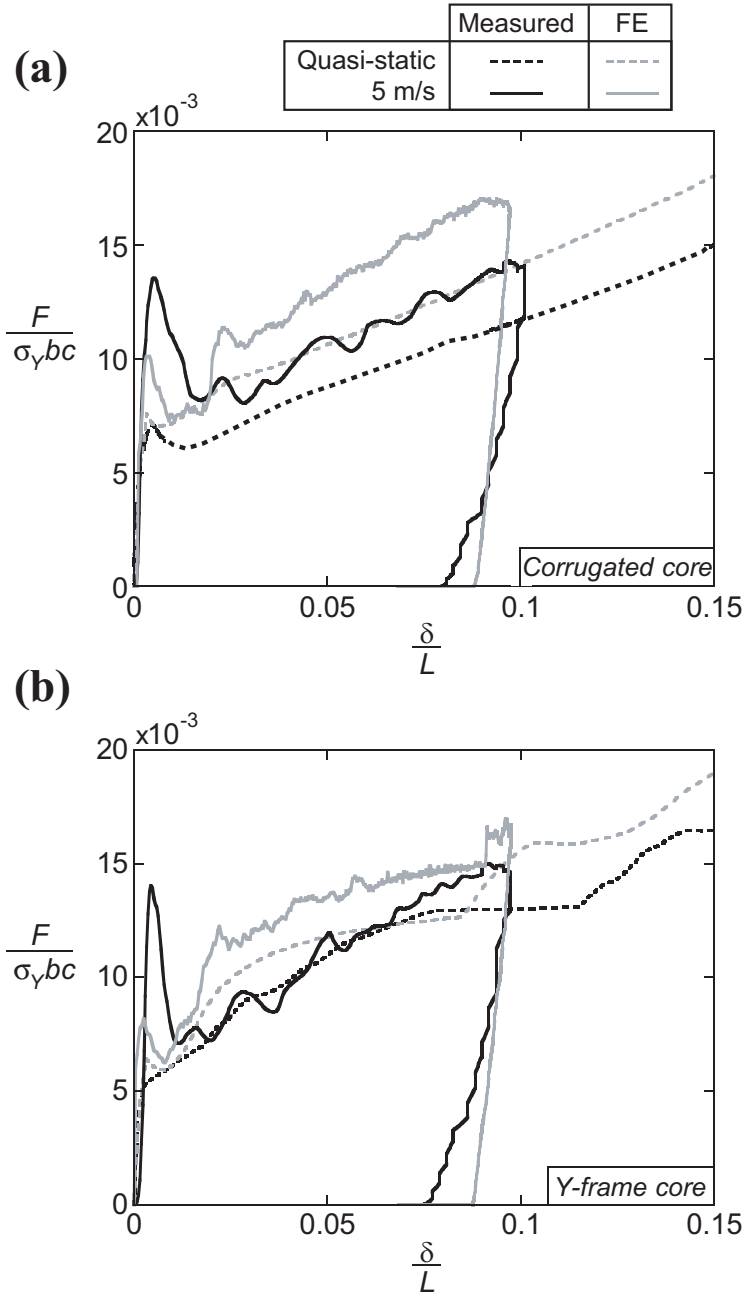


**Figure 5.7:** Quasi-static and 5 m/s responses of clamped sandwich beams with (a) a corrugated core and (b) a Y-frame core.

The initial peak load of clamped beams is significantly higher at 5 m/s than for quasi-

static loading; again, this is due to the inertia of the mid-span roller as demonstrated in the previous section. For the corrugated core, the post-peak hardening response measured at 5 m/s is stronger than the quasi-static response, see Fig. 5.7(a). In contrast, the post-peak hardening response appears to be relatively insensitive to the loading velocity for the Y-frame core, see Fig. 5.7(b). High-speed images taken during the drop weight tests revealed that the test fixture was unable to ensure perfectly clamped boundary conditions; a displacement of the order of 1-2 mm was observed at the clamped ends. The compliance of the testing rig softens the post-peak response of clamped beams and it is more important at 5 m/s than during quasi-static tests.

### 5.3.3 Collapse mechanisms

The simply supported and clamped sandwich beams tested both collapse by indentation under quasi-static loading, recall Section 4.3.3 on page 82. To verify whether the collapse mechanism is the same at 5 m/s, high-speed images of the dynamic tests performed on a sandwich beam with a Y-frame core are shown in Fig. 5.8(a) and (b) for simply supported and clamped boundary conditions, respectively. For both end conditions, the images indicate clearly that the beam collapses by indentation of the core underneath the mid-span roller. High-speed images of the drop weight tests performed on the corrugated core (not shown here) also indicate that the beam fails by indentation. Hence, for the limited number of experiments done, it appears that sandwich beams which collapse quasi-statically by indentation also fail by indentation at 5 m/s.

The number of experiments done was limited because the drop weight tests do not allow us to measure accurately the peak load of the beam. No drop weight tests have been performed on sandwich beams which collapse quasi-statically by Brazier plastic buckling. Will these sandwich beams also fail by Brazier plastic buckling at 5 m/s? This question will be addressed below using the finite element method.

## 5.4 Finite element predictions

Finite element simulations were performed with the following objectives: (i) to gain additional insight into the drop weight tests and (ii) to compare the peak load

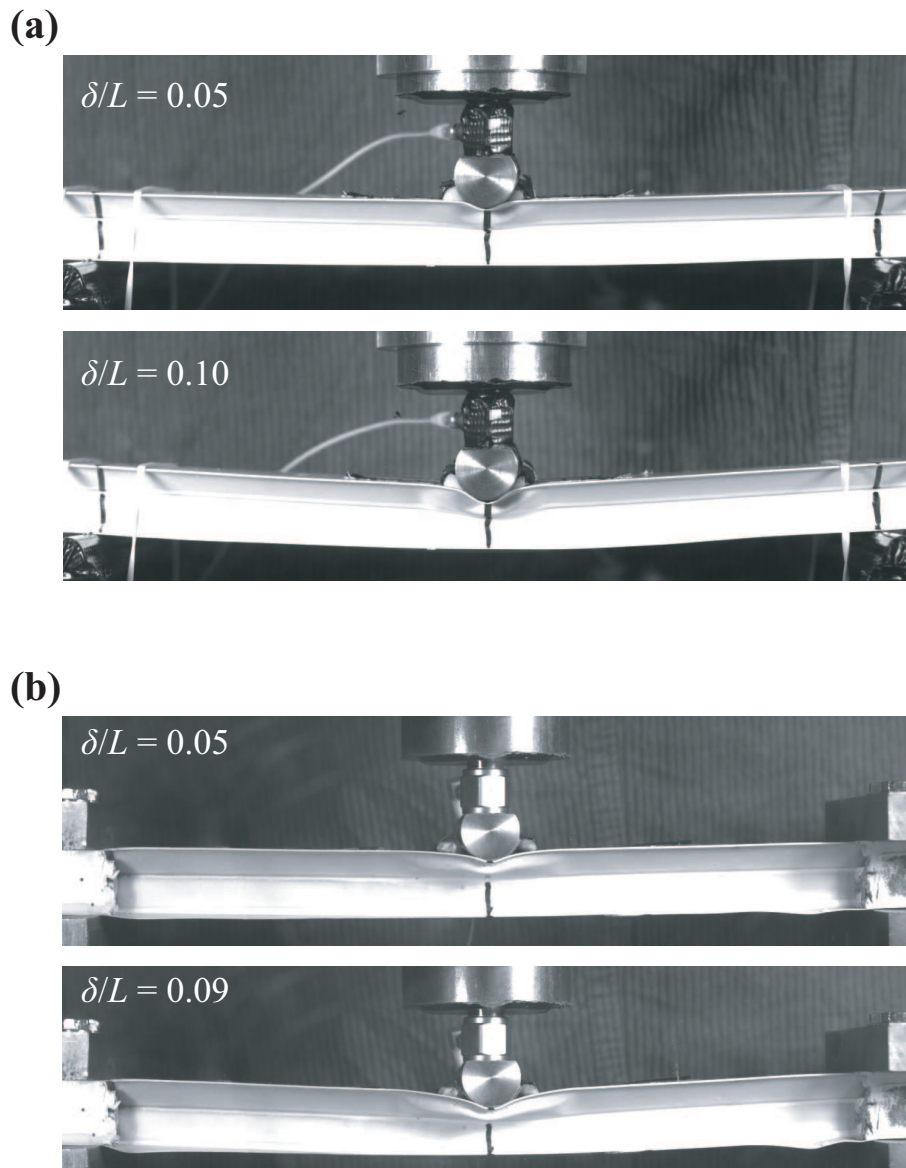


**Figure 5.8:** High-speed images captured during a drop weight test at 5 m/s on (a) a simply supported and (b) a clamped sandwich beam with a Y-frame core. The deformed beams are shown for two selected values of mid-span roller displacement  $\delta/L$ . All images are showing a side view of the beam.

and collapse mechanism obtained at 5 m/s to the ones obtained under quasi-static loading.

### 5.4.1 Comparison between simulations and measurements

The FE predictions for all sandwich beams tested are included in Fig. 5.5 and 5.7 for simply supported and clamped boundary conditions, respectively. In each figure, results are shown for the corrugated core in part (a) and for the Y-frame core in part (b). Simulations for the quasi-static beam responses are also included; they are reproduced from Chapter 4.

The simulations underestimate the measured 5 m/s responses of simply supported beams, see Fig. 5.5. The large discrepancy between the measured and predicted peak load is attributed to the fact that impact between the projectile and the assembly of the mid-span roller and load cell is not included in the simulations. Additional FE simulations in which all parts used in the experiments are modelled as deformable solids are presented in Appendix 5.A as an attempt to capture the measured peak load more accurately. In addition, an analytical model given in Appendix 5.B gives additional insight into the contact force generated by the impact of the projectile on the assembly of the mid-span roller and load cell.

The post-peak response of simply supported beams measured at 5 m/s is also slightly underestimated by the FE method. This discrepancy is traced to the fact that the simulations assume a frictionless contact between the beam and the rollers. As a result of underestimating the force, the simulations significantly over-predict the maximum mid-span roller displacement of simply supported sandwich beams; for the Y-frame core, the maximum mid-span roller displacement measured is  $\delta_{max}/L = 0.13$  whereas the simulations predicts  $\delta_{max}/L = 0.18$ .

The initial peak load of clamped beams measured at 5 m/s is also underestimated by the simulations for the same reason mentioned above for simply supported beams. However, the post-peak hardening response of clamped beams at 5 m/s is over-predicted by the FE calculations, see Fig. 5.7. This is attributed to the fact that perfect clamping conditions were assumed in the simulations whereas the test fixture was not able to achieve this. The maximum mid-span roller displacement predicted by the FE analysis is in good agreement with the experiments, but this is the result of first underestimating the initial peak load and then over-predicting the post-peak measured response of clamped beams.

### 5.4.2 Sensitivity of the peak load and collapse mechanism to the loading velocity

The experimental investigation reported in Section 5.3 has an important limitation; the finite mass of the mid-span roller and load cell does not allow us to measure accurately the peak load on the sandwich beam. To overcome this problem, the finite element method is used in this section to compare the predicted peak loads in the quasi-static and 5 m/s simulations of sandwich beams that collapse quasi-statically by (i) indentation and (ii) Brazier plastic buckling. This comparison will allow us to evaluate if one of the two collapse mechanisms is more sensitive to velocity.

Simply supported and clamped sandwich beams with a corrugated core or a Y-frame core are considered. Similarly to the work done in Chapter 4, two types of beams are analysed:

- (i) beams of dimensions shown in Fig. 5.1 with front-and-back faces present and
- (ii) beams with cores of dimensions given in Fig. 5.1, but with a front face of thickness  $2t = 0.6$  mm and no back face.

Both designs have an equal mass, but beams with front-and-back faces present collapse quasi-statically by indentation whereas beams with the back face absent collapse by Brazier plastic buckling, recall Chapter 4. In all cases, the beam span was kept fixed at  $2L = 250$  mm as used in the experimental study. All other details of the finite element models were the same as those prescribed in Section 5.2.3, except that the mid-span roller was given a constant velocity of 5 m/s instead of an initial velocity. Numerical experimentation revealed that this modification had only a minor effect on the simulated response.

The simulated quasi-static and 5 m/s responses are compared in Fig. 5.9. Beams with front-and-back faces present are shown in part (a) with a corrugated core and in part (b) with a Y-frame core. Likewise, beams with the back face absent are given in parts (c) and (d) for the corrugated and Y-frame cores, respectively. In each plot, results are shown for simply supported and clamped boundary conditions.

The results in Fig. 5.9 indicate that the peak load predicted at 5 m/s is (i) insensitive to the choice of boundary conditions and (ii) exceeds the quasi-static value in all cases. This increase is more important for the corrugated core than for the Y-frame

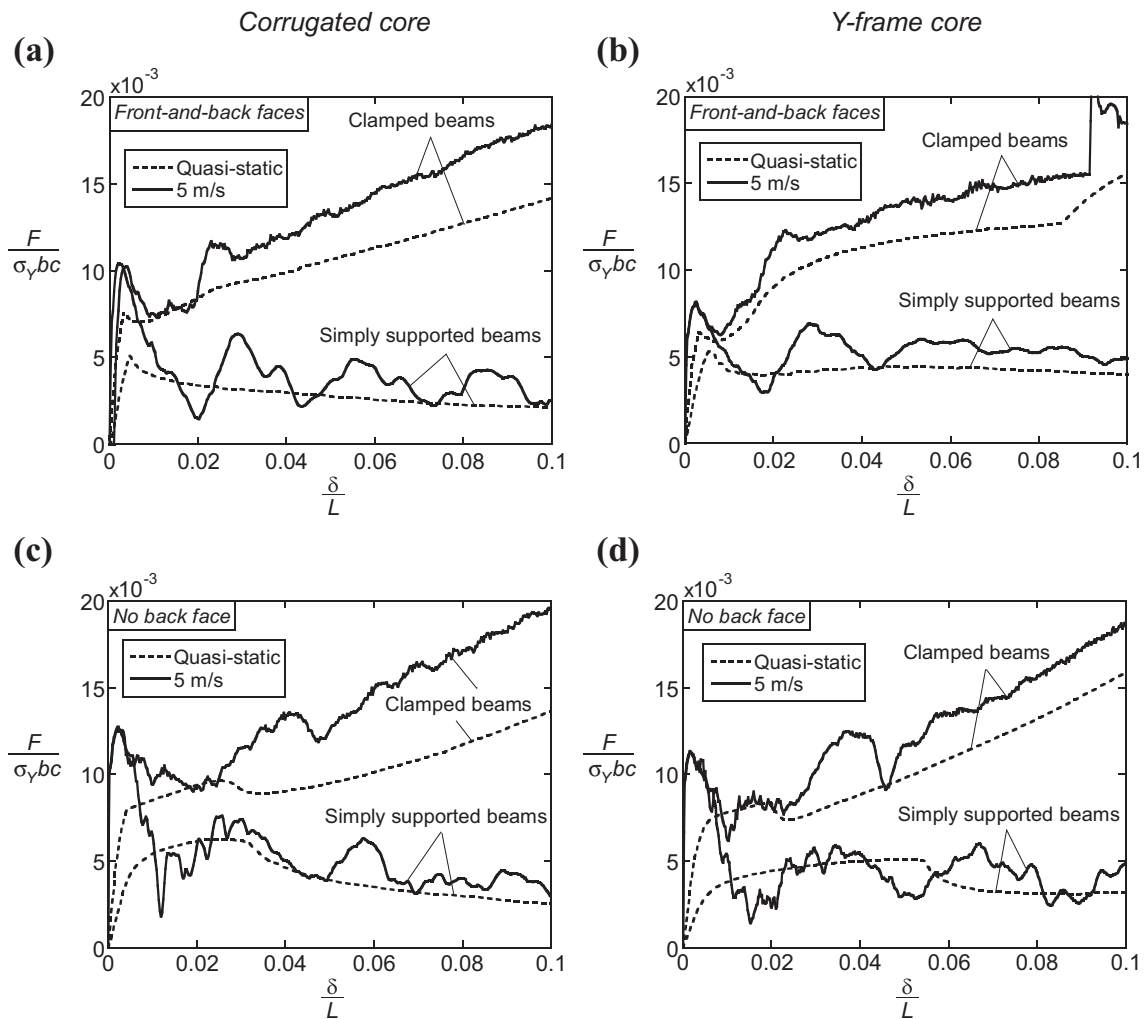


**Figure 5.9:** FE predictions of the quasi-static and 5 m/s responses of simply supported and clamped sandwich beams. Beams with front-and-back faces are shown with (a) a corrugated core and (b) a Y-frame core. Likewise, beams with the back face absent are shown with (a) a corrugated core and (b) a Y-frame core. Beams with front-and-back faces present collapse quasi-statically by indentation whereas those with the back face absent fail quasi-statically by Brazier plastic buckling.

core, compare Fig. 5.9(a) and (b). Moreover, the increase in peak load is sensitive to the allocation of face-sheet material; the increase is greater for sandwich beams with the back face absent than for those with front-and-back faces present. This can be attributed to the finite mass of the front face; recall that beams without a back face have a thicker front face than beams with front-and-back faces present.

The FE simulations revealed a change in collapse mechanism: beams that failed quasi-statically by Brazier plastic buckling collapsed by indentation at 5 m/s. To demonstrate this, contours of equivalent plastic strain  $\bar{\epsilon}_{pl}$  are shown in Table 5.1 for simply supported sandwich beams with a Y-frame core. Predictions are shown

for sandwich beams with and without a back face. For each beam, results obtained quasi-statically are compared to those at 5 m/s. In all cases, the distribution of equivalent plastic strain is plotted on a side view of the beam focusing on a portion of length  $0.35L$  from the beam mid-span. The results are shown for a value of mid-span roller displacement just after the peak load.

The results in Table 5.1 indicate clearly that sandwich beams with front-and-back faces collapse by indentation for both quasi-static loading and at 5 m/s. In both cases, the distribution of equivalent plastic strain is localised underneath the mid-span roller. In addition, the maximum equivalent plastic strain obtained quasi-statically is similar to that predicted at 5 m/s. In contrast, the equivalent plastic strain distribution obtained quasi-statically for a beam with the back face absent is significantly different from that obtained at 5 m/s; for quasi-static loading, a diffuse plastic hinge is formed at mid-span whereas at 5 m/s, the plastic strain is localised underneath the mid-span roller. This indicates a change in collapse mechanism: beams that collapse quasi-statically by Brazier plastic buckling fail by indentation at 5 m/s.

	Front-and-back faces $\delta/L = 0.02$	No back face $\delta/L = 0.05$
Quasi-static		
5 m/s		

**Table 5.1:** Equivalent plastic strain distribution for simply supported sandwich beams with a Y-frame core. Beams with and without a back face are shown. Results are given for quasi-static loading and 5 m/s. All images are showing a side view of the beam focusing on a portion of length  $0.35L$  from the beam mid-span.

## 5.5 Concluding remarks

The response of a sandwich hull to a ship collision was investigated in the laboratory using a drop weight apparatus. Drop weight tests, with an impact velocity of 5 m/s, were performed on stainless steel sandwich beams with a corrugated core and a Y-frame core. The tests were conducted on simply supported and clamped sandwich beams, with the prismatic axis of the core aligned with the longitudinal axis of the beam. The experimental setup did not allow us to measure the dynamic peak load accurately; the finite mass of the mid-span roller significantly increased the measured peak load. This problem can be minimised by reducing the mass of the mid-span roller and future work should consider using a polycarbonate roller instead of the steel and aluminium rollers used in this study. Nevertheless, the measurements did capture the post-peak force with adequate precision. For most beams tested, the post-peak response measured at 5 m/s was slightly stronger than the one measured quasi-statically.

Three-dimensional finite element models were developed to gain additional insight into the experiments. The predicted post-peak forces were found to be in reasonable agreement with the measurements for both simply supported and clamped beams. The finite element method was also used to investigate whether the peak load and collapse mechanism obtained quasi-statically are different at 5 m/s. A sandwich beam, which collapses quasi-statically by indentation, was also found to fail by indentation at 5 m/s. In contrast, a sandwich beam that fails quasi-statically by Brazier plastic buckling was found to collapse by indentation at 5 m/s. Finally, the peak loads predicted at 5 m/s were found to be (i) independent of the boundary conditions and (ii) higher than those obtained for quasi-static loading. The finite mass of the front face was identified as an important factor contributing to this increase of the peak load.

### 5.A Finite element predictions with the projectile and roller modelled as deformable parts

The impact between the projectile and the assembly of the load cell and mid-span roller was not considered in the finite element simulations detailed above; only the impact between the mid-span roller and the sandwich beam was modelled, see Sec-

tion 5.2.3. The influence of this modelling assumption on the simulated responses at 5 m/s is analysed in this appendix. This will be done by comparing the results obtained previously to additional simulations in which the projectile and the assembly of the mid-span roller and load cell are fully-meshed and modelled as separate parts.

### 5.A.1 Simulations without the rubber pad

An additional finite element model was developed in which the projectile and the assembly of the steel mid-span roller and load cell are modelled as two separate parts as shown in Fig. 5.10. Note that the rubber pad, placed at the bottom of the projectile in the experiments, was not modelled in the simulations.

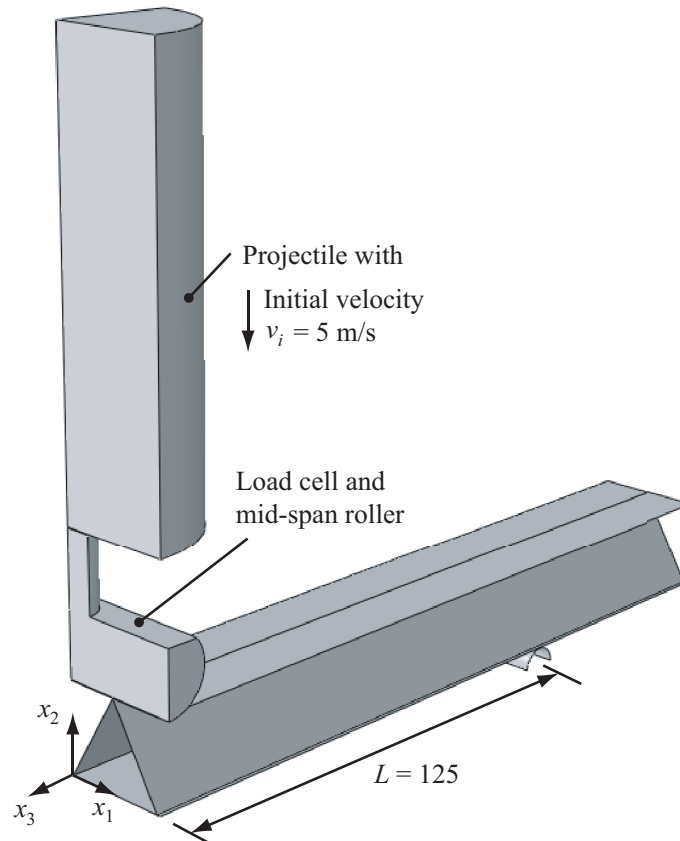


**Figure 5.10:** Finite element model with the projectile and the assembly of the load cell and mid-span roller modelled as two separate deformable parts. The model is shown for a simply supported sandwich beam with a corrugated core. All dimensions in mm.

The projectile and the assembly of the mid-span roller and load cell had the same dimensions as those used in the experiments, see Fig. 5.2(a). It is sufficient to

model only one quarter of these two parts, applying symmetric boundary conditions on  $x_1 = 0$  and  $x_3 = 0$  planes, see Fig. 5.10. The projectile was meshed with linear hexahedral elements (C3D8R in Abaqus notation) whereas the assembly of the mid-span roller and load cell was discretised using tetrahedral elements (C3D4 in Abaqus notation). Both parts were modelled as isotropic elastic solids with material properties representative of steel: a density  $\rho = 7900 \text{ kg/m}^3$ , a Young's modulus  $E = 210 \text{ GPa}$  and a Poisson's ratio  $\nu = 0.3$ . The projectile was given an initial downward velocity  $v_i = 5 \text{ m/s}$  and the interaction between all parts was defined as a hard frictionless contact. Finally, the sandwich beam and the support roller were modelled according to the prescription detailed previously in Section 5.2.3.

The response predicted by this additional finite element model is shown in Fig. 5.11 for a simply supported sandwich beam with a corrugated core. Two contact forces are plotted:

- (i) the contact force between the projectile and the assembly of the load cell and mid-span roller is given in part (a) and
- (ii) the contact force between the mid-span roller and the sandwich beam is shown in part (b).

The latter is compared to the results of simulations shown previously where the

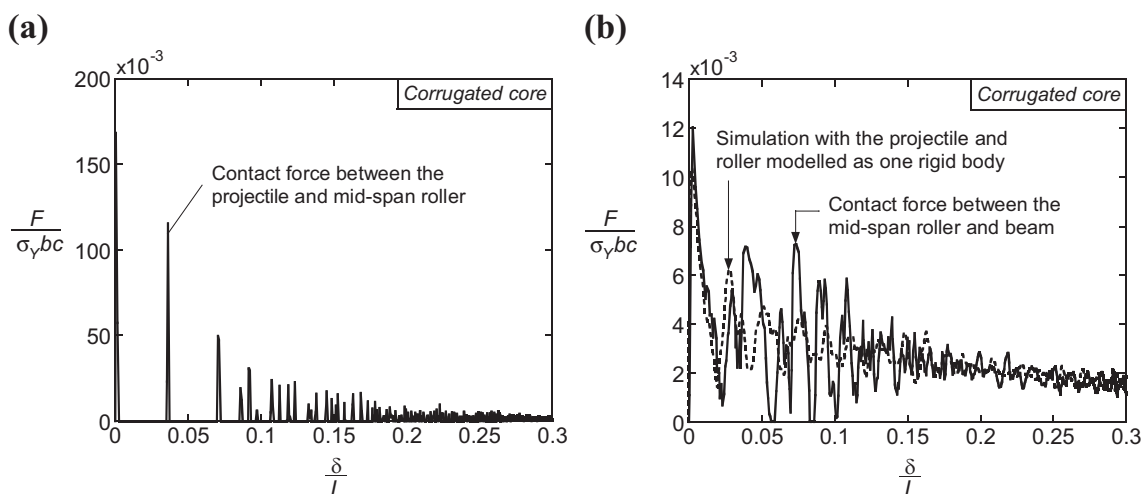


**Figure 5.11:** Simulated 5 m/s response of a simply supported beam with a corrugated core. The projectile and the mid-span roller are modelled as separate deformable parts in the simulations. The contact forces between (a) the projectile and the mid-span roller and (b) the mid-span roller and the beam are given. The simulations presented in Section 5.4.1 where the projectile and mid-span roller were modelled as one rigid body are included in part (b) for comparison.

projectile and mid-span roller were modelled as one rigid body. The results shown in Fig. 5.11(b) indicate that the assumption of modelling the projectile and mid-span roller as a single rigid body instead of two deformable entities has very little influence on the simulated dynamic response.

The contact force between the projectile and the mid-span roller, see Fig. 5.11(a), reveals that the two parts come in contact for a very short duration and then separate in several occasions at the beginning of the simulation for  $\delta/L < 0.1$ . This was not observed in the experiments because of the additional damping introduced by the rubber pad at the bottom of the projectile, see Fig. 5.5(a). The finite element model was then modified to take into account the rubber pad in the simulations. This is presented in the next section.

### 5.A.2 Simulations with the rubber pad

It was necessary to measure the compressive response of the rubber pad used in the experiments to take it into account in the simulations. To do so, the projectile, with the rubber pad, and the assembly of the mid-span roller and load cell were loaded in compression using a screw-driven test machine. The quasi-static compressive response measured at a strain-rate  $\dot{\epsilon} = 10^{-3} \text{ s}^{-1}$  is shown in Fig. 5.12(a), where the contact pressure is plotted as a function of the compressive displacement. The compressive displacement was measured using a laser extensometer whereas the contact force was measured using the load cell of the testing machine. The contact pressure was calculated by dividing the contact force by the contact area of the load cell ( $127 \text{ mm}^2$ ).

The loading and unloading compressive responses of the rubber pad are given in Fig. 5.12(a); the rubber pad exhibit a pronounced hysteresis. For a compressive displacement inferior to 1 mm, the response of the rubber pad is approximately linear with a stiffness of 2.5 kN/mm. This stiffness is significantly softer than that of the piezoelectric load cell which has a stiffness of 1050 kN/mm according to the data sheet of the manufacturer.

The rubber pad used in the experiments was not modelled as a separate part in the FE simulations. Instead, the “softened” contact option of Abaqus was used. According to the documentation this contact option can be used to model a soft, thin layer on one or both contact surfaces. The contact pressure versus penetration relationship was tabulated in Abaqus from the loading part of the measured

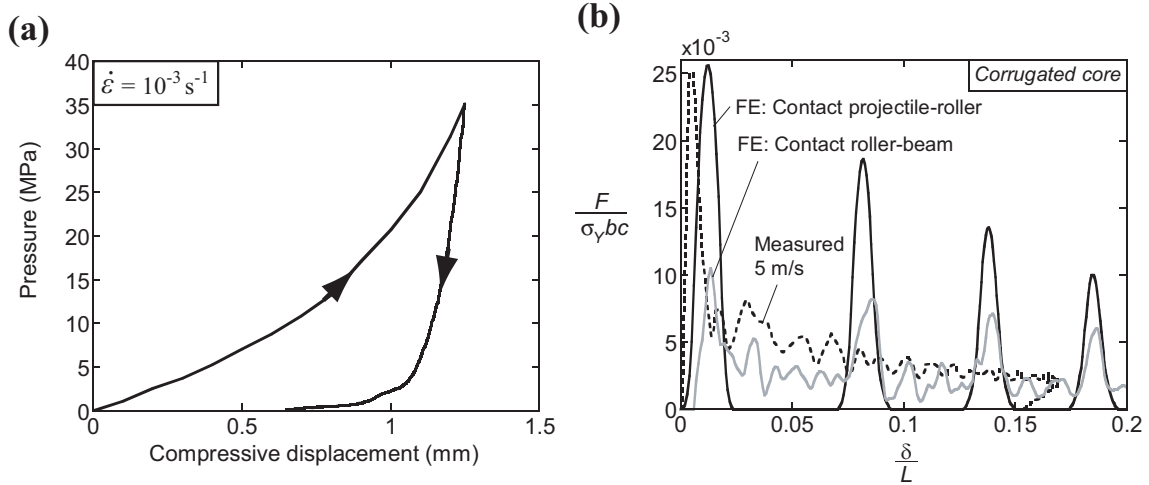


**Figure 5.12:** (a) Measured quasi-static ( $\dot{\epsilon} = 10^{-3} \text{ s}^{-1}$ ) compressive response of the rubber pad used in the drop weight experiments. (b) Comparison between the measured and simulated 5 m/s responses of a simply supported beam with a corrugated core. The measured response is reproduced from Fig. 5.5(a) whereas the simulations are using the data shown in part (a) to model the contact between the projectile and the mid-span roller.

compressive response of the rubber pad shown in Fig. 5.12(a). This change in the contact option was the only modification done to the FE model detailed above in Section 5.A.1.

The results predicted by the FE method using the softened contact option are presented in Fig. 5.12(b) for a simply supported beam with a corrugated core. Predictions of the contact force are given for (i) the contact between the projectile and mid-span roller (where the rubber pad is) and (ii) the contact between the mid-span roller and the beam. In addition, the measured response at 5 m/s, presented in Fig. 5.5(a), is reproduced in Fig. 5.12(b) for comparison purposes. The peak load of the simulated contact force, between the projectile and the mid-span roller, is in satisfactory agreement with measured peak load. However, there is an important discrepancy between the simulated and measured post-peak responses. This is due to the fact that the simulations assume the contact response to be perfectly elastic and does not take into account the pronounced hysteresis of the rubber pad as observed in Fig. 5.12(a). Also, this analysis neglects the strain-rate sensitivity of the rubber, which is likely to be stiffer at 5 m/s than under quasi-static loading. Nevertheless, the simulations shown in Fig. 5.12(b) give a valuable insight into the experiments; the results indicate that the peak load measured at 5 m/s is influenced by (i) the mass of the mid-span roller and load cell and (ii) the damping of the rubber pad.

## 5.B Analytical prediction of the contact force

An analytical model is presented here to estimate the contact force between the projectile and the assembly of the mid-span roller and load cell. The model is illustrated in Fig. 5.13 and has the following elements:

1. a rigid projectile of mass  $M$ ,
2. a spring of stiffness  $k$  representing the rubber pad used in the experiments and
3. a second rigid body of mass  $m$  representing the assembly of the mid-span roller and load cell.

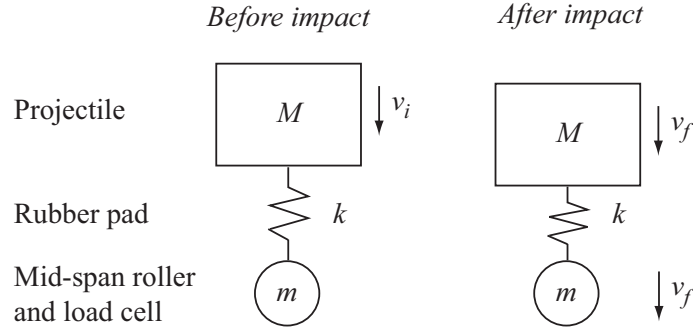


**Figure 5.13:** Analytical model to predict the contact force between the projectile and the assembly of the mid-span roller and load cell.

The projectile has a given initial velocity  $v_i$  before hitting the assembly of the mid-span roller and load cell, which is at rest before the collision. After the collision, the two bodies are assumed to adhere to each other and travel together with a common velocity  $v_f$ . Conservation of momentum provides that:

$$v_f = \frac{Mv_i}{M + m} \quad . \quad (5.2)$$

The change in kinetic energy is assumed to compress the spring by a displacement  $u$ , which generates a force  $P = ku$ . Hence, conservation of energy dictates that:

$$\frac{Mv_i^2}{2} = \frac{P^2}{2k} + \frac{(M + m)v_f^2}{2} \quad . \quad (5.3)$$

Substituting Eq. (5.2) in Eq. (5.3) and rearranging gives:

$$P = \sqrt{\frac{kMmv_i^2}{M + m}} \quad . \quad (5.4)$$

This equation provides an estimation of the force  $P$  generated during the collision of the projectile and the assembly of the mid-span roller and load cell. It is insightful to estimate the value of  $P$  for parameters used in the experimental study. First, the stiffness of the rubber pad can be estimated to  $k = 2.5$  kN/mm from the measured compressive response shown previously in Fig. 5.12(a). Tests on simply supported beams were done with a projectile of mass  $M = 2$  kg and an impact velocity  $v_i = 5$  m/s. Finally, the assembly of the steel mid-span roller and load cell has a combined mass  $m = 0.146$  kg. Using these values, the contact force  $P = 2.9$  kN which corresponds to  $P/(\sigma_Y bc) = 0.0119$ . Replacing the steel mid-span roller by an aluminium roller reduces  $m$  to 0.064 kg, and for this new value of  $m$  the force  $P = 2$  kN, which corresponds to  $P/(\sigma_Y bc) = 0.008$ . These values of  $P$  are significantly lower than the measured peak loads, see Fig. 5.6, because the finite mass and stiffness of the sandwich beam tested is not included in this analytical model. However, this simple model is able to capture the strong influence of the mass  $m$  upon the contact force  $P$  generated during the collision of the projectile and the assembly of the mid-span roller and load cell.

# Chapter 6

## Dynamic indentation of prismatic sandwich panels

### Summary

The dynamic indentation response of stainless steel sandwich panels with a corrugated core or a Y-frame core was simulated using the finite element method. The effect of the loading velocity upon the indentation response is assessed by indenting the panels with a constant velocity ranging from quasi-static loading to 100 m/s. The influence of the indenter's geometry is also addressed by considering two different indenters: a flat-bottomed indenter and a cylindrical roller. The predictions indicated that the indentation load applied to the front face is equal to the load transmitted to the back face for velocities below approximately 10 m/s. For such low velocities, inertia stabilisation effects were found to increase the dynamic initial peak load above its quasi-static value. This strengthening effect was more important for the corrugated core than for the Y-frame core. For loading velocities greater than 10 m/s, the indentation force applied to the front face exceeded the force transmitted to the back face due to wave propagation effects. The dynamic indentation response was found to be very sensitive to the size of the flat-bottomed indenter; increasing its width increased the importance of both inertia stabilisation and wave propagation effects. In contrast, increasing the roller diameter had a much smaller effect on the dynamic indentation response. Finally, the simulations indicated that material strain-rate sensitivity has only a minor effect on the dynamic indentation response of both lab-scale and full-scale sandwich panels.

### 6.1 Introduction

The quasi-static three-point bending response of sandwich beams with a corrugated core or a Y-frame core was investigated in Chapter 4 of this thesis and two collapse mechanisms were identified: short beams were found to collapse by indentation whereas long beams failed by Brazier plastic buckling. Beams that failed quasi-statically by indentation were also found to collapse by indentation when they were subjected to an impact at 5 m/s, recall Chapter 5. In contrast, beams that collapsed quasi-statically by Brazier plastic buckling were found to fail by indentation at 5 m/s. These findings obtained in the laboratory are in line with the results of full-scale collision tests performed on the Y-frame sandwich hull; these experiments revealed that the structure deforms by indentation, with the inner hull undergoing negligible plastic deformation (Wevers and Vredeveldt, 1999). Hence, these lab-scale and full-scale results indicate that the deformation of a sandwich structure during a ship collision at 5 m/s is adequately represented by its indentation response. However, little is known about the effect of the loading velocity upon the dynamic indentation response of the structure; is the response at 1 m/s different from the one at 10 m/s?

The work of Tilbrook et al. (2007) can help to answer this question. The authors investigated the dynamic compressive response of corrugated and Y-frame sandwich cores at velocities ranging from 1-100 m/s. Two dynamic strengthening mechanisms were identified: (i) inertia stabilisation of the core members against buckling and (ii) wave propagation effects. The first mechanism was predominant at low crushing velocities and the second one was active for high velocities. What will be the importance of those dynamic strengthening effects when the loading conditions are changed from uniform compression to localised indentation? In this study, the finite element method is used to address this question for both sandwich panels with a corrugated core or a Y-frame core.

The objective of this chapter is to analyse the sensitivity of the indentation response to (i) the loading velocity, (ii) the shape of the indenter and (iii) the size of the indenter. Velocities varying from quasi-static loading to 100 m/s are considered. Ship collisions are likely to occur below 10 m/s, but the range from 10-100 m/s is also examined for two reasons: (i) it is of interest for other industrial applications such as automotive or rail transport and (ii) to allow comparison with the results of Tilbrook et al. (2007) which covered velocities ranging from 1-100 m/s. Two shapes of indenters are used in this study: a flat-bottomed indenter and a cylindrical roller.

For each indenter, two different sizes are considered. Note that if the size of the indenter is infinitely large, the panel is loaded in uniform compression. As uniform compression represents the limiting case in this study, the results of Tilbrook et al. (2007) are reviewed below.

### 6.1.1 Review of the dynamic uniform compressive response

The dynamic compressive response of corrugated and Y-frame cores was studied experimentally and numerically by Tilbrook et al. (2007). Their simulations were repeated as part of this study and the key results are presented below. For a complete discussion of the subject, the reader is referred to Tilbrook et al. (2007).

The boundary conditions used to simulate the dynamic uniform compressive response are shown in Fig. 6.1(a). All degrees-of-freedom are constrained to zero on the back face whereas the front face has a constant downward velocity  $V_0$  ranging from 1 to 100 m/s. To simulate the quasi-static compressive response, the velocity  $V_0$  was replaced by a prescribed downward displacement  $\delta$ . A complete description of the finite element model is given in Appendix 6.A.

The quasi-static and 10 m/s compressive responses are shown in Fig. 6.2(a) for the corrugated core and in Fig. 6.2(b) for the Y-frame core. The nominal compressive stress is plotted as a function of the nominal compressive strain  $\delta/c$ , where the core compression is  $\delta$  and the core thickness is  $c = 22$  mm. The nominal compressive stress on the front face is defined as:

$$\sigma_f = \frac{F_f}{bL} \quad , \quad (6.1)$$

and that on the back face is:

$$\sigma_b = \frac{F_b}{bL} \quad , \quad (6.2)$$

where the width of the panel is  $b = 26.5$  mm, the length of the panel (in the prismatic direction  $x_3$ ) is  $L$  and the normal component of the front face and back face reaction forces are  $F_f$  and  $F_b$ , respectively.

The quasi-static and dynamic compressive responses are both characterised by an initial elastic regime up to a peak stress  $\sigma_{pk}$ , followed by a steeply softening response

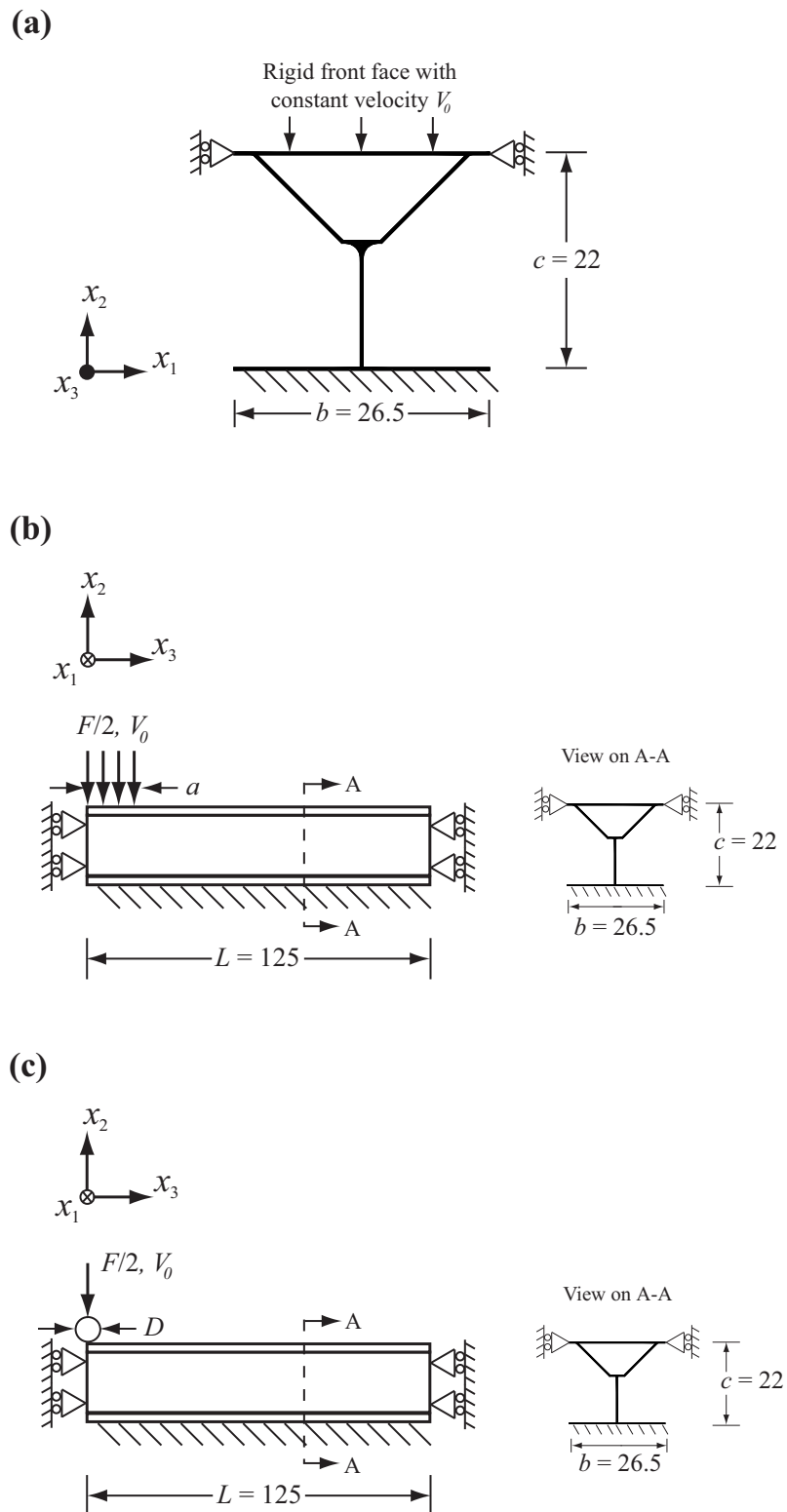


**Figure 6.1:** Finite element models used to simulate (a) uniform compression, (b) indentation by a flat-bottomed indenter and (c) indentation by a cylindrical roller. The models are shown for a sandwich panel with a Y-frame core. All dimensions are in mm.

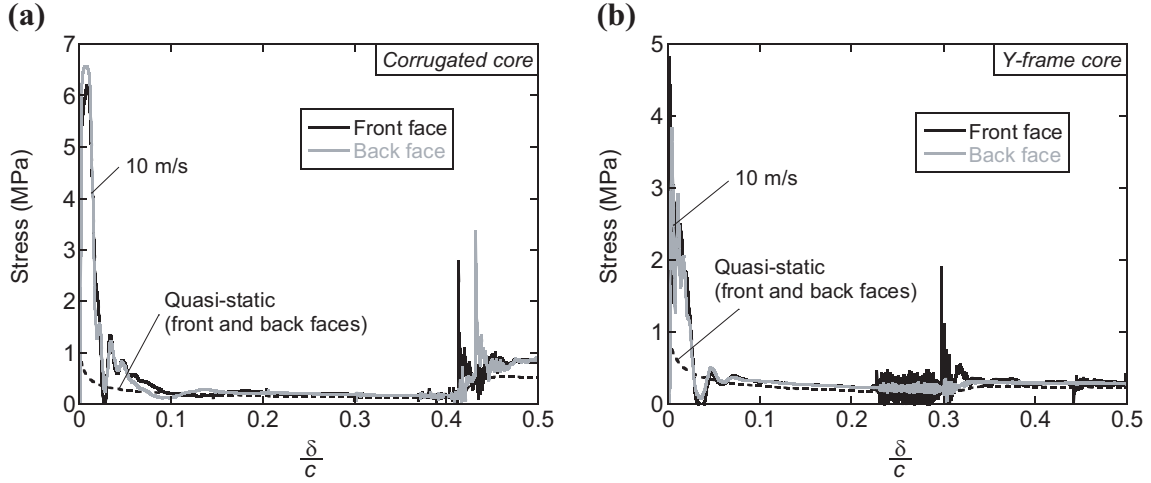


**Figure 6.2:** Uniform compressive responses of sandwich panels with (a) a corrugated core and (b) a Y-frame core. Results are given for quasi-static loading and for crushing at 10 m/s. These simulations were re-executed based on previous work done by Tilbrook et al. (2007).

due to buckling of the core members. Both core topologies have a quasi-static peak stress  $\sigma_{pk}^{qs} \approx 1$  MPa which corresponds to the elastic buckling strength of the core members. Increasing the loading velocity to 10 m/s, increases significantly the peak stress, and this increase is more important for the corrugated core than for the Y-frame core.

The effect of velocity on the dynamic compressive peak stress  $\sigma_{pk}^d$  is shown in Fig. 6.3(a), where the results are normalised by the quasi-static compressive peak stress  $\sigma_{pk}^{qs}$ . Likewise, the dynamic average stress  $\sigma_{av}^d$ , normalised by the quasi-static average stress  $\sigma_{av}^{qs}$ , is plotted in Fig. 6.3(b) as a function of velocity. The average stress, up to a nominal core compression of 20%, is defined as:

$$\sigma_{av} = \int_0^{0.2} \sigma d(\delta/c) \quad , \quad (6.3)$$

and gives a measure of the core crushing resistance after the peak stress. The results in Fig. 6.3 are given for both corrugated and Y-frame cores and for both stresses on the front and back faces.

Two regimes can be identified in Fig. 6.3:

1. At low crushing velocities,  $V_0 \leq 10$  m/s, the front and back face stresses are approximately equal and increase with increasing velocity. The dynamic stresses are higher than their corresponding quasi-static values and this strengthening

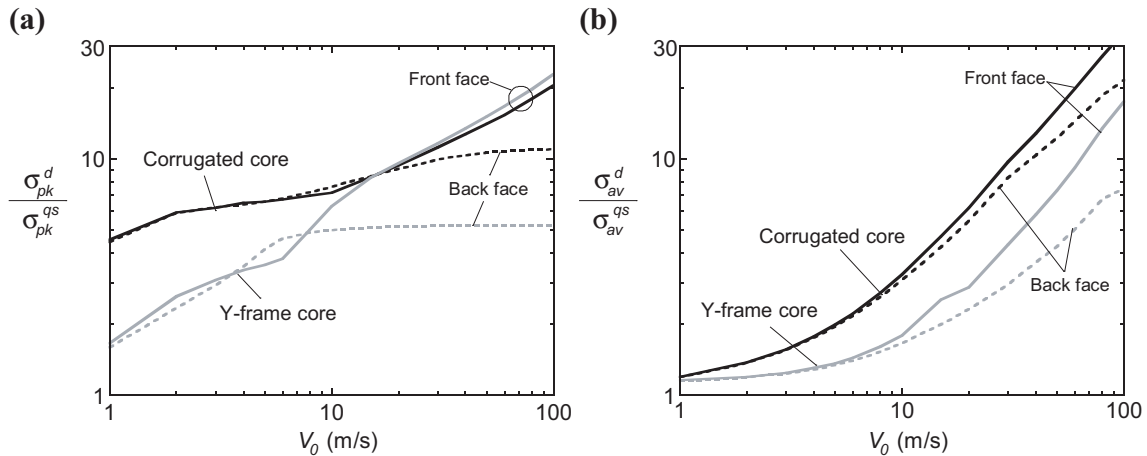


**Figure 6.3:** (a) The normalised peak stress and (b) the normalised average stress up to  $\delta/c = 0.2$  for corrugated and Y-frame sandwich cores crushed at a constant velocity  $V_0$ . Those simulations were re-executed based on previous work done by Tilbrook et al. (2007).

effect is mainly due to inertia stabilisation of the core members against elastic buckling. In line with the results of Calladine and English (1984), inertia effects are more important for the stretching-dominated corrugated core than for the bending-dominated Y-frame core. In addition, inertia effects have a greater influence on the peak stress (Fig. 6.3(a)) than on the average stress (Fig. 6.3(b)).

- For velocities greater than approximately 10 m/s, the peak stress on the back face is roughly constant whereas the peak stress on the front face increases with increasing velocity. This indicates that the peak stress is governed by plastic wave propagation. Note that the normalised peak stress on the front face is relatively insensitive to the core topology. In contrast, the normalised peak stress transmitted to the back face is less for the Y-frame core than for the corrugated core.

In this chapter, the dynamic indentation response will be simulated for a flat-bottomed indenter of width  $2a$  and a cylindrical roller of diameter  $D$  as shown in Fig. 6.1(b) and (c), respectively. The results presented in this section for dynamic uniform compression represent the case of an infinitely large indenter with  $a = L$  or  $D \rightarrow \infty$ . What will be the influence of decreasing  $a$  and  $D$  on the results shown in Fig. 6.3? This question will be addressed for both corrugated and Y-frame cores.

### 6.1.2 Scope of study

First, a description of the finite element models used to simulate the dynamic indentation response is given in Section 6.2. Second, the dynamic indentation responses and corresponding deformation modes are presented for selected loading velocities. Finally, the effects of velocity, indenter size and material rate-sensitivity upon the dynamic indentation response are considered in turn.

## 6.2 Finite element models

The commercial finite element code Abaqus (version 6.10) was used to simulate the quasi-static and dynamic indentation responses of sandwich panels with a corrugated core or a Y-frame core. The cross-sectional dimensions of each core are given in Fig. 6.4. Both cores have a relative density  $\bar{\rho} = 0.025$  and are approximately 1:20 scale models of the cores used in a ship hull. Both core topologies have a unit cell of width  $b = 26.5$  mm and a core thickness  $c = 22$  mm. The core members and the face-sheets have a thickness  $t = 0.3$  mm. The core is assumed to be perfectly bonded to the face-sheets to produce a sandwich panel of half-length  $L = 125$  mm, see Fig. 6.1(b,c). Four noded linear shell elements with reduced integration (S4R in Abaqus notation) were used to discretise the sandwich panels with an average mesh size of 0.5 mm. A convergence study indicated that further refinement of the mesh did not improve significantly the results.

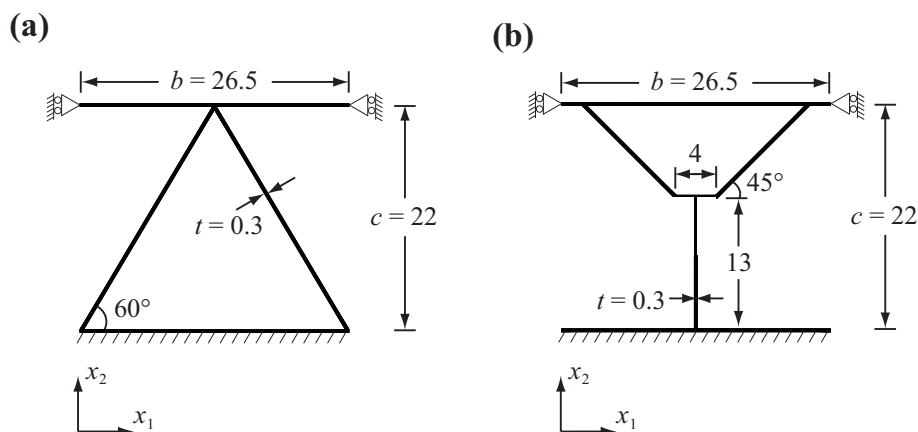


**Figure 6.4:** Cross-sectional dimensions of the sandwich panels: (a) corrugated core and (b) Y-frame core. All dimensions in mm.

The boundary conditions were applied as follows. All degrees-of-freedom were con-

strained to zero on the back face of the panel, see Fig. 6.1(b,c). Symmetric boundary conditions were applied underneath the indenter ( $x_3 = 0$ ) and at the right end of the panel ( $x_3 = L$ ). Similarly, symmetric boundary conditions were also applied on both sides of the panel unit cell, see Fig. 6.4.

The indentation response of the sandwich panels was simulated for two different indenters:

1. A flat-bottomed indenter of width  $2a$ , see Fig. 6.1(b). To simplify the analysis, this loading condition was achieved by prescribing a constant velocity  $V_0$  over a width  $a$  of the front face. Two values of width were considered,  $2a = 12.5$  and  $50$  mm corresponding to  $a/L$  ratios of  $0.05$  and  $0.2$ , respectively.
2. A cylindrical roller of diameter  $D$ , as shown in Fig. 6.1(c). The roller was modelled as a rigid body in the simulations and had a prescribed constant velocity  $V_0$ . Calculations were performed for two roller diameters,  $D = 9$  and  $66$  mm corresponding to  $D/c$  ratios of  $0.41$  and  $3$ , respectively.

The interaction between the roller and the front face, and between all potentially contacting surfaces of the sandwich panel, was modelled as a hard frictionless contact. Numerical experimentation revealed that the indentation response is insensitive to the coefficient of friction used in the contact properties.

The dynamic indentation response was simulated for velocities  $V_0$  ranging from  $1$  to  $100$  m/s. Those simulations were performed using the explicit solver of Abaqus. On the other hand, the implicit solver of Abaqus was used to predict the quasi-static indentation response. For quasi-static simulations, the velocity  $V_0$  was replaced by a prescribed displacement  $\delta$ .

### 6.2.1 Geometric imperfections

A geometric imperfection was introduced in both core topologies. The shape of the imperfection had the form of the first mode of elastic buckling and the amplitude was set equal to the sheet thickness  $t = 0.3$  mm. The elastic buckling calculations were performed under uniform compression and the face-sheets were considered rigid, such that the imperfection affected the core only and not the face-sheets. The same geometric imperfection was used by Tilbrook et al. (2007) to simulate the dynamic compressive responses of corrugated and Y-frame cores, and their predictions were found to be in good agreement with experiments. In addition, Tilbrook et al. (2007)

mentioned that the dynamic stress versus strain response is relatively imperfection-insensitive, but the deformed shape varies with the choice of imperfection.

## 6.2.2 Material properties

The material properties were chosen to be representative of AISI 304 stainless steel. The material was modelled as a rate-dependent J2-flow theory solid with a density  $\rho = 7900 \text{ kg/m}^3$ , a Young's modulus  $E = 210 \text{ GPa}$ , a Poisson's ratio  $\nu = 0.3$  and a quasi-static ( $10^{-3} \text{ s}^{-1}$ ) yield strength  $\sigma_Y = 210 \text{ MPa}$ . The hardening plastic behaviour, at strain-rates in the range  $10^{-3} \text{ s}^{-1} \leq \dot{\epsilon} \leq 10^4 \text{ s}^{-1}$ , was tabulated in Abaqus using the prescription described previously in Section 5.2.3 and employing the data shown in Fig. 5.4(a).

## 6.3 Results

The results of the finite element predictions are presented as follows. First, the dynamic indentation responses and the deformed meshes of both corrugated and Y-frame sandwich panels are presented for selected velocities. Second, the influence of the loading velocity and of the indenter geometry upon the initial peak load and the average indentation load is examined. Third, the load transmitted to the back face of the panel is analysed in details and finally, the influence of material strain-rate sensitivity upon the dynamic indentation response is assessed.

### 6.3.1 Indentation responses

The responses of sandwich panels indented by (i) a flat-bottomed indenter of normalised width  $a/L = 0.05$  and (ii) a roller of normalised diameter  $D/c = 0.41$  are shown in Fig. 6.5 and 6.6, respectively. Results are given for both corrugated and Y-frame cores. The responses are shown for selected velocities  $V_0$ : the quasi-static and 1 m/s responses are both shown in parts (a,b); the responses at 10 m/s are shown in parts (c,d) and the responses at 100 m/s are given in parts (e,f). In each plot, the indentation depth  $\delta$  is normalised by the core thickness  $c = 22 \text{ mm}$  whereas the load  $F$  is normalised by  $\sigma_Y bc$ , where the quasi-static yield strength is  $\sigma_Y = 210 \text{ MPa}$  and the width of the panel is  $b = 26.5 \text{ mm}$ . Both the load applied to the front

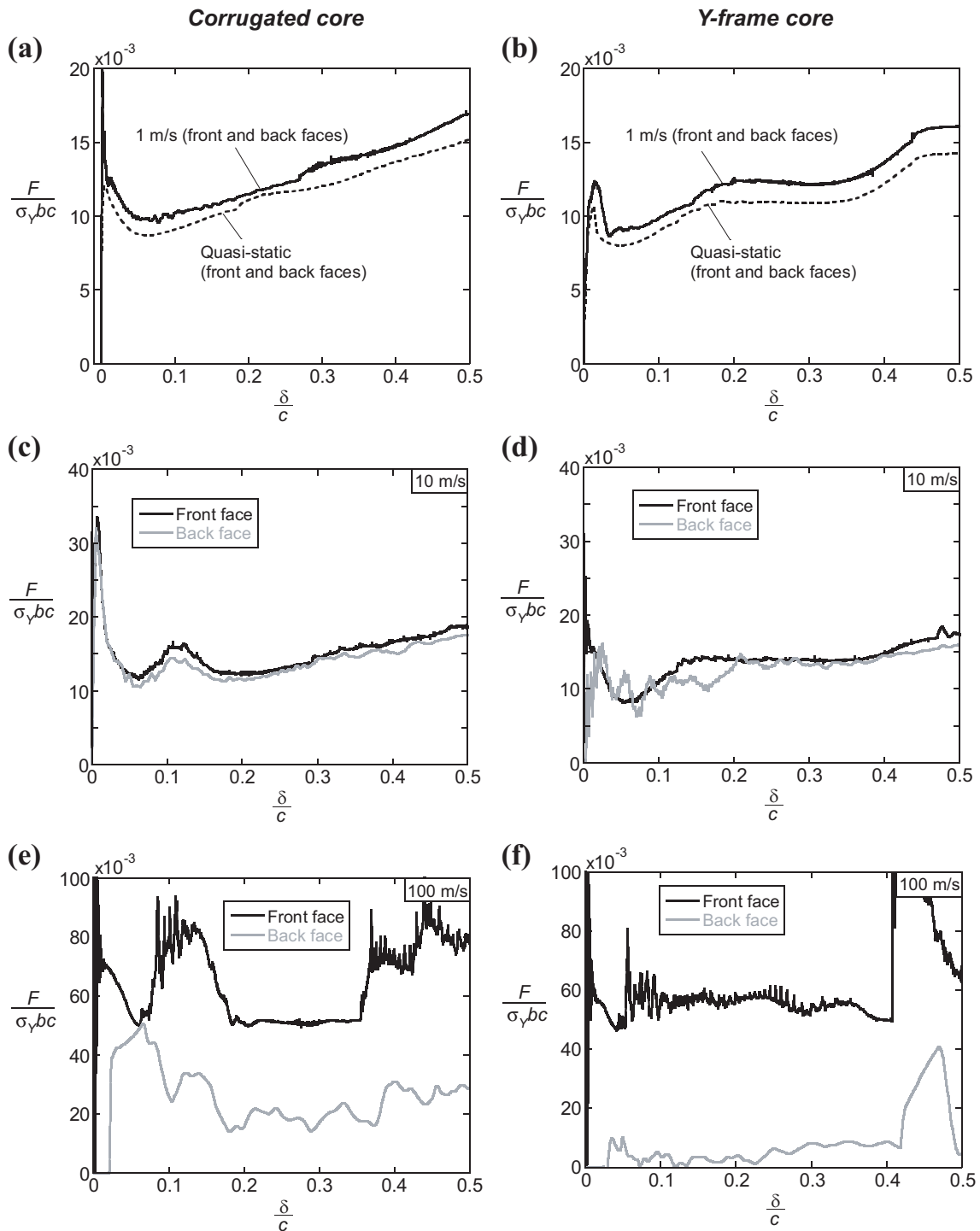
face and the load transmitted to the back face of the sandwich panel are plotted in Fig. 6.5 and 6.6. The total back face force is the summation of the normal reaction force for all nodes on the back face.

At low velocities,  $V_0 \leq 10$  m/s, the forces on the front and back faces are approximately equal over the entire deformation history, see Fig. 6.5(a-d) and 6.6(a-d). The indentation response is characterised by an elastic regime up to an initial peak load  $F_{pk}$ . Subsequently, the panel softens and then re-hardens due to longitudinal stretching of the front face. The initial peak load is sensitive to the core topology; sandwich panels with a corrugated core are at least 12% stronger than those with a Y-frame core. The initial peak load is also sensitive to the loading velocity;  $F_{pk}$  increases with increasing  $V_0$ .

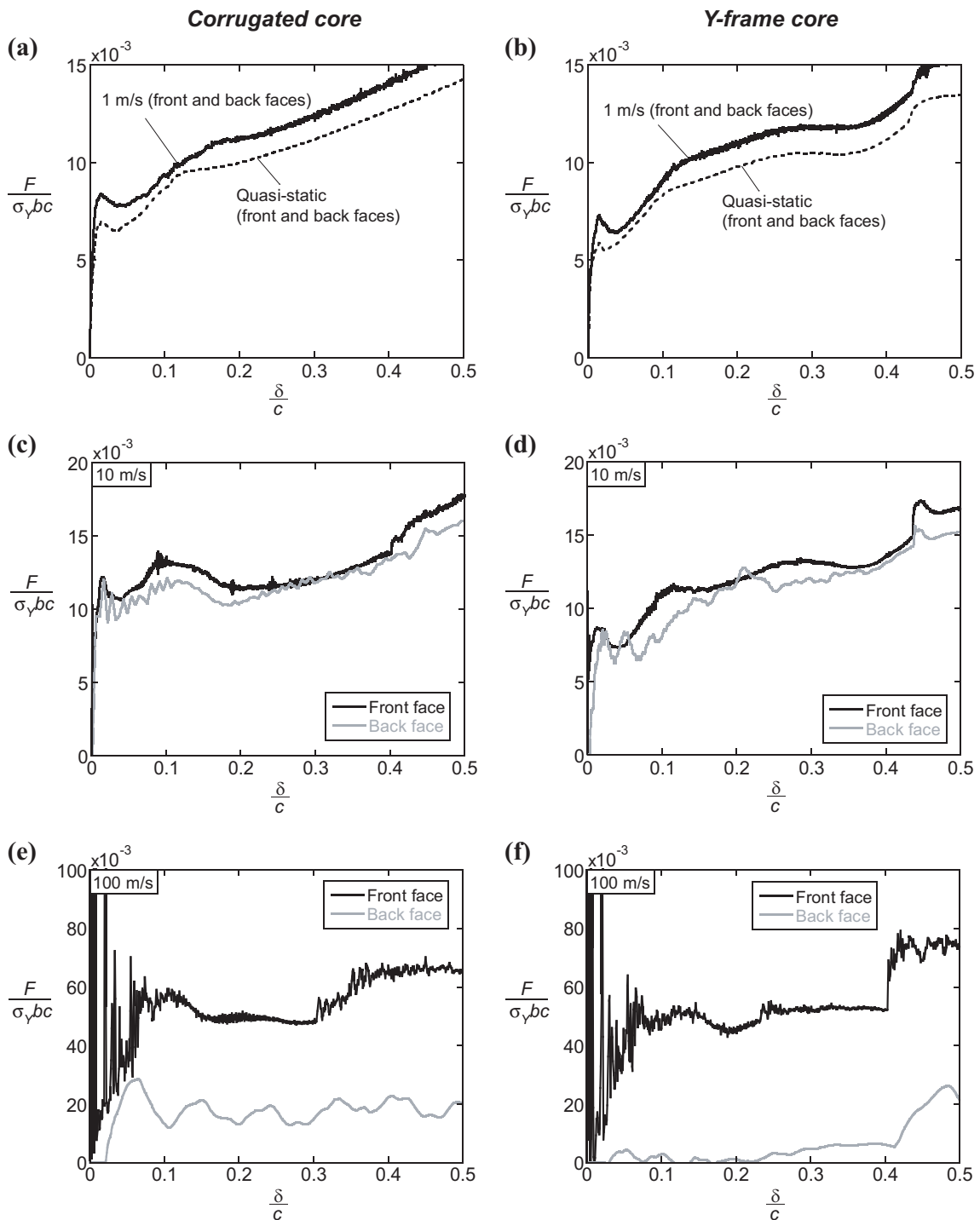
When the velocity is increased to 100 m/s, the force on the front face largely exceeds the force transmitted to the back face over the entire deformation history, see Fig. 6.5(e,f) and 6.6(e,f). At such a high velocity, the core topology has a minimal influence on the force applied to the front face, but it has a strong effect on the load transmitted to the back face; the force on the back face is significantly higher for the corrugated core than for the Y-frame core. Note that for panels indented by a cylindrical roller, the force on the front face is particularly noisy at the beginning of the response ( $\delta/c < 0.1$ ), see Fig. 6.6(e,f). This is due to the fact that the roller and front face come in contact and then separate on a few occasions before a permanent contact is established. The contact noise is significantly less important at lower velocities; see for example the responses at 10 m/s in Fig. 6.6(c,d).

### 6.3.2 Deformed meshes

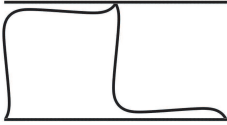
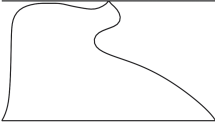
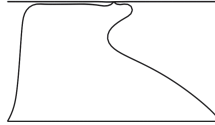
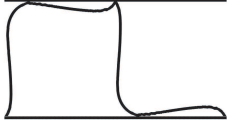
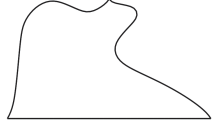
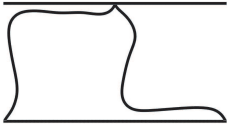
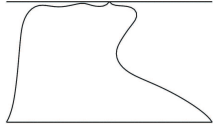
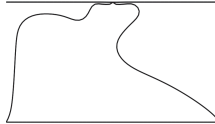
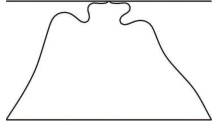
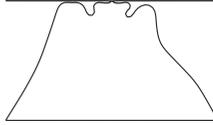
The deformed meshes, associated with the responses shown in Fig. 6.5 and 6.6, are given in Table 6.1 for panels with a corrugated core and in Table 6.2 for panels with a Y-frame core. In each table, the deformed meshes of panels indented by a flat-bottomed indenter ( $a/L = 0.05$ ) and a cylindrical roller ( $D/c = 0.41$ ) are shown at selected velocities. The deformed cross-section underneath the indenter is shown along with a side view of the sandwich panel. For comparison purposes, the deformed meshes obtained under uniform compression are also included. All images are shown for  $\delta/c = 0.35$ .



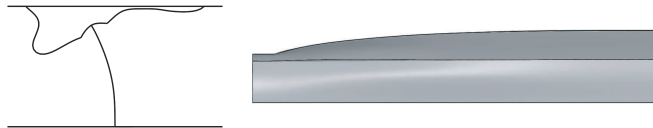
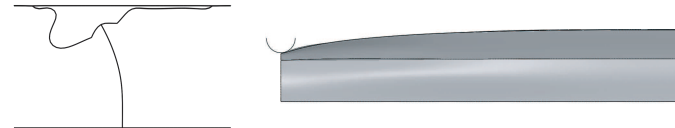
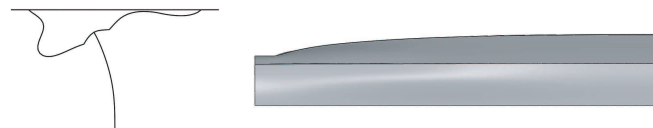
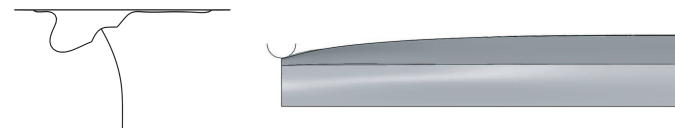
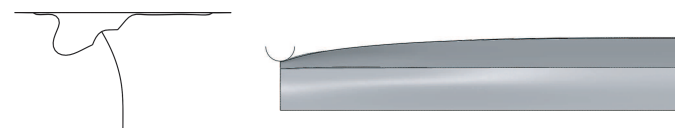
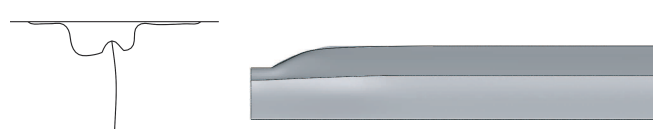
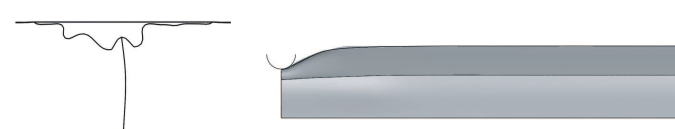
**Figure 6.5:** Responses of sandwich panels indented by a flat-bottomed indenter of normalised width  $a/L = 0.05$ . Results are shown at selected velocities: quasi-static and 1 m/s for (a) corrugated core and (b) Y-frame core; 10 m/s for (c) corrugated core and (d) Y-frame core and 100 m/s for (e) corrugated core and (f) Y-frame core.



**Figure 6.6:** Responses of sandwich panels indented by a cylindrical roller of normalised diameter  $D/c = 0.41$ . Results are shown at selected velocities: quasi-static and 1 m/s for (a) corrugated core and (b) Y-frame core; 10 m/s for (c) corrugated core and (d) Y-frame core and 100 m/s for (e) corrugated core and (f) Y-frame core.

$V_0$	Uniform compression	Indentation $a/L = 0.05$		Indentation $D/c = 0.41$	
Quasi-static					
1 m/s					
10 m/s					
100 m/s					

**Table 6.1:** Deformed meshes of sandwich panels with a corrugated core shown at selected velocities. The results are given for uniform compression, indentation by a flat-bottomed indenter of normalised width  $a/L = 0.05$  and indentation by a cylindrical roller of normalised diameter  $D/c = 0.41$ . For indentation, the cross-section underneath the indenter is shown along with a side view of the panel. All images are given for  $\delta/c = 0.35$ .

$V_0$	Uniform compression	Indentation $a/L = 0.05$		Indentation $D/c = 0.41$	
Quasi-static					
1 m/s					
10 m/s					
100 m/s					

**Table 6.2:** Deformed meshes of sandwich panels with a Y-frame core shown at selected velocities. The results are given for uniform compression, indentation by a flat-bottomed indenter of normalised width  $a/L = 0.05$  and indentation by a cylindrical roller of normalised diameter  $D/c = 0.41$ . For indentation, the cross-section underneath the indenter is shown along with a side view of the panel. All images are given for  $\delta/c = 0.35$ .

First, consider the influence of velocity on the deformation modes. The deformed meshes at 1 and 10 m/s are very similar to those obtained quasi-statically. However, the deformed meshes at 100 m/s are considerably different from the quasi-static results; deformation is localised near the front face of the panel. This deformation mode is indicative of plastic wave propagation effects and it is also consistent with the indentation responses presented above; for  $V_0 = 100$  m/s, the force applied on the front face exceeds the force transmitted to the back face, recall Fig. 6.5(e,f) and 6.6(e,f).

Second, consider the effect of the indenter geometry upon the deformation modes. The deformed cross-sections of panels indented by a flat-bottomed indenter ( $a/L = 0.05$ ) are very similar to those of panels indented by a cylindrical roller ( $D/c = 0.41$ ). Furthermore, the deformed cross-sections obtained for localised indentation (for both the flat-bottomed indenter and the cylindrical roller) are comparable to those obtained for uniform compression. These observations hold true for both corrugated and Y-frame core topologies.

### 6.3.3 Influence of velocity

The effect of velocity upon the initial peak load is shown in Fig. 6.7(a) for panels indented by a flat-bottomed indenter with  $a/L = 0.05$ , and in Fig. 6.8(a) for panels indented a cylindrical roller with  $D/c = 0.41$ . In both figures, the dynamic initial peak load  $F_{pk}^d$  is normalised by the quasi-static initial peak load  $F_{pk}^{qs}$ . The results are plotted for velocities ranging from 1 to 30 m/s only because it is difficult to evaluate accurately the initial peak load at higher velocities, see for example the indentation responses at 100 m/s in Fig. 6.6(e,f).

The average load is also plotted as a function of velocity in part (b) of Fig. 6.7 and 6.8. Similarly to the average stress defined in Eq. (6.3), the average load up to  $\delta/c = 0.2$  is defined as:

$$F_{av} = \int_0^{0.2} F d(\delta/c) \quad . \quad (6.4)$$

The dynamic average load  $F_{av}^d$  is normalised by the quasi-static average load  $F_{av}^{qs}$  in Fig. 6.7 and 6.8. In each plot, the results are given for both the corrugated core and the Y-frame core and for both forces on the front face and on the back face.

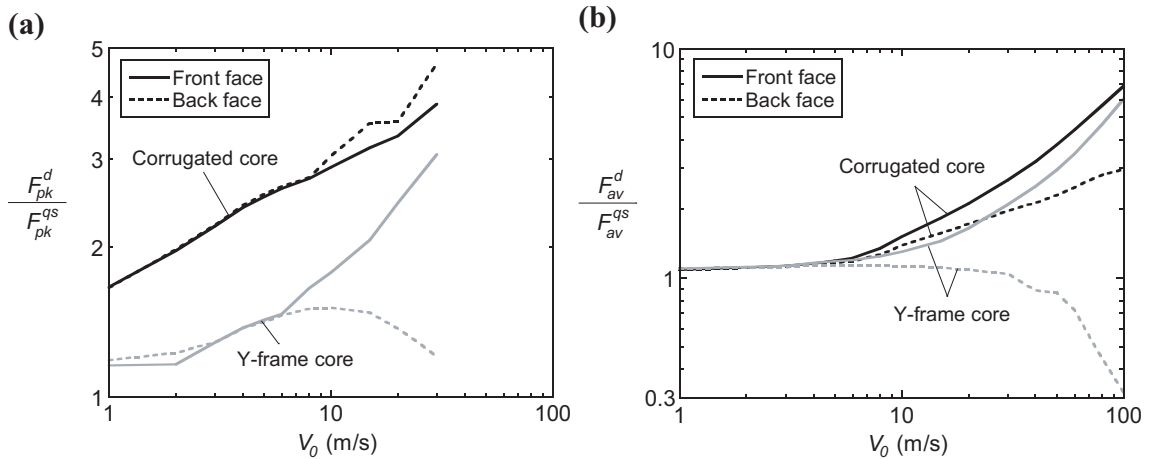


**Figure 6.7:** (a) The normalised initial peak load and (b) the normalised average load up to  $\delta/c = 0.2$  for corrugated and Y-frame sandwich panels indented at a constant velocity  $V_0$  by a flat-bottomed indenter of normalised width  $a/L = 0.05$ .

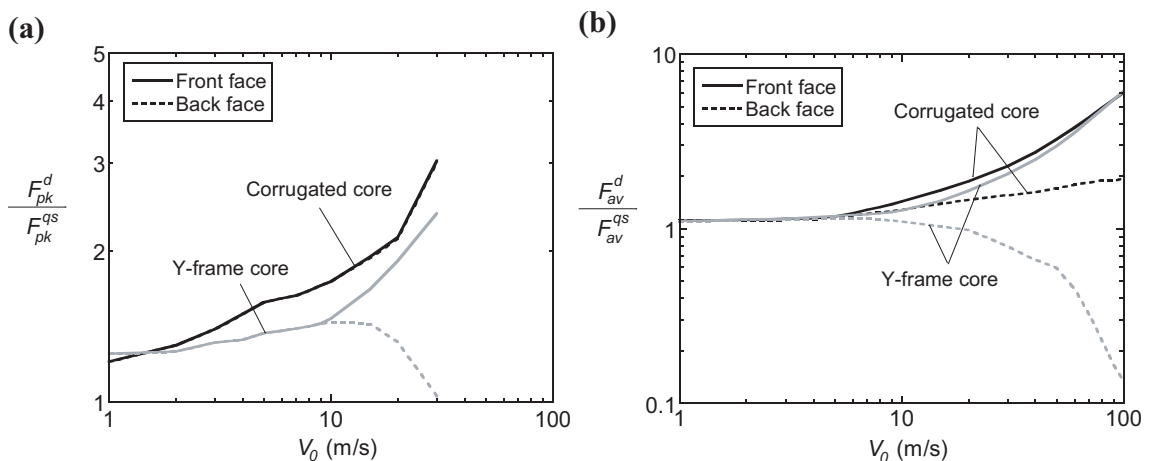


**Figure 6.8:** (a) The normalised initial peak load and (b) the normalised average load up to  $\delta/c = 0.2$  for corrugated and Y-frame sandwich panels indented at a constant velocity  $V_0$  by a cylindrical roller of normalised diameter  $D/c = 0.41$ .

The normalised initial peak load and the normalised average load on the front and back faces are approximately equal for velocities ranging from 1 to 10 m/s. Even at such low velocities, the dynamic initial peak load is greater than its quasi-static value, and increases slightly with increasing velocity due to inertia stabilisation effects. Inertia effects are more important for the corrugated core than for the Y-frame core, see Fig. 6.7(a). In addition, the normalised initial peak loads of panels indented by a flat-bottomed indenter (Fig. 6.7(a)) display a greater sensitivity to velocity than those indented by a cylindrical roller (Fig. 6.8(a)). In contrast, inertia effects have no influence on the normalised average load;  $F_{av}^d/F_{av}^{qs}$  is relatively insensitive to velocity and to the choice of core topology for indentation velocities

between 1 and 10 m/s.

The average force applied on the front face exceeds the force transmitted to the back face when the velocity is greater than roughly 10 m/s, see Fig. 6.7(b) and 6.8(b), and this is due to wave propagation effects. For velocities between 10 and 100 m/s, the normalised average load on the front face increases with increasing velocity and display a mild sensitivity to the core topology;  $F_{av}^d/F_{av}^{qs}$  is slightly higher for the corrugated core than for the Y-frame core. In contrast, the normalised average load on the back face is highly sensitivity to the choice of core; the load transmitted to the back face for the corrugated core significantly exceeds that for the Y-frame core. In fact, the normalised average load transmitted to the back face for the Y-frame core decreases with increasing velocity. To explain this result, the force distribution on the back face will be analysed in Section 6.3.5.

### 6.3.4 Influence of indenter size

The effect of the indenter size on the normalised initial peak load and on the normalised average load is shown in Fig. 6.9 for panels indented by a flat-bottomed indenter and in Fig. 6.10 for panels indented by a cylindrical roller. In each figure, the normalised initial peak loads are shown in parts (a) and (b) for the corrugated core and the Y-frame core, respectively. Likewise, the normalised average loads are given in part (c) for the corrugated core and in part (d) for the Y-frame core. In each plot, the results are given for two values of indenter size and for uniform compression.

It is clear from Fig. 6.9 and 6.10 that the dynamic uniform compression response is more sensitive to velocity than the localised indentation response; values of  $F_{pk}^d/F_{pk}^{qs}$  and  $F_{av}^d/F_{av}^{qs}$  for uniform compression always exceed those obtained for indentation. The width of the flat-bottomed indenter has a strong influence on the normalised initial peak load; increasing  $a/L$  from 0.05 to 0.20 increases  $F_{pk}^d/F_{pk}^{qs}$  by a factor of approximately two for both the corrugated core and the Y-frame core. In contrast, the roller diameter has only a mild effect on the normalised initial peak loads; increasing  $D/c$  from 0.41 to 3 increases  $F_{pk}^d/F_{pk}^{qs}$  by 45% at the most.

The normalised average loads are less sensitive to the size of the indenter than the normalised initial peak loads. Note that the normalised average load applied to the front face starts to exceed the normalised average load transmitted to the back face at approximately 10 m/s in all cases considered. Hence, the velocity at which the

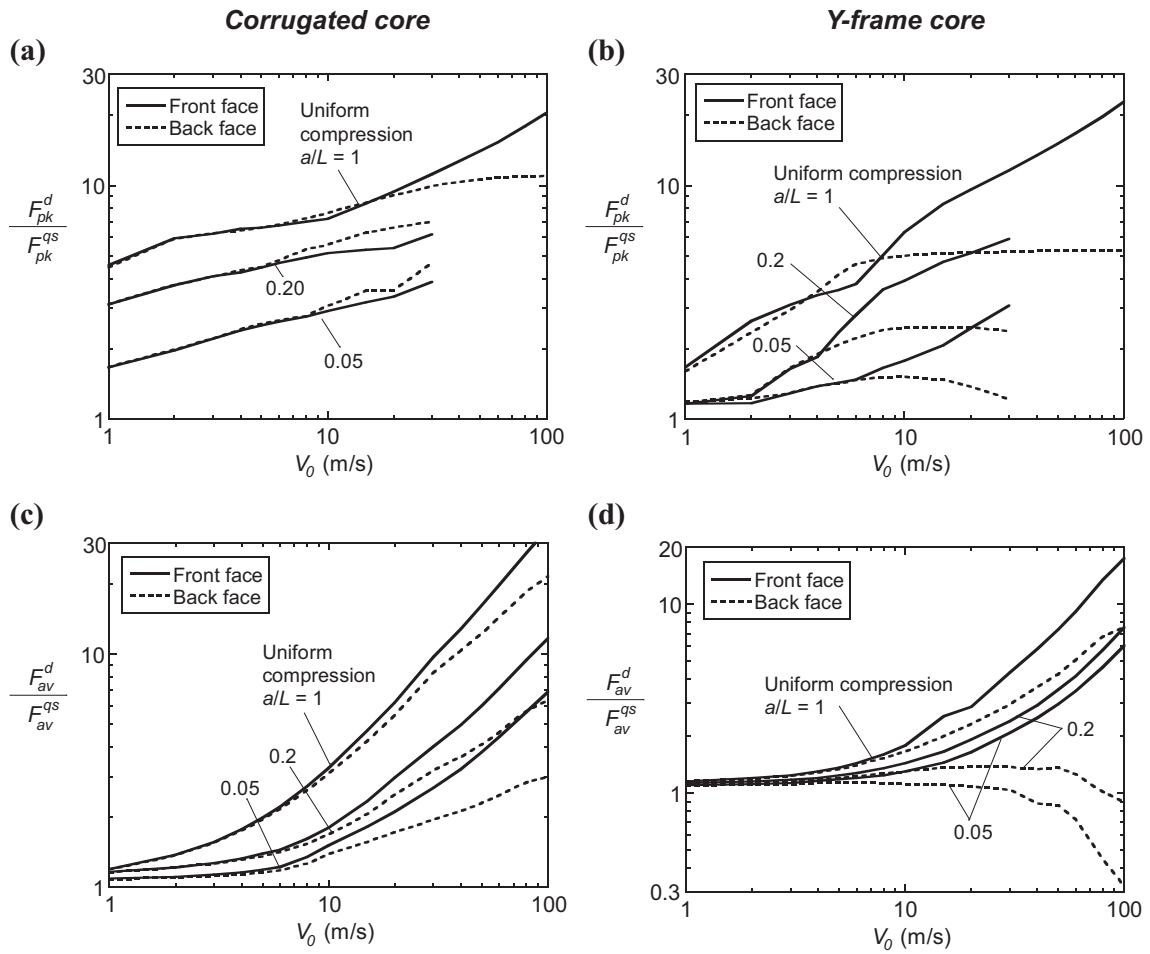


**Figure 6.9:** Influence of the normalised width  $a/L$  of the flat-bottomed indenter on the normalised initial peak load for (a) the corrugated core and (b) the Y-frame core. Likewise, the influence of  $a/L$  on the normalised average load up to  $\delta/c = 0.2$  is shown for (c) the corrugated core and (d) the Y-frame core.

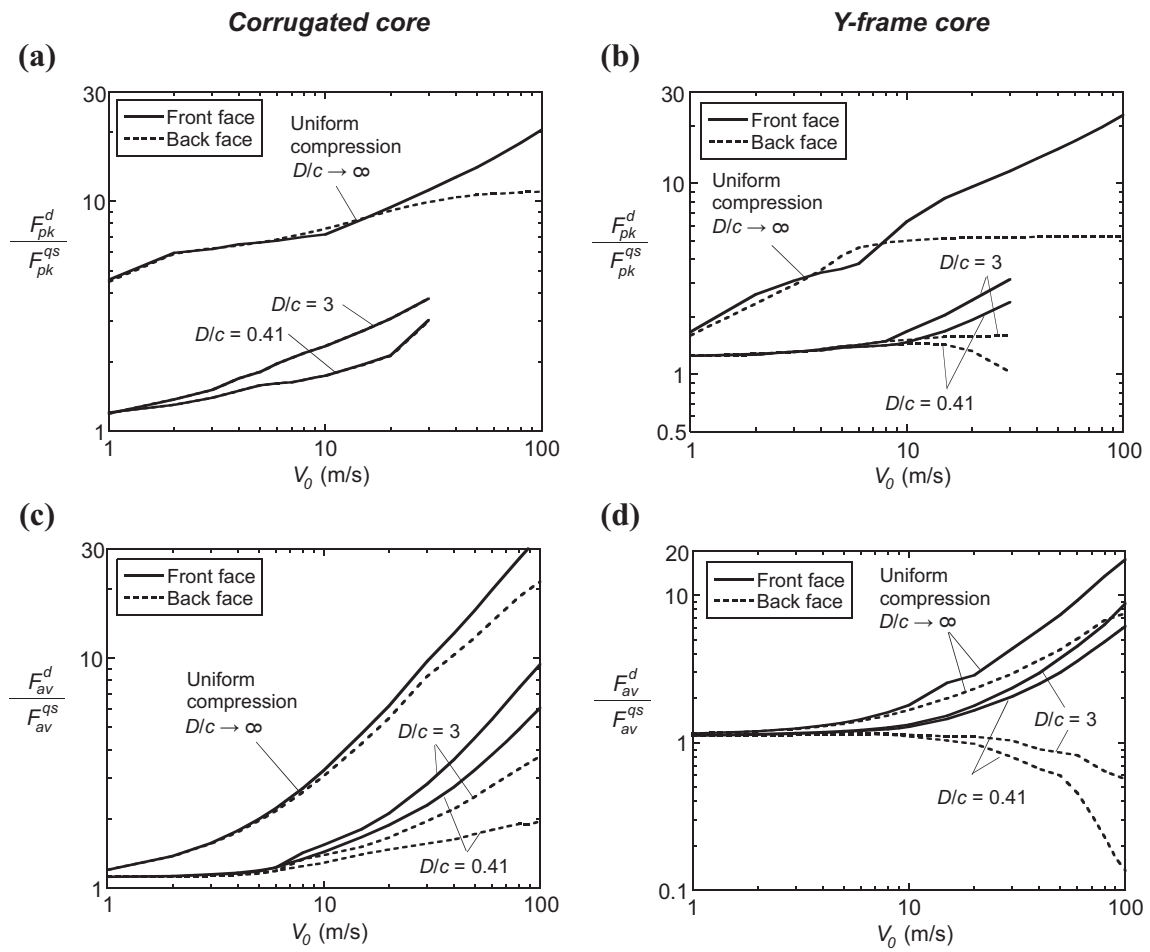


**Figure 6.10:** Influence of normalised roller diameter  $D/c$  on the normalised initial peak load for (a) the corrugated core and (b) the Y-frame core. Likewise, the influence of  $D/c$  on the normalised average load up to  $\delta/c = 0.2$  is shown for (c) the corrugated core and (d) the Y-frame core.

force equilibrium between the front and back faces is lost appears to be relatively insensitive to the geometry of the indenter.

### 6.3.5 Force distribution on the back face

In all simulations, the back face of the sandwich panel is fully-clamped against translational and rotational displacements, see Fig. 6.1(b,c). It is anticipated that the normal traction on the back face will be positive underneath the indenter, but negative at the right end of the panel. Consequently, the total force transmitted to the back face is the sum of positive and negative forces, and in this section their relative proportions are analysed.

The distribution of the normal traction  $T$  on the back face, at an indentation depth  $\delta/c = 0.2$ , is plotted in Fig. 6.11 for sandwich panels indented by a cylindrical roller with  $D/c = 0.41$ . Results are given for the corrugated core in part (a) and for the Y-frame core in part (b). In each plot, the normal traction distributions are shown for three selected values of velocity  $V_0$ . As expected, the normal traction is in general positive underneath the indenter (around  $x_3 = 0$ ), and negative at the right end (around  $x_3 = L$ ). The transition between the positive and negative traction occurs at a position  $x_3^t$ , which is sensitive to velocity;  $x_3^t$  decreases with increasing  $V_0$ . The transition  $x_3^t$  is also sensitive to the core topology; values of  $x_3^t$  are lower for the corrugated core than for the Y-frame core.

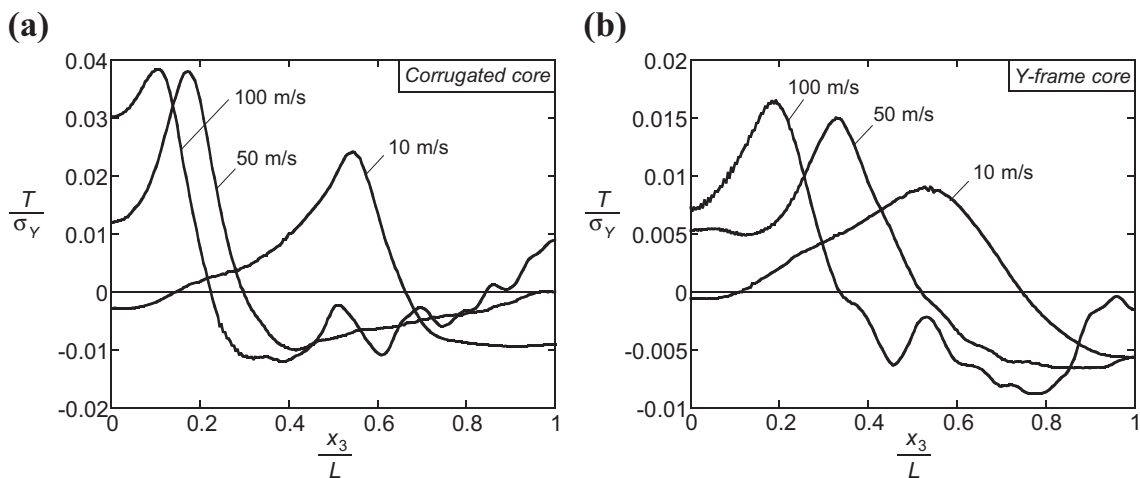


**Figure 6.11:** Distribution of the normal traction  $T$  on the back face at an indentation depth  $\delta/c = 0.2$ . Results are shown for a sandwich panel indented by a cylindrical roller of normalised diameter  $D/c = 0.41$ : (a) corrugated core and (b) Y-frame core.

The total force transmitted to the back face at  $\delta/c = 0.2$  is obtained by integrating the curves shown in Fig. 6.11. The total positive and negative traction forces exerted on the back face are compared in Table 6.3. For the corrugated core, the total positive and negative traction forces are both increasing with increasing velocity. On the other hand, for the Y-frame core, the total positive traction force is almost insensitive to velocity whereas the total negative traction force increases with increasing velocity. Consequently, the total force on the back face decreases with increasing velocity. This result explains why  $F_{av}^d/F_{av}^{qs}$  for the back face is going below unity at high velocities for the Y-frame core in Fig. 6.9(d) and 6.10(d).

$V_0$ (m/s)	Back face traction force $F/(\sigma_y bc)$ ( $10^{-3}$ )					
	Corrugated core			Y-frame core		
	Positive	Negative	Total	Positive	Negative	Total
10	27.9	-17.2	10.7	17.8	-5.9	11.9
50	34.8	-20.3	14.5	22.2	-14.0	8.2
100	37.7	-24.7	13.0	19.3	-18.0	1.3

**Table 6.3:** Positive and negative traction forces on the back face of a sandwich panel indented by a cylindrical roller of normalised diameter  $D/c = 0.41$ . The forces are for an indentation depth  $\delta/c = 0.2$ , the values are integrated from the curves shown in Fig. 6.11.

### 6.3.6 Influence of material strain-rate sensitivity

The compressive strain-rate experienced by the core members underneath the indenter scales with  $\dot{\epsilon} \approx V_0/c$ . Therefore, increasing the size of the structure reduces the strain-rate that it experiences. Tilbrook et al. (2007) demonstrated that material strain-rate sensitivity has a negligible effect upon the dynamic compressive response of corrugated and Y-frame cores. Note that the cores analysed by Tilbrook et al. (2007) had the same dimensions as those considered in this study. In this section, the influence of material strain-rate sensitivity on the dynamic indentation response will be evaluated by comparing the results of three FE models:

- (i) A lab-scale sandwich panel of dimensions presented in Section 6.2 and modelled with a rate-dependent solid. This is the FE model used in all simulations presented above.
- (ii) The same sandwich panel as model (i), but modelled as a rate-independent solid. The uniaxial tensile response of the material was tabulated from the

quasi-static response ( $10^{-3} \text{ s}^{-1}$ ) plotted in Fig. 5.4(a).

- (iii) A full-scale sandwich panel with the dimensions presented in Section 6.2 increased by a factor of 20. The material was modelled as a rate-dependent solid.

These three sandwich panels were indented by a cylindrical roller of normalised diameter  $D/c = 0.41$  and the results are shown in Fig. 6.12. The normalised peak loads for the three models are given in Fig. 6.12(a) and (b) for the corrugated core and the Y-frame core, respectively. Likewise, the normalised average loads up to  $\delta/c = 0.2$  are shown in Fig. 6.12(c) for the corrugated core and Fig. 6.12(d)

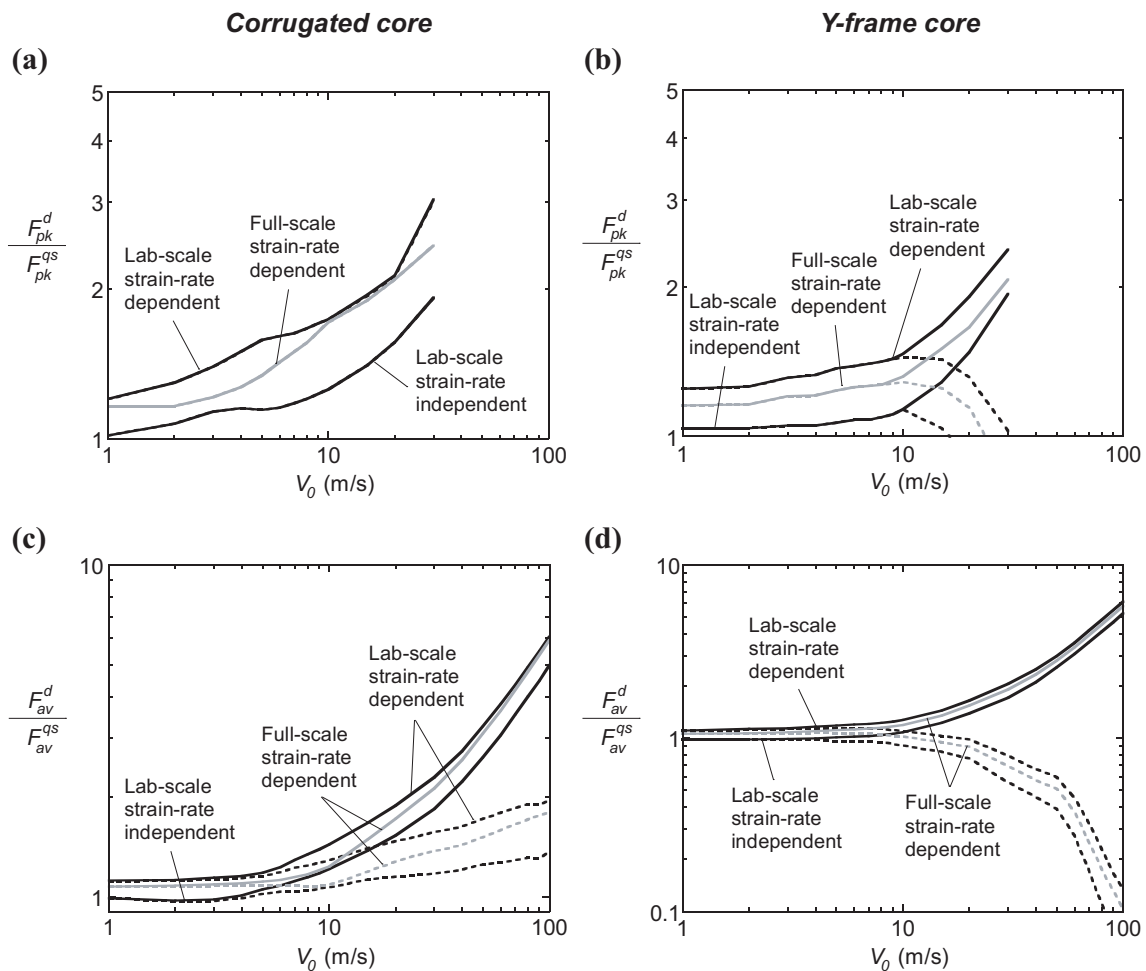


**Figure 6.12:** Influence of scale and material strain-rate sensitivity on the normalised initial peak load for (a) the corrugated core and (b) the Y-frame core. Likewise, the influence of scale and material strain-rate sensitivity on the normalised average load up to  $\delta/c = 0.2$  is shown for (c) the corrugated core and (d) the Y-frame core. Results are shown for panels indented by a cylindrical roller of normalised diameter  $D/c = 0.41$ . The force on the front and back faces are given by solid and dashed lines, respectively.

for the Y-frame core. Comparing the results of models (i) and (ii) indicate that neglecting the material strain-rate sensitivity decreases the normalised average loads by about 15%. As expected, the results for full-scale sandwich panels, model (iii), show that the effect of material strain-rate sensitivity is less important when the size of the panel is increased. Nevertheless, the normalised peak loads and the normalised average loads for model (iii) are higher than those obtained for the strain-rate independent simulations (model (ii)). The results presented in Fig. 6.12 confirm that material strain-rate sensitivity has a small influence of the dynamic indentation responses of corrugated and Y-frame sandwich panels. Consequently, the results presented above for lab-scale specimens are adequate to represent the behaviour of full-scale sandwich structures.

## 6.4 Concluding remarks

The finite element method was used to investigate the dynamic indentation response of stainless steel sandwich panels with a corrugated core and a Y-frame core. The panels were indented at a constant velocity ranging from quasi-static loading to 100 m/s, and two different indenters were considered; a flat-bottomed indenter and a cylindrical roller.

The indentation force applied to the front face of the panel was equal to the force transmitted to the back face for velocities below 10 m/s. Even for such low velocities, inertia stabilisation effects were found to increase the dynamic initial peak load above its quasi-static value, and this effect was more important for the corrugated core than for the Y-frame core. At velocities greater than 10 m/s, the force applied to the front face exceeded the force transmitted to the back face due to wave propagation effects. The force applied to the front face was mildly sensitive to the core topology; however, the force transmitted to the back face was significantly higher for panels with a corrugated core than for those with a Y-frame core.

The ratio of the dynamic initial peak load divided by its quasi-static value was found to be sensitive to the size of the indenter. Increasing the width of the flat-bottomed indenter increased this ratio significantly whereas increasing the roller diameter had a smaller effect on this quantity. Furthermore, a comparison of the deformed meshes revealed that the deformation modes are sensitive to velocity, but relatively insensitive to the indenter shape and size. Finally, the simulations demonstrated that

material rate-sensitivity has only a mild effect on the dynamic indentation response of lab-scale sandwich panels. Consequently, the results on lab-scale sandwich panels are representative of full-scale panels.

### 6.A Finite element model for uniform compression

The dynamic uniform compressive responses of corrugated and Y-frame cores were simulated using the commercial software Abaqus (version 6.10). The dimensions of both cores were identical to those shown in Fig. 6.4, except that the Y-frame core had a fillet, with a radius of 1.5 mm, between the Y-frame leg and the horizontal flange, see Fig. 6.1(a). This local reinforcement was also present in the simulations of Tilbrook et al. (2007); the authors found that it was necessary to obtain a good agreement with their experimental results.

Both core topologies were meshed with four-noded plane strain quadrilateral elements (CPE4R in Abaqus notation). An average mesh size of  $t/8 = 0.0375$  mm was used in all calculations; additional mesh refinements did not improve significantly the accuracy of the results. The geometric imperfection and the material properties were the same as those employed for the dynamic indentation simulations, see Sections 6.2.1 and 6.2.2, respectively.

The front and back faces were modelled as rigid surfaces. All degrees-of-freedom were constrained to zero on the back face whereas the front face had a constant downward velocity  $V_0$ , see Fig. 6.1(a). The crushing velocity  $V_0$  was varied from 1 to 100 m/s and the dynamic simulations were executed with the explicit solver of Abaqus. For the quasi-static simulations, the constant velocity was replaced by a prescribed displacement  $\delta$  and the simulations were executed using the implicit solver of Abaqus. A hard frictionless contact was defined between all surfaces of the model.

# Chapter 7

## Conclusions and future work

As mentioned in Section 1.3, the objectives of this thesis were: (i) to explore how a surface treatment can improve the strength of a lattice material and (ii) to investigate the collapse response of two competing prismatic sandwich cores employed in ship hulls. The first objective was treated in Chapter 3 whereas the second objective was addressed in Chapter 4 for quasi-static loading and in Chapters 5 and 6 for dynamic loading. The conclusions reached in Chapters 3 to 6 are summarised below in relation to those two objectives. This chapter ends with recommendations for future work.

### 7.1 Compressive response of a carburised pyramidal lattice

- The finite element method was used to simulate the quasi-static compressive response of a pyramidal lattice made from (i) tubes and (ii) solid struts.
- First, the influence of strain hardening was investigated by comparing the response of a lattice made from a perfectly plastic solid ( $E_t = 0$ ) to one made from stainless steel ( $E_t = 2$  GPa). Strain hardening was found to increase the peak compressive stress of lattices with a slenderness ratio  $l/d < 10$ . However, strain hardening had no influence on the collapse mode of the lattice.
- Second, the effect of carburisation was examined. Carburisation is a surface treatment that increases the yield strength of the material. The collapse mode

of the pyramidal lattice was found to be sensitive to carburisation; the transition between plastic and elastic buckling occurred at a lower slenderness ratio when the lattice was carburised. In addition, carburisation increased the peak compressive stress of the lattice, except for those collapsing by elastic buckling.

- The pyramidal lattice made from carburised tubes was found to possess a compressive strength superior to that of other metallic lattices made from aluminium or titanium.

### 7.2 The influence of the back face on the bending response of prismatic sandwich beams

- Sandwich beams with a corrugated core or a Y-frame core were manufactured by brazing together stainless steel sheets. Their quasi-static three-point bending responses were measured under simply supported and clamped boundary conditions. The role of the back face was assessed by comparing the response of beams with (i) front-and-back faces present and (ii) front face present, but the back face absent.
- The measured responses were in good agreement with finite element simulations.
- Two collapse mechanisms were identified: short panels collapse by indentation whereas long panels fail by Brazier plastic buckling. Panels without a back face have a superior indentation strength than those with front-and-back faces present. In contrast, the Brazier plastic buckling strength of panels with front-and-back faces present exceeds that of panels without a back face.
- For both collapse mechanisms, concentrating the mass of the sandwich panel in the core increased the three-point bending strength of the structure.

### 7.3 Drop weight tests on prismatic sandwich beams

- Simply supported and clamped sandwich beams with a corrugated core or a Y-frame core were subjected to an impact at 5 m/s using a drop weight

apparatus. The responses measured at 5 m/s were compared to their quasi-static responses to assess the influence of the loading velocity.

- The peak load at 5 m/s could not be measured accurately due to an artifact of the experimental setup. However, the post-peak response was captured precisely and it was found to be slightly stronger at 5 m/s than for quasi-static loading.
- The measured post-peak response was in reasonable agreement with three-dimensional finite element predictions.
- Experiments and simulations have shown that a sandwich beam which collapses quasi-statically by indentation also fails by indentation at 5 m/s. In contrast, predictions have shown that a sandwich beam which fails quasi-statically by Brazier plastic buckling collapses by indentation at 5 m/s.
- For all sandwich beams considered, simulations indicated that the peak load at 5 m/s exceeds its quasi-static value. The mass of the front face was found to be an important factor contributing to this increase.

## 7.4 Dynamic indentation of prismatic sandwich panels

- The finite element method was used to simulate the dynamic indentation response of stainless steel sandwich panels with a corrugated core or a Y-frame core. The indentation response was simulated for velocities ranging from quasi-static loading to 100 m/s, and two different indenters were considered: a flat-bottomed indenter and a cylindrical roller.
- The indentation force applied to the front face of the panel was approximately equal to the force transmitted to the back face for velocities below 10 m/s. Even for such low indentation velocities, the dynamic initial peak load was found to be higher than its quasi-static value due to inertia stabilisation effects. This strengthening effect was more important for the corrugated core than for the Y-frame core.
- For indentation velocities greater than 10 m/s, the force applied on the front face exceeded the force transmitted to the back face due to wave propagation

effects. The force transmitted to the back face was higher for the corrugated core than for the Y-frame core.

- Increasing the width of the flat-bottomed indenter was found to enhance both inertia stabilisation and wave propagation effects. In contrast, increasing the roller diameter had only a mild effect of the dynamic indentation response.
- Material strain-rate effects were found to have a small influence on the dynamic indentation response of both lab-scale and full-scale sandwich panels.

## 7.5 Future work

### 7.5.1 Dynamic compressive response of a hollow pyramidal lattice

The pyramidal lattice made from hollow tubes possesses a high quasi-static compressive strength at low densities, recall Fig. 2.7(a). However, the dynamic compressive response of the lattice has not been investigated yet, neither experimentally nor numerically. The dynamic compressive response of a pyramidal lattice made from solid struts has been measured by Lee et al. (2006) and similar tests should be repeated on the hollow pyramidal lattice. In addition, finite element simulations should be performed to capture the influence of geometry and crushing velocity upon the compressive response of the hollow pyramidal lattice. A similar numerical investigation was performed by McShane (2007) for the corrugated core.

### 7.5.2 Measured compressive response of a carburised pyramidal lattice

The finite element simulations shown in Chapter 3 demonstrated that carburisation can increase significantly the peak compressive strength of a pyramidal lattice. Those simulations should be compared to experimental tests to evaluate their accuracy. In addition, the residual stress and the embrittlement caused by carburisation were neglected in the simulations of Chapter 3. Experimental data is necessary to determine if this hypothesis is adequate.

### 7.5.3 Fracture of corrugated and Y-frame sandwich panels

The experiments performed in Chapters 4 and 5 allowed us to investigate the structural collapse of corrugated and Y-frame sandwich panels. However, none of the specimens were tested up to material failure, *i.e.* fracture. The accreditation of a new ship hull design is often based on the energy that the structure can absorb before perforation. Thus, it is important for shipbuilders to (i) understand the key factors governing the onset of fracture and (ii) predict accurately the fracture process in large scale structures. Fracture of monolithic plates has been investigated by several authors, see for example Stoughton (2000), Wisselink (2000) and Balden and Nurick (2005), but future studies should extend this work to sandwich structures.

First, quasi-static three-point bending tests should be performed on corrugated and Y-frame sandwich panels up to the onset of fracture. These test specimens should be made from shipbuilding steel and assembled by a conventional welding route. It is known that the toughness of a metallic plate scales with its thickness; hence, the dimensions of the test panels should be similar to those of a full-scale ship structure. Finally, it is also important that the boundary conditions applied to the test specimens are representative of a full-scale sandwich hull structure.

Second, these experimental tests should be compared to finite element simulations. The simulations will require the calibration of a fracture criterion such as Johnson-Cook (Johnson and Cook, 1985) or Cockcroft-Latham (Cockcroft and Latham, 1968). Finite element predictions of fracture are usually sensitive to the mesh size and to the type elements. Consequently, an additional challenge is to determine if accurate fracture predictions can be obtained for large scale ship structures discretised with a coarse mesh of shell elements.

## Published work

Chapter 4 has been published in an international scientific journal and the reference is given below. Additional publications on Chapters 3, 5 and 6 are also in preparation.

L. St-Pierre, N.A. Fleck, and V.S. Deshpande. Sandwich beams with corrugated and Y-frame cores: does the back face contribute to the bending response? *Journal of Applied Mechanics*, 79(1), 011002 (13 pages), 2012.



# Bibliography

- T. Abdulla, A. Yerokhin, and R. Goodall. Effect of plasma electrolytic oxidation coating on the specific strength of open-cell aluminium foams. *Materials and Design*, 32(7):3742–3749, 2011.
- H.G. Allen. *Analysis and design of structural sandwich panels*. Pergamon Press, Oxford, UK, 1969.
- J. Amdahl and D. Kavlie. Design of tankers for grounding and collision. In *International Conference on Technologies for Marine Environment Preservation*, pages 167–174, Tokyo, Japan, 1995.
- K.R.F. Andrews, G.L. England, and E. Ghani. Classification of the axial collapse of cylindrical tubes under quasi-static loading. *International Journal of Mechanical Sciences*, 25(9-10):687–696, 1983.
- M.F. Ashby. Cellular solids - scaling of properties. In Michael Scheffler and Paolo Colombo, editors, *Cellular Ceramics: Structure, Manufacturing, Properties and Applications*. Wiley, Weinheim, Germany, 2005.
- M.F. Ashby. The properties of foams and lattices. *Philosophical Transactions of the Royal Society A*, 364:15–30, 2006.
- M.F. Ashby. *Material selection in mechanical design*. Butterworth-Heinemann, Oxford, UK, 4<sup>th</sup> edition, 2010.
- M.F. Ashby, A.G. Evans, N.A. Fleck, L.J. Gibson, and H.N.G. Wadley. *Metal foams: a design guide*. Butterworth-Heinemann, Oxford, UK, 2000.
- V.H. Balden and G.N. Nurick. Numerical simulation of the post-failure motion of steel plates subjected to blast loading. *International Journal of Impact Engineering*, 32(14):14–34, 2005.

## Bibliography

---

- H. Bart-Smith, J.W. Hutchinson, and A.G. Evans. Measurement and analysis of the structural performance of cellular metal sandwich construction. *International Journal of Mechanical Sciences*, 43(8):1945–1963, 2001.
- E. Bele, B.A. Bouwhuis, C. Codd, and G.D. Hibbard. Structural ceramic coatings in composite microtruss cellular materials. *Acta Materialia*, 59(15):6145–6154, 2011.
- L.G. Brazier. On the flexure of thin cylindrical shells and other “thin” sections. *Proceedings of the Royal Society A*, 116(773):104–114, 1927.
- J. Broekhuijsen. *Ductile failure criteria and energy absorption capacity of the Y-shape test section*. M.sc. thesis, TU Delft, 2003.
- P. Burgherr. In-depth analysis of accidental oil spills from tankers in the context of global spill trends from all sources. *Journal of Hazardous Materials*, 140(1-2):245–56, 2007.
- C.R. Calladine. *Theory of shell structures*. Cambridge University Press, Cambridge, UK, 1983.
- C.R. Calladine and R.W. English. Strain-rate and inertia effects in the collapse of two types of energy-absorbing structure. *International Journal of Mechanical Sciences*, 26(11-12):689–701, 1984.
- Y. Cao, F. Ernst, and G.M. Michal. Colossal carbon supersaturation in austenitic stainless steels carburized at low temperature. *Acta Materialia*, 51(14):4171–4181, 2003.
- B. Castanié, C. Bouvet, Y. Aminanda, J.-J. Barrau, and P. Thevenet. Modelling of low-energy/low-velocity impact on Nomex honeycomb sandwich structures with metallic skins. *International Journal of Impact Engineering*, 35(7):620–634, 2008.
- C. Chen, A.-M. Harte, and N.A. Fleck. The plastic collapse of sandwich beams with a metallic foam core. *International Journal of Mechanical Sciences*, 43:1483–1506, 2001.
- S. Chiras, D.R. Mumm, A.G. Evans, N. Wicks, J.W. Hutchinson, K. Dharmasena, H.N.G. Wadley, and S. Fichter. The structural performance of near-optimized truss core panels. *International Journal of Solids and Structures*, 39(15):4093–4115, 2002.

- M.G. Cockcroft and D.J. Latham. Ductility and workability of metals. *Journal of the Institute of Metals*, 96:33–39, 1968.
- F. Côté, V.S. Deshpande, N.A. Fleck, and A.G. Evans. The out-of-plane compressive behavior of metallic honeycombs. *Materials Science and Engineering A*, 380(1-2): 272–280, 2004.
- F. Côté, V.S. Deshpande, N.A. Fleck, and A.G. Evans. The compressive and shear responses of corrugated and diamond lattice materials. *International Journal of Solids and Structures*, 43(20):6220–6242, 2006.
- F. Côté, N.A. Fleck, and V.S. Deshpande. Fatigue performance of sandwich beams with a pyramidal core. *International Journal of Fatigue*, 29(8):1402–1412, 2007.
- V. Crupi and R. Montanini. Aluminium foam sandwiches collapse modes under static and dynamic three-point bending. *International Journal of Impact Engineering*, 34(3):509–521, 2007.
- V. Crupi, G. Epasto, and E. Guglielmino. Collapse modes in aluminium honeycomb sandwich panels under bending and impact loading. *International Journal of Impact Engineering*, 43:6–15, 2012.
- V.S. Deshpande and N.A. Fleck. Isotropic constitutive models for metallic foams. *Journal of the Mechanics and Physics of Solids*, 48(6-7):1253–1283, 2000a.
- V.S. Deshpande and N.A. Fleck. High strain rate compressive behaviour of aluminium alloy foams. *International Journal of Impact Engineering*, 24:277–298, 2000b.
- V.S. Deshpande and N.A. Fleck. Collapse of truss core sandwich beams in 3-point bending. *International Journal of Solids and Structures*, 38(36-37):6275–6305, 2001.
- V.S. Deshpande, N.A. Fleck, and M.F. Ashby. Effective properties of the octet-truss lattice material. *Journal of the Mechanics and Physics of Solids*, 49(8):1747–1769, 2001.
- K.P. Dharmasena, H.N.G. Wadley, Z. Xue, and J.W. Hutchinson. Mechanical response of metallic honeycomb sandwich panel structures to high-intensity dynamic loading. *International Journal of Impact Engineering*, 35(9):1063–1074, 2008.
- K.P. Dharmasena, H.N.G. Wadley, K. Williams, Z. Xue, and J.W. Hutchinson.

## Bibliography

---

- Response of metallic pyramidal lattice core sandwich panels to high intensity impulsive loading in air. *International Journal of Impact Engineering*, 38(5):275–289, 2011.
- C.S. Dunleavy, J.A. Curran, and T.W. Clyne. Plasma electrolytic oxidation of aluminium networks to form a metal-cored ceramic composite hybrid material. *Composites Science and Technology*, 71(6):908–915, 2011.
- H. Endo, Y. Yamada, and H. Kawano. Verification on the effectiveness of buffer bow structure through FEM simulation. In *Third International Conference on Collision and Grounding of Ships*, pages 151–159, Izu, Japan, 2004.
- A.G. Evans, J.W. Hutchinson, N.A. Fleck, M.F. Ashby, and H.N.G. Wadley. The topological design of multifunctional cellular metals. *Progress in Materials Science*, 46(3-4):309–327, 2001.
- W. Fairbairn. *An account of the construction of the Britannia and Conway tubular bridges*. John Weale, London, UK, 1849.
- E. Ferri, E. Antinucci, M.Y. He, J.W. Hutchinson, F.W. Zok, and A.G. Evans. Dynamic buckling of impulsively loaded prismatic cores. *Journal of Mechanics of Materials and Structures*, 1(8):1345–1365, 2006.
- N.A. Fleck and V.S. Deshpande. The resistance of clamped sandwich beams to shock loading. *Journal of Applied Mechanics*, 71(3):386, 2004.
- N.A. Fleck, V.S. Deshpande, and M.F. Ashby. Micro-architected materials: past, present and future. *Proceedings of the Royal Society A*, 466(2121):2495–2516, 2010.
- P. Friis-Hansen and B.C. Simonsen. Gracat: software for grounding and collision risk analysis. *Marine Structures*, 15(4-5):383–401, 2002.
- G. Galileo. *Discorsi e dimostrazioni matematiche, intorno due nuove scienze*. Elsevier, Leiden, The Netherlands, 1638.
- L.J. Gibson and M.F. Ashby. *Cellular solids, structure and properties*. Cambridge University Press, Cambridge, UK, second edition, 1997.
- L.J. Gibson, M.F. Ashby, and B.A. Harley. *Cellular materials in nature and medicine*. Cambridge University Press, Cambridge, UK, 2010.
- B. van de Graaf, J. Broekhuijsen, A.W. Vredeveltdt, and A. van de Ven. Construction

- aspects for the Schelde Y-shape crashworthy hull structure. In *Third International Conference on Collision and Grounding of Ships*, pages 229–233, Izu, Japan, 2004.
- S.R. Guillow, G. Lu, and R.H. Grzebieta. Quasi-static axial compression of thin-walled circular aluminium tubes. *International Journal of Mechanical Sciences*, 43(9):2103–2123, 2001.
- M.A. Hazizan and W.J. Cantwell. The low velocity impact response of an aluminium honeycomb sandwich structure. *Composites Part B: Engineering*, 34(8):679–687, 2003.
- A. Herrmann, P. Zahlen, and I. Zuardy. Sandwich structures technology in commercial aviation: present applications and future trends. In O.T. Thomsen, E. Bozhevolnaya, and A. Lyckegaard, editors, *Sandwich structures 7: advancing with sandwich structures and materials, Proceedings of the 7th International Conference on Sandwich Structures*, pages 13–26, Aalborg, Denmark, 2005.
- R.G. Hutchinson, N. Wicks, A.G. Evans, N.A. Fleck, and J.W. Hutchinson. Kagomé plate structures for actuation. *International Journal of Solids and Structures*, 40(25):6969–6980, 2003.
- S. Hyun, A.M. Karlsson, S. Torquato, and A.G. Evans. Simulated properties of Kagomé and tetragonal truss core panels. *International Journal of Solids and Structures*, 40(25):6989–6998, 2003.
- ISSC. Collision and grounding. In *16<sup>th</sup> International Ship and Offshore Structures Congress*, volume 2, Southampton, UK, 2006a.
- ISSC. Dynamic response. In *16<sup>th</sup> International Ship and Offshore Structures Congress*, volume 1, Southampton, UK, 2006b.
- ISSC. Quasi-static response. In *16<sup>th</sup> International Ship and Offshore Structures Congress*, volume 1, Southampton, UK, 2006c.
- G.R. Johnson and W.H. Cook. Fracture characteristics of three metals subjected to various strains, strain rates, temperatures and pressures. *Engineering Fracture Mechanics*, 21(1):31 – 48, 1985.
- N. Jones. On the collision protection of ships. *Nuclear Engineering and Design*, 38(2):229–240, 1976.

## Bibliography

---

- N. Jones. A literature survey on the collision and grounding protection of ships. Technical report, U.S. Coast Guard Headquarters, Washington, DC, USA, 1979.
- N. Jones. *Structural impact*. Cambridge University Press, Cambridge, UK, 1989.
- D. Karagiozova and N. Jones. Dynamic elastic-plastic buckling phenomena in a rod due to axial impact. *International Journal of Impact Engineering*, 18(7-8): 919–947, 1996.
- K. Kawaichi, T. Kuroiwa, and H. Sueoka. On the structural design of mid-deck tanker. In *International Conference on Technologies for Marine Environment Preservation*, page 213218, Tokyo, Japan, 1995.
- A. Konter, J. Broekhuijsen, and A. Vredeveldt. A quantitative assessment of the factors contributing to the accuracy of ship collision predictions with the finite element method. In *Third International Conference on Collision and Grounding of Ships*, Izu, Japan, 2004.
- G.W. Kooistra and H.N.G. Wadley. Lattice truss structures from expanded metal sheet. *Materials and Design*, 28(2):507–514, 2007.
- G.W. Kooistra, V.S. Deshpande, and H.N.G. Wadley. Compressive behavior of age hardenable tetrahedral lattice truss structures made from aluminium. *Acta Materialia*, 52(14):4229–4237, 2004.
- G.W. Kooistra, V.S. Deshpande, and H.N.G. Wadley. Hierarchical Corrugated Core Sandwich Panel Concepts. *Journal of Applied Mechanics*, 74(2):259, 2007.
- P. Kujala, M. Hänninen, T. Arola, and J. Ylitalo. Analysis of the marine traffic safety in the gulf of finland. *Reliability Engineering and System Safety*, 94(8): 1349–1357, 2009.
- S. Lee, F. Barthelat, J.W. Hutchinson, and H.D. Espinosa. Dynamic failure of metallic pyramidal truss core materials Experiments and modeling. *International Journal of Plasticity*, 22(11):2118–2145, 2006.
- E. Lehmann and J. Peschmann. Energy absorption by the steel structure of ships in the event of collisions. *Marine Structures*, 15(4-5):429–441, 2005.
- Y. Liang, A.V. Spuskanyuk, S.E. Flores, D.R. Hayhurst, J.W. Hutchinson, R.M. McMeeking, and A.G. Evans. The response of metallic sandwich panels to water blast. *Journal of Applied Mechanics*, 74(1):81, 2007.

- LR. Statistical analysis of classification society records for oil tanker grounding and collisions. Technical Report 2078-3-0, Lloyd's Register of Shipping, London, UK, 1991.
- T.J. Lu, H.A. Stone, and M.F. Ashby. Heat transfer in open-cell metal foams. *Acta Materialia*, 46(10):3619–3635, 1998.
- T.J. Lu, L. Valdevit, and A.G. Evans. Active cooling by metallic sandwich structures with periodic cores. *Progress in Materials Science*, 50(7):789–815, 2005.
- H. Ludolph. The unsinkable ship - development of the y-shape support web. In *Second International Conference on Collision and Grounding of Ships*, Copenhagen, Denmark, 2001.
- S.P. Mai and N.A. Fleck. Reticulated tubes: effective elastic properties and actuation response. *Proceedings of the Royal Society A*, 465(2103):685–708, 2009.
- M. Matsumoto, K. Masai, and T. Wajima. New technologies for railway trains. *Hitachi Review*, 48(3):134–138, 1999.
- T.M. McCormack, R. Miller, O. Kesler, and L.J. Gibson. Failure of sandwich beams with metallic foam cores. *International Journal of Solids and Structures*, 38(28-29):4901–4920, 2001.
- G.J. McShane. *Underwater blast response of metallic sandwich structures*. Phd thesis, University of Cambridge, 2007.
- G.J. McShane, D.D. Radford, V.S. Deshpande, and N.A. Fleck. The response of clamped sandwich plates with lattice cores subjected to shock loading. *European Journal of Mechanics - A/Solids*, 25(2):215–229, 2006.
- G.J. McShane, V.S. Deshpande, and N.A. Fleck. The underwater blast resistance of metallic sandwich beams with prismatic lattice cores. *Journal of Applied Mechanics*, 74(2):352, 2007.
- M. Meo, R. Vignjevic, and G. Marengo. The response of honeycomb sandwich panels under low-velocity impact loading. *International Journal of Mechanical Sciences*, 47(9):1301–1325, 2005.
- G. Michal, F. Ernst, H. Kahn, Y. Cao, F. Oba, N. Agarwal, and A.H. Heuer. Carbon supersaturation due to paraequilibrium carburization: Stainless steels with greatly improved mechanical properties. *Acta Materialia*, 54(6):1597–1606, 2006.

## Bibliography

---

- V.U. Minorsky. An analysis of ship collisions with reference to protection of nuclear power plants. *Journal of Ship Research*, 3(2):1–4, 1959.
- H. Naar, P. Kujalaa, B.C. Simonsen, and H. Ludolph. Comparison of the crash-worthiness of various bottom and side structures. *Marine Structures*, 15:443–460, 2002.
- T.G. Nieha, K. Higashi, and J. Wadsworth. Effect of cell morphology on the compressive properties of open-cell aluminum foams. *Materials Science and Engineering A*, 283(1-2):105–110, 2000.
- O. Ozguc, P.K. Das, and N. Barltrop. A comparative study on the structural integrity of single and double side skin bulk carriers under collision damage. *Marine Structures*, 18(7-8):511–547, 2005.
- J.K. Paik. Innovative structural designs of tankers against ship collisions and grounding: a recent state-of-the-art review. *Marine Technology*, 40(1):25–33, 2003.
- J.H. Park, S.K. Ha, K.W. Kang, C.W. Kim, and H.S. Kim. Impact damage resistance of sandwich structure subjected to low velocity impact. *Journal of Materials Processing Technology*, 201(1-3):425–430, 2008.
- A. Paul and U. Ramamurty. Strain rate sensitivity of a closed-cell aluminum foam. *Materials Science and Engineering A*, 281(1-2):1–7, 2000.
- C.B.W. Pedersen, V.S. Deshpande, and N.A. Fleck. Compressive response of the y-shaped sandwich core. *European Journal of Mechanics - A/Solids*, 25(1):125–141, 2006.
- P.T. Pedersen. Collision risk for fixed offshore structures close to high-density shipping lanes. *Journal of Engineering for the Maritime Environmental*, 216(1):29–44, 2002.
- P.T. Pedersen and S. Zhang. On impact mechanics in ship collisions. *Marine Structures*, 11(10):429–449, 1998.
- P.T. Pedersen and S. Zhang. Absorbed energy in ship collision and grounding revisiting minorsky’s empirical method. *Journal of Ship Research*, 44(2):140–154, 2000.
- P.T. Pedersen, S. Valsgard, D. Olsen, and S. Spangenberg. Ship impacts: bow collisions. *International Journal of Impact Engineering*, 13(2):163–187, 1993.

- S.M. Pingle, N.A. Fleck, V.S. Deshpande, and H.N.G. Wadley. Collapse mechanism maps for a hollow pyramidal lattice. *Proceedings of the Royal Society A*, 467 (2128):985–1011, 2011a.
- S.M. Pingle, N.A. Fleck, V.S. Deshpande, and H.N.G. Wadley. Collapse mechanism maps for the hollow pyramidal core of a sandwich panel under transverse shear. *International Journal of Solids and Structures*, 48:3417–3430, 2011b.
- F.J. Plantema. *Sandwich construction; the bending and buckling of sandwich beams, plates, and shells*. Wiley, New York, USA, 1966.
- X. Qiu, V.S. Deshpande, and N.A. Fleck. Finite element analysis of the dynamic response of clamped sandwich beams subject to shock loading. *European Journal of Mechanics - A/Solids*, 22(6):801–814, 2003.
- D.T. Queheillalt and H.N.G. Wadley. Cellular metal lattices with hollow trusses. *Acta Materialia*, 53(2):303–313, 2005a.
- D.T. Queheillalt and H.N.G. Wadley. Pyramidal lattice truss structures with hollow trusses. *Materials Science and Engineering A*, 397(1-2):132–137, 2005b.
- D.T. Queheillalt and H.N.G. Wadley. Hollow pyramidal lattice truss structures. *International Journal of Materials Research*, 4:389–400, 2011.
- D.D. Radford, V.S. Deshpande, and N.A. Fleck. The use of metal foam projectiles to simulate shock loading on a structure. *International Journal of Impact Engineering*, 31(9):1152–1171, 2005.
- D.D. Radford, N.A. Fleck, and V.S. Deshpande. The response of clamped sandwich beams subjected to shock loading. *International Journal of Impact Engineering*, 32(6):968–987, 2006a.
- D.D. Radford, G.J. McShane, V.S. Deshpande, and N.A. Fleck. The response of clamped sandwich plates with metallic foam cores to simulated blast loading. *International Journal of Solids and Structures*, 43(7-8):2243–2259, 2006b.
- D.D. Radford, G.J. McShane, V.S. Deshpande, and N.A. Fleck. Dynamic compressive response of stainless-steel square honeycombs. *Journal of Applied Mechanics*, 74(4):658, 2007.
- H.J. Rathbun, Z. Wei, M.Y. He, F.W. Zok, A.G. Evans, D.J. Sypeck, and H.N.G. Wadley. Measurement and simulation of the performance of a lightweight metallic

## Bibliography

---

- sandwich structure with a tetrahedral truss core. *Journal of Applied Mechanics*, 71(3):368–374, 2004.
- H.J. Rathbun, F.W. Zok, and a.G. Evans. Strength optimization of metallic sandwich panels subject to bending. *International Journal of Solids and Structures*, 42(26):6643–6661, 2005.
- H.J. Rathbun, D.D. Radford, Z. Xue, M.Y. He, J. Yang, V.S. Deshpande, N.A. Fleck, J.W. Hutchinson, F.W. Zok, and A.G. Evans. Performance of metallic honeycomb-core sandwich beams under shock loading. *International Journal of Solids and Structures*, 43(6):1746–1763, 2006a.
- H.J. Rathbun, F.W. Zok, S.A. Waltner, C. Mercer, A.G. Evans, D.T. Queheillalt, and H.N.G. Wadley. Structural performance of metallic sandwich beams with hollow truss cores. *Acta Materialia*, 54(20):5509–5518, 2006b.
- V. Rubino, V.S. Deshpande, and N.A. Fleck. The collapse response of sandwich beams with a Y-frame core subjected to distributed and local loading. *International Journal of Mechanical Sciences*, 50(2):233–246, 2008a.
- V. Rubino, V.S. Deshpande, and N.A. Fleck. The dynamic response of end-clamped sandwich beams with a Y-frame or corrugated core. *International Journal of Impact Engineering*, 35(8):829–844, 2008b.
- V. Rubino, V.S. Deshpande, and N.A. Fleck. The dynamic response of clamped rectangular Y-frame and corrugated core sandwich plates. *European Journal of Mechanics - A/Solids*, 28(1):14–24, 2009.
- V. Rubino, V.S. Deshpande, and N.A. Fleck. The three-point bending of Y-frame and corrugated core sandwich beams. *International Journal of Mechanical Sciences*, 52(3):485–494, 2010.
- B.P. Russell. *The micromechanics of composite lattice materials*. Phd thesis, University of Cambridge, 2009.
- Y. Seki, M.S. Schneider, and M.A. Meyers. Structure and mechanical behavior of a toucan beak. *Acta Materialia*, 53(20):5281–5296, 2005.
- K.B. Shin, J.Y. Lee, and S.H. Cho. An experimental study of low-velocity impact responses of sandwich panels for Korean low floor bus. *Composite Structures*, 84(3):228–240, 2008.

- F.M. Shuaieb and P.D. Soden. Indentation failure of composite sandwich beams. *Composites Science and Technology*, 57(910):1249–1259, 1997.
- B.C. Simonsen. *Mechanics of ship grounding*. Phd thesis, Technical University of Denmark, 1997.
- B.C. Simonsen and R. Törnqvist. Experimental and numerical modelling of ductile crack propagation in large-scale shell structures. *Marine Structures*, 17(1):1–27, 2004.
- S.K. Skinner and W.K. Reilly. The exxon valdez oil spill. Technical report, The National Response Team, 1989.
- P.D. Soden. Indentation of composite sandwich beams. *Journal of Strain Analysis*, 31(5):353–360, 1996.
- C.A. Steeves and N.A. Fleck. Collapse mechanism of sandwich beams with composite faces and a foam core, loaded in three-point bending. part i: analytical models and minimum weight design. *International Journal of Mechanical Sciences*, 46(4): 561–583, 2004.
- T.B. Stoughton. A general forming limit criterion for sheet metal forming. *International Journal of Mechanical Sciences*, 42(1):1–27, 2000.
- M.G. Stout and P.S. Follansbee. Strain-rate sensitivity, strain-hardening, and yield behaviour of 304l stainless steel. *Journal of Engineering Materials and Technology*, 108(4):344–353, 1986.
- D.D. Symons, R.G. Hutchinson, and N.A. Fleck. Actuation of the Kagomé Double-Layer Grid. Part 1: Prediction of performance of the perfect structure. *Journal of the Mechanics and Physics of Solids*, 53(8):1855–1874, 2005a.
- D.D. Symons, J. Shieh, and N.A. Fleck. Actuation of the Kagomé Double-Layer Grid. Part 2: Effect of imperfections on the measured and predicted actuation stiffness. *Journal of the Mechanics and Physics of Solids*, 53(8):1875–1891, 2005b.
- D.J. Sypeck and H.N.G. Wadley. Cellular metal truss core sandwich structures. *Advanced Engineering Materials*, 4(10):759–764, 2002.
- K. Tabri, J. Broekhuijsen, J. Matusiak, and P. Varsta. Analytical modelling of ship collision based on full-scale experiments. *Marine Structures*, 22(1):42–61, 2009.
- V.L. Tagarielli and N.A. Fleck. A comparison of the structural response of clamped

## Bibliography

---

- and simply supported sandwich beams with aluminium faces and a metal foam core. *Journal of Applied Mechanics*, 72(3):408–417, 2005.
- G. Taylor. The use of flat-ended projectiles for determining dynamic yield stress i theoretical considerations. *Proceedings of the Royal Society A*, 194:289–299, 1948.
- M.T. Tilbrook, D.D. Radford, V.S. Deshpande, and N.A. Fleck. Dynamic crushing of sandwich panels with prismatic lattice cores. *International Journal of Solids and Structures*, 44(18-19):6101–6123, 2007.
- S.P. Timoshenko and J.M. Gere. *Theory of elastic stability*. McGraw-Hill, 2<sup>nd</sup> edition, 1963.
- R. Törnqvist. *Design of crashworthy ship structures*. PhD thesis, Technical University of Denmark, 2003.
- R. Törnqvist and B.C. Simonsen. Safety and structural crashworthiness of ship structures: modelling tools and application in design. In *Third International Conference on Collision and Grounding of Ships*, pages 25–27, Izu, Japan, 2004.
- T.C. Triantafillou and L.J. Gibson. Minimum weight design of foam core sandwich panels for a given strength. *Materials Science and Engineering*, 95:55–62, 1987a.
- T.C. Triantafillou and L.J. Gibson. Failure mode maps for foam core sandwich beams. *Materials Science and Engineering*, 95:37–53, 1987b.
- J. Urban. *Crushing and fracture of lightweight structures*. PhD thesis, Technical University of Denmark, 2002.
- L. Valdevit, J.W. Hutchinson, and A.G. Evans. Structurally optimized sandwich panels with prismatic cores. *International Journal of Solids and Structures*, 41(18-19):5105–5124, 2004.
- L. Valdevit, A. Pantano, H.A. Stone, and A.G. Evans. Optimal active cooling performance of metallic sandwich panels with prismatic cores. *International Journal of Heat and Mass Transfer*, 49(21-22):3819–3830, 2006a.
- L. Valdevit, Z. Wei, C. Mercer, F.W. Zok, and A.G. Evans. Structural performance of near-optimal sandwich panels with corrugated cores. *International Journal of Solids and Structures*, 43(16):4888–4905, 2006b.
- D.G. Vaughn and J.W. Hutchinson. Bucklewaves. *European Journal of Mechanics - A/Solids*, 25(1):1–12, 2006.

- D.G. Vaughn, J.M. Canning, and J.W. Hutchinson. Coupled plastic wave propagation and column buckling. *Journal of Applied Mechanics*, 72(1):139–146, 2005.
- J.R. Vinson. Sandwich structures: past, present, and future. In O.T. Thomsen, E. Bozhevolnaya, and A. Lyckegaard, editors, *Sandwich structures 7: advancing with sandwich structures and materials, Proceedings of the 7th International Conference on Sandwich Structures*, pages 3–12, Aalborg, Denmark, 2005.
- A.W. Vredeveldt and A.S. Roeters. ADN safety equivalence 550 m<sup>3</sup> gas tanker fitted with Y-type side structure. In *9<sup>th</sup> Symposium on practical design of ships and other floating structures*, pages 317–321, Lubeck-Travemuende, Germany, 2004.
- H.N.G. Wadley. Cellular metals manufacturing. *Advanced Engineering Materials*, 10(4):726–733, 2002.
- J.C. Wallach and L.J. Gibson. Mechanical behavior of a three-dimensional truss material. *International Journal of Solids and Structures*, 38(40-41):7181–7196, 2001.
- G. Wang, K. Arita, and D. Liu. Behavior of a double hull in a variety of stranding or collision scenarios. *Marine Structures*, 13(3):147–187, 2000.
- J. Wang, A.G. Evans, K. Dharmasena, and H.N.G. Wadley. On the performance of truss panels with Kagomé cores. *International Journal of Solids and Structures*, 40(25):6981–6988, 2003.
- Z. Wei, F.W. Zok, and A.G. Evans. Design of sandwich panels with prismatic cores. *Journal of Engineering Materials and Technology*, 128(2):186–192, 2006.
- L.J. Wevers and A.W. Vredeveldt. Full scale ship collision experiments 1998. Technical Report 98-CMC-R1725, TNO, Delft, The Netherlands, 1999.
- N. Wicks and J.W. Hutchinson. Optimal truss plates. *International Journal of Solids and Structures*, 38(30-31):5165–5183, 2001.
- N. Wicks and J.W. Hutchinson. Performance of sandwich plates with truss cores. *Mechanics of Materials*, 36(8):739–751, August 2004.
- H.H. Wisselink. *An analysis of guillotining and slitting - Finite element simulations*. PhD thesis, University of Twente, 2000.
- Z. Xue and J.W. Hutchinson. A comparative study of impulse-resistant metal sandwich plates. *International Journal of Impact Engineering*, 30(10):1283–1305, 2004.

## Bibliography

---

- Y. Yamada and H. Endo. Collapse strength of the buffer bow structure in oblique collision. In *Third International Conference on Collision and Grounding of Ships*, pages 160–171, Izu, Japan, 2004.
- J. Yu, E. Wang, J. Li, and Z. Zheng. Static and low-velocity impact behavior of sandwich beams with closed-cell aluminum-foam core in three-point bending. *International Journal of Impact Engineering*, 35(8):885–894, 2008.
- J.L. Yu, X. Wang, Z.G. Wei, and E.H. Wang. Deformation and failure mechanism of dynamically loaded sandwich beams with aluminum-foam core. *International Journal of Impact Engineering*, 28:331–347, 2003.
- D. Zenkert. *An introduction to sandwich construction*. Warley, West Midlands, UK, 1995.
- S. Zhang. *Mechanics of ship collisions*. Phd thesis, Technical University of Denmark, 1999.
- F.W. Zok, S.A. Waltner, Z. Wei, H.J. Rathbun, R.M. McMeeking, and A.G. Evans. A protocol for characterizing the structural performance of metallic sandwich panels: application to pyramidal truss cores. *International Journal of Solids and Structures*, 41(22-23):6249–6271, 2004.
- F.W. Zok, H.J. Rathbun, M. He, E. Ferri, C. Mercer, R.M. McMeeking, and A.G. Evans. Structural performance of metallic sandwich panels with square honeycomb cores. *Philosophical Magazine*, 85(26-27):3207–3234, 2005.